BIMETALLIC NANOCRYSTALS FOR APPLICATIONS IN PLASMONICS AND CATALYSIS

A Dissertation
Presented to
The Academic Faculty

by

Xiaojun Sun

In Partial Fulfillment
of the Requirements for the Degree
Doctor of Philosophy in the
School of Materials Science and Engineering

Georgia Institute of Technology
December 2017

BIMETALLIC NANOCRYSTALS FOR APPLICATIONS IN PLASMONICS AND CATALYSIS

Approved by:

Dr. Dong Qin, Advisor
School of Materials Science and Engineering
Georgia Institute of Technology

Dr. Vladimir Tsukruk
School of Materials Science and Engineering
Georgia Institute of Technology

Dr. Meilin Liu
School of Materials Science and Engineering
Georgia Institute of Technology

Dr. Z. John Zhang
School of Chemistry and Biochemistry
Georgia Institute of Technology

Dr. Zhiqun Lin
School of Materials Science and Engineering
Georgia Institute of Technology

Date Approved: August 2, 2017

Dedicated to my beloved family.

ACKNOWLEDGEMENT

First and foremost, I express my deepest gratitude to my research advisor, Professor Dong Qin, for her enthusiasm, inspiring guidance, and continuous support throughout my graduate life at Georgia Tech. She gives me her trust for choosing research projects and provides her critical opinions and abundant resources to complete these projects. I sincerely acknowledge Professor Meilin Liu, Professor Vladimir Tsukruk, Professor Zhiqun Lin, and Professor John Zhang for their helpful suggestions and kind considerations to serve on my dissertation committee.

Secondly, I am grateful to all the members of Qin lab and our collaborators. In particular, I appreciate support from Dr. Yin Yang, who generously shared his first-hand experience when I was new to the group. Special thanks go to present and former group members, Yiren Wu, Jae Wan Ahn, Zheyu Luo, Junki Kim, Nina Su, Dr. Yun Zhang, Zhiwei Zhang, Dr. Jumei Li, Dr. Jiawei Zhang, Chia-Wei Wang, and Professor Sarah A. Winget, for their support, encouragement, and delightful moments in the lab. I also sincerely appreciate the support from our collaborators, Professor Younan Xia of Georgia Tech, Professor Jingyue Liu of Arizona State University, Dr. Yong Ding, Dr. Kyle D. Gilroy, Dr. Xuan Yang, Dr. Dong Su, and Dr. Tobias A. F. König, for their contribution to my projects.

Finally, I am indebt to my parents, Mr. Zhixiong Sun and Ms. Yufang Huang, for their unconditional support and boundless love over the years. And lastly, I owe my special thanks to Miss Yingge Zhang for all her love and support.

TABLE OF CONTENTS

LIST OF TABLES

LIST OF FIGURES

LIST OF SYMBOLS AND ABBREVIATIONS

k	wave factor
γ	surface energy
ε_r	real part of dielectric constant
ε_i.	imaginary part of dielectric constant
Ag	silver
$AgNO_3$	silver nitrate
Ag_2O	silver oxide
4-AP	4-aminophenol
4-ATP	4-aminothiophenol
Au	gold
1,4-BDT	1,4-benzenedithiol
C_{abs}	absorption cross section
C_{ext}	extinction cross section
C_{scat}	scattering cross section
CA	citric acid
CTAC	cetyltrimethylammonium chloride
CV	cyclic voltammetry
DDA	discrete dipole approximation
DI	deionized
ECSA	electrochemical active surface areas
EDS	energy dispersive X-ray spectroscopy

EELS	electron energy loss spectroscopy
EF	enhancement factor
E-fields	electromagnetic fields
EG	ethylene glycol
$E_{out}\omega$	incident excitation
$E_{out}(\omega\text{-}\omega_v)$	Stokes shifted Raman electromagnetic fields
$Fe(NO_3)_3$	iron nitrate
HAABF-STEM	high-angle annular bright-field scanning transmission electron microscopy
HAADF-STEM	high-angle annular dark-field scanning transmission electron microscopy
$HAuCl_4$	chloroauric acid
H_2Asc	ascorbic acid
$HAsc^-$	ascorbate monoanion
H_2O_2	hydrogen peroxide
ICP-MS	inductively coupled plasma mass spectrometer
$I_{SERS}\omega_v$,	enhanced Raman intensity
$I_{NRS}\omega_v$,	normal Raman intensity
j_K	kinetic current density
$j_{k,mass}$	mass activity
$j_{k,specific}$	specific activity
LSP	localized surface plasmon
LSPR	localized surface plasmon resonance

$NaBH_4$	sodium borohydride
NaOH	sodium hydroxide
Na_2PdCl_4	sodium tetrachloropalladate
N_{surf}	number of molecules bound to the metal surface
N_{vol}	number of molecules in excitation volume
NIR	near-infrared
4-NP	4-nitrophenol
4-NTP	4-nitrothiophenol
ORR	oxygen reduction reaction
Pd	palladium
PDMS	polydimethylsiloxane
PEMFC	proton-exchange membrane fuel cells
R_{gal}	rate of galvanic replacement reaction
R_{red}	rate of reduction reaction
RDE	rotating disk electrode
PSP	propagating surface plasmon
Pt	platinum
PVP	poly(vinylpyrrolidone)
Q	quality factor
R	radius
SEM	scanning electron microscopy
SERS	surface-enhanced Raman scattering
TEM	transmission electron microscopy

trans-DMAB	*trans*-4,4’-dimercaptoazobezene
XPS	X-ray photoelectron spectroscopy

SUMMARY

Bimetallic nanocrystals have received growing interest owing to their diversified properties and promising applications. Seeded growth serves as a powerful route to bimetallic nanocrystals but its capability is limited by galvanic replacement reaction when the seed is more reactive than the deposited metal. This dissertation documents two strategies for achieving galvanic replacement-free seeded growth of a second metal (M: Au, Pd, or Pt) on Ag nanocrystals. The first strategy relies on the co-titration of $AgNO_3$ and a precursor to M for the generation of Ag and M atoms *via* co-reduction, followed by the co-deposition on Ag nanocubes for the generation of Ag@Ag-M core-frame nanocubes. The resultant Ag@Ag-Au core-frame nanocubes exhibit enhanced surface-enhanced Raman scattering (SERS) activity at an excitation wavelength of 785 nm. On the other hand, the Ag@Ag-Pd nanocubes can play as a dual catalyst for probing stepwise catalytic reduction and oxidation reactions by SERS. The second strategy involves the use of hydroxide to transform Ag nanocubes into Ag@Au and Ag@Pt core-shell nanocubes under an alkaline condition. Upon the removal of Ag cores, the Ag@Au core-shell nanocubes can be converted into Au nanoboxes with wall thickness less than 2 nm and well-defined openings at corners. These nanoboxes embrace strong absorption in the near-infrared region for potential biomedical applications. In comparison, the Ag@Pt nanocubes can be transformed into Pt-based nanocages. These nanocages exhibit improved catalytic activity toward the oxygen reduction reaction (ORR). Collectively, this work greatly expands the utility of seeded growth for the rational design and synthesis of bimetallic nanocrystals with well-defined structures and desired properties.

CHAPTER 1. INTRODUCTION

1.1 Noble-Metal Nanocrystals

In the bulk form, noble metals embrace incredible values because of their rarity in the Earth's crust and their popular use in metallurgy and ornamentation.[1] When shrinking down to nanoscale structures, they play important roles in the development of new applications in catalysis,[2–4] sensing,[5,6] bio-imaging,[7,8] and biomedicines[9,10] owing to their unique properties arising from size confinement. For example, when the size of a metal nanostructure is smaller than the wavelength of incident light, the free electrons in the metal will interact with the light strongly through a phenomenon known as surface plasmonic resonance.[11–14] In this case, the metal nanostructure can serve as an "antenna" to convert light into localized electromagnetic fields (E-fields), and ultimately have it directed to desired directions/locations. By controlling the size, shape, and composition of a nanostructure, one can effectively manipulate the light with remarkable accuracy.[15] Among various noble metals, silver (Ag) and gold (Au) are the two promising plasmonic materials, and their unique properties make them well-suited for a wide variety of photonic applications.[16–18] On the other hand, palladium (Pd) and platinum (Pt) are extremely valuable metals owning to their exceptional and unique properties as a heterogeneous catalyst. For example, Pd nanoparticles have been widely used in the catalytic converters that could transform up to 90% of the harmful exhaust into less harmful substances such as CO_2 and N_2.[19] Pd is also remarkable for its extraordinary capacity to absorb H_2. For example, it can absorb up to 900 times of its own volume of H_2 at room temperature,

making it an efficient and safe storage medium for H_2.[20] In comparison, Pt is an effective catalyst toward many reactions that include CO oxidation in catalytic converters, nitric acid production, petroleum cracking, and oxygen reduction reaction (ORR) in proton-exchange membrane fuel cells (PEMFC).[21–25]

1.1.1 Localized Surface Plasmon Resonance (LSPR)

Ag is arguably the most important material in plasmonics. Plasmonic nanostructures can generate propagating surface plasmons (PSPs) or localized surface plasmons (LSPs) depending on their geometric shapes and dimensions.[26,27] For example, PSPs will be excited when light interacts with a Ag nanowire with one dimension larger than the wavelength of light (Figure 1.1A). Because the electric field associated with the light (E_0) is not uniform across the structure, the excited free electrons would create PSP traveling along the surface of the nanowire.[28] In contrast, LSPs are supported by structures such as a Ag nanosphere with three dimensions that are much smaller than the wavelength of incident light (Figure 1.1B).[29] In this case, the nanosphere would experience uniform E_0, and as a result, the conduction electrons can be displaced from the surface followed by their oscillation collectively. When the frequency of incident photons matches the natural frequency of surface electrons, the resonance condition will be fulfilled to achieve strong oscillation known as localized surface plasmon resonance (LSPR).

Mie theory is often used to describe the LSPR by calculating the extinction cross section (absorption and scattering) of a metal nanosphere:[30]

$$C_{ext} = \frac{24\pi^2 R^3 \varepsilon_m^{3/2}}{\lambda}\left[\frac{\varepsilon_i}{(\varepsilon_r + 2\varepsilon_m)^2 + \varepsilon_i^2}\right] \qquad \text{(Eq.1)}$$

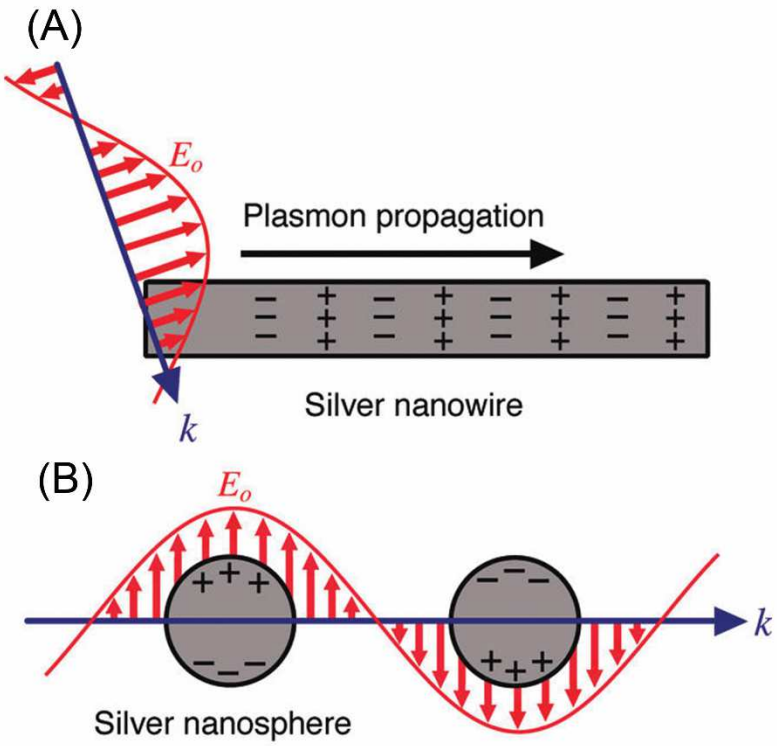

Figure 1.1. Schematic illustration of two types of plasmonic nanostructures excited by an incident light with a wave vector of k and an electric field of E_0: (A) a silver nanowire with one dimension much greater than the wavelength of light; and (B) a silver nanosphere with a radius much smaller than the wavelength of light. Copyright 2011 American Chemical Society.[34]

where C_{ext} is the extinction cross section, R is the radius, and ε_m is the relative dielectric constant of the medium. This equation indicates that the interaction between a metal nanosphere and light depends strongly on the dielectric constants of the metal (ε_r and ε_i). To accomplish the resonance condition with maximized C_{ext}, both the term of $\varepsilon_r + 2\varepsilon_m$ and ε_i should be close to zero if the radius of the nanosphere and $\varepsilon_m^{3/2}$ are fixed. Typically, Ag and Au have negative values of ε_r and extremely small values of ε_i (Figure 1.2), making them good candidates for fulfilling the requirement of resonance condition.

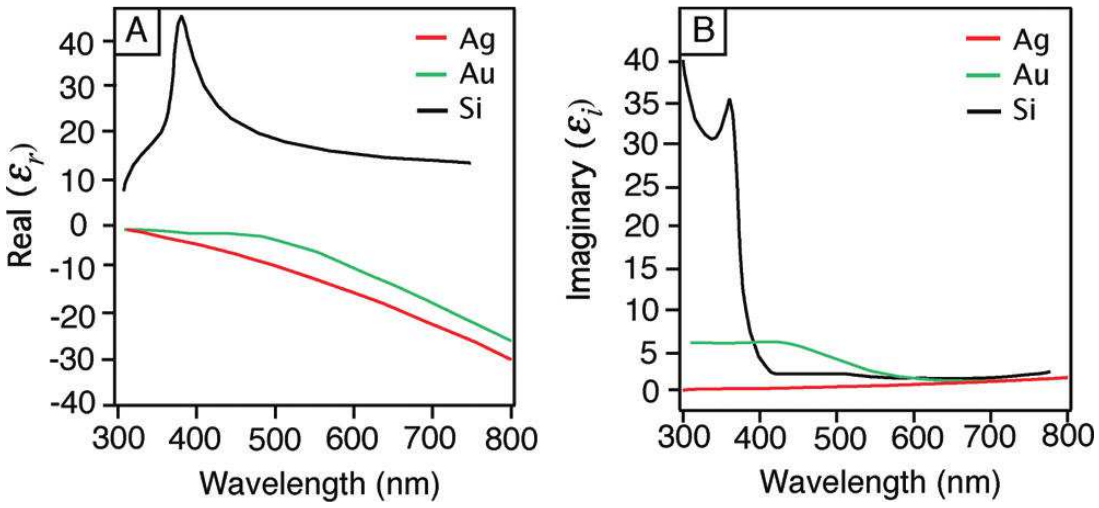

Figure 1.2. Plot of the (A) real, ε_r, and (B) imaginary, ε_i, components of the dielectric function of Ag, Au, and Si as a function of wavelength. Copyright 2011 American Chemical Society.[34]

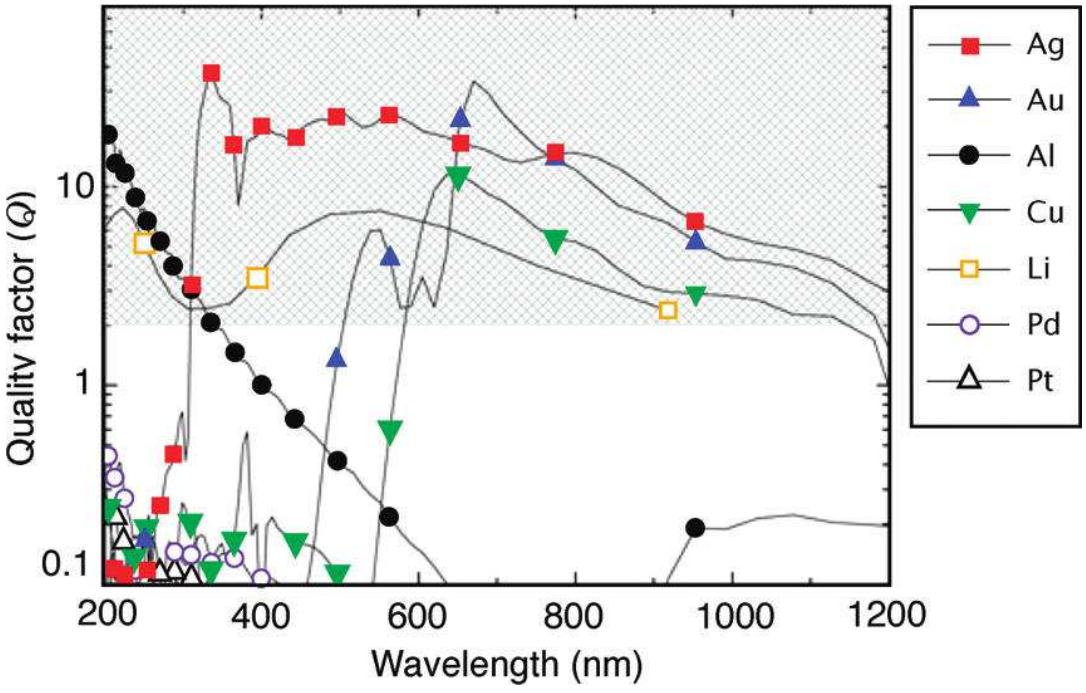

Figure 1.3. Quality factor (Q) of the LSPR for a metal/air interface. A higher Q denotes less damping and thus a stronger plasmon resonance. The shaded area represents the region of interest for many plasmonic applications. Copyright 2009 Elsevier.[31]

Another approach is to compare the surface plasmon strength of different metals with respect to wavelength is to introduce the quality factor (Q):[31]

$$Q = \frac{w(d\varepsilon_r / dw)}{2(\varepsilon_i)^2} \qquad \text{(Eq.2)}$$

In Figure 1.3, the Q values are plotted for a number of metals, among which Ag exhibits the highest Q across the spectrum from 300–1100 nm. In comparison, other metals can only reach a relative high value with a narrow coverage of wavelength. For example, Au and Cu, are only suitable in the range from 500–900 nm.[32] While Li has a high value of Q in the range of 300–1000 nm, it is too reactive to handle in a practical manner. It is also worth mentioning that both Pd and Pt are extremely poor plasmonic materials because of the very weak coupling between their free electrons and visible light, but they are excellent catalysts for a large number of chemical reactions.

It has been well-established that the plasmonic properties of metal nanostructures can be manipulated by a set of physical parameters that include size, shape, morphology, and chemical composition. Using Ag nanocrystals as a model system, the most straightforward approach to tailor the LSPR properties is to manipulate their sizes.[27,30,33,34] For example, Xia and his co-workers have demonstrated that the LSPR peak of Ag nanocubes can be tuned from 420 to 600 nm by increasing the edge length from 36 to 172 nm.[35] With an increase in size, the charge separation would become larger and ultimately the electron oscillation would become slower, leading to a red shift for the LSPR peak position. Amazingly, such a linear relationship between edge length and in-plane dipole LSPR peak can serve as a simple criterion for the preparation of Ag nanocubes with different edge lengths. For example, in a typical synthesis, one can monitor the growth of

Ag nanocubes by monitoring the change in the LSPR peak position.[36] On the other hand, the size can control the ratio of absorption to scattering.[30] When the radius (R) of a nanoparticle is much smaller than the wavelength of light ($2\pi R << \lambda$), the absorption and scattering cross sections are directly proportional to R^3 and R^6, respectively.[37] Figure 1.4 shows the absorption, scattering and extinction spectra calculated for Ag nanospheres of 40 and 140 nm, respectively, in diameter.[38] For the 40-nm sphere, scattering is slightly stronger than absorption. When the size is increased from 40 to 140 nm, scattering is predominant with a cross section that is 30 times greater than that of absorption.

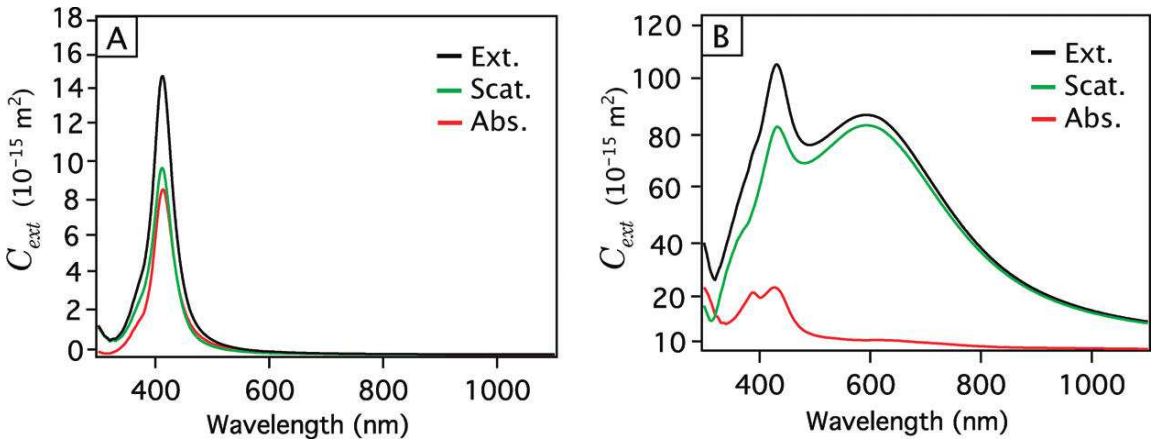

Figure 1.4. (A) Extinction (black, experimental result), scattering (green), and absorption (red) spectra of Ag nanospheres (A) 40 nm and (B) 140 nm, respectively, in diameter calculated using Mie theory in water. The extinction spectrum of the larger spheres is dominated by scattering and has a broad shoulder owing to the contributions from the quadrupole plasmon modes. The smaller sphere exhibits a narrow LSPR peak, and the absorption and scattering cross sections are nearly equivalent. Copyright 2011 American Chemical Society.[34]

The LSPR properties are highly sensitive to the change in shape or morphology of Ag nanocrystals.[39] Figure 1.5, A-D, shows the TEM images of the 58-nm Ag nanocubes before and after a solvothermal process in the presence of 0.1 mM PVP for 1, 3, and 6 h, respectively. A significant change in morphology for the Ag nanocubes was observed, starting from relinquishment of sharp corners and edges, followed by continuous rounding toward the formation of Ag nanospheres by t = 6 h. Figure 1.6 shows UV-vis spectra taken from the aqueous suspension of Ag nanocrystals obtained at time points shown in Figure 1.5. For the original 58-nm Ag nanocubes, the UV-vis spectrum showed a strong peak at 468 nm (peak 1), two shoulders at 430 nm (peak 2) and 386 nm (peak 3), and a weak peak at 348 nm (peak 4), respectively. Calculations with the discrete dipole approximation (DDA) method indicates that the physical origins of peaks 1 and 3 can be attributed to dipole resonances while that of peak 2 can be ascribed to a quadrupole resonance, and that the dipole contribution is significantly stronger in quantity.[43] However, both DDA and finite difference time domain (FDTD) electrodynamics calculation have not yet predicted the existence of peak 4. During the evolution from cubes to spheres, the strong dipole peak 1 was blue shifted with its intensity being retained at the same level while the weak dipole peak 3 was only in presence for the cubes. This observation may result from the increase in symmetry of nanocrystals during the transformation from cubes to spheres. The quadrupole peak 2 was also blue-shifted with a gradual decrease in intensity. The unassigned peaks 4 showed a trend similar to that of the weak dipole resonance peak 3, suggesting that both peaks might arise from the sharp edges and corners of the Ag nanocubes. In principle, nanocrystals with sharp corners could facilitate the charge separation and thereby the electron oscillation is hindered, resulting in reduced resonance

frequency (with the dipole LSPR peak shifted to the red). The sharpness of corners also affects the E-fields created in the proximity to the surfaces of nanocrystals.[18,40,41] For example, a Ag nanocube with sharp corners and edges can generate E-fields that are 2,000 times stronger than those created by a Ag nanosphere with a similar size.[42]

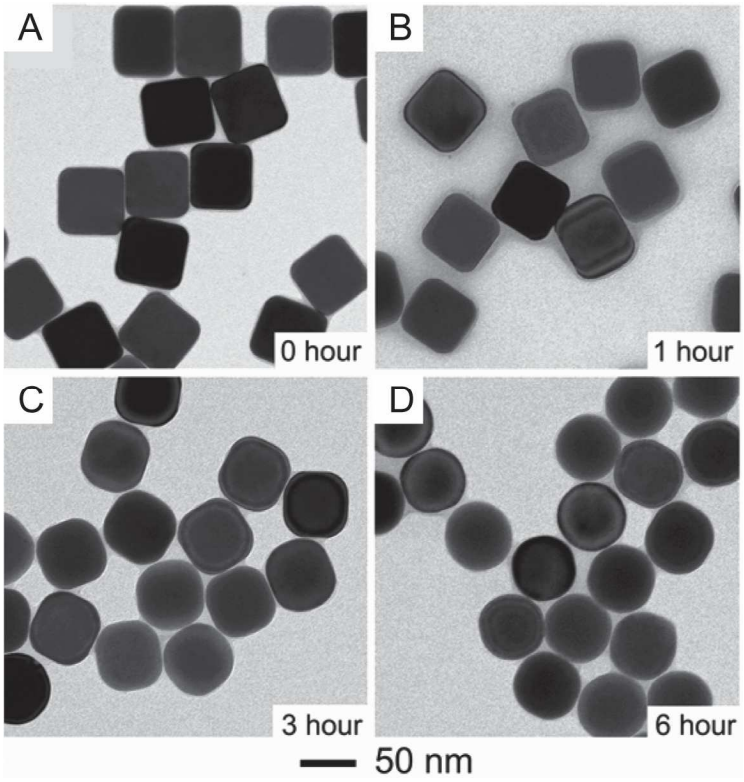

Figure 1.5. TEM images of Ag nanocubes after treatment in DI water at 160 ºC for (A) 0, (B) 1 (C) 3, and (D) 6 h.

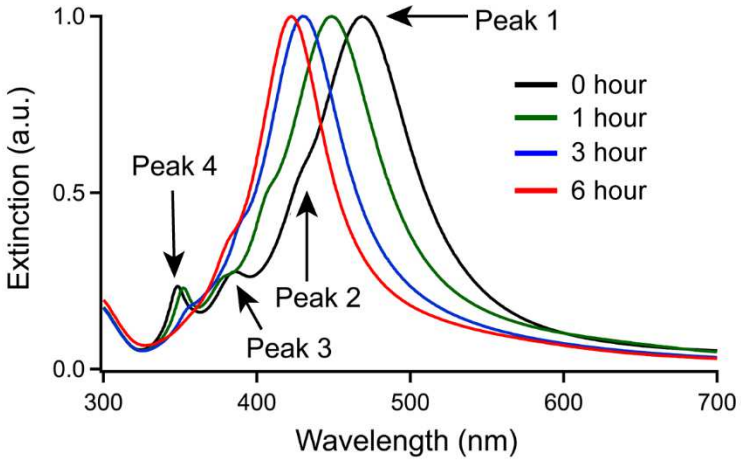

Figure 1.6. UV-vis spectra of Ag nanocubes with different extents of truncation at corners.

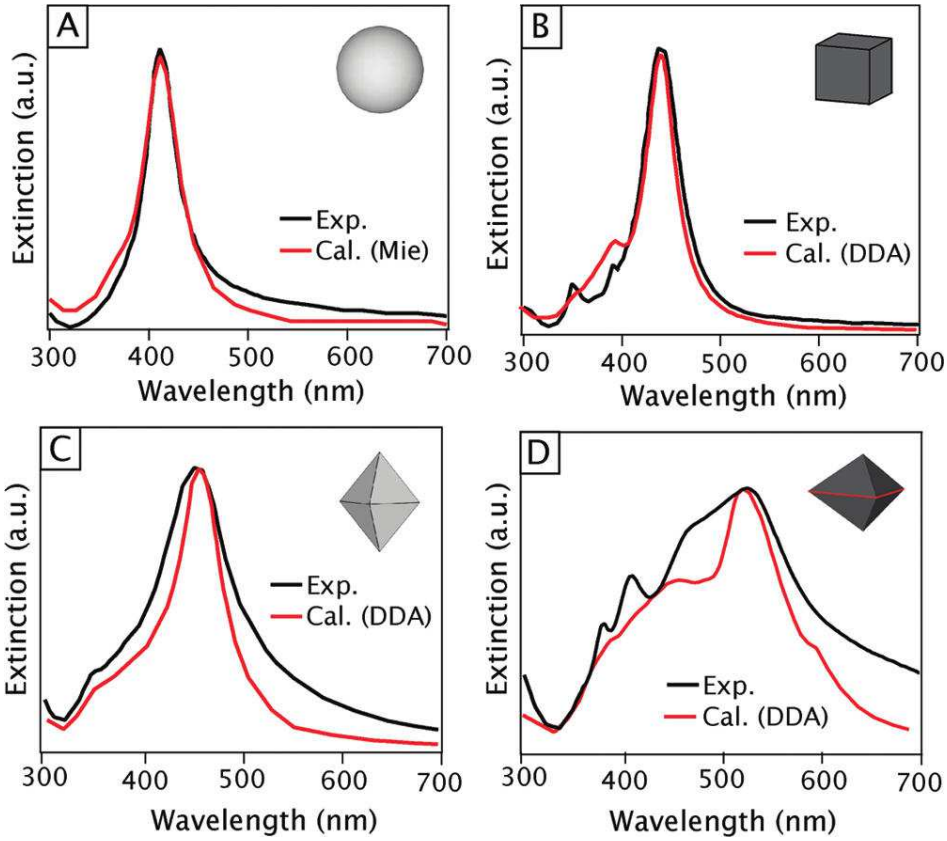

Figure 1.7. Experimental (black) and calculated (red) extinction spectra of: (A) Ag nanospheres with a diameter of 40 nm; (B) cubes with an edge length of 40 nm; (C) octahedrons with an edge length of 40 nm; and (D) right bipyramids with an edge length of 75 nm. Copyright 2011 American Chemical Society.[102]

Figure 1.7 shows the extinction spectra of Ag nanocrystals with a set of geometric shapes (sphere, cube, bipyramid, and octahedron). The spectra are calculated using the Mie theory (for the sphere) and DDA method (for other shapes), respectively, together with the experimental data.[35,43] Based on these observations, one can easily understand the rules of thumb for controlling the LSPR properties by tailoring the shape or morphology of a nanocrystal. Firstly, the number of LSPR peaks increases as the symmetry of nanocrystals decreases. For example, the nanosphere only has one peak located around 420 nm while the nanocube and bipyramid embrace two or more than three distinctive peaks. With higher symmetry, the electrons in a nanocrystal will have less polarization modes. In comparison, the electrons in nanocrystals with a lower symmetry can be polarized along multiple directions, leading to several extinction peaks. It is also anticipated that nanocrystals with centrosymmetric element (such as sphere, cube, octahedron) is essential to the formation of strong dipole, contributing to strong absorption and scattering properties.

Secondly, by creating hollow interiors, the LSPR peaks of metal nanostructures can be greatly shifted to the red while maintaining the size of the structure.[44] Figure 1.8 shows LSPR spectra of aqueous suspensions of Ag nanocubes before and after they had reacted with different amounts of $HAuCl_4$ in the presence of a reducing agent as such ascorbic acid. The LSPR peak of the Ag nanocubes was continuously shifted from 434 to 566 nm during the transformation of Ag nanocubes into Ag-Au hollow nanocubes.[44,45]

Thirdly, because Au and Ag nanocrystals have their own distinctive LSPR properties, the LSPR properties of the resultant nanoparticles made of Ag-Au alloys are sensitive to the elemental composition.[46] Figure 1.9 shows the UV-vis spectra of Au-Ag alloy nanoparticles that were prepared in an aqueous solution through the co-reduction of

$HAuCl_4$ (Au precursor) and $AgNO_3$ (Ag precursor) at various mole fractions, with sodium citrate serving as a reducing agent.[47] It was found that the LSPR peak position of Au nanoparticles was blue-shifted linearly with the increase in Ag content.

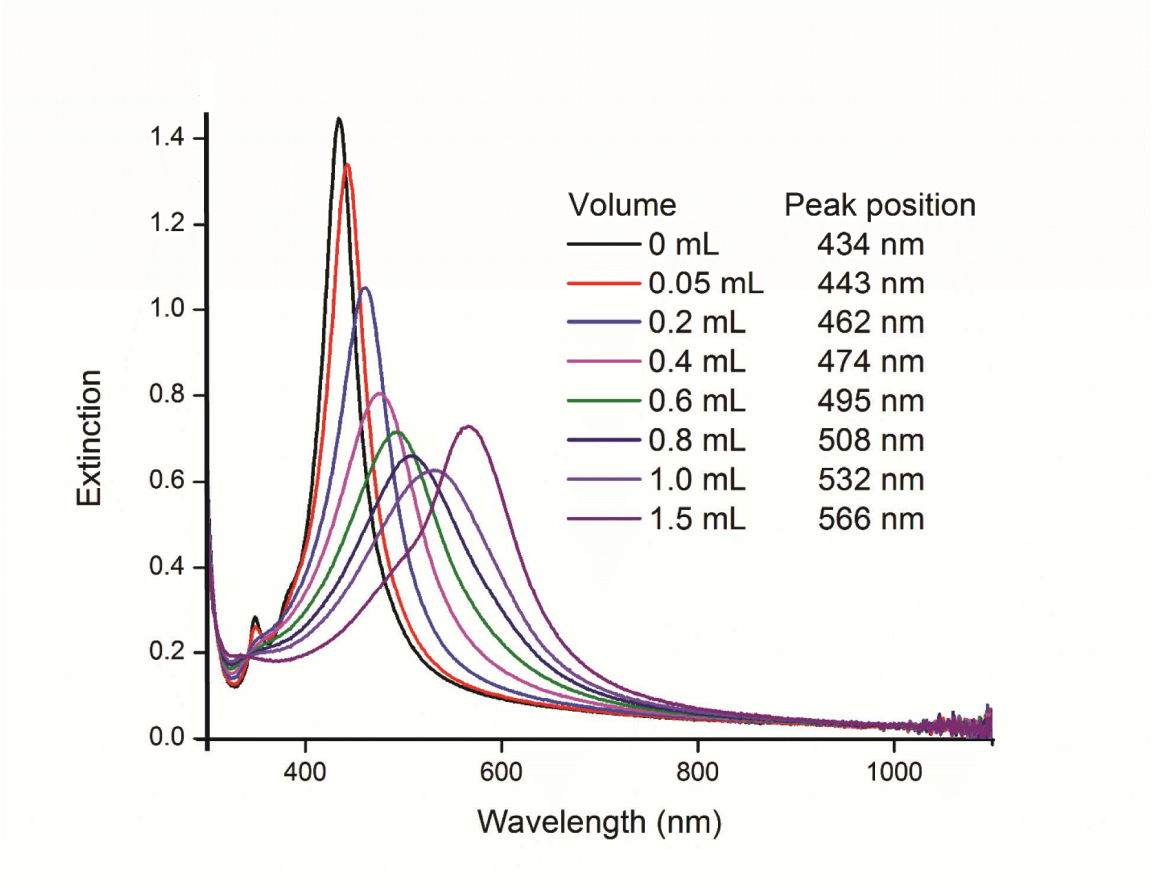

Figure 1.8. UV-vis spectra of Ag nanocubes before and after they had reacted with increasing amounts of $HAuCl_4$ in the presence of a reducing agent such as ascorbic acid.

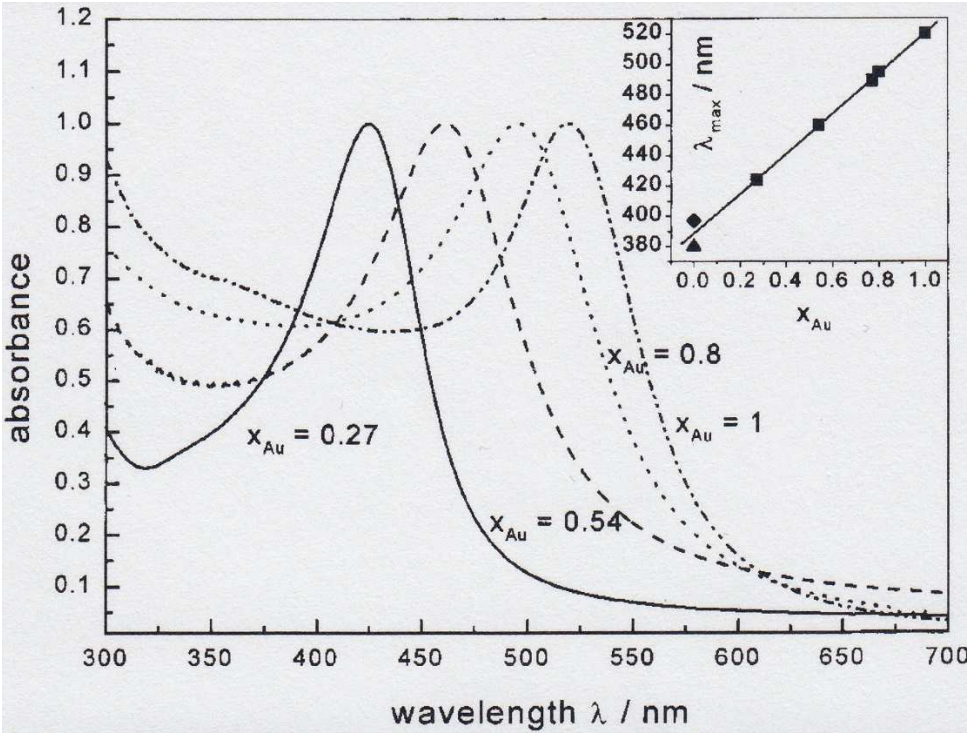

Figure 1.9. UV-vis spectra of Au and Au-Ag alloy nanoparticles with varying Au mole fraction, χ_{Au}. The inset shows how the absorption maximum of the plasmon band depends on the composition. Copyright 1999 American Chemical Society.[126]

1.1.2 Surface-Enhanced Raman Scattering (SERS)

Raman spectroscopy can reveal the "fingerprint" information of molecules from their vibrational transitions.[48] Unfortunately, the extremely small Raman scattering cross section, typically between 10^{-30} and 10^{-25} cm^2 per molecule,[49] makes it challenging to compete with laser-induced fluorescence spectroscopy (with a cross section on the order of 10^{-16} cm^2 per molecule) for trace detection.[50] Since the discovery by Van Duyne and Jeanmaire in 1977,[51] surface-enhanced Raman spectroscopy (SERS) has emerged as a powerful tool for detecting the molecules adsorbed on metal nanostructures with unprecedented sensitivity. After several decades of exploration, it is well-established that

SERS relies on the enhancement of electromagnetic fields around a metal nanostructure to enlarge the Raman scattering cross sections of molecules in proximity to the surface. To this end, many groups have demonstrated that Ag and Au nanocrystals with sharp corners and edges could enhance the Raman scattering cross by 10^{10} or 10^{11} folds in terms of enhancement factor (EF).[48,52] Also, it was found that the SERS activity of Ag nanocrystals was at least one order of magnitude higher than Au nanocrystals with a similar size and shape.[34] As a result, Ag-based SERS substrates have been extensively used for the trace detection of chemical and biological species.[53–57] Unfortunately, the susceptibility of Ag to oxidation often results in changes to the morphology and thereby deterioration of their SERS performance.

In a typical SERS measurement, EF is often used to quantify the effect of the amplification using the following equation:[58,59]

$$EF_{SERS}(\omega_\upsilon)=\frac{\left|E_{out}(\omega)^2\right|\left|E_{out}(\omega-\omega_\upsilon)^2\right|}{E_0^4}=\frac{[I_{SERS}(\omega_\upsilon)/N_{surf}]}{[I_{NRS}(\omega_\upsilon)/N_{vol}]} \qquad \text{(Eq. 2)}$$

where $E_{out}(\omega)$ and $E_{out}(\omega-\omega_\upsilon)$ are the incident excitation and the resulting Stokes' shifted Raman electromagnetic fields, respectively. In practice, EF is calculated using the enhanced Raman intensity $I_{SERS}(\omega_\upsilon)$, the number of molecules bound to the metal surface N_{surf}, the normal Raman intensity $I_{NRS}(\omega_\upsilon)$, and the number of molecules in the excitation volume N_{vol}. The major challenge in calculating EF arises from the challenges in the accurate estimation of the number of molecules adsorbed on the surface.

1.1.3 Catalytic Properties

Among all the noble metals, Pt and Pd exhibit remarkable catalytic activity toward a wide range of reactions in industrial processes.[24,60–62] Today, the catalyst commonly used for oxygen reduction reaction (ORR) is based on 3-5 nm Pt nanoparticles supported on carbon (Pt/C). Because of the low specific activity and poor stability associated with such small particles with poorly defined shapes, a large amount of Pt is often required for their deposition on the cathode of a PEMFC device. One approach to reduce the use of Pt is to develop nanoparticles with hollow interiors and porous walls such as Pt-based nanocages.[63–68] In this structure, the Pt atoms located on the inner surface can also participate in the catalytic reaction, making it possible to achieve higher specific surface areas and thus improved mass activities. On the other hand, Pd is an important catalyst in the catalytic converters for CO oxidation, making it a good substitute of Pt because it offers comparable activity at much lower cost. Because Pd has the lowest energy barrier to the dissociation of H_2 into atomic hydrogen for the hydrogenation reaction of unsaturated compounds, Pd nanoparticles have the capacity to adsorb high volume of H_2, making them a great catalyst for hydrogenation and dehydrogenation reactions.[69,70] Additionally, Pd exhibits catalytic activity toward Suzuki,[71] Stille,[72] and Heck coupling reactions.[73,74] It is also worth mentioning that Au and Ag exhibit catalytic activities toward certain specific reactions. For example, Au nanoparticles with size smaller than 2 nm have been used as the catalyst for CO oxidation,[75] and Ag nanoparticles are often used as a catalyst for epoxidation reaction.[76]

1.2 Synthesis of Noble-Metal Nanocrystals

1.2.1 Synthesis of Silver Nanocrystals

The ability to synthesize Ag nanocrystals in a solution phase with controls in size and shape has created many excellent opportunities to develop plasmonic applications.[77–79] In a typical reaction, Ag(I) precursor is mixed with a reducing agent and a colloidal stabilizer in a solvent. Under desired reaction conditions, the Ag^+ ions are reduced to generate small clusters, which undergo nucleation and finally grow into the desired shape and size. Over the past several decades, the following methodologies have been developed for the production of Ag nanocrystals.

Citrated reduction: Lee and Meisel reported the synthesis of Ag nanoparticles by reducing $AgNO_3$ with citrate in an aqueous solution.[80] Because the reaction is conducted at an elevated temperature, it is extremely difficult to control the uniformity of the resultant nanoparticles. Additionally, it is very challenging to produce Ag nanoparticles with well-defined shapes because the growth mechanism remains elusive.[81–83]

Silver mirror reaction: Since the discovery by Justus von Liebig in 1835, this reaction has been widely used to coat Ag on other metal substrates in large quantity:[84]

$$RCHO + 2Ag\left(NH_3\right)_2^+ + 2OH^- \longrightarrow RCOOH + 2Ag + 4NH_3 + H_2O$$

In a typical process, $AgNO_3$ is the precursor to generate $Ag\left(NH_3\right)_2^+$ that is further reduced by an aldehyde-containing compound to produce elemental Ag. This reaction has been extended to prepare Ag nanoparticles with relative narrow size distribution, but it is still impossible to control the shape of the final products.

Polyol synthesis: As the most robust and versatile route to the preparation of Ag nanocrystals with controls in size and shape, one can maneuver the experimental parameters, such as temperature, concentrations of reagents, presence of trace ions, and

choice of reagents, to produce desired nanostructures such as wires, rods, right bipyramids, beams, cubes, and octahedrons.[16,78,85–87] In a typical process, ethylene glycol serves as the reducing agent and solvent.[77,88] Upon reduction of Ag(I) precursor to Ag element, the accumulation of Ag atoms leads to the formation of small Ag clusters, followed by their further growth into single-crystal, single-twinned, or multi-twinned seeds. Each type of seeds could continue to grow into products with different shapes using a capping agent to passivate various types of facets on the Ag seeds. For example, the capping of poly(vinylpyrrolidone) (PVP) and citrate toward {100} and {111} facets of Ag would lead to the formation of Ag nanocubes and octahedrons, respectively.[89]

1.2.2 Synthesis of Noble-Metal Nanocrystals *via* Seeded Growth

Unlike the methods listed in the aforementioned discussion, seeded growth uses the preformed nanocrystals as seeds for further growth, making it possible to separate nucleation from growth for the syntheses of mono- and bi-metallic nanocrystals with exquisite controls in size, shape, and composition.[90–93] In general, there are two categories of seeded growth: homogeneous and heterogeneous growth. When the seed crystal is composed of the same metal as the atoms being deposited on the surface, it is referred to as a homoepitaxial process. A typical example includes the growth of Ag on Ag seeds.[94,95] Alternatively, when the seeds and the added atoms are chemically different, it is defined as a heteroepitaxial process. In this case, if the metal being deposited has the same crystalline structure and lattice constant as the seed, the crystal structure of the seed would be transferred to the bimetallic nanocrystals *via* epitaxial overgrowth in an alloy, core-frame, or core-shell structure.[96–98]

Seeded growth was initially demonstrated by Murphy for the growth of Au nanorods with Au-based seeds[99] and by Xia for the synthesis of Ag nanowires with Pt-based seeds.[100] In recent years, this method has been extensively explored by many research groups and successfully extended to essentially all the noble metals in a mono- or bimetallic format.[71,97,99,101–108] By maneuvering the reduction kinetics involved in a growth process, it has also become feasible to control the growth pattern and thus symmetry of the resultant nanocrystals.[109–111] Despite the remarkable success, the capability of seeded growth is, however, critically limited by galvanic replacement when the deposited metal is less reactive than the seed (*e.g.*, when Ag nanocrystals are used as seeds for the growth of Au, Pd, or Pt). The involvement of galvanic replacement not only makes it hard to control the pathway and outcome of seeded growth but also places a fundamental restriction on the type of bimetallic nanocrystals that could be prepared through seeded growth.

1.2.3 Synthesis of Hollow Nanostructures by Galvanic Replacement Reaction

Galvanic replacement is an electrochemical process that involves the oxidation of a sacrificial metal template by ions of another metal having a higher reduction potential. It has been actively explored as a versatile route to the syntheses of bimetallic nanostructures with hollow interiors and highly tunable compositions, as well as novel optical and catalytic properties.[60,61,112–119] For example, the galvanic replacement reaction between Ag nanocubes and $HAuCl_4$ has been employed to produce hollow nanostructures made of Ag-Au alloys, together with porous walls. In a typical process, Au atoms are derived from a Au(III) precursor at the expense of three Ag atoms, followed by their deposition onto the surface of a Ag nanocube. Ultimately, the Ag nanocube is transformed into a nanobox and

then a nanocage through the interplay of alloying and dealloying between Au and Ag. In contrast to Ag nanocubes with their LSPR peaks positioned around 420 nm, these Ag-Au nanoboxes and nanocages exhibit LSPR peaks precisely tunable in the range of 500 nm to 1200 nm.[120,121] Likewise, galvanic replacement will also occur when Ag nanocubes are mixed with Na_2PdCl_4 or K_2PtCl_4 in an aqueous solution, leading to the formation of Ag-Pd or Ag-Pt bimetallic hollow nanostructures with tunable compositions and interesting catalytic properties.[62,113,114]

1.3 Motivation of the Research

Silver is arguably the best choice of material for plasmonics and related applications owing to its relatively low cost and favorable dielectric functions. The significant progress in the synthesis of Ag nanocrystals with controlled shapes and sizes provide many opportunities to tailor their properties and thus optimize their performance in a range of applications. In particular, Ag nanocrystals have been prepared with sharp features (*e.g.*, edges and corners) on the surface to drastically augment their SERS activity.[122] However, the sharp features tend to vanish due to the high susceptibility of Ag toward oxidative etching.[123] As another pitfall, Ag is limited in terms of catalytic application as it only shows activity toward oxidation reactions such as epoxidation,[124] not reduction reactions.

One can address the aforementioned limitations of Ag nanocrystals by introducing a second noble metal (M) such as Au, Pd, or Pt to generate Ag-M bimetallic nanocrystals.[125] In principle, Ag-M bimetallic nanocrystals can take at least three different configurations, in the form of alloy, core-frame, and core-shell, respectively. An alloy is a solid solution,

in which the Ag and M atoms are miscible to each other at the atomic scale. In the case of Ag and Au, alloy nanocrystals with tunable compositions can be obtained *via* a co-reduction route.[126] However, it is challenging to manipulate and control the shape taken by the alloy nanocrystals, primarily due to the lack of a capping agent that can selectively bind to the same facet of different metals. As for the Ag-M core-frame and core-shell nanocrystals, they can be readily prepared using seeded growth by simply depositing M atoms on the surface of preformed Ag nanocrystals. This approach immediately benefits from the large number of Ag nanocrystals that have been prepared with well-controlled shapes. When the M atoms are selectively deposited on the edges of a Ag nanocrystal, for example, a Ag@M core-frame nanocrystal is formed.[127] In this structure, the excellent plasmonic and SERS properties of the Ag core are well retained while the deposited M can bring in new catalytic capabilities. Alternatively, when the M atoms are conformally deposited on the entire surface, a Ag@M core-shell nanocrystal is created.[128] In this case, the M shell can greatly improve the chemical stability of the particle, in addition to the new catalytic properties associated with M. If the shell is kept below 1-2 nm thick, the excellent plasmonic and SERS properties of the Ag core can still be leveraged. Significantly, both SERS and catalytic properties can be integrated in the core-frame and core-shell nanocrystals to offer a unique probe for *in situ* detection and analysis of catalytic reactions by SERS.

1.4 Scope of the Research

The aim of this work is to develop galvanic-free seeded growth of a second metal M (M: Au, Pd, and Pt) on Ag nanocrystal seeds for the generation of Ag@M core-frame

and core-shell bimetallic nanocrystals and their derivatives. Our strategy involves the use of a parallel reaction to compete with and thus suppress the galvanic reaction. When Ag nanocrystals are mixed with a salt precursor to M in the presence of a reducing agent, the added M^{n+} can be reduced by both the Ag seeds (*via* galvanic replacement at a rate of R_{gal}) and reducing agent (*via* chemical reduction at a rate of R_{red}). Under $R_{red} > R_{gal}$, M^{n+} will be primarily reduced by the reducing agent instead of participating in the galvanic replacement. When self-nucleation is eliminated by titrating the precursor in a dropwise fashion, the M atoms derived from the chemical reduction can be directed to nucleate from the surface of the Ag seeds, generating Ag-M bimetallic nanocrystals with a core-frame or core-shell structure. The dissertation is organized into two main sections: *i*) galvanic-free seeded growth of M on Ag nanocubes for the generation of Ag@Ag-M core-frame nanocubes and Ag@M core-shell nanocubes, and *ii*) fabrication of Au-based nanoboxes and Pt-based nanocages for applications in plasmonics and catalysis.

In Chapter 2, with the use of Ag nanocubes as a model system, we describe one approach to the replacement-free synthesis of Ag@Ag-M (M: Au and Pd) core-frame nanocubes through seeded growth. The strategy involves the co-titration of aqueous M^{n+} and Ag^{+} ions into precursor into an aqueous mixture of Ag nanocubes, ascorbic acid (H_2Asc, a reducing agent), and PVP (a colloidal stabilizer) at pH = 3.2 under ambient condition. Because the added Ag^{+} ions are able to push the galvanic replacement backward, R_{gal} can be reduced to attain $R_{red} > R_{gal}$. As the proof-of-concept, we demonstrate the fabrication of Ag@Ag-Au core-frame nanocubes by co-titrating $AgNO_3$ and $HAuCl_4$ into an aqueous suspension of Ag nanocubes. When the molar ratio of $AgNO_3$ to $HAuCl_4$ is larger than three, we discover that the added Ag^{+} ions could effectively push the galvanic

replacement reaction between Ag nanocubes and $HAuCl_4$ backward and thus inhibit it, making it possible to achieve the co-reduction of the two precursors by H_2Asc without involving any galvanic replacement. By increasing the volumes of the two co-titrated precursors, we validate that the added $AgNO_3$ and $HAuCl_4$ are completely reduced to Ag and Au atoms, respectively, followed by their co-deposition onto the edges, corners, and then side faces of the Ag nanocubes in a fashion similar to seeded growth. As a result, the co-titration process offers an exquisite control over the relative amounts of Ag and Au atoms being deposited by simply varying the feeding ratio between the two precursors. We also demonstrate that the Ag@Ag-Au core-frame nanocubes exhibit unique plasmonic properties. Upon etching of the Ag templates from the core-frame nanocubes by an oxidant, we obtain Ag-Au nanoframes that could serve as an active catalyst for the reduction of 4-nitrophenol by $NaBH_4$. The co-titration methodology can be simply extended to the fabrication of Ag@Ag-Pd core-frame nanocubes by co-titration of Na_2PdCl_4 and $AgNO_3$. These core-frame nanocubes with an integrated catalytic activity from Pd and SERS activity from Ag can be used as a probe for monitoring stepwise reduction and oxidation reactions by SERS.

In Chapter 3, we describe another approach to the replacement-free synthesis of Ag@Au core-shell nanocubes *via* seeded growth. The synthesis involves the dropwise titration of aqueous $HAuCl_4$ precursor into an aqueous mixture of Ag nanocubes, H_2Asc, PVP, and NaOH at pH = 11.9. Different from the protocol used in the co-titration methodology described in Chapter 2, we include NaOH in the reaction solution and titrate $HAuCl_4$ precursor without any involvement of $AgNO_3$. To understand the mechanistic roles of hydroxide in controlling the deposition of Au on colloidal Ag nanocubes, we

perform a set of experiments by introducing different amounts of NaOH to adjust the initial pH of the reaction solution from 3.2 to 11.9, followed by the titration of $HAuCl_4$. We elucidate that the OH^- ions from NaOH can affect the reduction kinetics of the Au(III) precursor in a number of ways and thereby the deposition pathways of the Au atoms. First of all, the OH^- can accelerate the reduction kinetics by neutralizing H_2Asc into ascorbate monoanion ($HAsc^-$), the true player behind the reduction power of ascorbic acid. Secondly, the OH^- can neutralize the added $HAuCl_4$ and progressively transform $AuCl_4^-$ into $AuCl_3(OH)^-$, $AuCl_2(OH)_2^-$, $AuCl(OH)_3^-$, or $Au(OH)_4^-$ through ligand exchange, generating Au(III) precursors with increasingly lower reduction potentials and thus lower probability for galvanic replacement reaction with Ag nanocubes than $AuCl_4^-$. Thirdly, the OH^- can react with the Ag^+ ions released from the galvanic reaction to generate Ag_2O patches at the corners of Ag nanocubes. Our results indicate that, when the initial pH is controlled in the range of 10.3-11.9, the reduction of Au(III) is initiated by Ag nanocubes but dominated by $HAsc^-$ afterwards, leading to the formation of Ag@Au core-frame and then core-shell nanocubes.

In Chapter 4, we demonstrate the transformation of the Ag@Au core-shell nanocubes into cubic nanoboxes with a wall thickness below 2 nm, together with well-defined openings at the corners, while they are kept as compact as 20 nm. The success relies on the selective formation of Ag_2O patches at the corners of Ag nanocubes during the synthesis of Ag@Au core-shell nanocubes as described in Chapter 3. Specifically, when Au^{3+} is titrated into a suspension of Ag nanocubes with slight corner truncation in the presence of NaOH and H_2Asc, a small amount of Ag would be dissolved from the corners because of its galvanic replacement with Au^{3+}. Owing to the presence of OH^- ions,

Ag_2O is immediately formed at the corners, impeding further dissolution of Ag from the nanocubes. From this point, the resultant Au atoms are deposited on the side faces, followed by the conformal, layer-by-layer deposition of more Au formed through the redox reaction with $HAsc^-$. Later, the Ag_2O at the corners can be removed using a weak acid, making it feasible to completely etch away the Ag core without breaking the Au shell as thin as 2 nm. These Au nanoboxes exhibit strong absorption in the near infrared region for potential applications as contrast agents in optical imaging and as capsules in controlled release.

In Chapter 5, we develop a facile synthesis of Pt-Ag nanocages with wall thicknesses as thin as 2 nm by depositing a few atomic layers of Pt as conformal shells on Ag nanocubes and then removing the Ag template *via* selective wet etching. Similar to the protocol discussed in Chapter 3 for the synthesis of Ag@Au core-shell nanocubes, we inject H_2PtCl_6 into an aqueous mixture of Ag nanocubes, H_2Asc, NaOH, and PVP at an initial pH of 11.9 under ambient conditions. In this case, Pt(IV) ions can quickly form stable complexes with the nitrogen atoms in PVP, preventing them from evolving into $PtCl_5(OH)^{2-}$ and $PtCl_4(OH)_2^{2-}$ through ligand exchange with H_2O and OH^-. The Pt(IV) precursor should be mostly reduced by ascorbate monoanion derived from the neutralization of H_2Asc with NaOH under an alkaline condition. The newly formed Pt atoms are deposited onto the edges and then corners and side faces of Ag nanocubes, leading to the generation of $Ag@Pt_{3L}$ core-shell nanocubes with a conformal Pt shell thickness of only about three atomic layers (or *ca.* 0.6 nm). After the selective removal of Ag cores using an etchant based on $Fe(NO_3)_3$, we transform the core-shell nanocubes into Pt-Ag alloy nanocages with an ultrathin wall thickness of less than 2 nm. We further demonstrate that the as-obtained

nanocages with a composition of $Pt_{42}Ag_{58}$ exhibit enhanced catalytic activity toward the oxygen reduction reaction, with mass activity of 0.30 A mg^{-1} and specific activity of 0.93 mA/cm^2, which are 1.6 and 2.5 times greater than those of the Pt/C catalyst, respectively.

1.5 Notes to Chapter 1

Part of the chapter is adapted from the article "Enriching Silver Nanocrystals with a Second Noble Metal" published in *Accounts of Chemical Research*.[129]

1.6 References

(1) Wertime, T. A. Man's First Encounters With Metallurgy: Man's Discovery of Ores and Metals Helped to Shape His Sense of Science, Technology, and History. *Science* **1964**, *146*, 1257–1267.

(2) Burda, C.; Chen, X.; Narayanan, R.; El-Sayed, M. A. Chemistry and Properties of Nanocrystals of Different Shapes. *Chem. Rev.* **2005**, *105*, 1025–1102.

(3) Zhang, H.; Jin, M.; Xia, Y. Noble-Metal Nanocrystals with Concave Surfaces: Synthesis and Applications. *Angew. Chem. Int. Ed. Engl.* **2012**, *51*, 7656–7673.

(4) Joo, S. H.; Park, J. Y.; Tsung, C.-K.; Yamada, Y.; Yang, P.; Somorjai, G. A. Thermally Stable Pt/mesoporous Silica Core-Shell Nanocatalysts for High-Temperature Reactions. *Nat. Mater.* **2009**, *8*, 126–131.

(5) Haes, A. J.; Haynes, C. L.; McFarland, A. D.; Schatz, G. C.; Van Duyne, R. P.; Zou, S. Plasmonic Materials for Surface-Enhanced Sensing and Spectroscopy. *MRS Bull.* **2005**, *30*, 368–375.

(6) Willets, K. A.; Van Duyne, R. P. Localized Surface Plasmon Resonance Spectroscopy and Sensing. *Annu. Rev. Phys. Chem.* **2007**, *58*, 267–297.

(7) Xia, Y.; Li, W.; Cobley, C. M.; Chen, J.; Xia, X.; Zhang, Q.; Yang, M.; Cho, E. C.; Brown, P. K. Gold Nanocages: From Synthesis to Theranostic Applications. *Acc. Chem. Res.* **2011**, *44*, 914–924.

(8) Rosi, N. L.; Mirkin, C. A. Nanostructures in Biodiagnostics. *Chem. Rev.* **2005**, *105*, 1547–1562.

(9) Qian, X.; Peng, X.-H.; Ansari, D. O.; Yin-Goen, Q.; Chen, G. Z.; Shin, D. M.; Yang, L.; Young, A. N.; Wang, M. D.; Nie, S. In Vivo Tumor Targeting and Spectroscopic Detection with Surface-Enhanced Raman Nanoparticle Tags. *Nat. Biotechnol.* **2008**, *26*, 83–90.

(10) Lal, S.; Clare, S. E.; Halas, N. J. Nanoshell-Enabled Photothermal Cancer Therapy: Impending Clinical Impact. *Acc. Chem. Res.* **2008**, *41*, 1842–1851.

(11) Shalaev, V. M. Transforming Light. *Science* **2008**, *322*, 384–386.

(12) Brongersma, M. L.; Shalaev, V. M. The Case for Plasmonics. *Science* **2010**, *328*, 440–441.

(13) Gramotnev, D. K.; Bozhevolnyi, S. I. Nanofocusing of Electromagnetic Radiation. *Nat. Photonics* **2014**, *8*, 13–22.

(14) Schuller, J. A.; Barnard, E. S.; Cai, W.; Jun, Y. C.; White, J. S.; Brongersma, M. L. Plasmonics for Extreme Light Concentration and Manipulation. *Nat. Mater.* **2010**, *9*, 193–204.

(15) Barnes, W. L.; Dereux, A.; Ebbesen, T. W. Surface Plasmon Subwavelength Optics. *Nature* **2003**, *424*, 824–830.

(16) Wiley, B.; Sun, Y.; Xia, Y. Synthesis of Silver Nanostructures with Controlled Shapes and Properties. *Acc. Chem. Res.* **2007**, *40*, 1067–1076.

(17) Pyayt, A. L.; Wiley, B.; Xia, Y.; Chen, A.; Dalton, L. Integration of Photonic and Silver Nanowire Plasmonic Waveguides. *Nat. Nanotechnol.* **2008**, *3*, 660–665.

(18) Rang, M.; Jones, A. C.; Zhou, F.; Li, Z.-Y.; Wiley, B. J.; Xia, Y.; Raschke, M. B. Optical Near-Field Mapping of Plasmonic Nanoprisms. *Nano Lett.* **2008**, *8*, 3357–3363.

(19) Farrauto, R. J.; Heck, R. M. Catalytic Converters: State of the Art and Perspectives. *Catal. Today* **1999**, *51*, 351–360.

(20) Adams, B. D.; Chen, A. The Role of Palladium in a Hydrogen Economy. *Mater. Today* **2011**, *14*, 282–289.

(21) Mergler, Y. J.; Van Aalst, A.; Van Delft, J.; Nieuwenhuys, B. E. CO Oxidation over Promoted Pt Catalysts. *Appl. Catal. B Environ.* **1996**, *10*, 245–261.

(22) Gland, J. L.; Korchak, V. N. Ammonia Oxidation on a Stepped Platinum Single-Crystal Surface. *J. Catal.* **1978**, *53*, 9–23.

(23) Leite, L.; Benazzi, E.; Marchal-George, N. Hydrocracking of Phenanthrene over Bifunctional Pt Catalysts. *Catal. Today* **2001**, *65*, 241–247.

(24) Zhang, J.; Yang, H.; Fang, J.; Zou, S. Synthesis and Oxygen Reduction Activity of Shape-Controlled Pt_3Ni Nanopolyhedra. *Nano Lett.* **2010**, *10*, 638–644.

(25) Peng, Z.; Yang, H. Synthesis and Oxygen Reduction Electrocatalytic Property of Pt-on-Pd Bimetallic Heteronanostructures. *J. Am. Chem. Soc.* **2009**, *131*, 7542–7543.

(26) Lal, S.; Link, S.; Halas, N. J. Nano-Optics from Sensing to Waveguiding. *Nat. Photonics* **2007**, *1*, 641–648.

(27) Hutter, E.; Fendler, J. H. Exploitation of Localized Surface Plasmon Resonance. *Adv. Mater.* **2004**, *16*, 1685–1706.

(28) Sanders, A. W.; Routenberg, D. A.; Wiley, B. J.; Xia, Y.; Dufresne, E. R.; Reed, M. A. Observation of Plasmon Propagation, Redirection, and Fan-Out in Silver Nanowires. *Nano Lett.* **2006**, *6*, 1822–1826.

(29) Haes, A. J.; Van Duyne, R. P. A Unified View of Propagating and Localized Surface Plasmon Resonance Biosensors. *Anal. Bioanal. Chem.* **2004**, *379*, 920–930.

(30) Mulvaney, P. Surface Plasmon Spectroscopy of Nanosized Metal Particles. *Langmuir* **1996**, *12*, 788–800.

(31) Le Ru, E. C.; Etchegoin, P. G. *Principles of Surface-Enhanced Raman Spectroscopy: And Related Plasmonic Effects*; Elsevier, 2009.

(32) Wang, H.; Tam, F.; Grady, N. K.; Halas, N. J. Cu Nanoshells: Effects of Interband Transitions on the Nanoparticle Plasmon Resonance. *J. Phys. Chem. B* **2005**, *109*, 18218–18222.

(33) Wiley, B. J.; Im, S. H.; Li, Z.-Y.; McLellan, J.; Siekkinen, A.; Xia, Y. Maneuvering the Surface Plasmon Resonance of Silver Nanostructures through Shape-Controlled Synthesis. *J. Phys. Chem. B* **2006**, *110*, 15666–15675.

(34) Rycenga, M.; Cobley, C. M.; Zeng, J.; Li, W.; Moran, C. H.; Zhang, Q.; Qin, D.; Xia, Y. Controlling the Synthesis and Assembly of Silver Nanostructures for Plasmonic Applications. *Chem. Rev.* **2011**, *111*, 3669–3712.

(35) Cobley, C. M.; Rycenga, M.; Zhou, F.; Li, Z.-Y.; Xia, Y. Controlled Etching as a Route to High Quality Silver Nanospheres for Optical Studies. *J. Phys. Chem. C* **2009**, *113*, 16975–16982.

(36) Skrabalak, S. E.; Au, L.; Li, X.; Xia, Y. Facile Synthesis of Ag Nanocubes and Au Nanocages. *Nat. Protoc.* **2007**, *2*, 2182–2190.

(37) Hu, M.; Novo, C.; Funston, A.; Wang, H.; Staleva, H.; Zou, S.; Mulvaney, P.; Xia, Y.; Hartland, G. V. Dark-Field Microscopy Studies of Single Metal Nanoparticles: Understanding the Factors that Influence the Linewidth of the Localized Surface Plasmon Resonance. *J. Mater. Chem.* **2008**, *18*, 1949–1960.

(38) Kelly, K. L.; Coronado, E.; Zhao, L. L.; Schatz, G. C. The Optical Properties of Metal Nanoparticles: The Influence of Size, Shape, and Dielectric Environment. *J. Phys. Chem. B* **2003**, *107*, 668–677.

(39) Zhang, Q.; Li, W.; Wen, L. P.; Chen, J.; Xia, Y. Facile Synthesis of Ag Nanocubes of 30 to 70 nm in Edge Length with CF_3COOAg as a Precursor. *Chem. - A Eur. J.* **2010**, *16*, 10234–10239.

(40) Hao, E.; Schatz, G. C. Electromagnetic Fields around Silver Nanoparticles and Dimers. *J. Chem. Phys.* **2004**, *120*, 357–366.

(41) Zou, S.; Schatz, G. C. Silver Nanoparticle Array Structures That Produce Giant Enhancements in Electromagnetic Fields. *Chem. Phys. Lett.* **2005**, *403*, 62–67.

(42) Moskovits, M. Surface-Enhanced Raman Spectroscopy: A Brief Retrospective. *J.*

Raman Spectrosc. **2005**, *36*, 485–496.

(43) Amendola, V.; Bakr, O. M.; Stellacci, F. A Study of the Surface Plasmon Resonance of Silver Nanoparticles by the Discrete Dipole Approximation Method: Effect of Shape, Size, Structure, and Assembly. *Plasmonics* **2010**, *5*, 85–97.

(44) Lou, X. W. (David); Archer, L. A.; Yang, Z. Hollow Micro-/Nanostructures: Synthesis and Applications. *Adv. Mater.* **2008**, *20*, 3987–4019.

(45) Xia, Y.; Li, W.; Cobley, C. M.; Chen, J.; Xia, X.; Zhang, Q.; Yang, M.; Cho, E. C.; Brown, P. K. Gold Nanocages: From Synthesis to Theranostic Applications. *Acc. Chem. Res.* **2011**, *44*, 914–924.

(46) Zhang, Q.; Xie, J.; Liang, J.; Lee, J. Y. Synthesis of Monodisperse Ag-Au Alloy Nanoparticles with Independently Tunable Morphology, Composition, Size, and Surface Chemistry and Their 3-D Superlattices. *Adv. Funct. Mater.* **2009**, *19*, 1387–1398.

(47) Skrabalak, S. E.; Chen, J.; Sun, Y.; Lu, X.; Au, L.; Cobley, C. M.; Xia, Y. Gold Nanocages: Synthesis, Properties, and Applications. *Acc. Chem. Res.* **2008**, *41*, 1587–1595.

(48) Kneipp, J.; Kneipp, H.; Kneipp, K. SERS–A Single-Molecule and Nanoscale Tool for Bioanalytics. *Chem. Soc. Rev.* **2008**, *37*, 1052–1060.

(49) Smith, E.; Dent, G. *Modern Raman Spectroscopy - A Practical Approach*; John Wiley & Sons, Ltd: Chichester, UK, 2004.

(50) Schlucker, S. *Surface Enhanced Raman Spectroscopy*; Wiley-VCH Verlag GmbH & Co. KGaA: Weinheim, Germany, 2010.

(51) Jeanmaire, D. L.; Van Duyne, R. P. Surface Raman Spectroelectrochemistry. *J. Electroanal. Chem. Interfacial Electrochem.* **1977**, *84*, 1–20.

(52) Doering, W. E.; Nie, S. Spectroscopic Tags Using Dye-Embedded Nanoparticles and Surface-Enhanced Raman Scattering. *Anal. Chem*, **2003**, *75*, 6171–6176.

(53) Negri, P.; Jacobs, K. T.; Dada, O. O.; Schultz, Z. D. Ultrasensitive Surface-Enhanced Raman Scattering Flow Detector Using Hydrodynamic Focusing. *Anal. Chem.* **2013**, *85*, 10159–10166.

(54) Zhou, Q.; Zhang, X.; Huang, Y.; Li, Z.; Zhang, Z. Rapid Detection of Polychlorinated Biphenyls at Trace Levels in Real Environmental Samples by Surface-Enhanced Raman Scattering. *Sensors (Basel).* **2011**, *11*, 10851–10858.

(55) Guerrini, L.; Garcia-Ramos, J. V; Domingo, C.; Sanchez-Cortes, S. Sensing Polycyclic Aromatic Hydrocarbons with Dithiocarbamate-Functionalized Ag Nanoparticles by Surface-Enhanced Raman Scattering. *Anal. Chem.* **2009**, *81*, 953–960.

(56) Samal, A. K.; Polavarapu, L.; Rodal-Cedeira, S.; Liz-Marzán, L. M.; Pérez-Juste, J.; Pastoriza-Santos, I. Size Tunable Au@Ag Core-Shell Nanoparticles: Synthesis and

Surface-Enhanced Raman Scattering Properties. *Langmuir* **2013**, *29*, 15076–15082.

(57) Ngo, H. T.; Wang, H.-N.; Fales, A. M.; Vo-Dinh, T. Label-Free DNA Biosensor Based on SERS Molecular Sentinel on Nanowave Chip. *Anal. Chem.* **2013**, *85*, 6378–6383.

(58) McFarland, A. D.; Young, M. A.; Dieringer, J. A.;Van Duyne, R. P. Wavelength-Scanned Surface-Enhanced Raman Excitation Spectroscopy. *J. Phys. Chem. B* **2005**, 109, 11279–11285.

(59) Moore, C. B. *Chemical and Biochemical Applications of Lasers Volume IV*; Academic Press, 1979.

(60) Zhang, H.; Jin, M.; Wang, J.; Li, W.; Camargo, P. H. C.; Kim, M. J.; Yang, D.; Xie, Z.; Xia, Y. Synthesis of Pd-Pt Bimetallic Nanocrystals with a Concave Structure through a Bromide-Induced Galvanic Replacement Reaction. *J. Am. Chem. Soc.* **2011**, *133*, 6078–6089.

(61) Xie, S.; Jin, M.; Tao, J.; Wang, Y.; Xie, Z.; Zhu, Y.; Xia, Y. Synthesis and Characterization of Pd@M_xCu_{1-X} (M=Au, Pd, and Pt) Nanocages with Porous Walls and a Yolk-Shell Structure through Galvanic Replacement Reactions. *Chem. - A Eur. J.* **2012**, *18*, 14974–14980.

(62) Jiang, Y.; Lu, Y.; Han, D.; Zhang, Q.; Niu, L. Hollow Ag@Pd Core–shell Nanotubes as Highly Active Catalysts for the Electro-Oxidation of Formic Acid. *Nanotechnology*. **2012**, 23,105609-105617.

(63) Wang, X.; Figueroa-Cosme, L.; Yang, X.; Luo, M.; Liu, J.; Xie, Z.; Xia, Y. Pt-Based Icosahedral Nanocages: Using a Combination of {111} Facets, Twin Defects, and Ultrathin Walls to Greatly Enhance Their Activity toward Oxygen Reduction. *Nano Lett.* **2016**, *16*, 1467–1471.

(64) Hong, J. W.; Kang, S. W.; Choi, B.-S.; Kim, D.; Lee, S. B.; Han, S. W. Controlled Synthesis of Pd-Pt Alloy Hollow Nanostructures with Enhanced Catalytic Activities for Oxygen Reduction. *ACS Nano* **2012**, *6*, 2410–2419.

(65) Yang, X.; Roling, L. T.; Vara, M.; Elnabawy, A. O.; Zhao, M.; Hood, Z. D.; Bao, S.; Mavrikakis, M.; Xia, Y. Synthesis and Characterization of Pt?Ag Alloy Nanocages with Enhanced Activity and Durability toward Oxygen Reduction. *Nano Lett.* **2016**, *16*, 6644–6649.

(66) Wang, L.; Yamauchi, Y. Metallic Nanocages: Synthesis of Bimetallic Pt–Pd Hollow Nanoparticles with Dendritic Shells by Selective Chemical Etching. *J. Am. Chem. Soc.* **2013**, *135*, 16762–16765.

(67) Zhang, L.; Roling, L. T.; Wang, X.; Vara, M.; Chi, M.; Liu, J.; Choi, S.-I.; Park, J.; Herron, J. A.; Xie, Z.; Mavrikakis, M.; Xia, Y. Platinum-Based Nanocages with Subnanometer-Thick Walls and Well-Defined, Controllable Facets. *Science (80-.).* **2015**, *349*, 412–416.

(68) He, D. S.; He, D.; Wang, J.; Lin, Y.; Yin, P.; Hong, X.; Wu, Y.; Li, Y. Ultrathin Icosahedral Pt-Enriched Nanocage with Excellent Oxygen Reduction Reaction

Activity. *J. Am. Chem. Soc.* **2016**, *138*, 1494–1497.

(69) Teschner, D.; Vass, E.; Hävecker, M.; Zafeiratos, S.; Schnörch, P.; Sauer, H.; Knop-Gericke, A.; Schlögl, R.; Chamam, M.; Wootsch, A.; Canning, A. S.; Gamman, J. J.; Jackson, S. D.; McGregor, J.; Gladden, L. F. Alkyne Hydrogenation over Pd Catalysts: A New Paradigm. *J. Catal.* **2006**, *242*, 26–37.

(70) Nakatsuji, H.; Hada, M.; Yonezawa, T. Theoretical Study on the Catalytic Activity of Palladium for the Hydrogenation of Acetylene. *Surf. Sci.* **1987**, *185*, 319–342.

(71) Chen, Y. H.; Hung, H. H.; Huang, M. H. Seed-Mediated Synthesis of Palladium Nanorods and Branched Nanocrystals and Their Use as Recyclable Suzuki Coupling Reaction Catalysts. *J. Am. Chem. Soc.* **2009**, *131*, 9114–9121.

(72) Pacardo, D. B.; Sethi, M.; Jones, S. E.; Naik, R. R.; Knecht, M. R. Biomimetic Synthesis of Pd Nanocatalysts for the Stille Coupling Reaction. *ACS Nano* **2009**, *3*, 1288–1296.

(73) Zhou, X.; Luo, J.; Liu, J.; Peng, S.; Deng, G. J. Pd-Catalyzed Desulfitative Heck Coupling with Dioxygen as the Terminal Oxidant. *Org. Lett.* **2011**, *13*, 1432–1435.

(74) Amatore, C.; Jutand, A. Anionic Pd(0) and Pd(II) Intermediates in Palladium-Catalyzed Heck and Cross-Coupling Reactions. *Acc. Chem. Res.* **2000**, *33*, 314–321.

(75) Remediakis, I. N.; Lopez, N.; Nørskov, J. K. CO Oxidation on Rutile-Supported Au Nanoparticles. *Angew. Chem. Int. Ed.* **2005**, *44*, 1824–1826.

(76) Christopher, P.; Linic, S. Shape- and Size-Specific Chemistry of Ag Nanostructures in Catalytic Ethylene Epoxidation. *ChemCatChem* **2010**, *2*, 78–83.

(77) Sun, Y.; Xia, Y. Shape-Controlled Synthesis of Gold and Silver Nanoparticles. *Science* **2002**, *298*, 2176–2179.

(78) Tao, A.; Sinsermsuksakul, P.; Yang, P. Polyhedral Silver Nanocrystals with Distinct Scattering Signatures. *Angew. Chem. Int. Ed.* **2006**, *45*, 4597–4601.

(79) Jiang, M.; Cobley, CM.; Lim, B.; Xia, Y. Noble-Metal Nanostructures with Controlled Morphologies.

(80) Lee, P. C.; Meisel, D. Adsorption and Surface-Enhanced Raman of Dyes on Silver and Gold Sols. *J. Phys. Chem.* **1982**, *86*, 3391–3395.

(81) Pillai, Z. S.; Kamat, P. V. What Factors Control the Size and Shape of Silver Nanoparticles in the Citrate Ion Reduction Method? *J. Phys. Chem. B* **2004**, *108*, 945–951.

(82) Henglein, A.; Giersig, M. Formation of Colloidal Silver Nanoparticles: Capping Action of Citrate. *J. Phys. Chem. B* **1999**, *103*, 9533–9539.

(83) Koh, A. L.; Bao, K.; Khan, I.; Smith, W. E.; Kothleitner, G.; Nordlander, P.; Maier, S. A.; McComb, D. W. Electron Energy-Loss Spectroscopy (EELS) of Surface Plasmons in Single Silver Nanoparticles and Dimers: Influence of Beam Damage and Mapping of Dark Modes. *ACS Nano* **2009**, *3*, 3015–3022.

(84) Liebig, J. Ueber Versilberung Und Vergoldung von Glas. *Ann. der Chemie und Pharm.* **1856**, *98*, 132–139.

(85) Xia, Y.; Xiong, Y.; Lim, B.; Skrabalak, S. E. Shape-Controlled Synthesis of Metal Nanocrystals: Simple Chemistry Meets Complex Physics? *Angew. Chem. Int. Ed. Engl.* **2009**, *48*, 60–103.

(86) Wiley, B. J.; Wang, Z.; Wei, J.; Yin, Y.; Cobden, D. H.; Xia, Y. Synthesis and Electrical Characterization of Silver Nanobeams. *Nano Lett.* **2006**, *6*, 2273–2278.

(87) Tao, A. R.; Habas, S.; Yang, P. Shape Control of Colloidal Metal Nanocrystals. *Small* **2008**, *4*, 310–325.

(88) Skrabalak, S. E.; Wiley, B. J.; Kim, M.; Formo, E. V; Xia, Y. On the Polyol Synthesis of Silver Nanostructures: Glycolaldehyde as a Reducing Agent. *Nano Lett.* **2008**, *8*, 2077–2081.

(89) Sun, Y.; Mayers, B.; Herricks, T.; Xia, Y. Polyol Synthesis of Uniform Silver Nanowires: A Plausible Growth Mechanism and the Supporting Evidence. *Nano Lett.* **2003**, *3*, 955–960.

(90) Zhang, H.; Jin, M.; Xia, Y. Enhancing the Catalytic and Electrocatalytic Properties of Pt-Based Catalysts by Forming Bimetallic Nanocrystals with Pd. *Chem. Soc. Rev.* **2012**, *41*, 8035-8049.

(91) Gao, C.; Goebl, J.; Yin, Y. Seeded Growth Route to Noble Metal Nanostructures. *J. Mater. Chem. C* **2013**, *1*, 3898-3909.

(92) Lohse, S. E.; Burrows, N. D.; Scarabelli, L.; Liz-Marzán, L. M.; Murphy, C. J. Anisotropic Noble Metal Nanocrystal Growth: The Role of Halides. *Chem. Mater.* **2014**, *26*, 34–43.

(93) Niu, W.; Zhang, L.; Xu, G. Seed-Mediated Growth of Noble Metal Nanocrystals: Crystal Growth and Shape Control. *Nanoscale* **2013**, *5*, 3172–3181.

(94) Zhang, Q.; Li, W.; Moran, C.; Zeng, J.; Chen, J.; Wen, L.-P.; Xia, Y. Seed-Mediated Synthesis of Ag Nanocubes with Controllable Edge Lengths in the Range of 30-200 nm and Comparison of Their Optical Properties. *J. Am. Chem. Soc.* **2010**, *132*, 11372–11378.

(95) Zhang, Q.; Hu, Y.; Guo, S.; Goebl, J.; Yin, Y. Seeded Growth of Uniform Ag Nanoplates with High Aspect Ratio and Widely Tunable Surface Plasmon Bands. *Nano Lett.* **2010**, *10*, 5037–5042.

(96) Jiang, M.; Lim, B.; Tao, J.; Camargo, P. H. C.; Ma, C.; Zhu, Y.; Xia, Y. Epitaxial Overgrowth of Platinum on Palladium Nanocrystals. *Nanoscale* **2010**, *2*, 2406-2411.

(97) Fan, F. R.; Liu, D. Y.; Wu, Y. F.; Duan, S.; Xie, Z. X.; Jiang, Z. Y.; Tian, Z. Q. Epitaxial Growth of Heterogeneous Metal Nanocrystals: From Gold Nano-Octahedra to Palladium and Silver Nanocubes. *J. Am. Chem. Soc.* **2008**, *130*, 6949–6951.

(98) Huang, J.; Zhu, Y.; Lin, M.; Wang, Q.; Zhao, L.; Yang, Y.; Yao, K. X.; Han, Y. Site-Specific Growth of Au-Pd Alloy Horns on Au Nanorods: A Platform for Highly Sensitive Monitoring of Catalytic Reactions by Surface Enhancement Raman Spectroscopy. *J. Am. Chem. Soc.* **2013**, *135*, 8552–8561.

(99) Jana, N.; Gearheart, L. Wet Chemical Synthesis of Silver Nanorods and Nanowiresof Controllable Aspect Ratio. *Chem. Commun.* **2001**, *7*, 617–618.

(100) Sun, Y.; Gates, B.; Mayers, B.; Xia, Y. Crystalline Silver Nanowires by Soft Solution Processing. *Nano Lett.* **2002**, *2*, 165–168.

(101) Nikoobakht, B.; El-Sayed, M. A. Preparation and Growth Mechanism of Gold Nanorods (NRs) Using Seed-Mediated Growth Method. *Chem. Mater.* **2003**, *15*, 1957–1962.

(102) Zeng, J.; Zheng, Y.; Rycenga, M.; Tao, J.; Li, Z. Y.; Zhang, Q.; Zhu, Y.; Xia, Y. Controlling the Shapes of Silver Nanocrystals with Different Capping Agents. *J. Am. Chem. Soc.* **2010**, *132*, 8552–8553.

(103) Habas, S. E.; Lee, H.; Radmilovic, V.; Somorjai, G. A.; Yang, P. Shaping Binary Metal Nanocrystals through Epitaxial Seeded Growth. *Nat. Mater.* **2007**, *6*, 692–697.

(104) Xue, C.; Millstone, J. E.; Li, S.; Mirkin, C. A. Plasmon-Driven Synthesis of Triangular Core-Shell Nanoprisms from Gold Seeds. *Angew. Chem. Int. Ed.* **2007**, *46*, 8436–8439.

(105) Lim, B.; Jiang, M.; Camargo, P. H. C.; Cho, E. C.; Tao, J.; Lu, X.; Zhu, Y.; Xia, Y. Pd-Pt Bimetallic Nanodendrites with High Activity for Oxygen Reduction. *Science* **2009**, *324*, 1302–1305.

(106) Desantis, C. J.; Peverly, A. A.; Peters, D. G.; Skrabalak, S. E. Octopods versus Concave Nanocrystals: Control of Morphology by Manipulating the Kinetics of Seeded Growth via Co-Reduction. *Nano Lett.* **2011**, *11*, 2164–2168.

(107) Xie, S.; Lu, N.; Xie, Z.; Wang, J.; Kim, M. J.; Xia, Y. Synthesis of Pd-Rh Core-Frame Concave Nanocubes and Their Conversion to Rh Cubic Nanoframes by Selective Etching of the Pd Cores. *Angew. Chem. Int. Ed.* **2012**, *51*, 10266–10270.

(108) Peng, Z.; Wu, J.; Yang, H. Synthesis and Oxygen Reduction Electrocatalytic Property of Platinum Hollow and Platinum-on-Silver Nanoparticles. *Chem. Mater.* **2010**, *22*, 1098–1106.

(109) Zeng, J.; Zhu, C.; Tao, J.; Jin, M.; Zhang, H.; Li, Z. Y.; Zhu, Y.; Xia, Y. Controlling the Nucleation and Growth of Silver on Palladium Nanocubes by Manipulating the Reaction Kinetics. *Angew. Chem. Int. Ed.* **2012**, *51*, 2354–2358.

(110) Zhu, C.; Zeng, J.; Tao, J.; Johnson, M. C.; Schmidt-Krey, I.; Blubaugh, L.; Zhu, Y.; Gu, Z.; Xia, Y. Kinetically Controlled Overgrowth of Ag or Au on Pd Nanocrystal Seeds: From Hybrid Dimers to Nonconcentric and Concentric Bimetallic Nanocrystals. *J. Am. Chem. Soc.* **2012**, *134*, 15822–15831.

(111) Xia, X.; Xia, Y. Symmetry Breaking during Seeded Growth of Nanocrystals. *Nano Lett.* **2012**, *12*, 6038–6042.

(112) Sun, Y.; Xia, Y. Mechanistic Study on the Replacement Reaction between Silver Nanostructures and Chloroauric Acid in Aqueous Medium. *J. Am. Chem. Soc.* **2004**, *126*, 3892–3901.

(113) Chen, J.; Wiley, B.; McLellan, J.; Xiong, Y.; Li, Z. Y.; Xia, Y. Optical Properties of Pd-Ag and Pt-Ag Nanoboxes Synthesized via Galvanic Replacement Reactions. *Nano Lett.* **2005**, *5*, 2058–2062.

(114) Liang, H. P.; Zhang, H. M.; Hu, J. S.; Guo, Y. G.; Wan, L. J.; Bai, C. L. Pt Hollow Nanospheres: Facile Synthesis and Enhanced Electrocatalysts. *Angew. Chem. Int. Ed.* **2004**, *43*, 1540–1543.

(115) Vasquez, Y.; Sra, A. K.; Schaak, R. E. One-Pot Synthesis of Hollow Superparamagnetic CoPt Nanospheres. *J. Am. Chem. Soc.* **2005**, *127*, 12504–12505.

(116) Caixia, X.; Yan, Z.; Liqiang, X.; Xiufang, B.; Houyi, M.; Yi, D. Nanotubular Mesoporous PdCu Bimetallic Electrocatalysts toward Oxygen Reduction Reaction. *Chem. Mater.* **2009**, *21*, 3110–3116.

(117) Liu, R.; Sen, A. Unified Synthetic Approach to Silver Nanostructures by Galvanic Displacement Reaction on Copper: From Nanobelts to Nanoshells. *Chem. Mater.* **2012**, *24*, 48–54.

(118) Hong, J. W.; Kang, S. W.; Choi, B. S.; Kim, D.; Lee, S. B.; Han, S. W. Controlled Synthesis of Pd-Pt Alloy Hollow Nanostructures with Enhanced Catalytic Activities for Oxygen Reduction. *ACS Nano* **2012**, *6*, 2410–2419.

(119) Liu, M.; Zheng, Y.; Xie, S.; Li, N.; Lu, N.; Wang, J.; Kim, M. J.; Guo, L.; Xia, Y. Facile Synthesis of Pd-Ir Bimetallic Octapods and Nanocages through Galvanic Replacement and Co-Reduction, and Their Use for Hydrazine Decomposition. *Phys. Chem. Chem. Phys.* **2013**, *15*, 11822–11829.

(120) Chen, J.; Yang, M.; Zhang, Q.; Cho, E. C.; Cobley, C. M.; Kim, C.; Glaus, C.; Wang, L. V.; Welch, M. J.; Xia, Y. Gold Nanocages: A Novel Class of Multifunctional Nanomaterials for Theranostic Applications. *Adv. Func. Mater.* **2010**, *20*, 3684–3694.

(121) Perezjuste, J.; Pastorizasantos, I.; Liz-marzan, L.; Mulvaney, P. Gold Nanorods: Synthesis, Characterization and Applications. *Coord. Chem. Rev.* **2005**, *249*, 1870–1901.

(122) Xia, X.; Zeng, J.; McDearmon, B.; Zheng, Y.; Li, Q.; Xia, Y. Silver Nanocrystals with Concave Surfaces and Their Optical and Surface-Enhanced Raman Scattering Properties. *Angew. Chem. Int. Ed.* **2011**, *50*, 12542–12546.

(123) McLellan, J. M.; Siekkinen, A.; Chen, J.; Xia, Y. Comparison of the Surface-Enhanced Raman Scattering on Sharp and Truncated Silver Nanocubes. *Chem. Phys. Lett.* **2006**, *427*, 122–126.

(124) Christopher, P.; Xin, H.; Linic, S. Visible-Light-Enhanced Catalytic Oxidation Reactions on Plasmonic Silver Nanostructures. *Nat. Chem.* **2011**, *3*, 467–472.

(125) Gilroy, K. D.; Ruditskiy, A.; Peng, H. C.; Qin, D.; Xia, Y. Bimetallic Nanocrystals: Syntheses, Properties, and Applications. *Chem. Rev.* **2016**, *116*, 10414–10472.

(126) Link, S.; Wang, Z. L.; El-Sayed, M. A. Alloy Formation of Gold−Silver Nanoparticles and the Dependence of the Plasmon Absorption on Their Composition. *J. Phys. Chem. B* **1999**, *103*, 3529–3533.

(127) Li, J.; Liu, J.; Yang, Y.; Qin, D. Bifunctional Ag@Pd-Ag Nanocubes for Highly Sensitive Monitoring of Catalytic Reactions by Surface-Enhanced Raman Spectroscopy. *J. Am. Chem. Soc.* **2015**, *137*, 7039–7042.

(128) Yang, Y.; Liu, J.; Fu, Z. W.; Qin, D. Galvanic Replacement-Free Deposition of Au on Ag for Core-Shell Nanocubes with Enhanced Chemical Stability and SERS Activity. *J. Am. Chem. Soc.* **2014**, *136*, 8153–8156.

(129) Wu, Y.; Sun, X.; Yang, Y.; Li, J.; Zhang, Y.; Qin, D. Enriching Silver Nanocrystals with a Second Noble Metal. *Acc. Chem. Res.* **2017**, *50*, 1774–1784.

CHAPTER 2. FABRICATION OF BIMETALLIC CORE-FRAME NANOCUBES BY CO-REDUCTION AND CO-DEPOSITION

2.1. Introduction

Noble-metal nanocrystals have received growing interests in recent years owing to their fascinating properties and widespread use in applications that include heterogeneous catalysis,[1–3] plasmonics,[4] optoelectronics,[5] optical sensing,[6,7] biomedical imaging,[8,9] and nanomedicine.[10,11] As demonstrated by many examples, the performance of nanocrystals in all these applications can be greatly augmented by switching from monometallic to bimetallic systems. The inclusion of a second metal can enhance the properties and greatly expand the application landscape by bringing in new capabilities.[12-14] Among various methods, seeded growth has emerged as the foremost approach to the generation of bimetallic nanocrystals with many exquisite controls over the products.[15–18] As we discussed in Chapter 1, this approach involves the use of nanocrystals with a uniform size and shape as seeds for the heterogeneous nucleation and growth of the same or a different metal to produce nanocrystals with novel properties. By simply maneuvering the experimental parameters, including the type of precursor, the reducing agent, and the amount of precursor relative to the number of seeds involved, one can obtain nanocrystals with many different sizes, shapes, compositions, and structures.

Although seeded growth has been successfully applied to essentially all noble metals in both mono- and bimetallic formats,[16,19–28] its capability involving two different metals has long been limited by the galvanic replacement reaction between the seeds and the precursor to the second metal. For example, when seeds made of Ag are mixed with

$HAuCl_4$ (a precursor to Au), the more reactive Ag is spontaneously oxidized and dissolved (partially or completely) from the seeds.[29] Likewise, Ag seeds could also react with $PdCl_4^{2-}$ or $PtCl_6^{2-}$ in an aqueous solution, leading to their transformation into bimetallic hollow nanostructures comprised of a Ag-Pd or Ag-Pt alloy.[30–31] To this end, the destruction of the original seeds, which are supposed to serve as the physical templates only to guide the deposition of another metal, makes it difficult to control the growth pattern and generate the desired structures.

In principle, one could circumvent the galvanic replacement reaction between the seeds and a precursor to the other metal by introducing a faster parallel reduction reaction to compete with and thereby block the galvanic replacement reaction. The argument is that the precursor will be reduced to atoms immediately upon introduction into the reaction solution before it can undergo galvanic replacement with the seeds. As an illustration, when the aqueous $HAuCl_4$ solution is titrated into an aqueous suspension containing Ag nanocrystals in the presence of a strong reducing agent and a colloidal stabilizer, the added $HAuCl_4$ could be reduced by both the Ag (*via* galvanic replacement, with a rate of R_{gal}) and the reductant (*via* chemical reduction, with a rate of R_{red}). At $R_{red} > R_{gal}$, $HAuCl_4$ should be exclusively reduced by the reducing agent to generate Au atoms. In the absence of self-nucleation, the newly formed atoms will nucleate and then grow on the Ag seeds to generate bimetallic nanocrystals in a seeded-growth manner. Mirkin was among the first to demonstrate this concept by depositing corrugated Au on Ag nanoprisms for the formation of Ag-Au alloy shell on the surfaces of these nanocrystals.[32] Our group demonstrated the deposition of Au atoms on Ag nanocubes as conformal, ultrathin shells to generate Ag@Au core-shell nanocubes.[33]

Another approach to attaining the condition of $R_{red} > R_{gal}$ is to retard the galvanic replacement reaction between Ag and $HAuCl_4$ (*i.e.*, to reduce R_{gal}). To this end, Yin and co-workers introduced I^- ions into a system involving Ag nanoplates, $HAuCl_4$, and a reducing agent. The complexation of Au^{3+} with I^- ions could decrease the reduction potential of Au^{3+} and thereby reduce R_{gal}. Consequently, chemical reduction for the AuI_4^- precursor would generate Au atoms for their deposition onto the Ag nanoplates to generate Ag@Au core-shell nanoplates.[34,35] Using a similar approach, Kitaev and co-workers successfully deposited thin shells of Au on the surfaces of Ag decahedra or pentagonal nanorods by titrating aqueous $HAuCl_4$ into a suspension of the Ag nanocrystals at a rate of 3.2 nmol h^{-1} up to 12 h.[36] Their results suggest that an extremely low concentration of $HAuCl_4$ in the reaction solution could diminish R_{gal} and thus eliminate the possibility to generate pits on the Ag templates.

In this chapter, we report a systematic study that involves the co-titration of aqueous $AgNO_3$ and $HAuCl_4$ into an aqueous suspension of Ag nanocubes in the presence of a reducing agent such as ascorbic acid (H_2Asc) and poly(vinylpyrrolidone) (PVP) to retard the galvanic replacement reaction (*i.e.,* to reduce R_{gal}). We discovered that the supply of $AgNO_3$ and $HAuCl_4$ at a molar ratio of three and above could effectively impede the galvanic replacement reaction between Ag nanocubes and $AuCl_4^-$ by accelerating its reverse process, achieving co-deposition of Ag and Au atoms on the surfaces of Ag nanocubes. In contrast, when the molar ratio of $AgNO_3$ to $HAuCl_4$ was below three, the Ag nanocubes were transformed into Ag-Au hollow nanocubes due to the involvement of galvanic replacement between Ag and $AuCl_4^-$, in consistent with previous observations reported in the literature.[37] Most significantly, we validated that all the co-titrated $AgNO_3$

and $HAuCl_4$ precursors could be completely reduced by H_2Asc to produce Ag and Au atoms, followed by their co-deposition onto the Ag nanocubes. Because the specific surface free energies of the low-index facets on Ag nanocubes decrease in the order of $\gamma_{(110)} > \gamma_{(111)} > \gamma_{(100)}$, Ag and Au atoms derived from the reduction by H_2Asc should be sequentially deposited on the edges, corners, and side faces for the formation of Ag@Ag-Au core-frame and then core-shell nanocubes. As such, co-titration offers an exquisite control over the relative amounts of Ag and Au being deposited on the Ag nanocubes by simply varying the feeding ratio between their precursors. These Ag@Ag-Au core-frame nanocubes exhibit unique plasmonic properties, together with an improved surface-enhanced Raman scattering (SERS) performance relative to the original Ag nanocubes at 785 nm laser excitation. Upon etching with 3% H_2O_2, the Ag@Ag-Au core-frame nanocubes are transformed into Ag-enriched Ag-Au nanoframes with catalytic activity toward the reduction of 4-nitrophenol (4-NP) to 4-aminophenol (4-AP) by $NaBH_4$.

We also demonstrated the fabrication of Ag@Ag-Pd core-frame nanocubes by co-titrating Na_2PdCl_4 and $AgNO_3$ while keeping the other experimental parameters unaltered.[3] Because the reduction potential of $PdCl_4^{2-}$ is lower than that of $AuCl_4^-$ and thus decrease the driving force for galvanic replacement reaction, the lower limit of molar ratio between $AgNO_3$ and Na_2PdCl_4 can be reduced to 0.5. In this case, the added Na_2PdCl_4 precursor could only be partially reduced by H_2Asc, making it impossible to control the atomic ratio between the deposited Pd and Ag atoms. However, we could maneuver the elemental composition of the resultant nanostructures by varying the titration volume for both precursors. Similar to the Ag-Au system, the Ag and Pd atoms derived from the co-reduction are co-deposited on the edges, corners, and side faces of Ag nanocubes

progressively as the titration volume increases. The as-prepared Ag@Ag-Pd core-frame nanocubes can be used as a dual catalyst for probing stepwise Pd-catalyzed reduction and Ag-catalyzed oxidation reactions. Upon the removal of the Ag core, the resultant Ag-Pd nanoframes exhibited markedly enhanced catalytic activity toward the reduction of 4-NP to 4-AP, as well as great mechanical stability.

2.2 Experimental Section

Chemicals and Materials. Silver trifluoroacetate (CF_3COOAg, 98%), sodium hydrosulfide hydrate ($NaHS \cdot xH_2O$), aqueous hydrochloric acid (HCl, 37%), PVP with an average molecular weight of 29,000 (PVP-29k) or 55,000 (PVP-55k), gold(III) chloride trihydrate ($HAuCl_4 \cdot 3H_2O$, 99.9+%), silver nitrate ($AgNO_3$, 99+%), sodium tetrachloropalladate(II) (Na_2PdCl_4, 99.99+%), H_2Asc (99%), sodium borohydride ($NaBH_4$, 99.99%+), 1,4-benzenedithiol (1,4-BDT), 4-NP, 4-NTP, ethanol (200 proof), and hydrogen peroxide (H_2O_2, 30 wt.% in H_2O) were all acquired from Sigma-Aldrich. Sodium hydroxide (NaOH, 98+%) and acetone (99.5+%) were purchased from Alfa Aesar. Ethylene glycol (EG) was purchased from J. T. Baker. All chemicals were used as received. All the aqueous solutions were prepared using deionized (DI) water with a resistivity of 18.2 MΩ·cm at room temperature.

Synthesis of Ag nanocubes. We prepared Ag nanocubes by following a protocol developed by Xia and co-workers.[38] In a typical synthesis, 5 mL of EG was introduced into a 0.1-L round bottom flask and heated under magnetic stirring in an oil bath preset to 150 °C, followed by quick injection of NaHS (60 μL, 3 mM in EG). After 2 min, 0.5 mL of HCl (3 mM in EG) was quickly added, followed by the introduction of 1.25 mL of PVP-

55k (20 mg/mL in EG). After another 2 min, 0.4 mL of CF_3COOAg in EG (282 mM) was introduced. During the entire synthesis, the flask was capped with a glass stopper, except for the introduction of reagents. As soon as the major LSPR peak of the Ag nanocubes had been shifted to 436 nm, the reaction was quenched using an ice-water bath to obtain the Ag nanocubes. After mixing with acetone, the Ag nanocubes were collected by centrifugation at 6500 rpm for 5 min, washed with DI water three times, and re-dispersed in DI water for storage and future use. As shown in Figure 2.1, the Ag nanocubes had an average edge length of an average edge length of 39.2±1.6 nm, together with slight truncation at the corners and edges.

Synthesis of Ag@Ag-Au core-frame nanocubes and Ag-Au nanoframes. In a standard synthesis of core-frame nanocubes, 2 mL of PVP-29k (1 mM) aqueous solution was pipetted into a 23 mL glass vial, followed by the addition of 0.5 mL of aqueous H_2Asc (0.1 M) and 10 μL of the aqueous suspension of Ag nanocubes under magnetic stirring. Next, different volumes of aqueous $HAuCl_4$ solution (0.1 mM) and aqueous $AgNO_3$ solution (0.3 mM) were co-titrated at a rate of 20 μL/min using a syringe pump at room temperature. After the completion of co-titration, the reaction was continued for another 10 min. We then collected solids by centrifugation at 6000 rpm for 10 min, washed with DI water twice, and stored in DI water. The Ag-Au nanoframes were prepared by mixing 0.9 mL of the as-obtained Ag@Ag-Au nanocubes with 0.1 mL of 30% aqueous H_2O_2 (at a final concentration of 3%) for 1 h. The resultant nanocubes and nanoframes were washed with DI water twice and re-dispersed in DI water.

Synthesis of Ag@Ag-Pd core-frame nanocubes and Ag-Pd nanoframes. In a typical synthesis of core-frame nanocubes, 2 mL of aqueous PVP-29k (1 mM) was added

into a 23-mL glass vial, followed by the introduction of 0.5 mL of aqueous H_2Asc (0.1 M) and 10 μL of the aqueous suspension of Ag nanocubes under magnetic stirring. Next, different volumes of aqueous Na_2PdCl_4 (0.2 mM) and aqueous $AgNO_3$ (0.1 mM) were co-titrated into the solution with a rate of 20 μL/min using a syringe pump at room temperature. Upon the completion of co-titration, the reaction solution was magnetically stirred for another 24 h at room temperature. The products were collected by centrifugation at 8000 rpm for 15 min, washed with DI water three times, and stored in DI water for future use. For the synthesis of Ag-Pd nanoframes, we firstly followed the standard procedure for the synthesis of Ag@Ag-Pd core-frame by co-titrating Na_2PdCl_4 (0.1 mM) and aqueous $AgNO_3$ (0.1 mM) while keeping other parameters the same. After the collection of products by centrifugation at 8000 rpm for 15 min, we incubated them in 1.5 mL of 2.3% H_2O_2 for 1 h. The resultant Ag-Pd nanoframes were washed with DI water twice and then re-dispersed in DI water for further use.

SERS measurements. We fabricated a sample cell by attaching a polydimethylsiloxane (PDMS) block to a glass slide. We added 20 μL of liquid sample into a small hole punched in advance on the PDMS and then placed a glass cover slip with a thickness of 0.17 mm on the top to prevent solvent from evaporation. The cover slip was also used as a reference point when we lowered the focal plane 0.2 mm into the sample. The Raman spectra were recorded from the solution phase using a Renishaw inVia Raman spectrometer coupled with a Leica microscope with a 5× or 100× objective lens. We used the excitation wavelength of 532 nm equipped with a holographic notch filter with a grating of 2400 lines/mm or 785 nm equipped with a holographic notch filter with a grating of 1200 lines/mm. We started the measurements with a collection time of 1 s and adjusted the

focal plane to get stable SERS signals. To improve signal to noise ratio, we increased the collection time to 7 or 30 s.

SERS measurements of 1,4-BDT functionalized nanoparticles: The Ag nanocubes and Ag@Ag-Au core-frame nanocubes were collected by centrifugation at 4,500 rpm for 20 min and then functionalized with 1 mL of 1,4-BDT (10^{-4} M) in ethanol for 1 h at room temperature. The functionalized nanoparticles were collected by centrifugation at 4,200 rpm for 20 min, washed with DI once, collected again by centrifugation at 4,000 rpm for 20 min, and then dispersed in 1 mL of DI water for UV-vis measurement. Only when confirmed by UV-vis that there was no aggregation for the nanoparticles after surface functionalization with the probe molecule, we would proceed to perform SERS measurements. We maintained a concentration of approximately 4.2×10^{10} particles/mL for all samples.

In situ SERS monitoring of the reduction of 4-NTP by $NaBH_4$: The Ag nanocubes or Ag@Ag-Pd core-frame nanocubes were dispersed in 1 mL of 4-NTP (10^{-6} M) in ethanol for 1 h under ambient condition. The 4-NTP-functionalized nanocubes were washed with DI water twice and re-suspended in DI water to attain a concentration of approximately 8.7×10^{10} particles/mL. Upon mixing 0.1 mL of the nanocube suspension with 0.1 mL of 0.1 mg/mL aqueous $NaBH_4$ solution in a centrifuge tube, the reduction of 4-NTP on the surfaces of nanocubes proceeded at room temperature. By withdrawing 20 μL of the reaction solution every 2 min and placing the sample in a PDMS sample cell, we monitored the progress of the reaction by SERS. The SERS spectra were collected using a 5× objective lens with laser excitation at 532 nm (50 mW). We maintained a collection time of 7 s for all samples.

Catalytic characterization of Ag-Au and Ag-Pd nanoframes. In a typical measurement, 2 mL of 4-NP (0.2 mM), 5 mL of DI water, and 1 mL of $NaBH_4$ (50 mg/mL, freshly prepared, ice-cold) were added into a 23-mL glass vial, followed by the introduction of 1.4×10^{11} Ag-Au nanoframes as a catalyst to initiate the reaction. We monitored the progress of the reaction by withdrawing 1 mL of the solution every 2 min for the collection of UV-vis spectra in the range of 250−550 nm. We then plotted the absorbance at 400 nm as a function of reaction time. To evaluate the catalytic activities of Ag-Pd nanoframes, Ag@Ag-Pd nanocubes, and Ag nanocubes, we followed the same protocol but kept the number of nanoparticles at 1.5×10^{10}.

Instrumentation and characterization. The UV-vis spectra were recorded using a Cary 50 spectrometer (Agilent Technologies, Santa Clara, CA). The contents of Au and Ag were determined using an inductively coupled plasma mass spectrometer (ICP-MS, NexION 300Q, PerkinElmer, Waltham, MA). A routine centrifuge (Eppendorf 5430) was used for the collection and washing of samples and the preparation of ICP-MS sample. Transmission electron microscopy (TEM) images were taken using a Hitachi HT7700 microscope (Hitachi, Tokyo, Japan) operated at 120 kV. Scanning electron microscopy (SEM) images were captured using a Hitachi SU-8230 microscope operated at 20 kV. High-angle annular dark-field scanning TEM (HAADF-STEM) and energy dispersive spectroscopy (EDS) mapping were performed with a JEOL 2200FS STEM/TEM microscope equipped with a CEOS GmbH probe corrector operated at 200 kV. Raman spectra were taken using Renishaw InVia micro Raman system (Renishaw, Hoffman Estates, IL).

2.3 Results and Discussion

2.3.1 Ag@Ag-Au Core-Frame Nanocubes

We dispersed the Ag nanocubes (Figure 2.1) in an aqueous solution containing H_2Asc and PVP at in an initial pH of 3.2, followed by the co-titration of $AgNO_3$ and $HAuCl_4$ at a specific molar ratio using a dual-channel syringe pump at room temperature. It is worth mentioning that we cannot pre-mix these two precursors for single-channel titration because of the formation of AgCl precipitate. Also, we employed a slow co-titration rate of 20 μL/min to maintain $AgNO_3$ and $HAuCl_4$ at relatively low concentrations in the reaction system. As a result, we could avoid the formation of AgCl precipitate and the possible self-nucleation for both the Ag and Au atoms derived from the reduction of these precursors by H_2Asc. During the co-titration process, we collected aliquots of samples from the reaction solution at different co-titration volumes and characterized the products by elemental analysis, electron microscopy, and UV-vis spectroscopy.

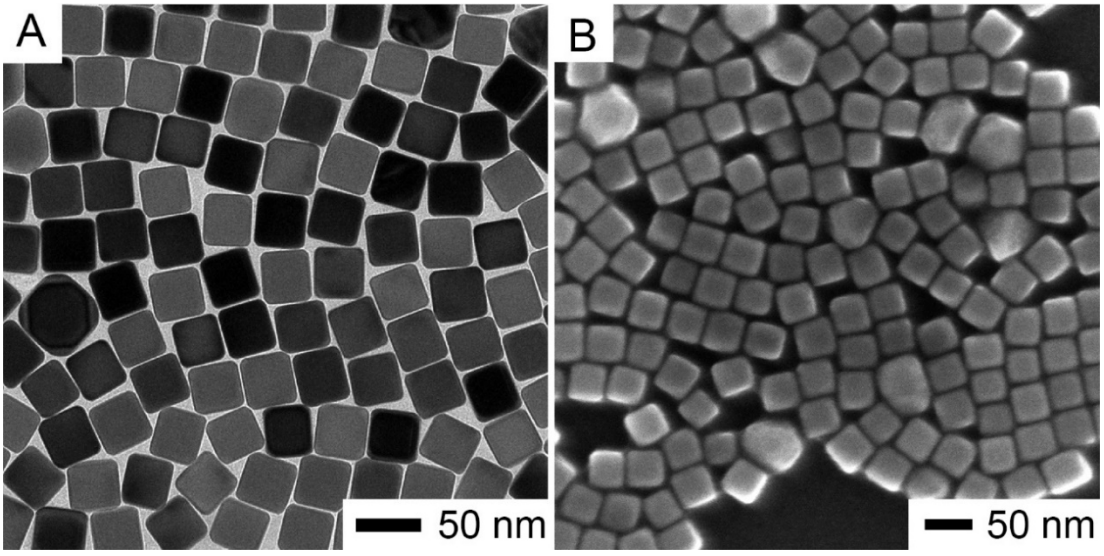

Figure 2.1. (A) TEM and (B) SEM images of the Ag nanocubes used in the present study.

2.3.1.1 Co-Reduction of $AgNO_3$ and $HAuCl_4$ by H_2Asc

We hypothesize that the co-reduction of $AgNO_3$ and $HAuCl_4$ by H_2Asc could generate Ag and Au atoms for their co-deposition onto the Ag nanocubes in a fashion similar to the conventional seeded growth. To quantify the co-reduction kinetics, we measured the Ag and Au contents in the as-obtained samples and the Ag^+ and Au^{3+} ions remaining in the reaction solution after the Ag nanocubes had reacted with different volumes for each precursor. Specifically, we collected both solid products and supernatants after centrifugation to determine their Ag and Au contents by ICP-MS analysis (Table 2.1). We found that the amounts of both Ag (after subtracting the Ag in the original nanocubes) and Au in the solid products increased linearly with the volumes of $AgNO_3$ and $HAuCl_4$ co-titrated into the reaction solution (Figure 2.2, solid lines). The deviations for Ag measurements were significantly larger than those for Au because of the difficulty to quantify the amount of newly deposited Ag due to the interference from the original Ag nanocubes. By assuming that the added precursors were completely reduced to Ag and Au atoms and then co-deposited on the Ag nanocubes, we also calculated the amounts of Ag and Au that would be added onto the Ag nanocubes at different co-titration volumes (Figure 2.2, dotted lines). Within reasonable errors, the added and actually deposited amounts of Ag and Au matched well for every sample. Furthermore, our ICP-MS analysis confirmed that the Ag and Au contents in the supernatants were below 8.6×10^{-4} and 2×10^{-5} mM, respectively, during the entire co-titration process (Table 2.1). Collectively, our data support the argument that the co-titrated $AgNO_3$ and $HAuCl_4$ precursors were completely reduced by H_2Asc to generate Ag and Au atoms, respectively, followed by their co-deposition onto the Ag nanocubes.

Table 2.1. The Ag and Au contents in the as-obtained Ag@Ag-Au nanocubes and supernatant collected from each synthesis using ICP-MS analysis.

Volume of $HAuCl_4$ (mL)	Ag deposited (μg)	Au deposited (μg)	Ag added (μg)	Au added (μg)	Ag ions in supernatant (μM)	Au ions in supernatant (μM)
0.2	8.9±2.2	2.9±0.4	5.92	2.748	0.046	0.020
0.4	11.3±1.4	5.9±0.8	11.84	5.496	0.068	0.013
0.6	16.9±4.4	9.9±1.4	17.76	8.244	0.086	0.015
0.8	21.9±4.3	12.6±2.0	23.68	10.992	0.066	0.018

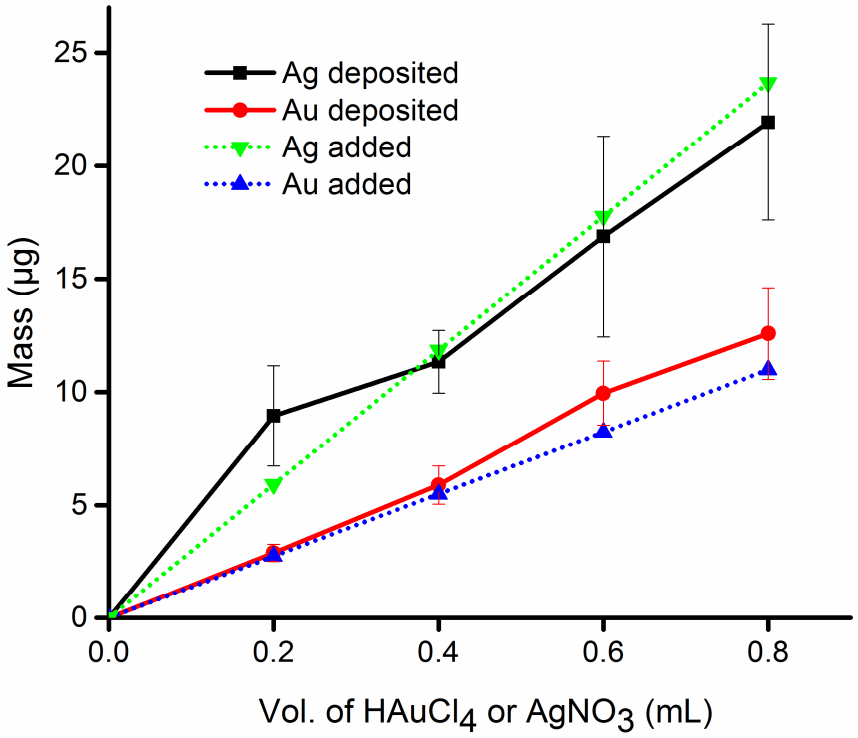

Figure 2.2. The amounts of Ag and Au deposited on Ag nanocubes when different volumes of aqueous $AgNO_3$ (0.3 mM) and aqueous $HAuCl_4$ (0.1 mM) were co-titrated into an aqueous suspension of Ag nanocubes in the presence of H_2Asc. The data points marked as "deposited" are the amounts of Ag and Au derived from ICP-MS analysis. The data points marked as "added" represent the amounts of Ag and Au calculated by assuming complete reduction for the added $AgNO_3$ and $HAuCl_4$, followed by co-deposition of the Ag and Au atoms onto the Ag nanocubes.

2.3.1.2 Co-deposition of Ag and Au on Ag Nanocubes

We used electron microscopy to resolve changes to the morphology of Ag nanocubes resulting from the co-deposition of Ag and Au. Figure 2.3 shows the TEM (left panel) and SEM (right panel) images of the Ag nanocubes after they had reacted with different volumes of 0.3 mM aqueous $AgNO_3$ and 0.1 mM aqueous $HAuCl_4$ in the presence of H_2Asc and PVP. With the addition of 0.2 or 0.4 mL for each precursor, TEM images indicated that the average edge length of the Ag nanocubes was increased from 39.2±1.6 nm to 40.9±2.3 (Figure 2.3A) and 42.8±1.64 nm (Figure 2.3C), respectively. The increase in size indicates the co-deposition of Ag and Au atoms onto the Ag nanocubes. The SEM images confirmed that the cubic shape of the original particles was well preserved and no pits could be identified on each particle (Figure 2.3, B and D), excluding the possible involvement of galvanic replacement between the Ag nanocubes and the added $HAuCl_4$. With further increase of the titration volume to 0.8 mL or 1.5 mL for each precursor, we did not observe any voids or pits from the TEM image of the nanocubes (Figure 2.3, E and G). The SEM images show more truncation at the corner sites of nanocubes (Figure 2.3, F and H), which could be attributed to the preferential deposition of Ag and Au atoms on the edges of the nanocubes.

To identify the deposition pathway of Ag-Au alloy, we used aqueous 3% H_2O_2 to selectively remove the Ag while leaving the Au intact. Figure 2.4 shows TEM images of the resultant nanostructures corresponding to the samples shown in Figure 2.3, A, C, E, and G, after etching for 1 h. With the introduction of 0.2 mL of each precursor, we observed the formation of Ag-Au nanoframes with thin ridges and some coverage for the {111} facets at the corner sites (Figure 2.4A). Our ICP-MS analysis revealed that the nanoframes

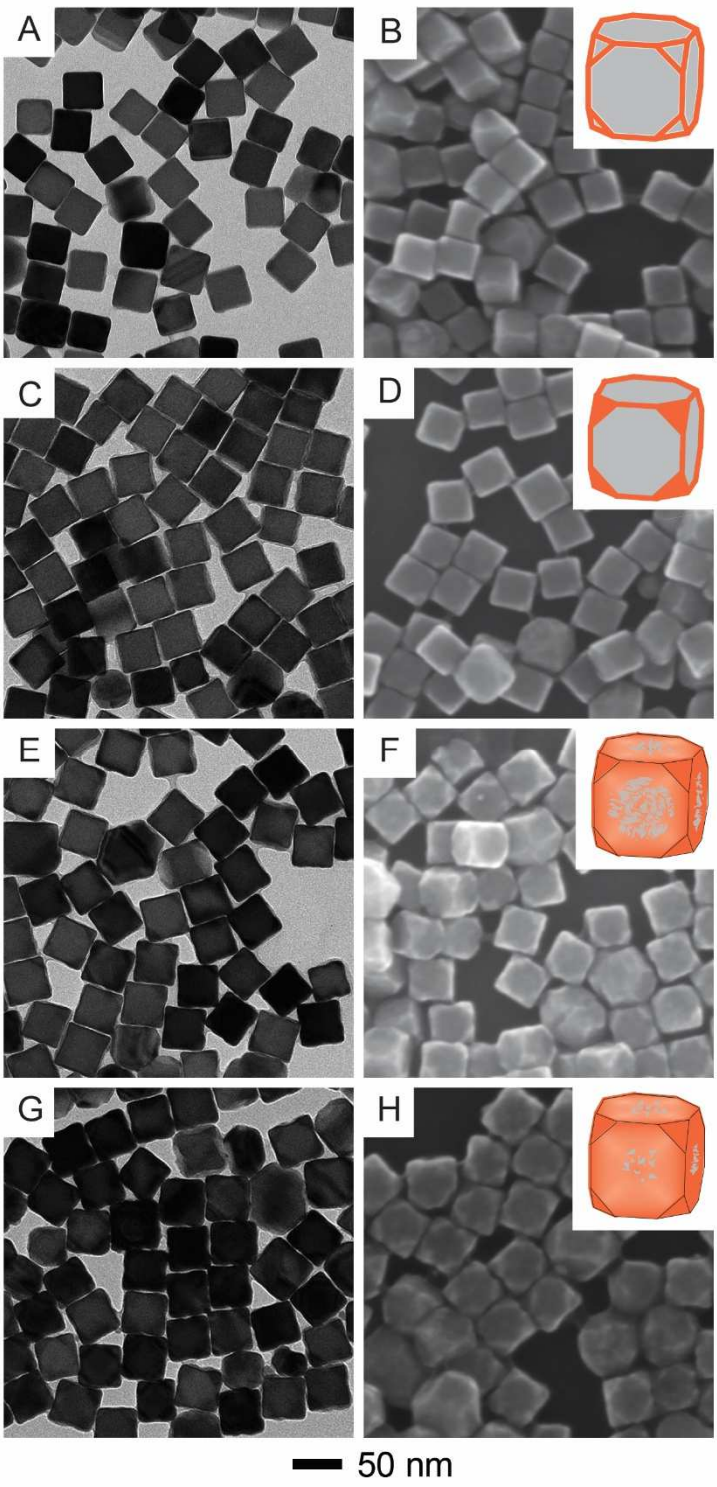

Figure 2.3. TEM (left panel) and SEM (right panel) images of Ag@Ag-Au nanocubes prepared by co-titrating different volumes of aqueous $AgNO_3$ (0.3 mM) and $HAuCl_4$ (0.1 mM): (A, B) 0.2, (C, D) 0.4, (E, F) 0.8, and (G, H) 1.5 mL for each precursor. The insets show models of the corresponding structures.

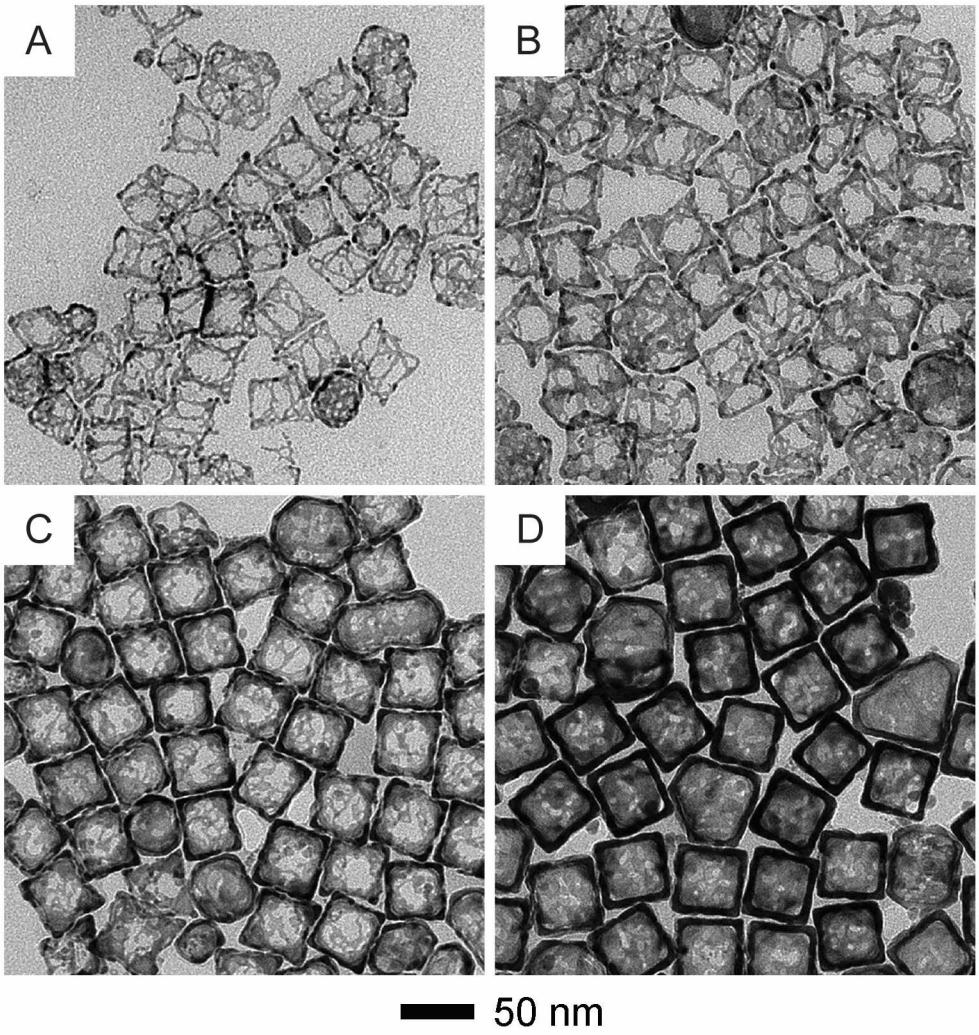

Figure 2.4. TEM images of Ag@Ag-Au nanocubes after treatment with 3% aqueous H_2O_2. The samples were prepared by co-titrating different volumes of aqueous $AgNO_3$ (0.3 mM) and $HAuCl_4$ (0.1 mM): (A) 0.2, (B) 0.4, (C) 0.8, and (D) 1.5 mL for each precursor.

were made of Ag and Au with a molar ratio at 2:1, indicating that the 3% H_2O_2 solution could not remove all the Ag in the deposited Ag-Au alloy. At 0.4 mL for each precursor, we noticed the formation of Ag-Au nanoframes with thicker ridges as well as flat planes at the corner sites, together with some deposition of Ag and Au on the side faces (Figure 2.4B). With a continuous increase in titration volume to 0.8 and then 1.5 mL for each precursor, we noticed that more Ag-Au showed up on the side faces of each nanocube,

leading to the formation of nanocages with decreasing porosity on the side faces (Figure 2.4, C and D).

Based on the results shown in Figures 2.2-2.4, we proposed a plausible mechanism that can account for the co-reduction and co-deposition of Ag and Au on Ag nanocubes (Figure 2.5). There are three competing reactions involved in the co-titration process: *i*) the galvanic replacement between Ag nanocubes and $HAuCl_4$, *ii*) the reduction of $HAuCl_4$ by H_2Asc, and *iii*) the reduction of $AgNO_3$ by H_2Asc. It is critical to co-titrate $AgNO_3$ and $HAuCl_4$ at a proper molar ratio in order to provide an adequate amount of Ag^+ ions in the reaction solution to effectively push the galvanic replacement reaction backward and ultimately block it. Also, it is essential to introduce the $AgNO_3$ precursor dropwise to keep the local concentration of Ag^+ ions at a sufficiently low level and thus eliminate the possible formation of AgCl precipitate due to the release of Cl^- ions from $HAuCl_4$. When the molar ratio of $AgNO_3$ to $HAuCl_4$ was increased to 3:1 and higher, we could achieve the condition of $R_{red} > R_{gal}$, and as a result, the added $HAuCl_4$ was immediately reduced by H_2Asc before it could participate in the galvanic reaction with the Ag nanocubes. Combined together, the co-reduction of $AgNO_3$ and $HAuCl_4$ by H_2Asc could generate Ag and Au atoms for their co-deposition onto the Ag nanocubes in a fashion similar to the conventional seeded growth. According to the standard reduction potentials of Ag^+/Ag (0.79 V) and $AuCl_4^-/Au$ (0.99 V) at room temperature,[39] we anticipate that $AuCl_4^-$ should be reduced firstly by H_2Asc to generate Au atoms for their deposition onto the Ag nanocubes. In the following step, Ag^+ ions will go through underpotential deposition onto the Au atoms to generate a Au-Ag alloy.[40] In a sense, we believe that the Au and Ag atoms were deposited concomitantly.[41,42] For nanocrystals with a face centered cubic (*fcc*)

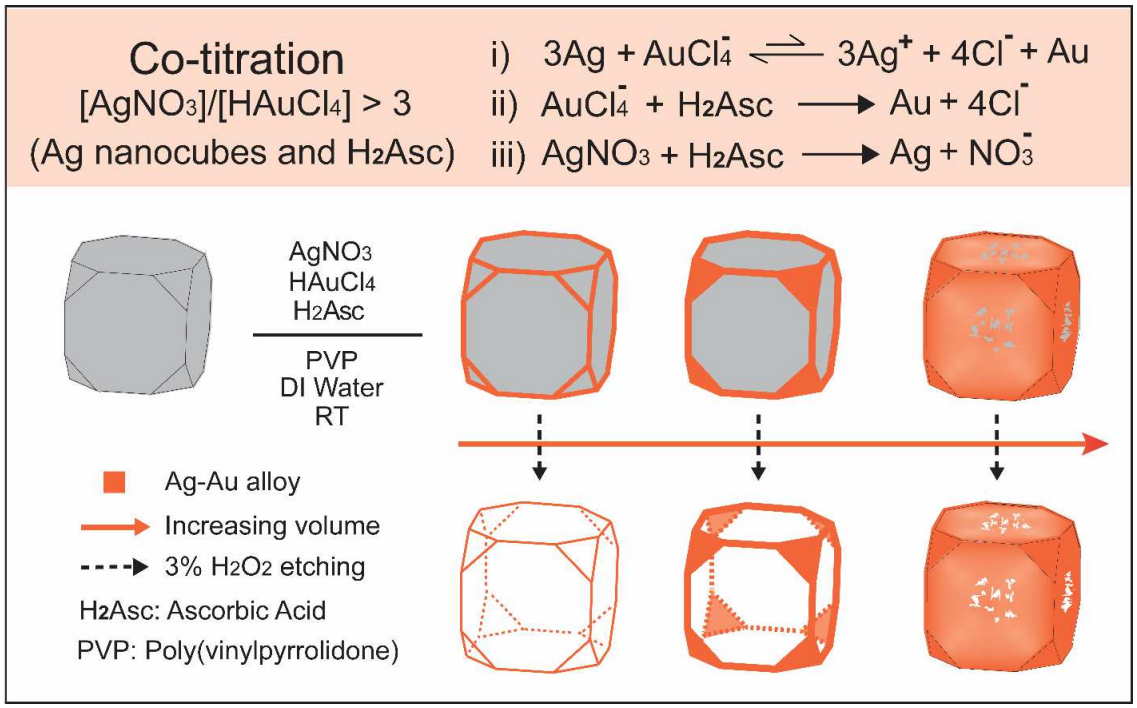

Figure 2.5. (top) A list of three competing reactions involved in the co-titration process. (bottom) Illustration of the transformation of a Ag nanocube into three types of Ag@Ag-Au nanocubes by increasing the volumes of the two co-titrated precursors, followed by removal of the Ag templates to generate Ag-Au nanoframes or nanocages.

structure, the specific surface free energies of its low-index facets should increase in the order of $\gamma_{111} < \gamma_{100} < \gamma_{110}$. At the early stage of co-deposition, the Ag and Au atoms should preferentially nucleate on the {110} facets with the highest energy, and as such, these atoms would be largely deposited on the edges of the Ag nanocube. As the volumes of the two precursors are increased, more atoms will be generated for their continuous deposition onto the {110} facets, followed by their successive migration *via* surface diffusion to the {111} facets (corners) and {100} facets (side faces) of the Ag nanocube, respectively,[43] leading to the formation of core-frame and finally core-shell nanocubes.

2.3.1.3 Plasmonic Properties of Ag@Ag-Au Core-Frame Nanocubes

It is well-known that Au and Ag nanocrystals have distinctive LSPR properties that are strongly dependent on parameters that include size, shape, morphology, and internal structure (solid *versus* hollow).[44] When these two metals are alloyed together, the LSPR properties should be sensitive to the elemental composition. Figure 2.6A shows UV-vis spectra of an aqueous suspension of the Ag nanocubes before and after they had reacted with different volumes of co-titrated 0.3 mM $AgNO_3$ and 0.1 mM $HAuCl_4$ in the presence of H_2Asc and PVP. Because we corrected the dilution factor caused by the titration of different volumes of the precursor solutions, the change in peak intensity could be directly correlated to the variation in extinction coefficient associated with the resultant products. With a co-titration volume of 0.05 and 0.1 mL (for each precursor), the major LSPR peak of the Ag nanocubes was red-shifted from 437 to 446 and 452 nm, respectively, together with a major drop in intensity and some broadening in width. According to previous studies, these changes to the LSPR features could be attributed to the deposition of Au and the scattering of light by the interface between Ag and Au, respectively.[45] With further increase of co-titration volume to 0.2, 0.4 and 0.8 mL, the major LSPR peak was red-shifted to 458, 469 and 475 nm, respectively, with slight increases for both intensity and width. The red-shift in peak position can be ascribed to the increase in edge length for the nanocubes. Because Ag has a stronger plasmon resonance than that of Au,[46] the increase in peak intensity for the samples obtained with co-titration volume increasing from 0.2 to 0.8 mL can be attributed to the deposition of a significantly larger amount of Ag than Au during the co-titration process. When the titration volume was further increased from 0.8 to 1.5 mL, however, the major LSPR peak was slightly blue-shift from 475 to 473 nm, together with an increase in intensity, suggesting the formation of nanocubes with significantly

truncated corners as the deposition progressed. The information derived from the UV-vis spectra is consistent with the observations by SEM and TEM imaging (see Figure 2.3, E-H). The spectra confirmed that the involvement of Au could be manipulated to tailor the LSPR properties of Ag nanocubes through the co-deposition of Ag and Au atoms at a well-controlled ratio and partial distribution.

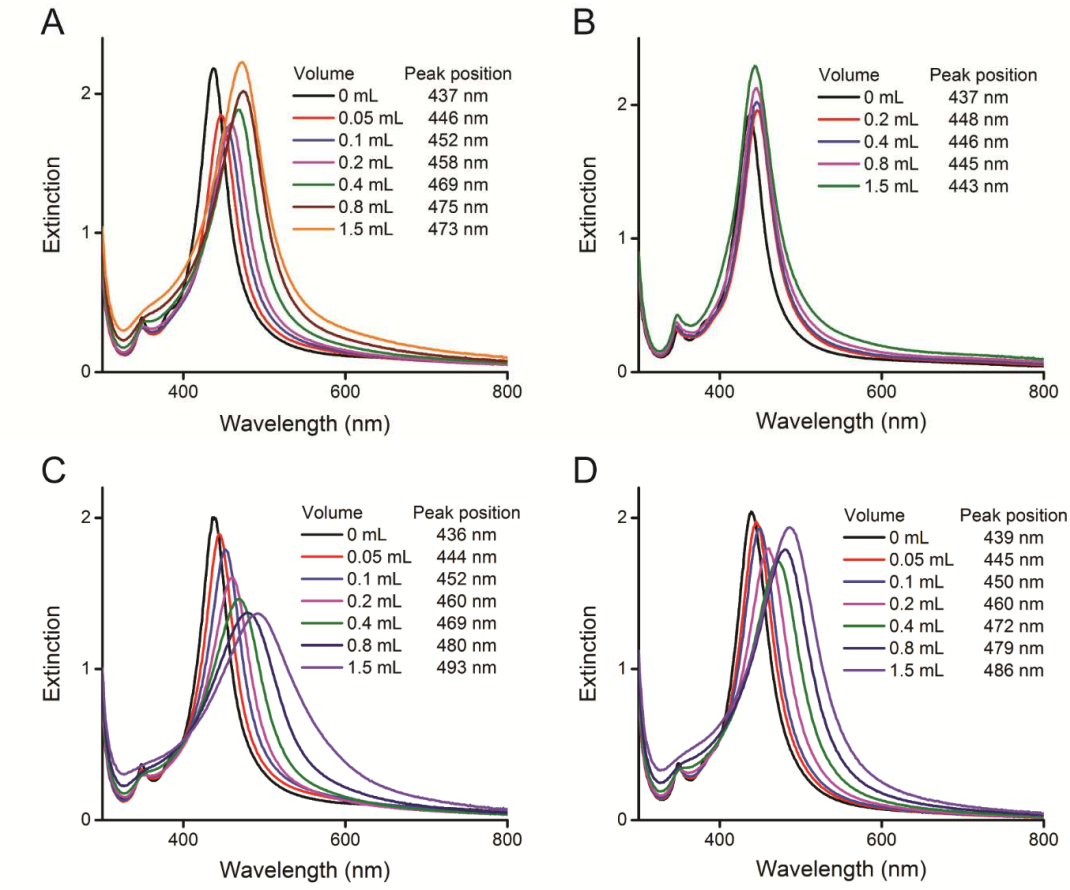

Figure 2.6. UV-vis spectra taken from an aqueous suspension of Ag nanocubes before and after they were titrated with different volumes (indicated on the curves) of (A) 0.3 mM $AgNO_3$ and 0.1 mM $HAuCl_4$, (B) 0.3 mM $AgNO_3$, (C) 0.1 mM $AgNO_3$ and 0.1 mM $HAuCl_4$, and (D) 0.2 mM $AgNO_3$ and 0.1 mM $HAuCl_4$ aqueous solutions.

To further elucidate the role of Au in manipulating the LSPR properties of Ag

nanocubes, we performed a control experiment in which we titrated different volumes of 0.3 mM $AgNO_3$ in the absence of $HAuCl_4$ while leaving the other experimental parameters unchanged. Figure 2.6B shows the UV-vis spectra of an aqueous suspension of the Ag nanocubes before and after they had reacted with different volumes of $AgNO_3$ in the presence of H_2Asc. Different from those shown in Figure 2.6A, we found that the LSPR peak of Ag nanocubes was red-shifted from 437 to 448 nm at 0.2 mL and then slightly blue-shifted from 448 to 443 nm as the titration volume was increased up to 1.5 mL. The red and blue shifts could be ascribed to the increase in dimension and corner truncation, respectively, during the deposition of Ag atoms.

We also monitored the changes to the LSPR of the Ag nanocubes when the molar ratio of the two precursors was below the threshold of 3 needed for the galvanic-free co-deposition. At a molar ratio of 1, as shown in Figure 2.6C, we found that the LSPR peak of the Ag nanocubes was continuously shifted to the red, together with a decrease in intensity. At a co-titration volume of 0.4 mL, the LSPR peak was changed from 437 to 469 nm and there was more broadening in peak width, indicating the involvement of galvanic replacement reaction. At 1.5 mL, the LSPR peak was further shifted to 493 nm with considerably broadening in peak width. When the molar ratio was set to 2, Figure 2.6D indicates that the LSPR peak of the Ag nanocubes was constantly shifted to the red, together with peak broadening and increase in peak intensity at 0.8 and 1.5 mL, respectively. These results suggest that, when an inadequate amount of $AgNO_3$ was involved in the co-titration process to inhibit galvanic replacement reaction, the Ag nanocubes were transformed into hollow nanostructures made of an Au-Ag alloy, consistent with our previous study.[37] Figure 2.7 shows TEM images of three products that

were prepared by co-titrating aqueous $AgNO_3$ and $HAuCl_4$ when $AgNO_3$ was in sufficiently involved, confirming the transformation of Ag nanocubes into Ag-Au hollow nanocubes.

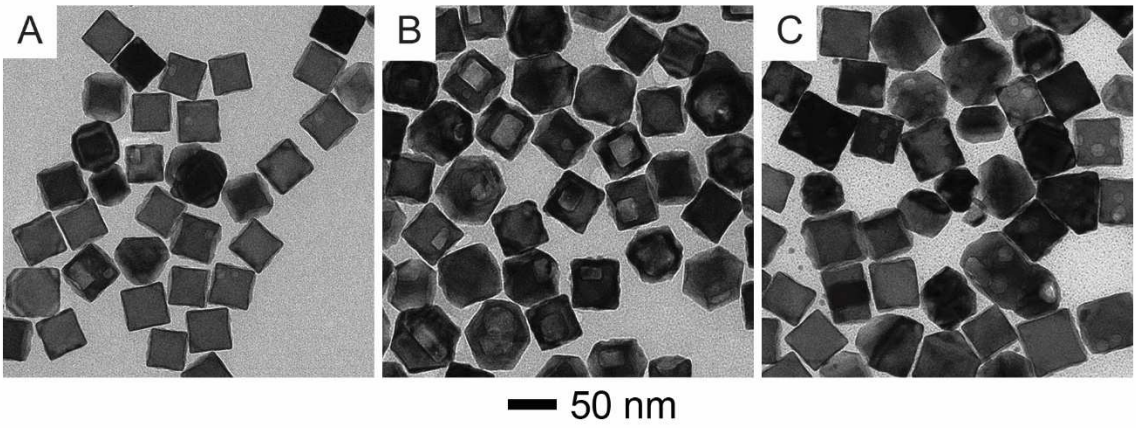

Figure 2.7. TEM images of Ag-Au hollow nanocubes prepared by co-titrating aqueous $AgNO_3$ (0.1 mM) and $HAuCl_4$ (0.1 mM) at (A) 0.4 mL and (B) 1.5 mL for each precursor. (C) TEM image of Ag-Au hollow nanocubes prepared by co-titrating aqueous $AgNO_3$ (0.2 mM) and $HAuCl_4$ (0.1 mM) at 0.8 mL for each precursor.

To evaluate the role of Au atoms in affecting the SERS activity of Ag nanocubes, we collected the SERS spectra of 1,4-BDT molecules adsorbed on the surfaces of the Ag nanocubes and Ag@Ag-Au nanocubes obtained by co-titrating 0.4 mL of 0.3 mM $AgNO_3$ and 0.1 mM $HAuCl_4$. In this case, the Ag and Au atoms were co-deposited at corners and edges of Ag nanocubes with a Ag to Au molar ratio of 3:1 (see Figure 2.3, C and D). It is also worth noting that the corners and edges are often referred as to the sites where the electromagnetic field was greatly enhanced upon laser excitation. As a result, the deposition of Ag-Au alloy would make an impact on the SERS activity of the Ag nanocubes. Interestingly, we observed distinctive SERS properties for the Ag@Ag-Au

nanocubes when excited at visible and near-infrared wavelengths. At 532 nm laser

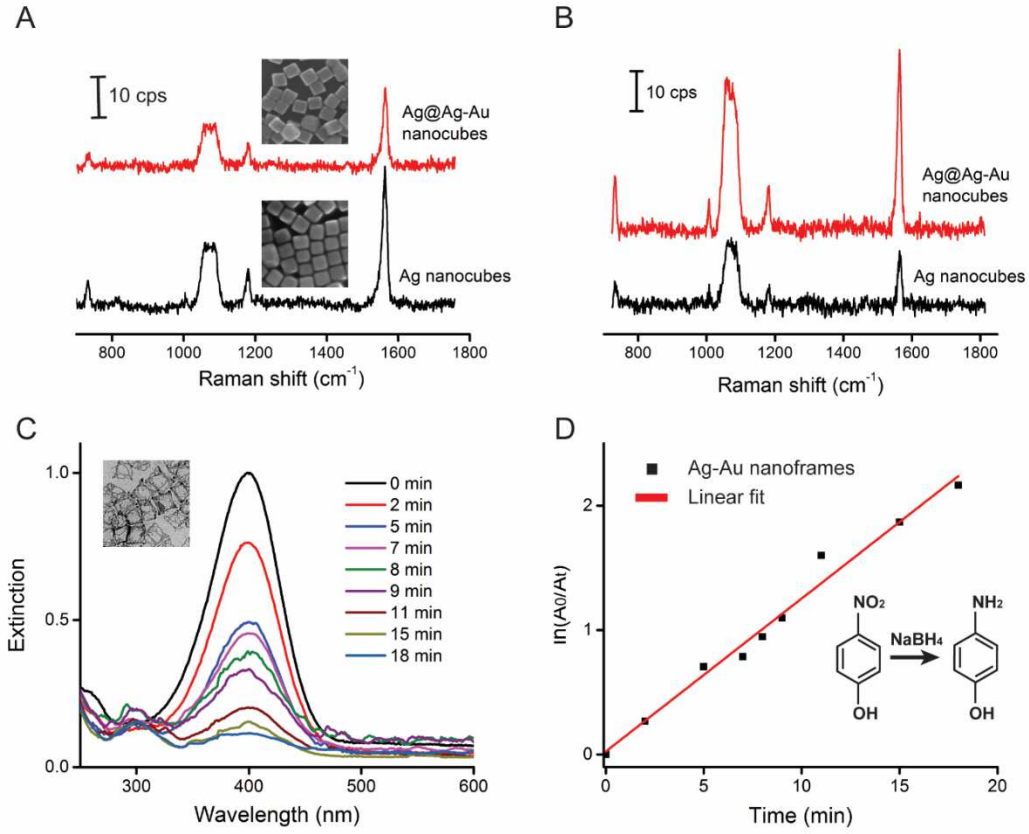

Figure 2.8. SERS spectra taken from 1,4-BDT adsorbed on the Ag and Ag@Ag-Au core-frame nanocubes, respectively, at excitation wavelengths of (A) 532 nm and (B) 785 nm, respectively. The Ag@Ag-Au nanocubes were prepared by co-titrating 0.4 mL of $AgNO_3$ (0.3 mM) and 0.4 mL of $HAuCl_4$ (0.1 mM) into an aqueous suspension of Ag nanocubes in the presence of H_2Asc. (C) Time-dependent UV-vis absorption spectra recorded at different time points for the reduction of 4-NP by $NaBH_4$ at room temperature in the presence of Ag-Au nanoframes as a catalyst. (D) Plot of $\ln[A_0/A_t]$ versus time for the peak at 400 nm. The catalyst was prepared by co-titrating 0.2 mL of $AgNO_3$ (0.3 mM) and 0.2 mL of $HAuCl_4$ (0.1 mM) into an aqueous suspension of Ag nanocubes in the presence of H_2Asc, followed by the treatment with 3% aqueous H_2O_2 for 1 h.

excitation, we found that the SERS peak at 1562 cm^{-1} (the benzene ring mode 8a) decreased in intensity upon the co-deposition of Ag and Au atoms at 3:1 atomic ratio (Figure 2.8A). This result suggests that even the inclusion of a small amount of Au atoms

onto the surfaces of Ag nanocubes would lead to strong plasmon damping at visible excitation wavelength due to the inter-band transition of Au at 2.5 eV (~500 nm),[47] leading to an attenuation in the SERS intensity. By switching the laser excitation to 785 nm, we noticed that the intensity of the same SERS peak at 1562 cm^{-1} was increased by ~3 times (Figure 2.8B), suggesting that the involvement of Au atoms on the surfaces of Ag nanocubes could enhance their SERS activity in the near-infrared region. Such enhancement could be attributed to the deposition of Au atoms onto the Ag nanocubes. Because the Au-S bond is stronger than that of the Ag-S bond, there should be more significant charge transfer between a Au surface and the adsorbed probe molecules, resulting in stronger chemical enhancement. This observation is consistent with our previous findings.[48] Collectively, our results suggest that co-deposition of Ag and Au atoms onto the surfaces of Ag nanocubes would extend the SERS activity of Ag nanocubes into near infrared region for applications in biological sensing.

2.3.1.4 Catalytic Properties of Ag-Au Nanoframes

In addition to the unique LSPR and SERS properties for the Ag@Ag-Au core-frame nanocubes, we also investigated the catalytic properties of nanoframes made of Ag-Au alloy upon the removal of Ag templates. It is anticipated that nanoframes should embrace significantly improved catalytic activity because of enormous specific surface areas when compared to their solid counterparts.[49–51] Specifically, we prepared the sample with a co-titration volume of 0.2 mL for each precursor, and as a result, the Ag and Au atoms with a Ag to Au molar ratio of 3:1 were deposited on the edges of Ag nanocubes (see Figure 2.3, A and B). Upon etching of the core-frame nanocubes in an aqueous 3% H_2O_2 for 1 h, we

obtained Ag-Au nanoframes with thin ridges and opening on the {111} facets (see Figure 2.4A). Our ICP-MS analysis indicates that the nanoframes are made of Ag and Au with a Ag to Au molar ratio of 2:1. This data suggest that 3% H_2O_2 could remove Ag from the cores (pure Ag), as well as some of the Ag atoms in the newly deposited Ag-Au alloy. We used these Ag-enriched Ag-Au nanoframes as a catalyst for the reduction of 4-NP to 4-AP by $NaBH_4$.[52] Upon the introduction of 1.42×10^{11} nanoframes, we collected a series of UV-vis spectra as a function of time (Figure 2.8C). By monitoring the decay of the absorption peak at 400 nm, we plotted $\ln[A_0/A_t]$ as a function of time and obtained a straight line (Figure 2.8D). Our result indicates that the reaction followed the first-order kinetics, with a rate constant of 0.123 min^{-1}. Although the rate constant of the Ag-Au nanoframes was one order of magnitude smaller than the value reported for Au nanocages,[53] they are attractive for the development of cost-effective catalysts through the inclusion of a large amount of Ag.

2.3.2 Ag@Ag-Pd Core-Frame Nanocubes

Among noble metals, it is well-known that Ag and Au nanocrystals embrace strong LSPR peaks in the visible region for SERS applications.[54,55] However, Ag and Au nanocrystals could catalyze a limited number of chemical reactions.[56] In comparison, Pd and Pt nanocrystals are excellent catalysts that can catalyze a larger number of chemical reactions,[57-60] but both of them exhibit extremely poor SERS activity due to the very weak coupling between their free electrons and the visible light.[61] For instance, the SERS EF of 40-nm Pd nanocubes are only 10^3-10^4, which are 10^4 folds weaker than that of Ag nanocubes with a similar size.[62] One strategy to integrate the SERS and catalytic properties

on a single nanocrystal is to directly deposit Pd or Pt on the surfaces of Au or Ag nanocrystals for the formation of bimetallic nanocrystals with dual functionality.

2.3.2.1 Co-Deposition of Ag and Pd on Ag Nanocubes

In a typical synthesis, we co-titrated different volumes of 0.2 mM Na_2PdCl_4 and 0.1 mM $AgNO_3$ into the suspension of Ag nanocubes in the presence of H_2Asc and PVP.[63] Figure 2.9, A-C, shows TEM images of the Ag@Ag-Pd nanocubes obtained by adding 0.1, 0.2, and 0.3 mL of each precursor. The resultant nanocubes remained a cubic shape without pits or holes, suggesting that the galvanic replacement reaction was completely inhibited. The sharpened corners and edges of the nanocubes suggest the preferential deposition of Pd and Ag atoms on the edges of the nanocubes. We then used ICP-MS to confirm and

Table 2.2. The Pd and Ag contents in the as-prepared Ag@Ag-Pd nanocubes collected from each synthesis using ICP-MS analysis.

Volumes of the two precursors (mL)	Mass of Pd (μg)	Mass of Ag (μg)	Pd content[a] (wt%)
0.1, 0.1	1.11	49.1	2.21±0.22
0.2, 0.2	2.08	55.1	3.63±0.26
0.3, 0.3	2.83	58.4	4.63±0.30
0.5, 0.5	4.66	59.5	7.27±0.19

[a]The Pd weight percentage (wt%) was calculated from the mass ratio of Pd to Ag plus Pd in the solid, the standard deviations were obtained from three experimental runs.

quantify the content of Pd in the resultant nanocubes. The Pd content increased from 2.2 to 4.6% as the titration volume increased from 0.1 to 0.3 mL (Table 2.2). We further collected aberration-corrected high-angle annular dark-field scanning TEM (HAADF-STEM) and

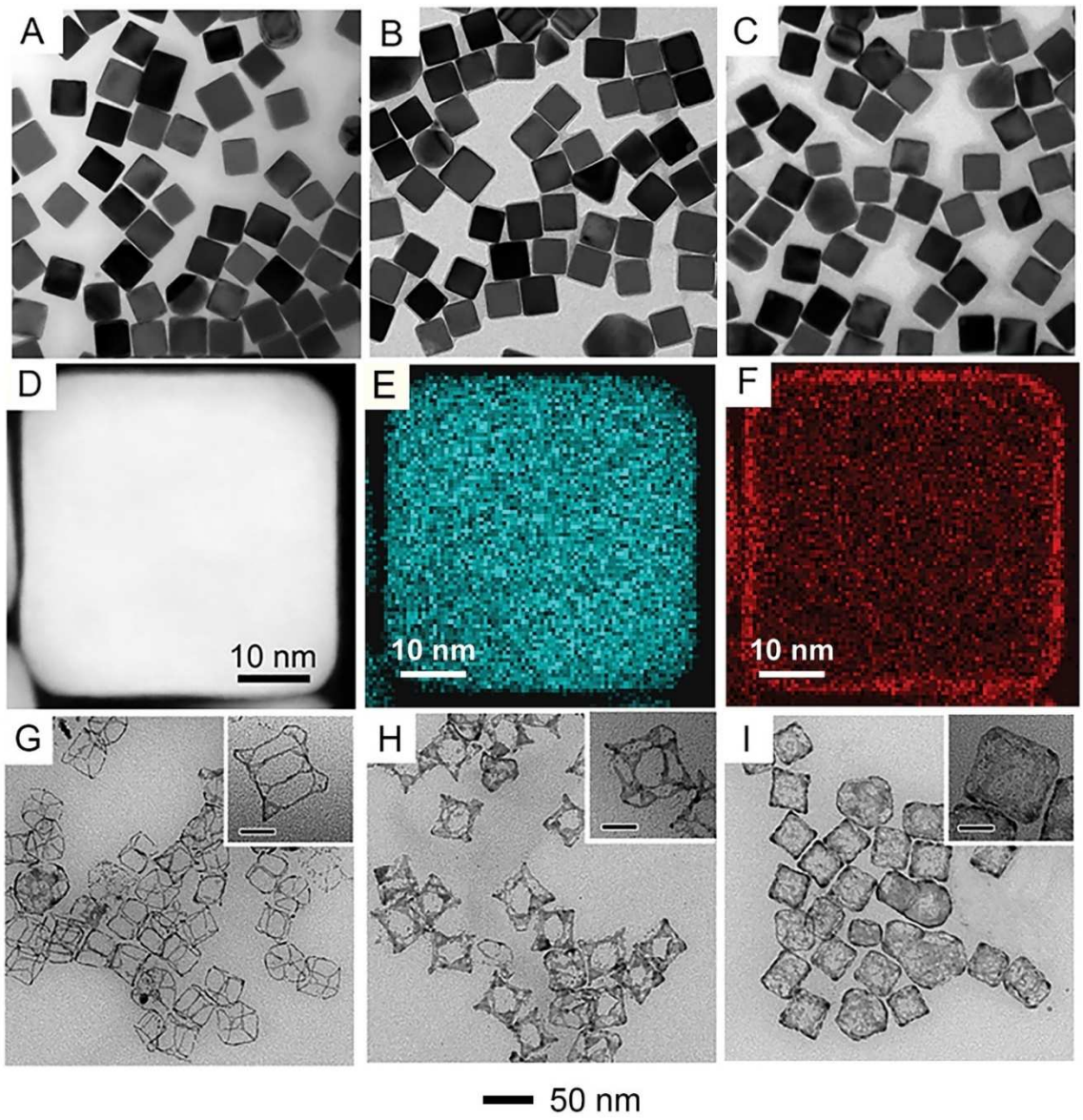

Figure 2.9. (A-C) TEM images of Ag@Ag-Pd nanocubes prepared by co-titrating aqueous Na_2PdCl_4 (0.2 mM) and $AgNO_3$ (0.1 mM), at 0.1, 0.2, and 0.3 mL for each precursor, into an aqueous suspension of Ag nanocubes in the presence of H_2Asc and PVP. (D) HAADF−STEM image, and (E, F) EDS mapping of Ag (blue) and Pd (red) of one individual Ag@Ag-Pd nanocube shown in B. (G-I) TEM images of the resultant structures after etching of samples shown in (A-C) with 3% H_2O_2. The scale bars in the insets are 20 nm.

energy dispersive X-ray spectroscopy (EDS) mapping images (Figure 2.9, D-F) from the nanocube to confirm that the Pd was mainly deposited on the edges and corners at a titration

volume of 0.2 mL. To resolve the distribution of Pd atoms on the surface of Ag nanocubes, we treated the as-obtained Ag@Ag-Pd nanocubes shown in Figure 2.9, A-C, with 3% H_2O_2 to remove the Ag core. Figure 2.9, G-I, shows the resultant nanostructures after etching for 1 h. At 0.1 mL, we observed the transformation of solids into nanoframes with thin ridges and little coverage for the {111} facets at the corners (Figure 2.9G). As the volume was increased to 0.2 and 0.3 mL, nanoframes with thicker ridges (Figure 2.9H) and nanocages (Figure 2.9I) were produced, respectively. Taken together, we believe that the Pd and Ag atoms would preferentially nucleate on the high-energy {110} facets and thereby these atoms would be largely confined to the edges of Ag nanocubes, consistent with previous findings in the synthesis of Ag@Ag-Au core-frame nanocubes in Session 2.3.1 (see Figure 2.4, A and B). As the volumes of Pd and Ag precursors were increased to 0.2 and 0.3 mL, respectively, more atoms were generated for their deposition onto the {110} facets, making the ridges thicker. Our results suggest that some atoms could sequentially migrate to the {111} facets (corners) and then {100} facets (side faces) of the Ag nanocubes by surface diffusion. Because it is difficult to resolve the deposition sites for the newly formed Ag atoms, we assumed that Pd and Ag atoms were deposited concomitantly.

2.3.2.2 Ag@Ag-Pd Core-Frame Nanocubes for Probing Catalytic Reactions by SERS

By simply decorating the surface of Ag nanocubes with Pd, we demonstrated that the Ag@Ag-Pd core-frame nanocubes could serve as a unique SERS probe for probing the Pd-catalyzed reduction of 4-NTP by $NaBH_4$ to produce 4-ATP and the subsequent Ag-catalyzed oxidation of 4-ATP to *trans*-4,4'-dimercaptoazobezene (*trans*-DMAB) by the O_2

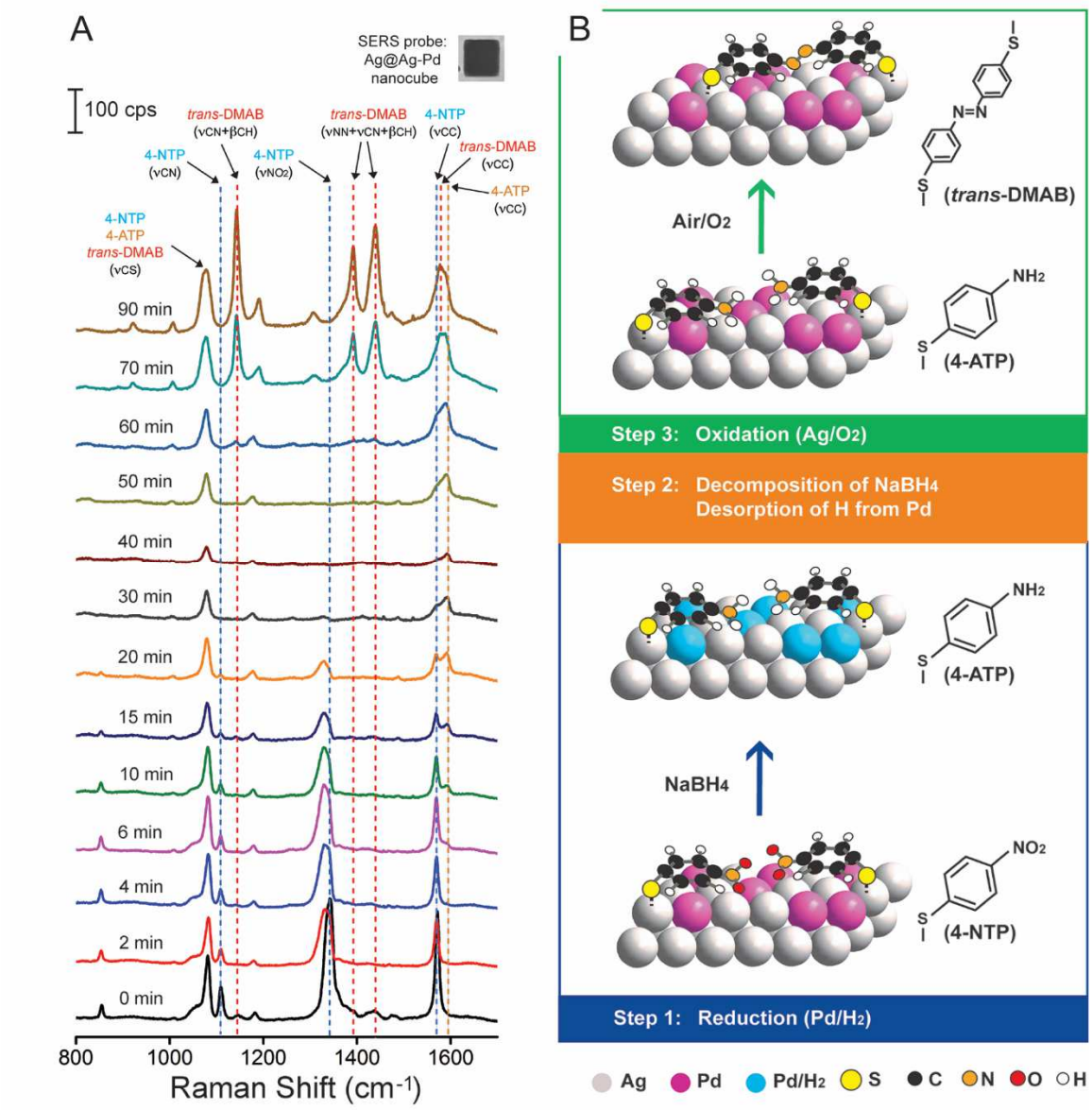

Figure 2.10. (A) Time-dependent SERS spectra for monitoring the reduction of 4-NTP by $NaBH_4$ on Ag@Ag-Pd nanocubes with 2.2 wt.% Pd. (B) Schematic illustration showing the stepwise reactions involving the Pd-catalyzed reduction of 4-NTP by $NaBH_4$ and Ag-catalyzed oxidation of 4-ATP by the O_2 from air.

from air.[64] Figure 2.10A shows the time-dependent SERS spectra collected from the 4-NTP absorbed on the Ag@Ag-Pd core-frame nanocubes containing 2.2 wt.% of Pd. At t = 0 min, we observed three characteristic bands of 4-NTP at 1108 cm^{-1} (ν_{CN}), 1336 cm^{-1}

(ν_{NO2}), and 1572 cm^{-1} (ν_{CC}).[65] Upon the introduction of $NaBH_4$, the ν_{NO2} band was slightly shifted from 1336 to 1330 cm^{-1} at t = 2 min, while other bands remained essentially the same. At t = 6 min, a shoulder peak appeared at 1595 cm^{-1}, which can be assigned to the ν_{CC} of 4-ATP.[66] As the reaction further progressed to 20 min, the ν_{CC} band of 4-ATP increased in intensity while both ν_{NO2} and ν_{CN} bands decreased in intensity. At t = 30 min, both the ν_{CN} and ν_{NO2} bands of 4-NTP were no longer observable. By 40 min, all the three bands of 4-NTP disappeared and the remaining peaks can be assigned to the ν_{CS}, β_{C-H}, and ν_{CC} of 4-ATP, respectively, indicating the complete transformation from 4-NTP to 4-ATP. In the next 20 min, the three peaks of 4-ATP remained the same in position while their intensities were increased. At t = 70 min, we observed three new peaks at 1142 cm^{-1}, 1388 cm^{-1}, and 1429 cm^{-1}, which can be assigned to the $\beta_{CH}+\nu_{CN}$, $\nu_{NN}+\nu_{CN}$, and $\nu_{NN}+\beta_{CH}$ of *trans*-DMAB, respectively.[67] These bands remained unaltered up to 90 min, except for slight increase in intensity. The SERS data suggests that the 4-ATP adsorbed on the surface of the core-frame nanocubes could be oxidized by the O_2 from air to generate *trans*-DMAB.

Based on the SERS data, Figure 2.10B outlines the proposed mechanism. In the first step, the 4-NTP molecules preferentially adsorb with a configuration parallel to the Ag surface through the Ag-S linkage. The formation of *trans*-DMAB rather than *cis*-DMAB supports our argument about the orientation of molecules on the surface. When $NaBH_4$ is introduced, it will decompose to produce H_2, followed by their adsorption and dissociation on the Pd surface to generate H atoms.[68] The atomic hydrogen can rapidly reduce 4-NTP to 4-ATP. In the second step, the 4-ATP molecules remain on the surface of the catalyst under ambient conditions while the $NaBH_4$ remaining in the solution is completely decomposed. In the final step, the Ag surface activates the O_2 from air,[69] triggering Ag-

catalyzed oxidation and enabling the transformation from 4-ATP to *trans*-DMAB.

2.3.2.3 The Catalytic Properties of Ag-Pd Nanoframes

We demonstrated the synthesis of cubic Ag-Pd nanoframes by co-titrating different volumes of 0.1 mM Na_2PdCl_4 and 0.1 mM $AgNO_3$ to the aqueous suspension of Ag nanocubes containing H_2Asc and PVP, followed by selectively removing the Ag template in the core with a wet etchant such as aqueous H_2O_2. Figure 2.11A shows the TEM image of the resultant Ag@Ag-Pd nanocubes with titration volume of 0.4 mL for each precursor. We noticed that the cubic shape was indeed well-preserved and the edge length of the nanocubes was slightly increased from 39.2±1.6 to 41.2±2.1 nm. The increase in size indicates the co-deposition of Ag and Pd layers onto the Ag template, with a projected thickness about 1.2 nm. After etching the product with aqueous 2.3% H_2O_2 for 1 h, we obtained nanoframes with thin ridges and small openings situated on the {111} facets at the corners sites, as indicated by the TEM image in Figure 2.11B. By measuring 100 nanoframes from the TEM images, we obtained a thickness of 1.7±0.2 for the ridges, comparable to the value of 1.2 nm that was deduced from the change in edge length due to Ag/Pd deposition. Using ICP-MS, we confirmed that the nanoframes were made of Ag and Pd with an atomic ratio of Ag/Pd=4.2±0.3. This result suggests the formation of Ag-enriched Ag-Pd bimetallic nanoframes because H_2O_2 could not remove Ag from the deposited Ag-Pd alloy.

When the co-titration volume was increased to 0.8 mL for each precursor, Figure 2.11C shows the TEM image of the resultant Ag@Ag-Pd core-frame nanocubes. In this case, the Ag nanocubes were still kept in the cubic shape while their edge length was further

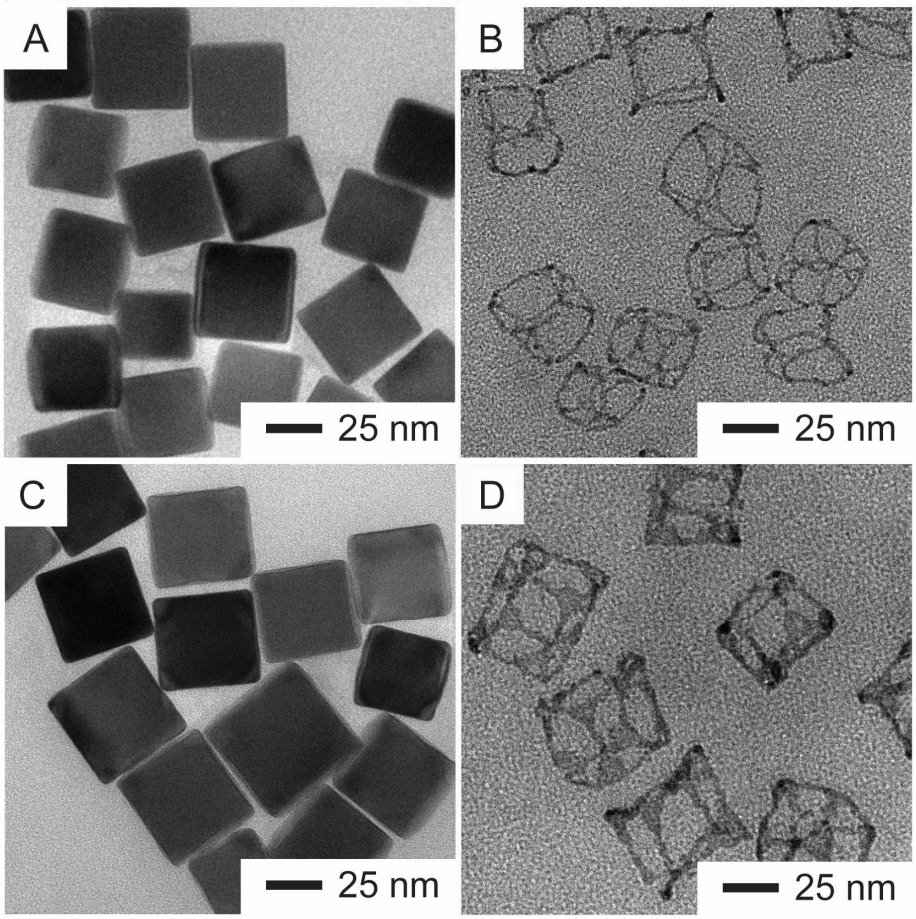

Figure 2.11. (A, C) TEM images of the two samples of Ag@Ag-Pd core-frame nanocubes prepared by co-titrating the Ag nanocubes with 0.4 and 0.8 mL, respectively, of $AgNO_3$ (0.1 mM) and Nd_2PdCl_4 (0.1 mM) solutions. (B, D) TEM images of the Ag-Pd nanoframes obtained by selectively removing the Ag templates in the Ag@Ag-Pd core-frame nanocubes with 2.3% aqueous H_2O_2.

increased to 42.9±1.9 nm. After etching with aqueous 2.3% H_2O_2 for 1 h, the nanocubes were transformed into nanoframes with thicker ridges and complete coverage at the corners, as indicated in Figure 2.11D. We believe that Pd and Ag atoms derived from the co-reduction by H_2Asc were initially deposited on the edges, but they could migrate to the corner sites for the generation of nanoframes with atoms at both edge and corner sites. Our ICP-MS analysis indicated that the atomic ratio of Ag and Pd atoms for the nanoframes was reduced to 2.6±0.3. This data suggests that the conversion yield of Ag precursor was

higher than that of Pd precursor in this synthesis. Collectively, our results demonstrated the feasibility to produce Ag-enriched Ag-Pd nanoframes with a good control over both morphology and composition through the co-titration of $AgNO_3$ and Na_2PdCl_4.

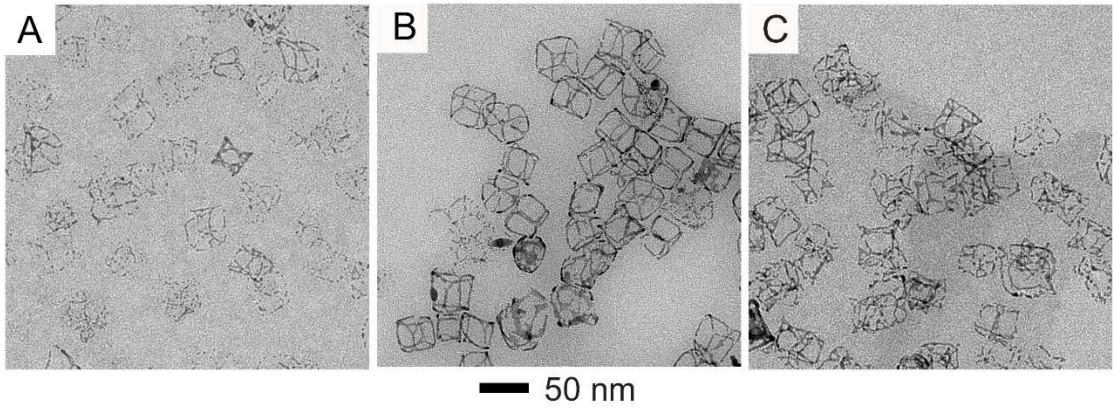

Figure 2.12. TEM images of the Ag-Pd nanoframes obtained by selectively removing the Ag cores (with 2.3% aqueous H_2O_2) from the Ag@Ag-Pd core-frame nanocubes prepared with (A) 0.4 mL of 0.2 mM $AgNO_3$ and 0.4 mL of 0.1 mM Na_2PdCl_4, (B) 0.1 mL of 0.1 mM $AgNO_3$ and 0.1 mL of 0.2 mM Na_2PdCl_4, and (C) 0.4 mL of 0.1 mM Na_2PdCl_4.

To further understand the role of co-titration in controlling the co-deposition of Ag and Pd atoms onto Ag template for the generation of bimetallic nanoframes, we also performed a set of experiments with different molar ratios between $AgNO_3$ and Na_2PdCl_4, $[AgNO_3]/[Na_2PdCl_4]$, while keeping all the other experimental parameters unaltered. Firstly, we increased the concentration of $AgNO_3$ from 0.1 to 0.2 mM while maintaining Na_2PdCl_4 at 0.1 mM to give $[AgNO_3]/[Na_2PdCl_4] = 2$. Figure 2.12A shows a TEM image of the nanoframes obtained at a co-titration volume of 0.4 mL for each precursor. In this case, with an increase in the amount of Ag precursor, we only obtained broken nanoframes. In this case, more Ag atoms derived from AA reduction were incorporated into the frames and the higher content of Ag in the Ag-Pd alloy would make the frames vulnerable to H_2O_2

etching, leading to broken nanoframes. In contrast, when we used 0.1 mM $AgNO_3$ and 0.2 mM Na_2PdCl_4 to attain a ratio of 0.5 for $[AgNO_3]/[Na_2PdCl_4]$, we observed the formation of nanoframes with uniform thickness at a co-titration volume of 0.1 mL for each precursor (Figure 2.12B). In this case, more Pd atoms were deposited onto the Ag nanocubes, leading to the formation of Ag-Pd alloys enriched in Pd than the sample shown in Figure 2.11B. The etching process could still successfully remove the Ag template without damaging the frame structure. To further validate the role of $AgNO_3$, we performed a control experiment by titrating Na_2PdCl_4 only into an aqueous suspension of Ag nanocubes in the presence of H_2Asc and PVP. As shown in Figure 2.12C, only broken nanoframes were obtained as the final product due to the limited amount of Pd deposited at the edge and corner sites. Taken together, these results suggest that the Ag atoms derived from the reduction of $AgNO_3$ would facilitate the co-deposition of Ag and Pd atoms for the formation of Ag-Pd alloy frames on the edge and corner sites of a nanocube, and ultimately protect the frame structure from breaking during H_2O_2 etching. Both the ratios and distributions of Ag and Pd atoms in the Ag-Pd alloy would ultimately determine the success in the formation Ag-Pd nanoframes with an unbroken structure and uniform ridge thickness.

Relative to their solid counterparts, the Ag-Pd bimetallic nanoframes with a highly open structure also showed greatly enhanced catalytic activity toward the reduction of 4-NP to 4-AP by $NaBH_4$. In a typical test, we prepared catalysts with a co-titration volume of 0.4 mL for each precursor for the production of bimetallic nanoframes with Ag and Pd molar ratio of 4.2:1 (see Figure 2.11A). Upon the introduction of 2.6 μg nanoframes

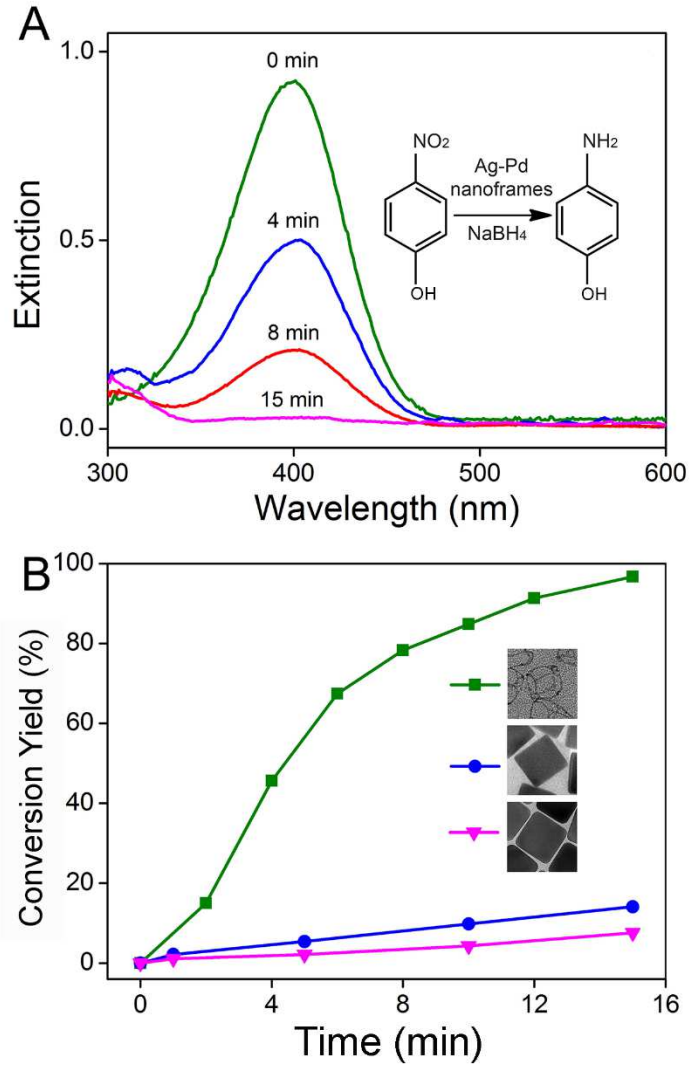

Figure 2.13. (A) UV-vis spectra taken from a 4-NP solution at different time intervals after the introduction of the Ag-Pd bimetallic nanoframes shown in Figure 2.11B. The spectra were obtained by subtracting the absorbance of the Ag-Pd nanoframes from the as-collected spectra. (B) Comparison of 4-NP reduction as a function of time for three different types of catalysts: Ag nanocubes (triangles), Ag@Ag-Pd core-frame nanocubes (circles), and Ag-Pd nanoframes (squares).

(determined by ICP-MS), we collected a series of UV-vis spectra (Figure 2.13A) to monitor the decay of the absorption peak of 4-NP at 400 nm as a function of time. We also collected UV-vis spectra from 4-NP solutions as a function of time when the reduction was catalyzed

by Ag@Ag-Pd core-frame nanocubes and Ag nanocubes, respectively. The number of catalytic particles was kept the same for these three different systems. To benchmark the catalytic performance, Figure 2.13B exhibits the adsorption (normalized to the initial value)

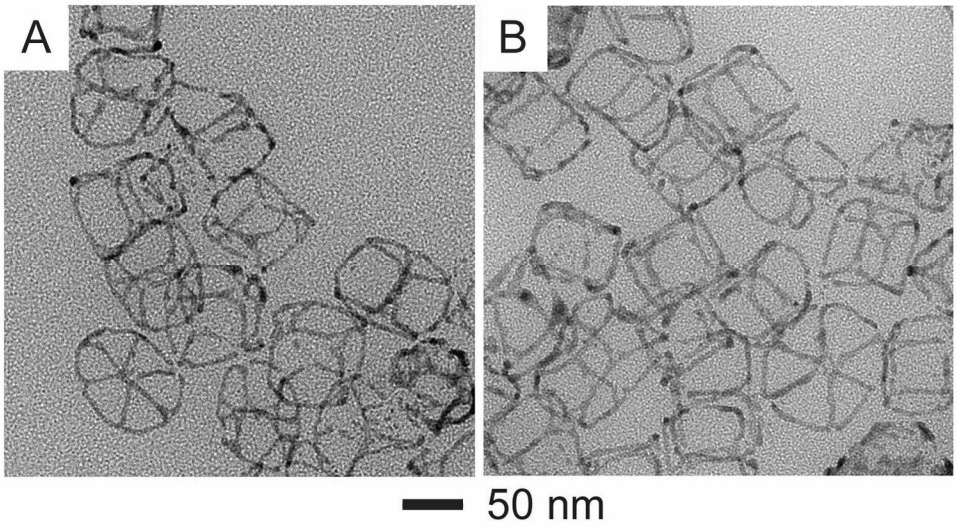

Figure 2.14. TEM images of the Ag-Pd nanoframes shown in Figure 2.11C after (A) centrifugation at 55,000 rpm for 30 min and (B) the catalytic reaction shown in Figure 2.13, respectively.

at the peak position of 4-NP (400 nm) as a function of time for these three systems. It was found that the reduction catalyzed by the Ag-enriched Ag-Pd nanoframes under ambient conditions would give a conversion yield of 98% over 12 min while the yields were only 31% and 10% when Ag@Ag-Pd nanocubes and Ag nanocubes were used as the catalysts, respectively. The higher catalytic activity of the Ag-Pd nanoframes might be related to their unique frame structure and thus high surface area. Additionally, as indicated in Figure 2.14, the cubic nanoframes made of Pd-Ag alloy were mechanically stable and the frame structure was well preserved after they had been centrifuged at 55,000 rpm for 30 min or

had gone through the catalytic reaction. We believe that this new class of hollow and porous alloyed nanostructures hold a great promise for catalytic applications owing to their high specific surface areas and other unique characteristics different from their individual components.[70–72]

2.4 Conclusions

We have demonstrated the co-deposition of Ag and Au atoms onto Ag nanocubes for the generation of Ag@Ag-Au nanocubes through the co-titration of $AgNO_3$ and $HAuCl_4$ in the presence of H_2Asc. The co-titration process could be used to effectively block the galvanic replacement reaction between Ag nanocubes and $HAuCl_4$ when the added $AgNO_3$ was in a sufficiently high proportion to push this reaction backward. Under this condition, the two precursors could be completely reduced by H_2Asc for the generation of Ag and Au atoms, followed by their co-deposition onto the Ag nanocubes in a fashion similar to the conventional seeded growth. Initially, the Ag and Au atoms are deposited on the edges and corners of the Ag nanocubes to generate Ag@Ag-Au core-frame nanocubes. As the co-titration volume is increased, more Ag and Au atoms are co-deposited at the edge and corner sites and then allowed to migrate to the side faces through surface diffusion. We can tailor the LSPR properties of the Ag nanocubes during their transformation into Ag@Ag-Au nanocubes in the visible region. The co-deposition of Ag and Au atoms on the surfaces of Ag nanocubes could be used to enhance the SERS activity of Ag nanocubes at an excitation wavelength of 785 nm. Upon the removal of Ag templates from the Ag@Ag-Au nanocubes by H_2O_2 etching, the as-obtained Ag-enriched Ag-Au nanoframes exhibit catalytic activity toward the reduction of 4-NP by $NaBH_4$.

We have further extended the co-titration methodology to produce Ag@Ag-Pd core-frame nanocubes by the co-titration of $AgNO_3$ and Na_2PdCl_4 in the presence of H_2Asc and PVP. We identify that the elemental composition of the resultant Ag@Ag-Pd nanocubes can be finely tuned by simply varying the titration volume of the precursors. We have demonstrated the use of Ag@Ag-Pd nanocubes as a dual catalyst and a unique SERS probe for catalyzing and probing stepwise reduction of 4-NTP to 4-ATP by $NaBH_4$ and the subsequent oxidation of 4-ATP to *trans*-DMAB by O_2 from the air under an ambient condition. Upon selective etching of the Ag core from the Ag@Ag-Pd core-shell nanocubes, the derivative Ag-Pd nanoframes shows high catalytic activities and great mechanical stability despite having ultrathin ridges and open structures.

2.5 Notes to Chapter 2

Part of this chapter is adapted from the paper "Co-titration of $AgNO_3$ and $HAuCl_4$: A new route to the synthesis of Ag@Ag-Au core-frame nanocubes with enhanced plasmonic and catalytic properties" published in *Journal of Materials Chemistry C*,[73] "A Dual Catalyst with SERS Activity for Probing Stepwise Reduction and Oxidation Reactions" published in *ChemNanoMat*,[74] "Ag-enriched Ag-Pd bimetallic nanoframes and their catalytic properties" published in *ChemNanoMat,*[75] and "Enriching Silver Nanocrystals with a Second Noble Metal" published in *Accounts of Chemical Research*.[76]

2.6 References

(1) Burda, C.; Chen, X.; Narayanan, R.; El–Sayed, M. A. Chemistry and Properties of Nanocrystals of Different Shapes. *Chem. Rev.* **2005**, *105*, 1025–1102.

(2) Zhang, H.; Jin, M.; Xia, Y. Enhancing the Catalytic and Electrocatalytic Properties

of Pt–Based Catalysts by Forming Bimetallic Nanocrystals with Pd. *Chem. Soc. Rev.* **2012**, *41*, 8035-8049.

(3) Joo, S. H.; Park, J. Y.; Tsung, C.–K.; Yamada, Y.; Yang, P.; Somorjai, G. A. Thermally Stable Pt/mesoporous Silica Core–Shell Nanocatalysts for High–Temperature Reactions. *Nat. Mater.* **2009**, *8*, 126–131.

(4) Halas, N. J.; Lal, S.; Chang, W.–S.; Link, S.; Nordlander, P. Plasmons in Strongly Coupled Metallic Nanostructures. *Chem. Rev.* **2011**, *111*, 3913–3961.

(5) Knight, M. W.; Sobhani, H.; Nordlander, P.; Halas, N. J. Photodetection with Active Optical Antennas. *Science* **2011**, *332*, 702–704.

(6) Haes, A. J.; Haynes, C. L.; McFarland, A. D.; Schatz, G. C.; Van Duyne, R. P.; Zou, S. Plasmonic Materials for Surface–Enhanced Sensing and Spectroscopy. *MRS Bull.* **2005**, *30*, 368–375.

(7) Willets, K. A.; Van Duyne, R. P. Localized Surface Plasmon Resonance Spectroscopy and Sensing. *Annu. Rev. Phys. Chem.* **2007**, *58*, 267–297.

(8) Xia, Y.; Li, W.; Cobley, C. M.; Chen, J.; Xia, X.; Zhang, Q.; Yang, M.; Cho, E. C.; Brown, P. K. Gold Nanocages: From Synthesis to Theranostic Applications. *Acc. Chem. Res.* **2011**, *44*, 914–924.

(9) Rosi, N. L.; Mirkin, C. A. Nanostructures in Biodiagnostics. *Chem. Rev*. **2005**, 1547–1562.

(10) Qian, X.; Peng, X.–H.; Ansari, D. O.; Yin–Goen, Q.; Chen, G. Z.; Shin, D. M.; Yang, L.; Young, A. N.; Wang, M. D.; Nie, S. In Vivo Tumor Targeting and Spectroscopic Detection with Surface–Enhanced Raman Nanoparticle Tags. *Nat. Biotechnol.* **2008**, *26*, 83–90.

(11) Lal, S.; Clare, S. E.; Halas, N. J. Nanoshell–Enabled Photothermal Cancer Therapy: Impending Clinical Impact. *Acc. Chem. Res.* **2008**, *41*, 1842–1851.

(12) Wang, D.; Li, Y. Bimetallic Nanocrystals: Liquid–Phase Synthesis and Catalytic Applications. *Adv. Mater.* **2011**, *23*, 1044–1060.

(13) Gilroy, K. D.; Ruditskiy, A.; Peng, H. C.; Qin, D.; Xia, Y. Bimetallic Nanocrystals: Syntheses, Properties, and Applications. *Chem. Rev.* **2016**, *116*, 10414–10472.

(14) Zhang, H.; Jin, M.; Xia, Y. Enhancing the Catalytic and Electrocatalytic Properties of Pt-Based Catalysts by Forming Bimetallic Nanocrystals with Pd. *Chem. Soc. Rev.* **2012**, *41*, 8035-8049.

(15) Gao, C.; Goebl, J.; Yin, Y. Seeded Growth Route to Noble Metal Nanostructures. *J. Mater. Chem. C* **2013**, *1*, 3898-3909.

(16) Lohse, S. E.; Burrows, N. D.; Scarabelli, L.; Liz–Marzán, L. M.; Murphy, C. J. Anisotropic Noble Metal Nanocrystal Growth: The Role of Halides. *Chem. Mater*. **2014**, *26*, 34–43.

(17) Niu, W.; Zhang, L.; Xu, G. Seed–Mediated Growth of Noble Metal Nanocrystals:

Crystal Growth and Shape Control. *Nanoscale* **2013**, *5*, 3172–3181.

(18) Nikoobakht, B.; El–Sayed, M. A. Preparation and Growth Mechanism of Gold Nanorods (NRs) Using Seed–Mediated Growth Method. *Chem. Mater.* **2003**, *15*, 1957–1962.

(19) Jana, N. R.; Gearheart, L.; Murphy, C. J. Wet Chemical Synthesis of High Aspect Ratio Cylindrical Gold Nanorods. *J. Phys. Chem. B* **2001**, *105*, 4065–4067.

(20) Sun, Y.; Mayers, B.; Herricks, T.; Xia, Y. Polyol Synthesis of Uniform Silver Nanowires: A Plausible Growth Mechanism and the Supporting Evidence. *Nano Lett.* **2003**, *3*, 955–960.

(21) Desantis, C. J.; Peverly, A. A.; Peters, D. G.; Skrabalak, S. E. Octopods versus Concave Nanocrystals: Control of Morphology by Manipulating the Kinetics of Seeded Growth via Co–Reduction. *Nano Lett.* **2011**, *11*, 2164–2168.

(22) Langille, M. R.; Personick, M. L.; Zhang, J.; Mirkin, C. A. Defining Rules for the Shape Evolution of Gold Nanoparticles. *J. Am. Chem. Soc.* **2012**, *134*, 14542–14554.

(23) Crane, C. C.; Tao, J.; Wang, F.; Zhu, Y.; Chen, J. Mask–Assisted Seeded Growth of Segmented Metallic Heteronanostructures. *J. Phys. Chem. C* **2014**, *118*, 28134–28142.

(24) Jing, H.; Zhang, Q.; Large, N.; Yu, C.; Blom, D. A.; Nordlander, P.; Wang, H. Tunable Plasmonic Nanoparticles with Catalytically Active High–Index Facets. *Nano Lett.* **2014**, *14*, 3674–3682.

(25) Peng, Z.; Yang, H. Synthesis and Oxygen Reduction Electrocatalytic Property of Pt–on–Pd Bimetallic Heteronanostructures. *J. Am. Chem. Soc.* **2009**, *131*, 7542–7543.

(26) Murphy, C. J.; Sau, T. K.; Gole, A. M.; Orendorff, C. J.; Gao, J.; Gou, L.; Hunyadi, S. E.; Li, T. Anisotropic Metal Nanoparticles: Synthesis, Assembly, and Optical Applications. *J. Phys. Chem. B* **2005**, *109*, 13857–13870.

(27) Guerrero–Martínez, A.; Barbosa, S.; Pastoriza–Santos, I.; Liz–Marzán, L. M. Nanostars Shine Bright for You. *Curr. Opin. Colloid Interface Sci.* **2011**, *16*, 118–127.

(28) Samal, A. K.; Polavarapu, L.; Rodal–Cedeira, S.; Liz–Marzán, L. M.; Pérez–Juste, J.; Pastoriza–Santos, I. Size Tunable Au@Ag Core–Shell Nanoparticles: Synthesis and Surface–Enhanced Raman Scattering Properties. *Langmuir* **2013**, *29*, 15076–15082.

(29) Xia, X.; Wang, Y.; Ruditskiy, A.; Xia, Y. 25th Anniversary Article: Galvanic Replacement: A Simple and Versatile Route to Hollow Nanostructures with Tunable and Well–Controlled Properties. *Adv. Mater.* **2013**, *25*, 6313–6332.

(30) Chen, J.; Wiley, B.; McLellan, J.; Xiong, Y.; Li, Z. Y.; Xia, Y. Optical Properties of Pd–Ag and Pt–Ag Nanoboxes Synthesized via Galvanic Replacement Reactions. *Nano Lett.* **2005**, *5*, 2058–2062.

(31) Hong, J. W.; Kang, S. W.; Choi, B.–S.; Kim, D.; Lee, S. B.; Han, S. W. Controlled Synthesis of Pd–Pt Alloy Hollow Nanostructures with Enhanced Catalytic Activities for Oxygen Reduction. *ACS Nano* **2012**, *6*, 2410–2419.

(32) Sanedrin, R. G.; Georganopoulou, D. G.; Park, S.; Mirkin, C. A. Seed-Mediated Growth of Bimetallic Prisms. *Adv. Mater.* **2005**, *17*, 1027–1031.

(33) Yang, Y.; Liu, J.; Fu, Z. W.; Qin, D. Galvanic Replacement-Free Deposition of Au on Ag for Core-Shell Nanocubes with Enhanced Chemical Stability and SERS Activity. *J. Am. Chem. Soc.* **2014**, *136*, 8153–8156.

(34) Gao, C.; Lu, Z.; Liu, Y.; Zhang, Q.; Chi, M.; Cheng, Q.; Yin, Y. Highly Stable Silver Nanoplates for Surface Plasmon Resonance Biosensing. *Angew. Chemie – Int. Ed.* **2012**, *51*, 5629–5633.

(35) Liu, H.; Liu, T.; Zhang, L.; Han, L.; Gao, C.; Yin, Y. Etching–Free Epitaxial Growth of Gold on Silver Nanostructures for High Chemical Stability and Plasmonic Activity. *Adv. Funct. Mater.* **2015**, *25*, 5435–5443.

(36) Murshid, N.; Gourevich, I.; Coombs, N.; Kitaev, V. Gold Plating of Silver Nanoparticles for Superior Stability and Preserved Plasmonic and Sensing Properties. *Chem. Commun. (Camb).* **2013**, *49*, 11355–11357.

(37) Yang, Y.; Zhang, Q.; Fu, Z.–W.; Qin, D. Transformation of Ag Nanocubes into Ag–Au Hollow Nanostructures with Enriched Ag Contents to Improve SERS Activity and Chemical Stability. *ACS Appl. Mater. Interfaces* **2014**, *6*, 3750–3757.

(38) Zhang, Q.; Li, W.; Wen, L. P.; Chen, J.; Xia, Y. Facile Synthesis of Ag Nanocubes of 30 to 70 Nm in Edge Length with CF_3COOAg as a Precursor. *Chem. – A Eur. J.* **2010**, *16*, 10234–10239.

(39) Milazzo, G.; Caroli, S.; Braun, R. D. Tables of Standard Electrode Potentials. *J. Electrochem. Soc.* **1978**, *125*, 261C.

(40) Herrero, E.; Buller, L. J.; Abruna, H. D. Underpotential Deposition at Single Crystal Surfaces of Au, Pt, Ag and Other Materials. *Chem. Rev.* **2001**, *101*, 1897–1930.

(41) Link, S.; Wang, Z. L.; El–Sayed, M. A. Alloy Formation of Gold−Silver Nanoparticles and the Dependence of the Plasmon Absorption on Their Composition. *J. Phys. Chem. B* **1999**, *103*, 3529–3533.

(42) Mallin, M. P.; Murphy, C. J. Solution–Phase Synthesis of Sub–10 Nm Au−Ag Alloy Nanoparticles. *Nano Lett.* **2002**, *2*, 1235–1237.

(43) Xia, X.; Xie, S.; Liu, M.; Peng, H.–C.; Lu, N.; Wang, J.; Kim, M. J.; Xia, Y. On the Role of Surface Diffusion in Determining the Shape or Morphology of Noble–Metal Nanocrystals. *Proc. Natl. Acad. Sci. U. S. A.* **2013**, *110*, 6669–6673.

(44) Rycenga, M.; Xia, X.; Moran, C. H.; Zhou, F.; Qin, D.; Li, Z. Y.; Xia, Y. Generation of Hot Spots with Silver Nanocubes for Single–Molecule Detection by Surface–Enhanced Raman Scattering. *Angew. Chemie – Int. Ed.* **2011**, *50*, 5473–5477.

(45) Wang, X.; Zhang, Z.; Hartland, G. V. Electronic Dephasing in Bimetallic Gold–Silver Nanoparticles Examined by Single Particle Spectroscopy. *J. Phys. Chem. B* **2005**, *109*, 20324–20330.

(46) Lismont, M.; Dreesen, L. Comparative Study of Ag and Au Nanoparticles Biosensors Based on Surface Plasmon Resonance Phenomenon. *Mater. Sci. Eng. C. Mater. Biol. Appl.* **2012**, *32*, 1437–1442.

(47) Johnson, P. B.; Christy, R. W. Optical Constants of the Noble Metals. *Phys. Rev. B* **1972**, *6*, 4370–4379.

(48) Yang, Y.; Liu, J.; Fu, Z. W.; Qin, D. Galvanic Replacement–Free Deposition of Au on Ag for Core–Shell Nanocubes with Enhanced Chemical Stability and SERS Activity. *J. Am. Chem. Soc.* **2014**, *136*, 8153–8156.

(49) Chen, C.; Kang, Y.; Huo, Z.; Zhu, Z.; Huang, W.; Xin, H. L.; Snyder, J. D.; Li, D.; Herron, J. A.; Mavrikakis, M.; Chi, M.; More, K. L.; Li, Y.; Markovic, N. M.; Somorjai, G. A.; Yang, P.; Stamenkovic, V. R. Highly Crystalline Multimetallic Nanoframes with Three–Dimensional Electrocatalytic Surfaces. *Science* **2014**, *343*, 1339–1343.

(50) Jing, H.; Wang, H. Structural Evolution of Ag–Pd Bimetallic Nanoparticles through Controlled Galvanic Replacement: Effects of Mild Reducing Agents. *Chem. Mater.* **2015**, *27*, 2172–2180.

(51) Zhang, W.; Rahmani, M.; Niu, W.; Ravaine, S.; Hong, M.; Lu, X. Tuning Interior Nanogaps of Double–Shelled Au/Ag Nanoboxes for Surface–Enhanced Raman Scattering. *Sci. Rep.* **2015**, *5*, 1-6.

(52) Pradhan, N.; Pal, A.; Pal, T. Catalytic Reduction of Aromatic Nitro Compounds by Coinage Metal Nanoparticles. *Langmuir* **2001**, *17*, 1800–1802.

(53) Zeng, J.; Zhang, Q.; Chen, J.; Xia, Y. A Comparison Study of the Catalytic Properties of Au–Based Nanocages, Nanoboxes, and Nanoparticles. *Nano Lett.* **2010**, *10*, 30–35.

(54) Kneipp, J.; Kneipp, H.; Kneipp, K. SERS–A Single-Molecule and Nanoscale Tool for Bioanalytics. *Chem. Soc. Rev.* **2008**, *37*, 1052–1060.

(55) Rycenga, M.; Cobley, C. M.; Zeng, J.; Li, W.; Moran, C. H.; Zhang, Q.; Qin, D.; Xia, Y. Controlling the Synthesis and Assembly of Silver Nanostructures for Plasmonic Applications. *Chem. Rev.* **2011**, *111*, 3669–3712.

(56) Xie, W.; Herrmann, C.; Kömpe, K.; Haase, M.; Schlücker, S. Synthesis of Bifunctional Au/Pt/Au Core/shell Nanoraspberries for in Situ SERS Monitoring of Platinum–Catalyzed Reactions. *J. Am. Chem. Soc.* **2011**, *133*, 19302–19305.

(57) Schalow, T.; Brandt, B.; Laurin, M.; Schauermann, S.; Libuda, J.; Freund, H. J. CO Oxidation on Partially Oxidized Pd Nanoparticles. *J. Catal.* **2006**, *242*, 58–70.

(58) Mazumder, V.; Sun, S. Oleylamine–Mediated Synthesis of Pd Nanoparticles for Catalytic Formic Acid Oxidation. *J. Am. Chem. Soc.* **2009**, *131*, 4588–4589.

(59) Miyaura, N.; Suzuki, A. Palladium–Catalyzed Cross–Coupling Reactions of Organoboron Compounds. *Chem. Rev.* **1995**, *95*, 2457–2483.

(60) Hong, J. W.; Kang, S. W.; Choi, B. S.; Kim, D.; Lee, S. B.; Han, S. W. Controlled Synthesis of Pd-Pt Alloy Hollow Nanostructures with Enhanced Catalytic Activities for Oxygen Reduction. *ACS Nano* **2012**, *6*, 2410–2419.

(61) Zhang, Y.; X.; Gao, X.; Weaver, M, J. Nature of surface bonding on voltammetrically oxidized noble metals in aqueous media as probed by real-time surface-enhanced Raman spectroscopy. *J. Phys. Chem.* **1993**, *97*, 8656-8663.

(62) Wiley, B. J., Chen, Y., McLellan, J. M., Xiong, Y., Li, Z. Y., Ginger, D., Xia, Y. Synthesis and optical properties of silver nanobars and nanorice. *Nano lett.* **2007**, *7*, 1032-1036.

(63) Li, J.; Liu, J.; Yang, Y.; Qin, D. Bifunctional Ag@Pd–Ag Nanocubes for Highly Sensitive Monitoring of Catalytic Reactions by Surface–Enhanced Raman Spectroscopy. *J. Am. Chem. Soc.* **2015**, *137*, 7039–7042.

(64) Li, J.; Wu, Y.; Sun, X.; Liu, J.; Winget, S. A.; Qin, D. A Dual Catalyst with SERS Activity for Probing Stepwise Reduction and Oxidation Reactions. *ChemNanoMat* **2016**, *2*, 786–790.

(65) Zhao, L.–B.; Chen, J.–L.; Zhang, M.; Wu, D.–Y.; Tian, Z.–Q. Theoretical Study on Electroreduction of P –Nitrothiophenol on Silver and Gold Electrode Surfaces. *J. Phys. Chem. C* **2015**, *119*, 4949–4958.

(66) Huang, Y.–F.; Wu, D.–Y.; Zhu, H.–P.; Zhao, L.–B.; Liu, G.–K.; Ren, B.; Tian, Z.–Q. Surface–Enhanced Raman Spectroscopic Study of p–Aminothiophenol. *Phys. Chem. Chem. Phys.* **2012**, *14*, 8485-8497.

(67) Stuart, C. M.; Frontiera, R. R.; Mathies, R. A. Excited–State Structure and Dynamics of Cis– and Trans–Azobenzene from Resonance Raman Intensity Analysis. *J. Phys. Chem. A* **2007**, *111*, 12072–12080.

(68) Nakatsuji, H.; Hada, M.; Yonezawa, T. Theoretical Study on the Catalytic Activity of Palladium for the Hydrogenation of Acetylene. *Surf. Sci.* **1987**, *185*, 319–342.

(69) Yu, W. Y.; Mullen, G. M.; Mullins, C. B. Hydrogen Adsorption and Absorption with Pd–Au Bimetallic Surfaces. *J. Phys. Chem. C* **2013**, *117*, 19535–19543.

(70) Zhang, S.; Metin, Ö.; Su, D.; Sun, S. Monodisperse AgPd Alloy Nanoparticles and Their Superior Catalysis for the Dehydrogenation of Formic Acid. *Angew. Chemie – Int. Ed.* **2013**, *52*, 3681–3684.

(71) Rong, H.; Cai, S.; Niu, Z.; Li, Y. Composition–Dependent Catalytic Activity of Bimetallic Nanocrystals: AgPd–Catalyzed Hydrodechlorination of 4–Chlorophenol. *ACS Catal.* **2013**, *3*, 1560–1563.

(72) Hu, C.; Mu, X.; Fan, J.; Ma, H.; Zhao, X.; Chen, G.; Zhou, Z.; Zheng, N. Interfacial Effects in PdAg Bimetallic Nanosheets for Selective Dehydrogenation of Formic Acid. *ChemNanoMat* **2016**, *2*, 28–32.

(73) Sun, X.; Qin, D. Co-Titration of $AgNO_3$ and $HAuCl_4$: A New Route to the Synthesis of Ag@Ag-Au Core-frame Nanocubes with Enhanced Plasmonic and Catalytic Properties. *J. Mater. Chem. C* **2015**, *3*, 11833–11841.

(74) Li, J.; Wu, Y.; Sun, X.; Liu, J.; Winget, S. A.; Qin, D. A Dual Catalyst with SERS Activity for Probing Stepwise Reduction and Oxidation Reactions. *ChemNanoMat* **2016**, *2*, 786–790.

(75) Li, J.; Sun, X.; Qin, D. Ag-Enriched Ag-Pd Bimetallic Nanoframes and Their Catalytic Properties. *ChemNanoMat* **2016**, *2*, 494–499.

(76) Wu, Y.; Sun, X.; Yang, Y.; Li, J.; Zhang, Y.; Qin, D. Enriching Silver Nanocrystals with a Second Noble Metal. *Acc. Chem. Res.* **2017**, *50*, 1774–1784.

CHAPTER 3. ON THE MECHANISTIC ROLES OF HYDROXIDE IN CONTROLLING THE DEPOSITION OF GOLD ON COLLOIDAL SILVER NANOCRYSTALS

3.1 Introduction

Despite the large number of demonstrations of Ag nanocrystals for a variety of applications, including those related to localized surface plasmon resonance (LSPR),[1-3] surface-enhanced Raman scattering (SERS),[4–7] colorimetric sensing,[8,9] and catalysis,[10,11] the ultimate performance of Ag nanocrystals is often compromised by their shape instability under an oxidative environment. In the case of Ag nanocubes, for example, the atoms located at corners and edges could be readily oxidized to Ag^+ ions, resulting in the transformation of shape and thus the deterioration of SERS activity.[12] On the other hand, while Ag has remarkable catalytic properties for oxidation reactions such as ethylene epoxidation,[11,13] its capability toward reduction reactions tends to be compromised when compared with other noble metals such as Pd and Pt.

One strategy to expand the application landscape of Ag nanocrystals is to introduce another noble metal (M) such as Au, Pd, or Pt to generate diversified and yet well-defined Ag-M bimetallic nanocrystals. For example, conformally coating the surface of Ag nanocubes with ultrathin shells made of Au could greatly improve their chemical stability under a corrosive environment.[14,15] Selective deposition of Pd atoms on the edges of Ag nanocubes has been demonstrated for the fabrication of Ag@Ag-Pd core-frame nanocubes that exhibit a combination of catalytic activities toward both oxidation and reduction

reactions (see examples in Chapter 2).[16-18] In particular, the presence of Ag in the cores of these nanostructures has led to the development of bifunctional probes capable of reporting the catalytic reactions *in situ* by SERS. In developing these advanced bimetallic nanocrystals, it is critical to be able to defeat the galvanic replacement reaction between the Ag nanocrystals and a precursor to M atoms.[14,19] Also, it is pivotal to control the sites at which the newly formed M atoms will be deposited.

Seed-mediated growth offers a powerful route to the aforementioned bimetallic nanocrystals. In a typical synthesis, Ag nanocrystals (the seeds) are dispersed in an aqueous solution containing ascorbic acid (H_2Asc, a forerunner of the reducing agent), and poly(vinylpyrrolidone) (PVP, a colloidal stabilizer), followed by the titration of a precursor solution. However, the capability of this approach is limited by galvanic replacement when the metal M is less reactive than Ag. The involvement of galvanic replacement will make it difficult to control the outcome of seeded growth and even cause degradation to the properties associated with the nanocrystals. To suppress the galvanic replacement, for example, between Au(III) and Ag, we demonstrated that it was essential to increase the pH of the reaction solution to a level above 11.2 by introducing sodium hydroxide (NaOH).[14] Our hypothesis was that the Au(III) precursor would be reduced by ascorbic acid exclusively before they could undertake galvanic replacement with Ag, leading to the generation of Au atoms for their conformal deposition on the Ag nanocrystals.[14] Despite the successful synthesis of Ag@Au core-shell nanocubes with a shell thickness controlled at three or six atomic layers, we were unable to pin down the mechanistic roles played by the NaOH added into the reaction system.

From the perspective of chemical reactions, the OH^- ions can serve a number of

different roles in a typical synthesis of Ag-Au bimetallic nanocrystals. Firstly, H_2Asc is a

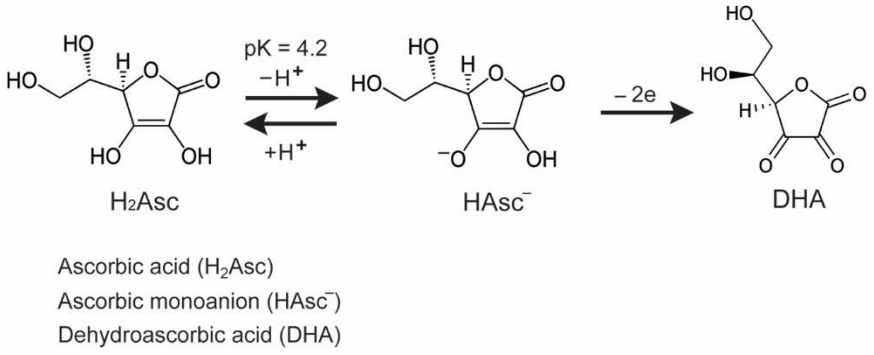

Figure 3.1. Structures of major chemical species associated with ascorbic acid dissolved in an aqueous solution (this figure is adapted with permission from ELSEVIER Biochimica et Biophysica Acta, ref. 20).

weak diprotic acid with dissociation constants of pKa_1=4.2 and pKa_2=11.6, respectively, at 25 °C.[20] According to literature, it is the ascorbate monoanion ($HAsc^-$), rather than the parental acid (H_2Asc), that can donate electrons and thus act as a reducing agent (Figure 3.1).[20] The dissociation equilibrium of H_2Asc into $HAsc^-$ and H^+ can be pushed to the right side as more OH^- is introduced, leading to a higher concentration for $HAsc^-$, the actual reducing agent. The increasingly accelerated reduction of the Au(III) precursor by $HAsc^-$ can eventually suppress the galvanic replacement reaction with the Ag nanocrystals. Secondly, it is well-established that $AuCl_4^-$ can progressively evolve into a series of complexes, including $AuCl_3(OH)^-$, $AuCl_2(OH)_2^-$ $AuCl(OH)_3^-$, and $Au(OH)_4^-$, through ligand exchange with OH^-.[21] In this case, the reduction potential of the Au(III) precursor will decrease when moving from $AuCl_4^-$ to $Au(OH)_4^-$, slowing down the reduction by both the $HAsc^-$ and the galvanic reaction.[22] The last but not least, the presence of Ag^+ ions (*e.g.*, released from the possible galvanic reaction) and OH^- in the same reaction solution can

result in the formation of Ag_2O, an oxide insoluble in an alkaline solution but soluble in an acidic solution.[23] When deposited on the Ag nanocrystals, the Ag_2O patches can mediate the dissolution behavior of Ag, as well as the deposition pattern of Au.

Herein we report a systematic study aiming to elucidate the explicit roles played by OH^- in controlling the pathways responsible for the transformation of Ag nanocubes into diversified Ag-Au bimetallic nanostructures. In a typical process, we dispersed Ag nanocubes in an aqueous solution containing H_2Asc, NaOH, and PVP, followed by the titration of aqueous $HAuCl_4$ using a syringe pump at room temperature. By introducing different amounts of NaOH prior to the titration of $HAuCl_4$, we could easily adjust the initial pH of the reaction solution from 3.2 to 11.9. After a set of survey experiments, we specifically focused on two conditions with the initial pH adjusted to 11.9 and 4.8, respectively. At an initial pH of 11.9, the reaction solution could be maintained alkaline (pH=11.9–10.0) during the titration of aqueous 0.1 mM $HAuCl_4$ up to 0.8 mL. In this case, the H_2Asc was neutralized by NaOH to generate $HAsc^-$ while the added $HAuCl_4$ was also quickly neutralized by OH^- to yield $AuCl_4^-$. For the first few drops of precursor solution, the $AuCl_4^-$ could still be reduced by Ag nanocubes through the galvanic replacement reaction before it underwent ligand exchange with OH^-. In this case, the Ag atoms were oxidized and dissolved from the corners while the resultant Au atoms were deposited on the edges of the Ag nanocubes. The released Ag^+ ions immediately reacted with the surrounding OH^- for the formation of Ag_2O patches at the corners, blocking the underlying Ag from further dissolution. Meanwhile, $AuCl(OH)_3^-$ and $Au(OH)_4^-$, both with lower reduction potentials than that of $AuCl_4^-$, were formed through ligand exchange with OH^-. These Au(III) species were quickly reduced by $HAsc^-$ for the production of Au atoms,

followed by their sequential deposition on the edges and side faces, leading to the generation of Ag@Au core-frame and then core-shell nanocubes. At an initial pH of 4.8, the reaction solution could be maintained acidic (pH=4.8–4.6) during the titration of aqueous 0.1 mM $HAuCl_4$ up to 0.8 mL. In this case, only some of the added H_2Asc was neutralized by NaOH to yield $HAsc^-$, slowing down the reduction kinetics. The added $HAuCl_4$ could still be neutralized to generate $AuCl_4^-$, which then evolved into $AuCl_3(OH)^-$ and $AuCl_2(OH)_2^-$ through ligand exchange. All these Au(III) species could undergo galvanic replacement with Ag nanocubes. However, the released Ag^+ ions could not be converted to Ag_2O under an acidic condition and, instead, they were reduced to Ag atoms by $HAsc^-$ and co-deposited with Au atoms on the Ag nanocubes. As a result, the Ag nanocubes were transformed into Ag@Ag-Au concave nanocubes with hollow interiors and alloyed walls.

3.2 Experimental Section

Chemicals and Materials. Silver trifluoroacetate (CF_3COOAg, 98%), gold(III) chloride trihydrate ($HAuCl_4 \cdot 3H_2O$, 99.9+%), sodium hydrosulfide hydrate ($NaHS \cdot xH_2O$), aqueous hydrochloric acid (HCl, 37%), PVP with an average molecular weight of 29,000 (PVP-29k) or 55,000 (PVP-55k), H_2Asc (99%), 4-nitrothiophenol (4-NTP), sodium borohydride ($NaBH_4$, 99.99%+), and hydrogen peroxide (H_2O_2, 30 wt.% in H_2O) were all acquired from Sigma-Aldrich. NaOH (98+%) was purchased from Alfa Aeser. Ethylene glycol (EG) was purchased from J. T. Baker. All chemicals were used as received. All the aqueous solutions were prepared using deionized (DI) water with a resistivity of 18.2

MΩ·cm at room temperature. The aqueous solutions of $HAuCl_4$ and NaOH used in the present work were 0.1 mM and 0.2 M, respectively, unless otherwise specified in the text.

Synthesis of Ag Nanocubes. We prepared Ag nanocubes with an edge length of 38.6±1.3 nm by following the protocol developed by Xia and co-workers.[24] After precipitation with acetone, the nanocubes were collected by centrifugation at 6500 rpm for 5 min, washed with DI water three times, and then dispersed in water for storage and further use.

Synthesis of Ag-Au Bimetallic Nanocubes. In a standard protocol, 2 mL of aqueous PVP-29k (1 mM) was added into a 23-mL glass vial, followed by the introduction of 0.5 mL of aqueous H_2Asc (0.1 M) and a specific volume (0.1, 0.2, 0.3, 0.4, 0.5 mL) of aqueous NaOH (0.2 M). After mixing under magnetic stirring, we pipetted 19 μL of the aqueous suspension of Ag nanocubes into the mixture with a final concentration of 4.2×10^{10} particles/mL. Afterwards, aqueous $HAuCl_4$ (0.1 mM) was titrated into the mixture using a syringe pump at a rate of 20 μL/min at room temperature. The reaction solution was maintained for another 10 min once the titration was completed. The products were collected by centrifugation at 6500 rpm for 12 min, washed twice with water, and then dispersed in water for further characterization.

Selective Etching of Ag from the Ag@Ag Core-Shell Nanocubes. We incubated the as-prepared sample in a solution containing 0.7 mL of PVP-29k (1 mM) and 0.3 mL of H_2Asc (0.1 M) at room temperature for 10 min. The particles were then collected by centrifugation at 6000 rpm for 12 min, followed by re-dispersion in 0.1 mL of water. We then introduced 1 mL of 3% H_2O_2 and the etching was allowed to proceed for 2 h. The final

products were collected by centrifugation at 13000 rpm for 18 min, followed by washing twice with DI water and re-dispersion in DI water for further characterization.

Selective Etching of Ag from Ag@Ag-Au Concave Nanocubes. We re-dispersed the as-obtained sample in 0.1 mL of DI water at room temperature. We then introduced 1 mL of 3% H_2O_2 and the etching was allowed to proceed for 2 h. The final products were collected by centrifugation at 13000 rpm for 18 min, followed by washing twice with water and re-dispersion in water for further characterization.

Analyzing the Galvanic Replacement Reaction between Ag Nanocubes and $HAuCl_4$ in the Absence and Presence of NaOH. In the absence of NaOH, we pipetted 2 mL of aqueous PVP-29k (1 mM) to 0.5 mL of water in a 23-ml glass vial and the pH was 4.3 for the reaction solution. To adjust the pH to 11.4, we prepared the aqueous reaction solution by introducing 2 mL PVP-29k (1 mM), 60 μL NaOH (0.2 M), and 0.44 mL water to a 23-ml glass vial. In each case, 19 μL of the aqueous suspension of Ag nanocubes was introduced, followed by the titration of 0.2, 0.4, 0.6, and 0.8 mL of aqueous $HAuCl_4$ (0.1 mM) using a syringe pump at a rate of 20 μL/min at room temperature. After the completion of titration, we waited for 10 min and then collected both solid and supernatant for inductively coupled plasma mass spectrometry (ICP-MS) measurements to determine the Au and Ag contents in each sample.

SERS Monitoring of the Reduction of 4-NTP by $NaBH_4$ using Ag@Au Core-Shell Nanocubes as a Probe. The Ag@Au core-shell nanocubes were functionalized with a 10^{-6} M solution of 4-NTP in ethanol for 1 h. The 4-NTP functionalized nanostructures were then collected by centrifugation at 5000 rpm for 20 min and washed with DI water twice. The washed nanostructures were re-dispersed in DI water at a concentration of

9.8×10^{10} particles/mL. Then 0.2 mL of the nanostructures suspension was mixed with 0.2 mL of 0.1 mg/mL $NaBH_4$ aqueous solution in a 1.5-mL centrifuge tube at room temperature. We withdrew 20 μL of the reaction solution every several minutes, placed in a PDMS cell to collect SERS spectra. We recorded the Raman spectra using a Renishaw inVia Raman spectrometer coupled with a Leica microscope with the use of a 5× objective lens. The excitation wavelength was 532 nm and the scattered light was dispersed using a holographic notch filter with a grating of 2,400 lines/mm. The spectra were collected with a collection time of 10 s at a laser power of 100 mW.

Instrumentation and Characterization. We collected the samples using Eppendorf 5430 (Eppendorf North America, Hauppauge, NY). The pH value was measured using a FiveEasy pH Meter (Mettler Toledo, Columbus, OH). The UV-vis spectra were collected using a Cary 50 spectrometer (Agilent Technologies, Santa Clara, CA). Transmission electron microscopy (TEM) images were taken using a Hitachi HT7700 microscope (Hitachi, Tokyo, Japan) operated at 120 kV. Scanning electron microscopy (SEM) images were captured using a Hitachi SU-8230 microscope operated at 20 kV. The contents of Au and Ag were determined using ICP-MS on NexION 300Q (PerkinElmer, Waltham, MA).

3.3 Results and Discussion

3.3.1 Deposition of Au on Ag Nanocubes at Different pH Values

To investigate the deposition of Au on Ag nanocubes at different pH values, we started with the preparation and characterization of aqueous suspensions containing the same amount of Ag nanocubes, H_2Asc, and PVP, but different amounts of NaOH. As shown

in Figure 3.2A, the pH value of the reaction solution containing 0.5 mL of 0.1 M H_2Asc increased from 3.2 to 4.1, 4.8, 10.3, 11.5 and 11.9 when 0.1, 0.2, 0.3, 0.4 and 0.5 mL of 0.2

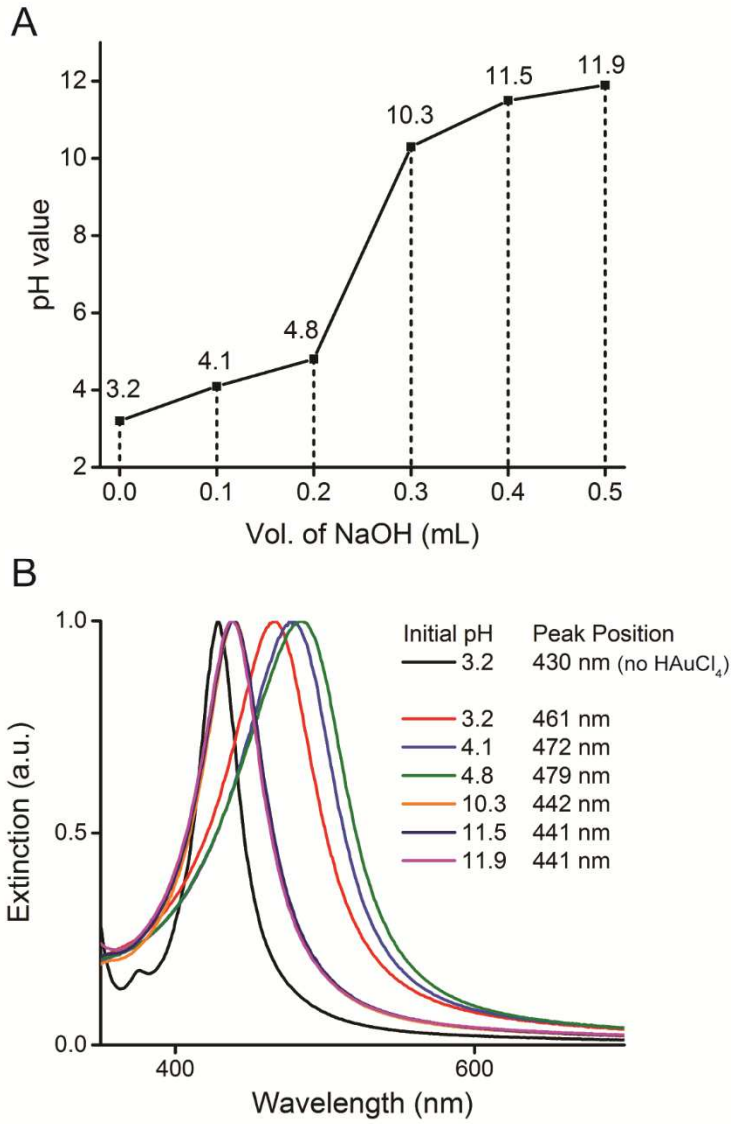

Figure 3.2. (A) pH value of a reaction solution as a function of the volume of 0.2 M aqueous NaOH added without the titration of aqueous $HAuCl_4$. (B) UV-vis spectra of Ag nanocubes before and after reacting with 0.4 mL of 0.1 mM aqueous $HAuCl_4$ at six different initial pH values for the reaction solutions.

M aqueous NaOH was added, respectively. This is a typical curve when a weak acid is

titrated with a strong base. Ascorbic acid is a weak diprotic acid, with *pK*a at 4.2 and 11.6, respectively.[20] After the addition of 0.25 mL of NaOH solution, the reaction solution (pH=7.2) should be dominated by ascorbate monoanion ($HAsc^-$) as all the H_2Asc (0.05 mmol) in the system should have been neutralized by the OH^- according to the following reaction:

$$H_2Asc + OH^- = HAsc^- + H_2O \qquad (3\text{-}1)$$

According to literature, it is $HAsc^-$, not H_2Asc, that can donate electrons and serve as a reducing agent (see Figure 3.1).[20] As such, we expect that the reducing power of the same aqueous solution of H_2Asc will differ significantly when its pH is adjusted to the alkaline and acidic regions because of the large difference in $HAsc^-$ concentration. The difference in reduction kinetics, in turn, would lead to the formation of distinct products when Ag nanocubes are reacted with $HAuCl_4$ in an aqueous system, as observed in our previous studies.[14,25]

In the initial survey experiments, we employed UV-vis spectroscopy to compare the LSPR properties of the Ag nanocubes before and after reacting with 0.4 mL of 0.1 mM aqueous $HAuCl_4$ titrated into the reaction solutions with different initial pH values. As shown in Figure 3.2B, when the initial pH was controlled at 3.2, 4.1, and 4.8, the major LSPR peak of the Ag nanocubes was notably shifted from 430 to 461, 472, and 479 nm, respectively. These results suggest that the reaction with $HAuCl_4$ caused major structural or morphological changes to the Ag nanocubes when the reaction solution was acidic, with an initial pH in the range of 3.2–4.8. In comparison, if the initial pH was tuned to 10.3,

11.5, and 11.9, the major LSPR peak of the Ag nanocubes only showed slight shift from 430 to 442, 441, and 441 nm, respectively. The insignificant shift in peak position indicates that the structure or morphology of the parental Ag nanocubes was largely preserved during the titration of $HAuCl_4$ when the reaction solution was alkaline, with an initial pH in the range of 10.3–11.9.

We then used electron microscopy to characterize the products obtained upon the titration of 0.4 mL of 0.1 mM $HAuCl_4$ solution in the presence of different amounts of NaOH and thus different initial pH values. Figure 3.3 shows SEM and TEM images of the as-obtained products. At an initial pH of 3.2 (*i.e.*, without adding any NaOH), the products exhibited slightly sharpened edges in addition to the observation of small pits on the surface (Figure 3.3A). The TEM image in Figure 3.3B confirms the presence of voids in most of the nanocubes. The formation of voids can be attributed to the involvement of galvanic replacement reaction between the Ag nanocubes and the Au(III) precursor titrated into the reaction solution. The released Ag^+ ions and the titrated Au(III) precursor were both reduced to atoms for their co-deposition onto the edges of the nanocubes, and as a result, their edges appeared to be sharpened, consistent with our previous findings.[25] When the initial pH was increased to 4.1 by adding 0.1 mL of the aqueous NaOH, the products also exhibited sharpened edges and corners, but with fewer voids and increased concaveness for the side faces (Figure 3.3, C and D). This observation suggests that the galvanic replacement reaction was retarded to a certain extent with the addition of NaOH. The increase in concaveness indicates that more atoms were preferentially deposited on the edges of the nanocubes. It is worth mentioning that the increase in concaveness could also contribute to the significant red-shift of the LSPR peak to 472 nm. When the initial pH was

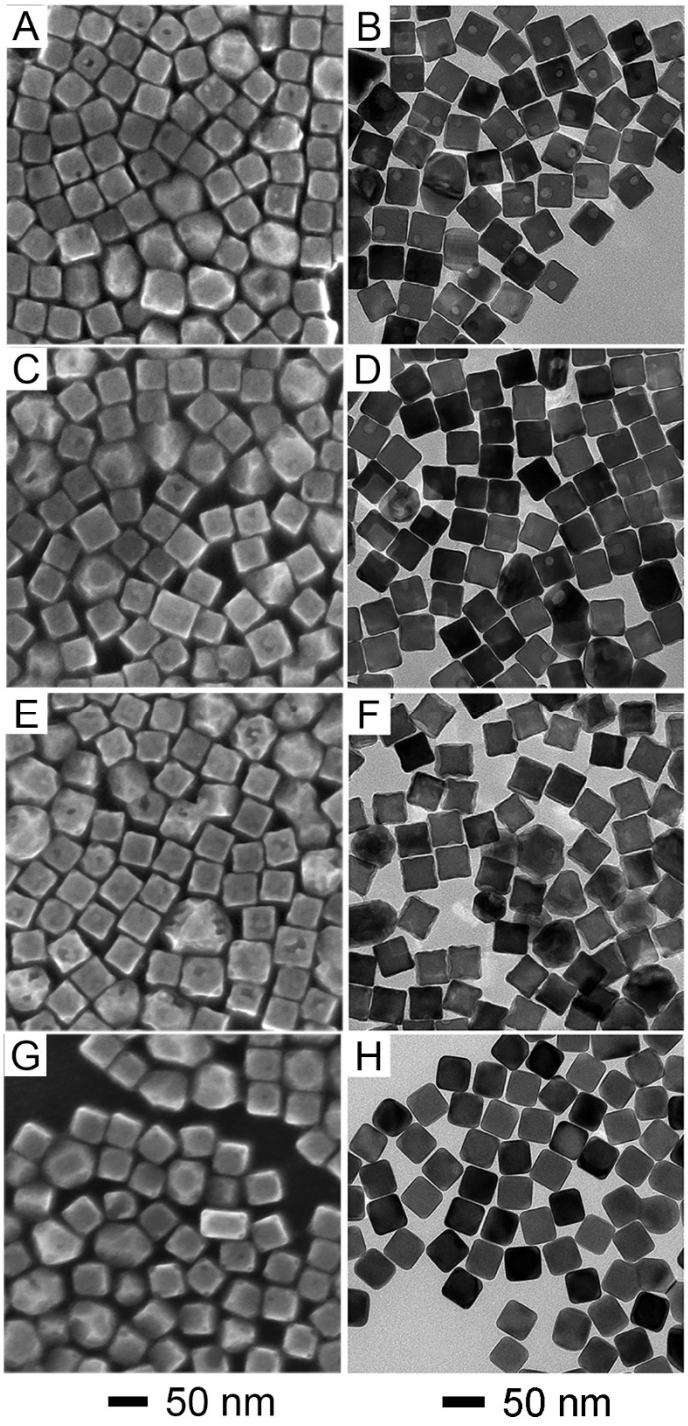

Figure 3.3. SEM (left panel) and TEM (right panel) images of Ag nanocubes after reacting with 0.4 mL of 0.1 mM aqueous $HAuCl_4$ at different initial pH values for the reaction solutions: (A, B) 3.2, (C, D) 4.1, (E, F) 4.8, and (G, H) 11.9, respectively.

further increased to 4.8 by introducing 0.2 mL of the aqueous NaOH, the SEM image indicates that the particles started to take a rough surface and more concave shape (Figure 3.3E), consistent with the observation of wavy edges observed under TEM (Figure 3.3F). The TEM image indicates the absence of voids in the nanocubes. In this case, the galvanic reaction was further suppressed because of the increase in initial pH. Again, the co-deposition of Au and Ag atoms on the edges gave rise to nanocubes with a concave shape, supporting the red-shift of LSPR peak position to 479 nm. When the initial pH of the reaction solution was further increased to the alkaline region with a pH of 11.9 by adding 0.5 mL of the aqueous NaOH, the as-obtained particles exhibited morphology similar to the parental Ag nanocubes, except for slight truncation at the corner sites (Figure 3.3, G and H). Under this circumstance, there was essentially no involvement of galvanic replacement reaction and the Au(III) precursor was reduced to Au atoms for their conformal deposition on the edges and side faces. The as-obtained particles showed an LSPR peak at 441 nm, closely resembling that of the original Ag nanocubes at 430 nm.

According to the outcomes of the survey experiments, the reaction can be divided into two major groups, corresponding to alkaline and acidic conditions, respectively. As such, we decided to focus on the products obtained by titrating different volumes of aqueous $HAuCl_4$ into aqueous suspensions of Ag nanocubes with an initial pH in the alkaline and acidic regions, respectively.

3.3.2 Deposition of Au on Ag Nanocubes under an Alkaline Condition

In this set of experiments, we introduced 0.5 mL of the aqueous NaOH into a mixture of Ag nanocubes, H_2Asc, and PVP to attain an initial pH of 11.9, followed by the titration

of different volumes of the aqueous $HAuCl_4$. As shown in Figure 3.4A, the pH of the reaction solution gradually decreased from 11.9 to 10.0 during the introduction of 0.8 mL of aqueous $HAuCl_4$ due to its acidic characteristic (pH=4.0 for a 0.1 mM aqueous solution).

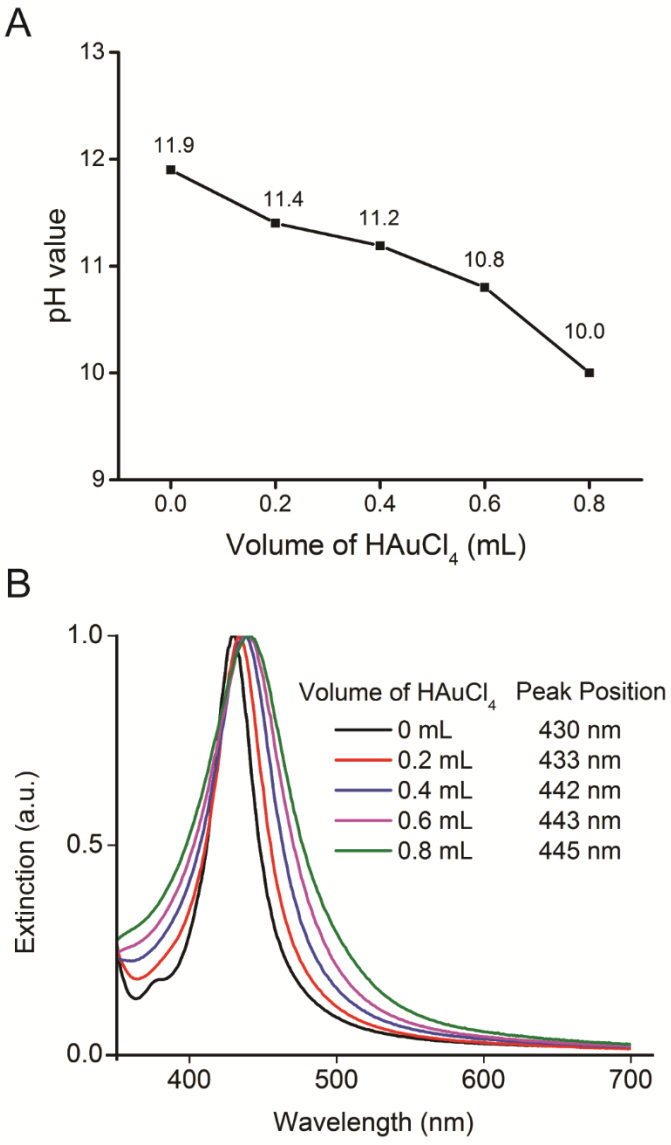

Figure 3.4. (A) During the titration of 0.1 mM aqueous $HAuCl_4$ solution, the change of pH in the reaction solution containing Ag nanocubes, H_2Asc, PVP and 0.5 mL of 0.2 M NaOH. (B) UV-Vis spectra recorded from suspension of the Ag nanocubes after reacting with different volumes of 0.1 mM aqueous $HAuCl_4$ at initial pH of 11.9.

Within this pH range, the solution of H_2Asc should be dominated by $HAsc^-$. We also characterized the LSPR properties of the Ag nanocubes before and after reacting with different amounts of $HAuCl_4$. Figure 3.4B shows that the major LSPR peak was only shifted from 430 to 445 nm, suggesting no involvement of galvanic replacement reaction.

Figure 3.5, A, C, and E, shows typical TEM images of the samples obtained at titration volumes of 0.2, 0.4, and 0.8 mL, respectively, for the $HAuCl_4$ solution. We noticed that their morphology was very similar to that of the original Ag nanocubes, except for an increase in edge length from 38.6±1.3 nm to 38.9±1.7 nm, 39.3±1.6 nm, 40.3±1.9 nm, respectively. To reveal the distribution of Au atoms on the surface of Ag nanocubes, we used 3% aqueous H_2O_2 to selectively remove Ag while leaving Au intact. Following one of our recently established protocols,[26] we collected aliquots of samples shown in Figure 3.5, A, C, and E and incubated them in an aqueous solution containing PVP-29k and H_2Asc for 10 min. The treated samples were then collected by centrifugation and etched in 3% H_2O_2. As shown in Figure 3.5B, nanoframes with pores at corners and sizes slightly smaller than the original nanocubes were formed upon the removal of Ag cores from the sample obtained with the titration of 0.2 mL of aqueous $HAuCl_4$. The nanoframes shrank in dimensions relative to the original nanocubes because they were not rigid enough to sustain the sample drying process. The small openings at the corners confirm that the Au atoms were preferentially deposited on the edges of the nanocubes with the corners largely uncovered. At 0.4 mL, the TEM image in Figure 3.5D shows that nanocages with pores at the corners and side faces were obtained after the removal of Ag cores. In this case, the Au atoms were deposited on the edges and side faces of the nanocubes for the generation of Ag@Au core-shell nanocubes. The integrity of the Au layer on side faces was

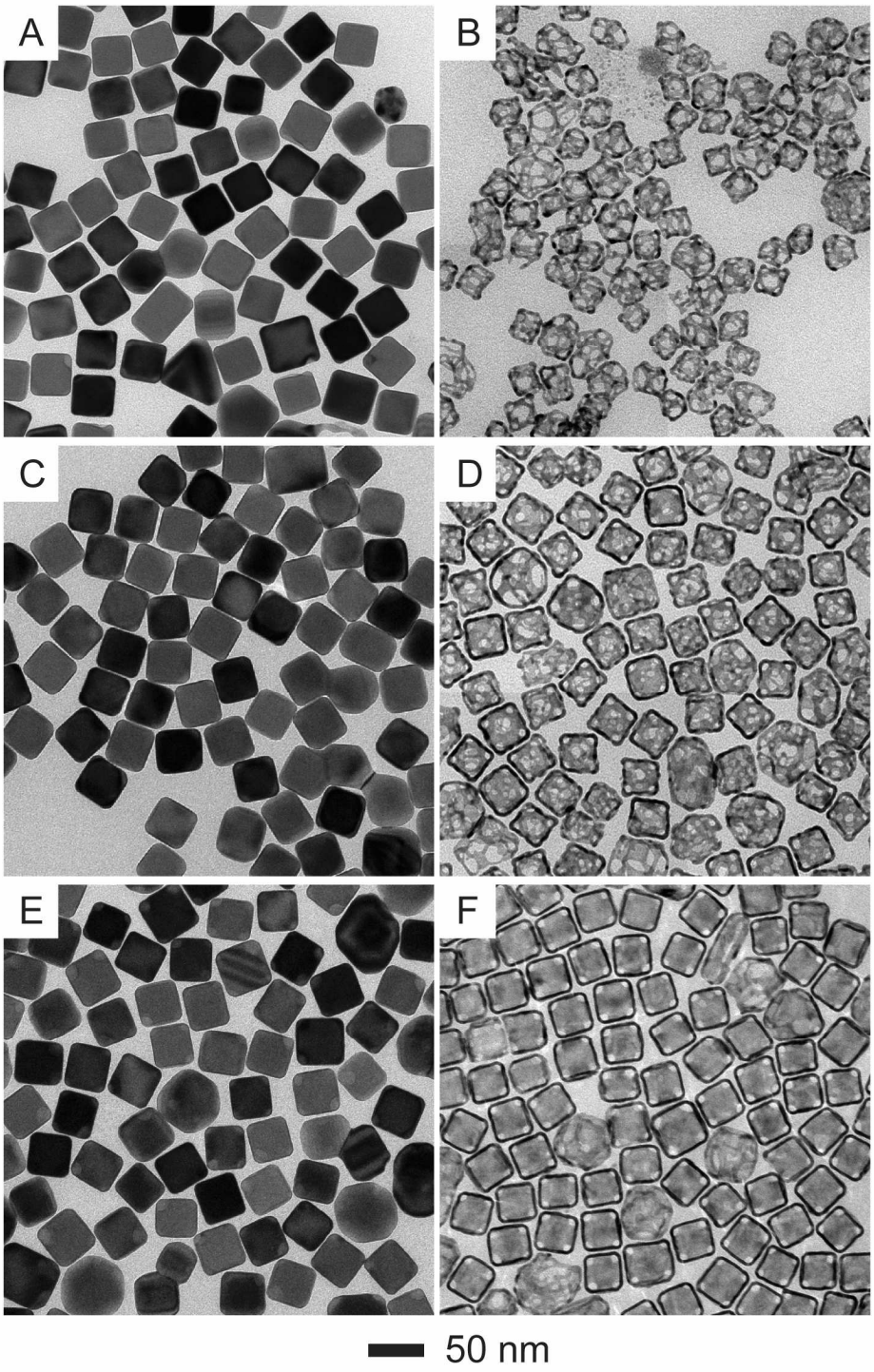

Figure 3.5. TEM images of products before (left panel) and after (right panel) treatment with H_2Asc and then 3% aqueous H_2O_2. The samples were prepared at an initial pH of 11.9 by titrating different volumes of 0.1 mM aqueous $HAuCl_4$: (A, B) 0.2, (C, D) 0.4, and (E, F) 0.8 mL, respectively.

compromised by the inadequate amount of $HAuCl_4$, and as a result, there were pores on the side faces after the removal of Ag template. The TEM image in Figure 3.5F shows the formation of nanoboxes with well-defined pores at the corner sites after the removal of Ag cores from the sample obtained with the addition of 0.8 mL of $HAuCl_4$. Comparing with the conventional nanocages reported in literature,[27] the nanoboxes exhibited well-defined openings at the corner sites and continuous side faces, suggesting that the Au atoms were continuously deposited on the side faces for the formation of thicker Au shells that could survive the etching process.

3.3.3 Deposition of Au on Ag Nanocubes under an Acid Condition

In this set of experiments, we performed a parallel study by adding 0.2 mL of the NaOH solution to attain an initial pH of 4.8 while keeping all the other parameters the same as in Figure 3.5. As shown in Figure 3.6A, the pH of the reaction solution was slightly decreased from 4.8 to 4.6 with the addition of 0.1 mM aqueous $HAuCl_4$ up to 0.8 mL. In contrast, at an initial pH of 4.8, the major LSPR peak of the Ag nanocubes was significantly shifted from 430 to 512 nm, as shown in Figure 3.6B. This result can be attributed to the presence of pits and voids formed through the galvanic replacement reaction and the increase in concaveness due to the preferential deposition of Au and Ag atoms on the edges.

Figure 3.7 shows TEM images of the samples obtained after adding different volumes of the $HAuCl_4$ solution and the corresponding structures after H_2O_2 etching. At a titration volume of 0.2 mL, we observed the transformation of Ag nanocubes into nanocubes with sharpened corners (Figure 3.7A) and then cubic nanoframes upon the removal of Ag cores (Figure 3.7B). Some nanoframes exhibited pores at the corners while the edges were

slightly distorted due to the lack of rigidity. When the volume of $HAuCl_4$ solution was increased to 0.4 and 0.8 mL, we noticed that more Au atoms were accumulated at the corners and edges, together with more pronounced surface roughness and surface concaveness, and void formation (Figure 3.7, C and E). These results support our argument

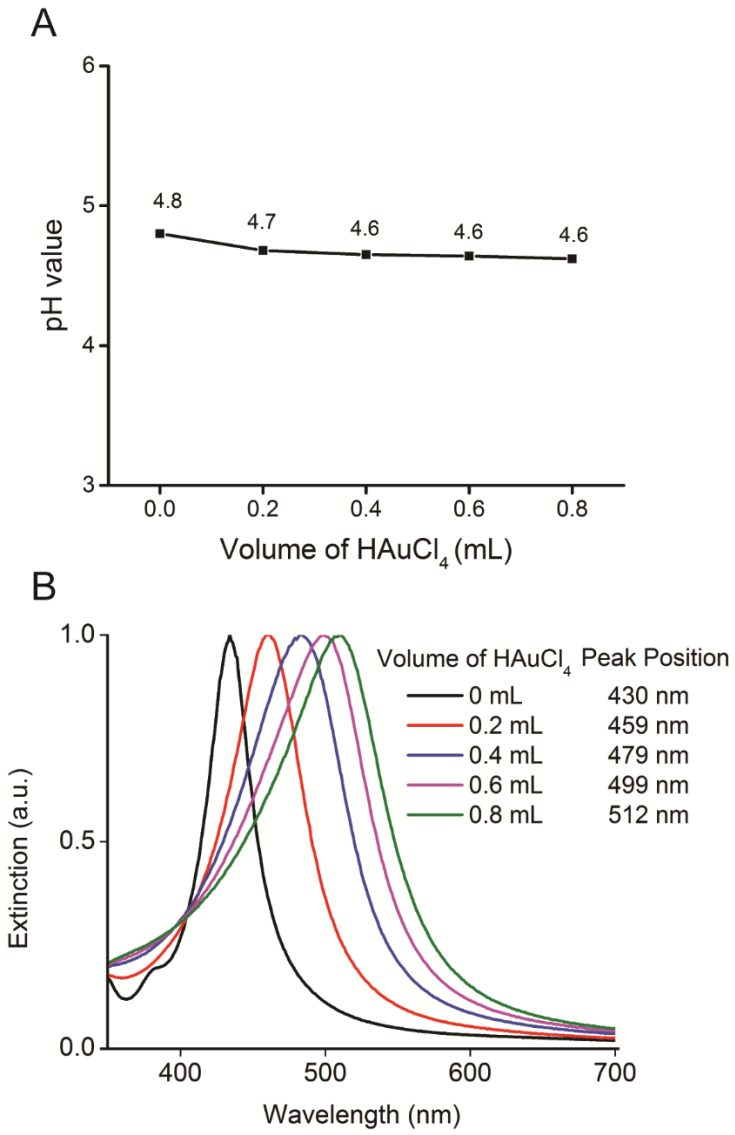

Figure 3.6. (A) During the titration of 0.1 mM aqueous $HAuCl_4$ solution, the change of pH in the reaction solution containing Ag nanocubes, H_2Asc, PVP and 0.2 mL of 0.2 M NaOH. (B) UV-Vis spectra recorded from suspension of the Ag nanocubes after reacting with different volumes of 0.1 mM aqueous $HAuCl_4$ at initial pH of 4.8.

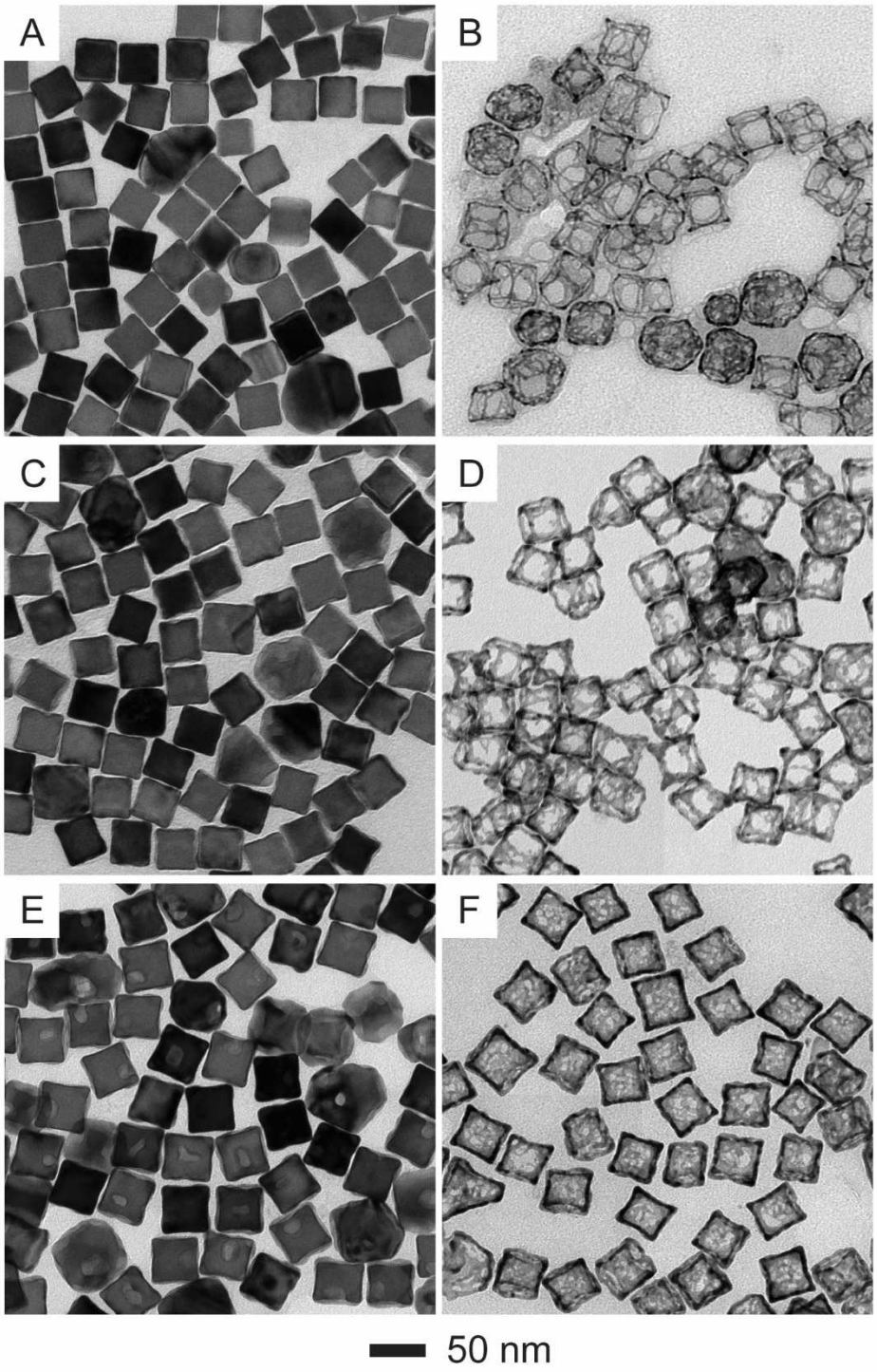

Figure 3.7. TEM images of products before (left panel) and after (right panel) treatment with 3% aqueous H_2O_2. The samples were prepared at an initial pH of 4.8 by titrating different volumes of 0.1 mM aqueous $HAuCl_4$: (A, B) 0.2, (C, D) 0.4, and (E, F) 0.8 mL, respectively.

that Ag could be continuously oxidized through the galvanic replacement reaction with Au(III) in an acidic solution. The released Ag^+ ions together with Au(III) were then reduced into atoms, followed by their deposition on the edges and corners of the Ag nanocubes. During the etching of Ag cores and the dealloying of Ag from their walls, the structures evolved into nanocages with decreasing porosity on the side faces (Figure 3.7, D and F). These results also suggest that the deposited Au and Ag atoms could migrate from edges and corners to the side faces as more precursor was introduced.

3.3.4 Two Proposed Pathways for the Fabrication of Ag-Au Bimetallic Nanocrystals

Based on the experimental results presented in Figures 3.5 and 3.7, we propose two scenarios to account for the reaction involving $HAuCl_4$, H_2Asc, and Ag nanocubes at pH initially adjusted to two different extremes (Figure 3.8). When the synthesis is conducted in an alkaline solution with an initial pH in the range of 10.3–11.9, galvanic replacement can still occur between the Ag nanocubes and the first few drops of aqueous $HAuCl_4$. The oxidation and dissolution of Ag atoms are initiated from the corners due to their lower reactivity than the atoms situated on the edges and side facets. The released Ag^+ ions immediately react with the surrounding OH^- ions to generate Ag_2O patches that ultimately cover the entire {111} facets at the corner sites. The Ag_2O patches can protect the underlying Ag atoms from further oxidation, so the galvanic reaction will cease shortly after it is initiated. From this point, the added $HAuCl_4$ is mostly converted to $AuCl(OH)_3^-$ and $Au(OH)_4^-$ through neutralization and ligand exchange with OH^- ions. These two species have lower reduction potentials than $AuCl_4^-$, helping suppress the galvanic replacement reaction. As a result, Au atoms are mainly produced through the chemical

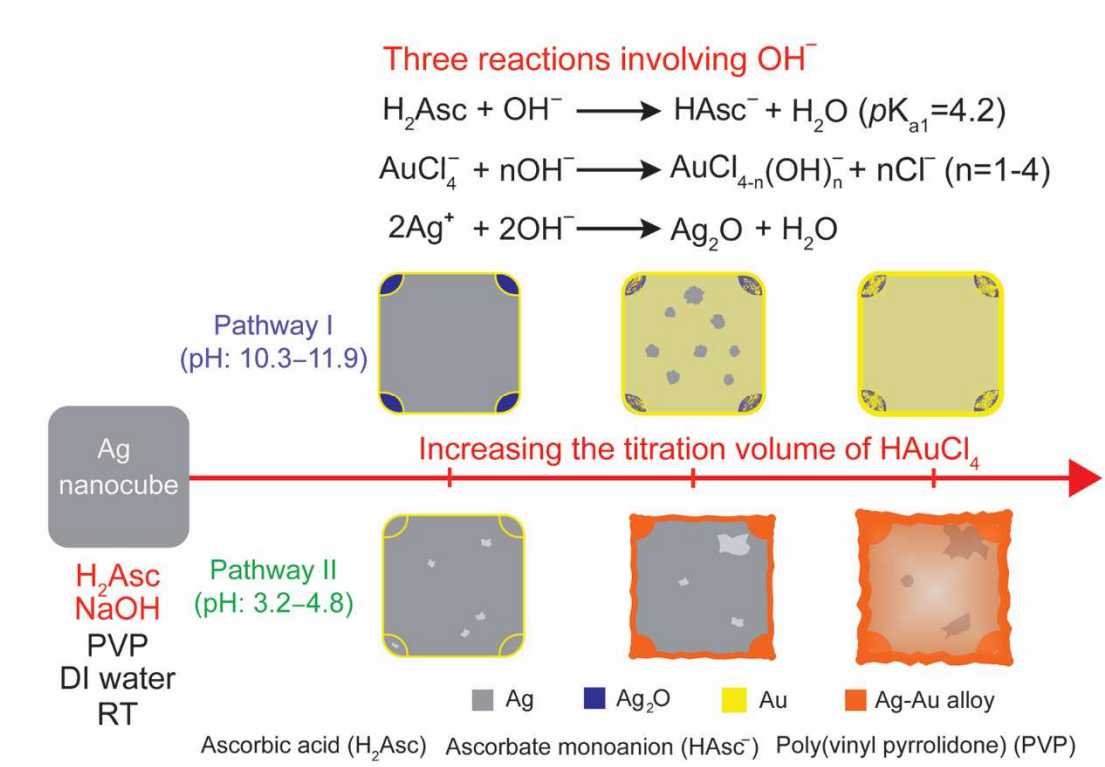

Figure 3.8. Schematic illustration of two pathways proposed to account for the formation of different types of Ag-Au bimetallic nanocrystals under alkaline and acidic conditions, respectively.

reduction by $HAsc^-$, followed by their preferential deposition on the edges of the nanocubes. As the synthesis proceeds with the introduction of more $HAuCl_4$, the side faces of nanocubes are also covered by Au atoms through direct deposition and/or surface diffusion from the edges. Due to the presence of oxide patches and therefore increase in nucleation energy barrier,[28] the Au atoms should not be directly deposited on the corners. As shown in Figure 3.9, we still observed the presence of Au at the corner sites of a nanocube. It is possible that surface diffusion could transport Au atoms from edges to corners, generating an ultrathin layer on top of the Ag_2O patches. Collectively, the final products are Ag@Au core-shell nanocubes with their corners covered by Ag_2O patches and then ultrathin Au layers. When the Ag_2O patches are removed with an acid to lift off the

Au deposited on the Ag_2O regions, followed by selective etching of the Ag cores by H_2O_2, the core-shell nanocubes evolve into Au-based nanoboxes with well-defined openings at the corner sites.

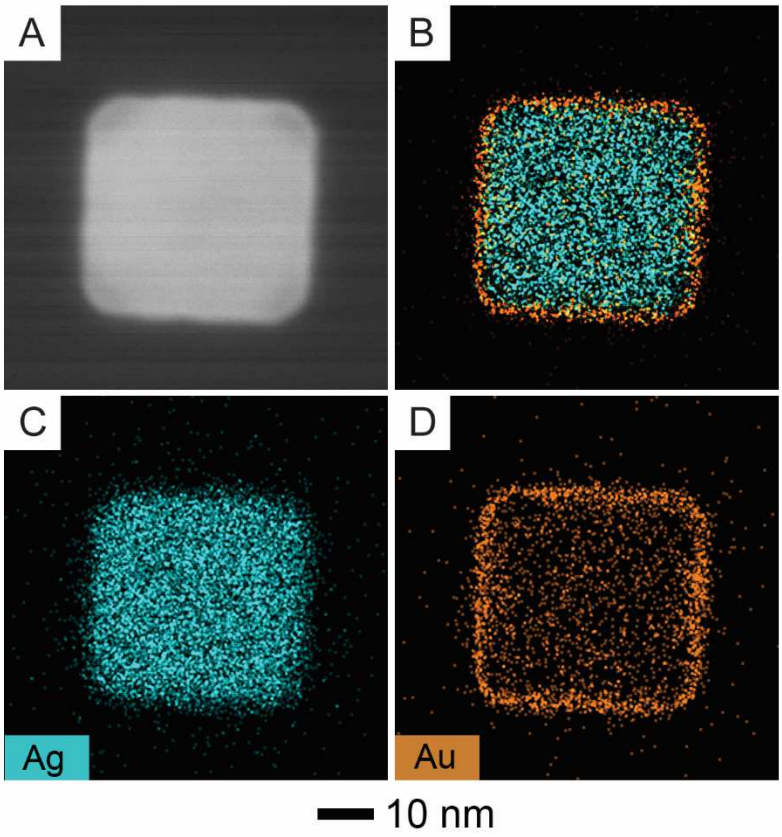

Figure 3.9. (A) STEM and (B−D) EDS mapping image of a Ag@Au nanocube prepared by reacting Ag nanocubes with 0.8 mL of 0.1 mM $HAuCl_4$ under alkaline condition (as shown in Figure 3.5E).

If the synthesis is conducted in an acidic solution with an initial pH in the range of 3.2–4.8, the reduction power of H_2Asc will be compromised due to a reduced concentration for $HAsc^-$. On the other hand, the titrated $HAuCl_4$ will dissociate into H^+ and $AuCl_4^-$, followed by the evolution of $AuCl_4^-$ into $AuCl_3(OH)^-$ and $AuCl_2(OH)_2^-$ through ligand

exchange. In this case, the Au(III) species can be reduced by both the Ag nanocubes and $HAsc^-$ through galvanic replacement and chemical reduction, respectively. The galvanic reaction tends to occur randomly from any site on a Ag nanocube while the resultant Au atoms are preferentially deposited on the edges. Because one Au atom is produced at the expenses of three Ag atoms during the galvanic reaction between Au(III) and Ag, a pit will be generated on the surface of a nanocube. As the titration volume of $HAuCl_4$ is increased, the Ag^+ ions will be continuously released from the Ag nanocube, further enlarging the pit. At the same time, the released Ag^+ ions and Au(III) species can both be reduced by $HAsc^-$ to generate Ag and Au atoms, respectively, followed by their co-deposition on the edges. Some of these atoms can migrate to the corners through surface diffusion, transforming the Ag nanocube into a Ag@Ag-Au core-frame nanocube with a cavity in the interior. As more $HAuCl_4$ is added, the cavity will be enlarged and the Ag and Au atoms resulting from the co-reduction will be continuously deposited on the edges and corners, followed by their diffusion to side faces. At the end, Ag@Ag-Au hollow nanocubes with concave side faces are formed. When the Ag cores are selectively removed through wet etching with H_2O_2, the nanocubes evolve into Au-Ag nanoboxes with pores on the side faces.

To further support our argument, we compared the standard reduction potentials of Ag^+, Au^{3+}, and H_2Asc at different pH values. Figure 3.10 plots their reduction potentials as a function of pH by taking their values from the literature.[22] As the pH is increased from 2 to 12, the reduction potential of Au(III)/Au(0) gradually decreases due to the transformation from $AuCl_4^-$ to $Au(OH)_4^-$. In contrast, there is little change in the reduction potential of Ag(I)/Ag(0) (0.80 V *vs.* SHE) up to pH = 6.3. As a result, the driving force for the galvanic replacement between Au(III) and Ag(0) should decrease as the pH is increased.

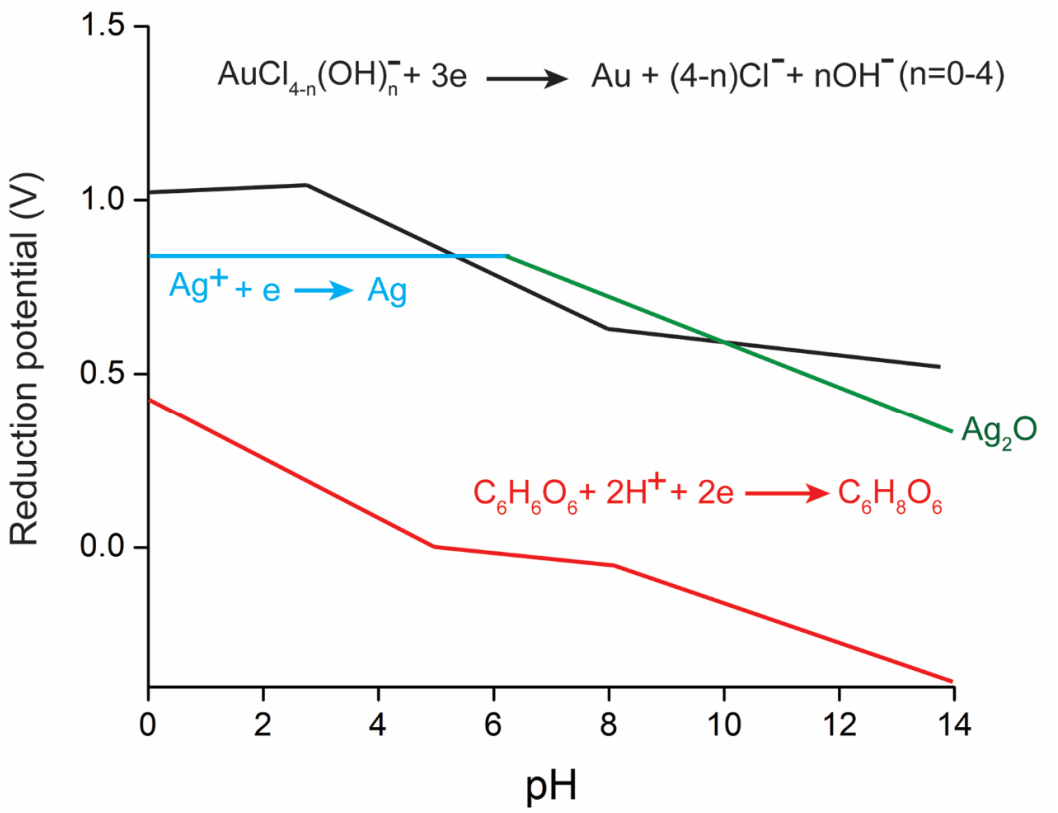

Figure 3.10. The standard reduction potentials of Ag^{+}, Au^{3+}, and H_2Asc at different pH values (this figure is reproduced with permission from ELSEVIER Colloids and Surfaces A: Physicochemical and Engineering Aspects, ref. 12).

It is worth mentioning that the increase in pH can neutralize more H_2Asc into $HAsc^{-}$, ultimately accelerating the reduction kinetics for the Au(III) precursor. As a result, the Au(III) precursor will be reduced primarily by $HAsc^{-}$ rather than the Ag nanocubes under the alkaline condition. We have also systematically studied and compared the extents of galvanic replacement in the absence or presence of NaOH (with no involvement of H_2Asc in both cases), at initial pH of 4.3 and 11.4, respectively. Specifically, we titrated different volumes of $HAuCl_4$ into the aqueous suspension of Ag nanocubes in the presence of PVP only and waited for 10 min before collecting both the solid and supernatant by centrifugation to determine the Ag and Au contents by ICP-MS. As shown in Figure 3.11,

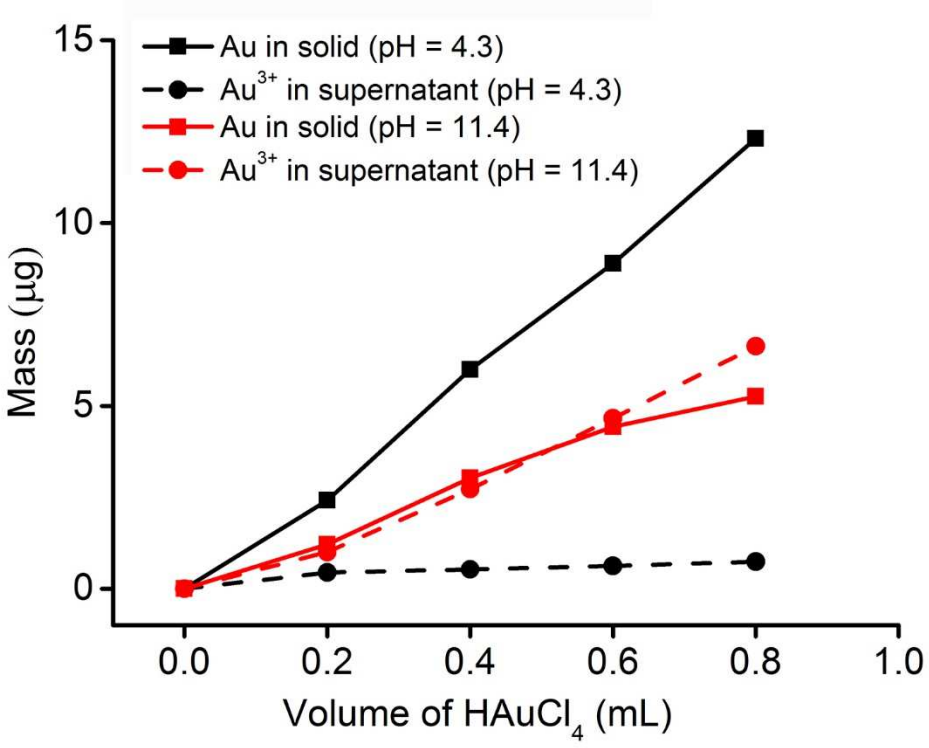

Figure 3.11. The amounts of Au deposited on the Ag nanocubes and remaining in the supernatant after the titration of different volumes of $HAuCl_4$ into the suspension of Ag nanocubes in the absence of H_2Asc at pH = 4.3 (without NaOH) and 11.4 (with NaOH), respectively.

in the absence of NaOH and at an initial pH of 4.3, the Au content in the solid products increased linearly with the volume of $HAuCl_4$ titrated into the reaction solution. At each titration volume, the Au(III) ions remaining in the supernatant was essentially zero. This data suggests that the added $HAuCl_4$ was completely reduced by the Ag nanocubes *via* the galvanic replacement reaction. In comparison, in the presence of NaOH at pH=11.4, only 50% of the titrated Au(III) precursor was converted to Au atoms for their deposition on the Ag nanocubes, indicating that the galvanic replacement reaction was significantly retarded. At an initial pH of 11.4, the added $AuCl_4^-$ is quickly converted to $AuCl(OH)_3^-$ and $Au(OH)_4^-$, both with lower reduction potentials than $AuCl_4^-$, making the galvanic reaction

with Ag more difficult. Additionally, any Ag^+ ions released from the Ag nanocubes will react with OH^- for the generation of Ag_2O on the surface of a Ag nanocube, further helping to inhibit the galvanic reaction.

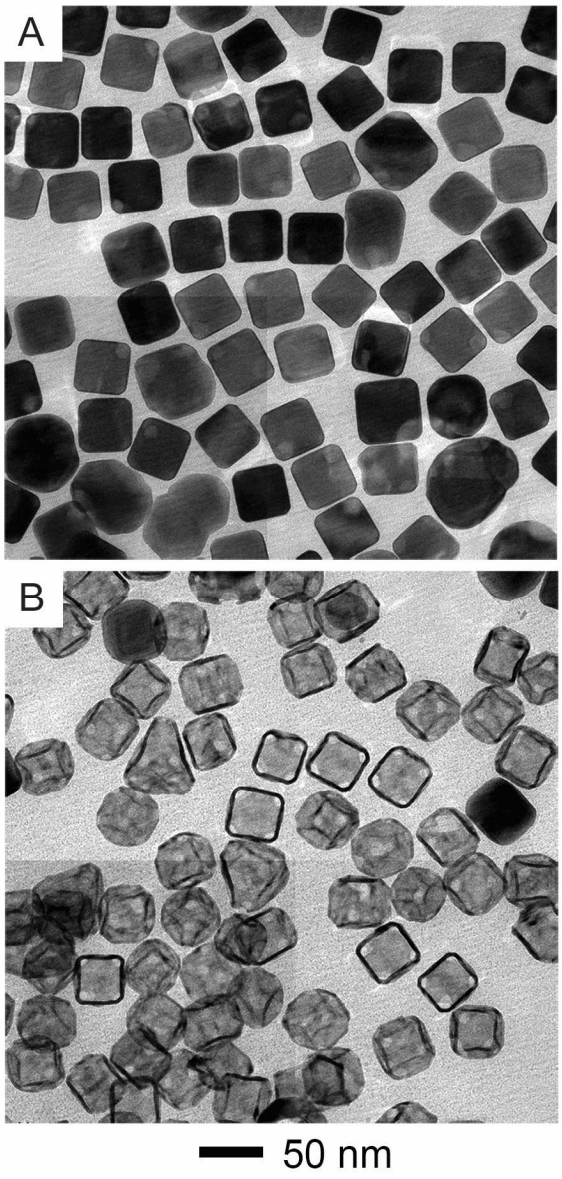

Figure 3.12. TEM images of products (A) before and (B) after treatment with H_2Asc and then 3% aqueous H_2O_2. The sample was prepared at an initial pH of 11.9 by titrating 0.8 mL of a pre-mixed solution prepared by mixing 0.03 mL of $HAuCl_4$ (10 mM) with 0.1 mL of NaOH (0.2 M) in 2.87 mL of water to obtain a 0.1 mM Au(III) precursor solution with pH=11.5.

We assume that the $HAuCl_4$ precursor titrated into the aqueous suspension of Ag nanocubes should be immediately neutralized by OH^- to yield $AuCl_4^-$ before it further undergoes ligand exchange to generate a mixture of $AuCl(OH)_3^-$ and $Au(OH)_4^-$ at pH>10.[21] To fully understand the role of ligand exchange between Cl^- and OH^- in affecting the deposition of Au on Ag nanocubes, we performed another control experiment. In this case, we pre-mixed 0.03 mL of $HAuCl_4$ (10 mM) with 0.1 mL of NaOH (0.2 M) in 2.87 mL of water to obtain a 0.1 mM Au(III) precursor solution with pH=11.5. We then titrated the Au(III) precursor solution into an aqueous suspension of Ag nanocubes in the presence of H_2Asc, NaOH, and PVP at an initial pH of 11.9. Figure 3.12A shows TEM image of the products obtained at a titration volume of 0.8 mL. The particles were essentially the same as those shown in Figure 3.5E. However, upon the removal of Ag cores by H_2O_2 etching, the resultant nanoboxes shown in Figure 3.12B are different from those shown in Figure 3.5F. In this case, we observed a significant population of nanoboxes without openings at the corners. This result clearly shows the difference between $AuCl_4^-$ and $Au(OH)_4^-$, suggesting that the conversion between them through the ligand exchange with OH^- was not instantaneous. Interestingly, the initial involvement of galvanic replacement between $AuCl_4^-$ and the Ag atoms located at the corners of nanocubes was instrumental to the formation of Au-based nanoboxes with well-defined openings at the corners.

3.3.5 Ag-Au Bimetallic Nanocrystals for Probing Reactions by SERS

We demonstrated the utility of Ag@Au core-shell nanocubes as a unique SERS probe for monitoring the reduction of 4-NTP by $NaBH_4$ in a colloidal suspension. Specifically, we followed the protocol to obtain Ag@Au core-shell nanocubes with the titration of 0.8

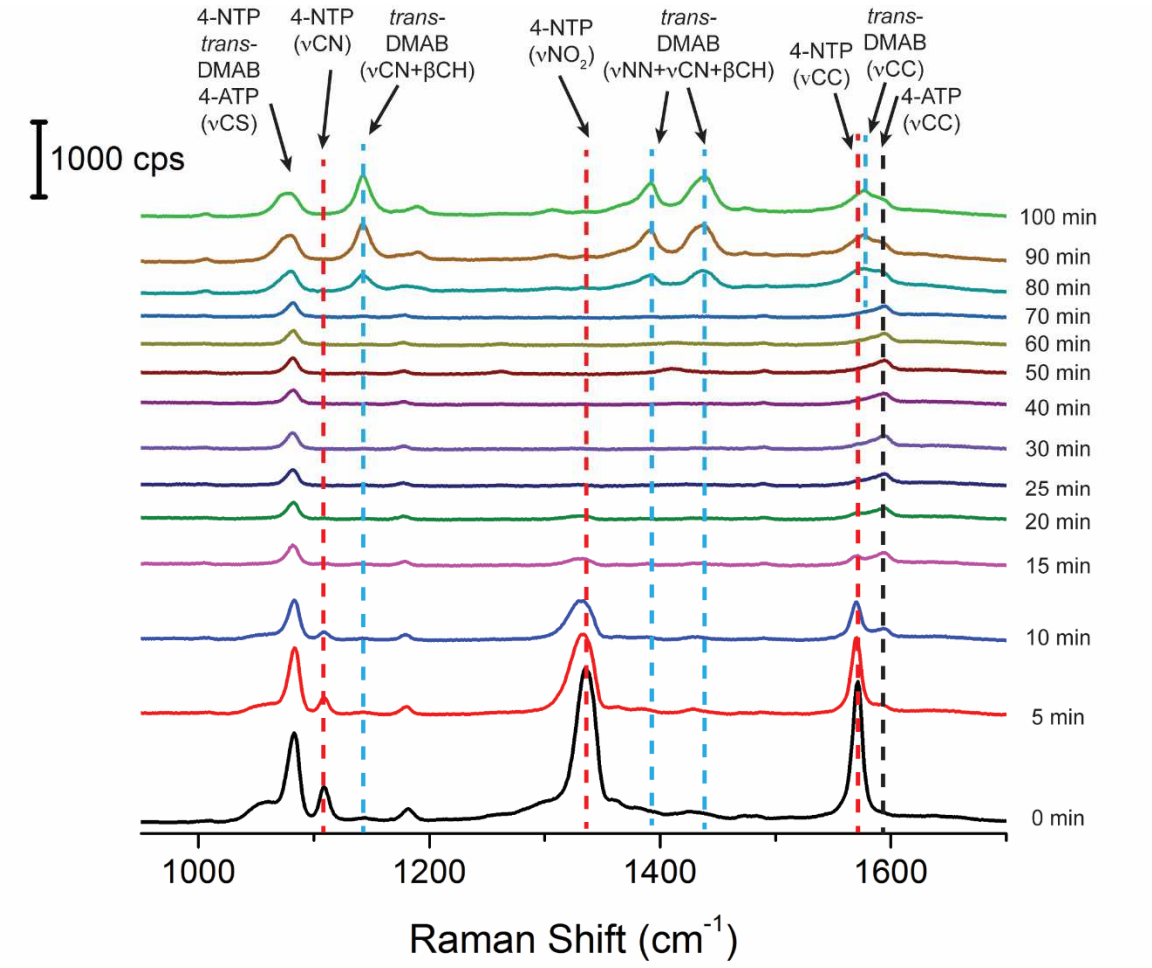

Figure 3.13. Time-dependent SERS spectra of 4-NTP-functionalized Ag@Au core-shell nanocubes collected before and after the addition of $NaBH_4$ solution into an aqueous suspension at the excitation wavelength of 532 nm. The nanoparticles were prepared with the titration of 0.8 mL of 0.1 mM $HAuCl_4$ solution.

mL of aqueous $HAuCl_4$ and then functionalized the nanoparticles with 4-NTP (see experimental section for details). After instigating the reduction with $NaBH_4$, we collected SERS spectra from the reaction solution at different time points at 532 nm laser excitation (Figure 3.13). At t=0, we observed three characteristic vibrational bands of 4-NTP (marked by dashed red lines) at 1108 cm^{-1} (C-N stretching, ν_{CN}), 1336 cm^{-1} (O-N-O stretching, ν_{NO2}), and 1572 cm^{-1} (C-C stretching, ν_{CC}),[29,30] respectively. At t = 5 min, the

ν_{NO_2} of 4-NTP was blue-shifted from 1336 to 1331 cm^{-1}, together with a decrease in intensity (26%). The intensities of ν_{CN} and ν_{CC} also decreased but their peak positions were essentially unaltered. As the reaction progressed to 10 min, the three signature bands of 4-NTP continuously decreased in intensity while the ν_{CC} of 4-ATP started to emerge at 1591 cm^{-1} (marked by a dashed black line). At *t*=15 min, we noticed that the continuing decrease and increase in the intensities for the ν_{CC} of 4-NTP and that of 4-ATP at 1572 and 1591 cm^{-1}, respectively, suggesting the conversion of 4-NTP to 4-ATP. At t= 20 min, we could no longer identify the bands of 4-NTP from the spectrum but a weak ν_{CC} of 4-ATP. From our previous work, we anticipated that the intensity of ν_{CC} for 4-ATP could become one-order of magnitude weaker than that of the band for 4-NTP after the reduction of 4-NTP by $NaBH_4$.[17] It is also possible that some of the 4-NTP attached to the surface could be desorbed by $NaBH_4$ due to a stronger binding of BH_4^- to Au.[31] Because the ν_{CS} band remained at 1082 cm^{-1}, we believe that some of the 4-ATP molecules were adsorbed on the surface of Ag@Au core-shell nanocubes. From 25 to 70 min, the SERS spectra remained essentially intact. At t=80 min, four peaks appeared at 1142 cm^{-1}, 1387 cm^{-1}, 1429 cm^{-1}, and 1577 cm^{-1}, with their assignments to the $\nu_{CN}+\beta_{CH}$, $\nu_{NN}+\nu_{CN}$, $\nu_{NN}+\beta_{CH}$, and ν_{CC} of *trans*-4,4'-dimercaptoazobenzene (*trans*-DMAB, marked by a dashed blue line), respectively.[32,33] The spectra remained essentially the same except for a slight increase in intensity for the peaks up to 100 min. Collectively, our data suggest that Au could catalyze the reduction of 4-NTP by $NaBH_4$. Once $NaBH_4$ was completely consumed in the reaction solution, any presence of Ag atoms in the outmost surface due to the fast interatomic diffusion between Au and Ag could activate O_2 in the aqueous solution for the oxidation of 4-ATP to *trans*-DMAB.[34,35] We have also collected the time-dependent SERS spectra

of 4-NPT using the Ag@Ag-Au hollow nanocubes obtained by the titration volume of 0.8 mL of aqueous $HAuCl_4$. As shown in Figure 3.14, we observed the similar behavior to those shown in Figure 3.13 except that the SERS activity of Ag@Ag-Au hollow nanocubes exhibited weaker SERS signal due to some loss of Ag.[25]

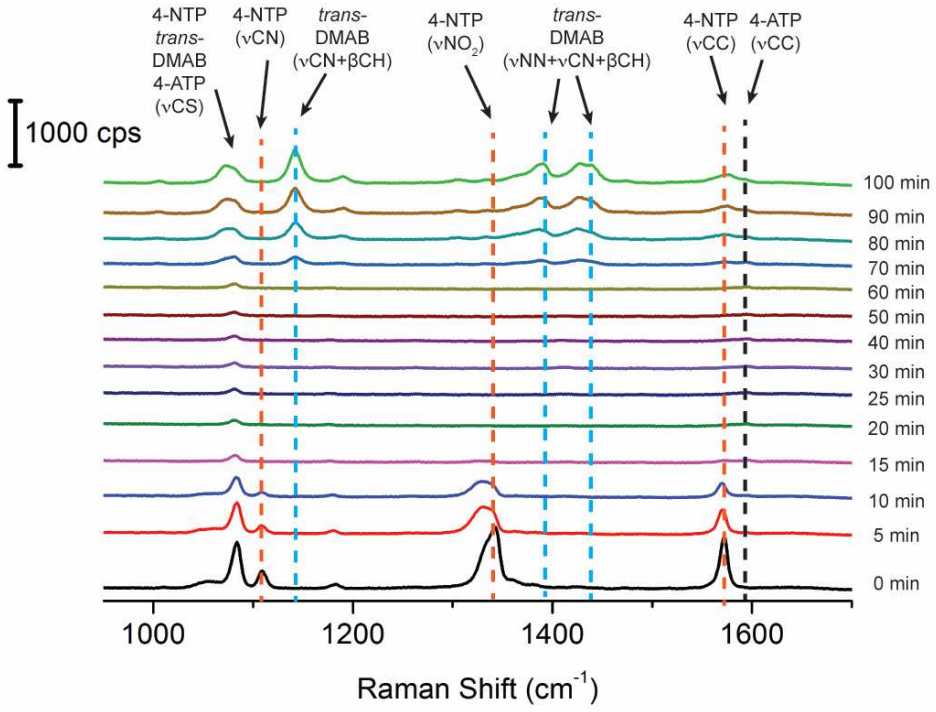

Figure 3.14. Time-dependent SERS spectra of 4-NTP-functionalized Ag@Ag-Au hollow nanocubes collected before and after the addition of $NaBH_4$ solution into an aqueous suspension at the excitation wavelength of 532 nm. The nanoparticles were prepared with the titration of 0.8 mL of 0.1 mM $HAuCl_4$ solution.

3.4 Conclusions

We have demonstrated the role of hydroxide in controlling the deposition of Au atoms on Ag nanocubes for the generation of Ag-Au bimetallic nanocubes with different structures. When we conduct the synthesis in an alkaline solution with an initial pH in the range of 10.3–11.9, H_2Asc is neutralized by OH^- to give $HAsc^-$, a strong reducing agent.

The $HAuCl_4$ precursor titrated into the aqueous suspension of Ag nanocubes is quickly neutralized by OH^- to yield $AuCl_4^-$. The $AuCl_4^-$ then undergo galvanic replacement with the Ag atoms situated at the corners of a nanocube to initiate the deposition of Au atoms at the edges. Due to the presence of OH^- ions, the released Ag^+ ions are immediately converted to Ag_2O, generating oxide patches at the corners. As such, the galvanic reaction will be terminated shortly after it is initiated, preventing further dissolution of Ag from the nanocube. Afterwards, $AuCl_4^-$ is progressively converted into $AuCl(OH)_3^-$ and $Au(OH)_4^-$ through ligand exchange, and Au atoms are continuously produced through the reduction by $HAsc^-$, followed by their deposition on the edges and side faces for the formation of a Ag@Au core-shell nanocube, with some Au deposition at the corners on top of Ag_2O. Selective removal of the Ag cores generates Au-based cubic nanoboxes with well-defined openings at the corners. When the initial pH of reaction solution was adjusted in the range of 3.2–4.8, the titrated $HAuCl_4$ precursor actually exists as a mixture of $AuCl_4^-$, $AuCl_3(OH)^-$ and $AuCl_2(OH)_2^-$ in the reaction solution. These Au(III) species will be reduced through both the galvanic reaction with Ag nanocubes and the chemical reduction by $HAsc^-$. Additionally, the released Ag^+ ions from the Ag nanocubes can be reduced by $HAsc^-$ to generate Ag atoms, followed by their co-deposition with Au atoms on the edges of nanocubes. The co-deposited Ag and Au atoms can spread to the corners and side faces by surface diffusion, eventually leading to the formation of Ag@Ag-Au concave nanocubes with hollow interiors as the volume of the titrated $HAuCl_4$ is increased. Selective removal of the Ag cores leads to the formation of nanoframes or nanoboxes with poorly defined pores on the side faces. We believe this mechanistic study of Au deposition on colloidal Ag nanocrystals can provide guidance for the rational design of Ag-based

bimetallic nanocrystals involving metals such as Au, Pd, and Pt for the fabrication of novel functional nanomaterials.

3.5 Notes to Chapter 3

Part of this chapter is adapted from the paper "Mechanistic Roles of Hydroxide in Controlling the Deposition of Gold on Colloidal Silver Nanocrystals" published in *Chemistry of Materials*.[36]

3.6 References

(1) Willets, K. A.; Van Duyne, R. P. Localized Surface Plasmon Resonance Spectroscopy and Sensing. *Annu. Rev. Phys. Chem.* **2007**, *58*, 267–297.

(2) Haes, A. J.; Haynes, C. L.; McFarland, A. D.; Schatz, G. C.; Van Duyne, R. P.; Zou, S. Plasmonic Materials for Surface-Enhanced Sensing and Spectroscopy. *MRS Bull.* **2005**, *30*, 368–375.

(3) Rycenga, M.; Cobley, C. M.; Zeng, J.; Li, W.; Moran, C. H.; Zhang, Q.; Qin, D.; Xia, Y. Controlling the Synthesis and Assembly of Silver Nanostructures for Plasmonic Applications. *Chem. Rev.* **2011**, *111*, 3669–3712.

(4) McLellan, J. M.; Li, Z.-Y.; Siekkinen, A. K.; Xia, Y. The SERS Activity of a Supported Ag Nanocube Strongly Depends on Its Orientation Relative to Laser Polarization. *Nano Lett.* **2007**, *7*, 1013–1017.

(5) Haes, A. J.; Van Duyne, R. P. A Nanoscale Optical Biosensor: Sensitivity and Selectivity of an Approach Based on the Localized Surface Plasmon Resonance Spectroscopy of Triangular Silver Nanoparticles. *J. Am. Chem. Soc.* **2002**, *124*, 10596–10604.

(6) Xia, X.; Zeng, J.; McDearmon, B.; Zheng, Y.; Xia, Y. Silver Nanocrystals with Concave Surfaces and Their Optical and Surface-Enhanced Raman Scattering Properties. *Angew. Chem. Int. Ed.* **2011**, *123*, 12750–12754.

(7) Xia, Y.; Xiong, Y.; Lim, B.; Skrabalak, S. E. Shape-Controlled Synthesis of Metal Nanocrystals: Simple Chemistry Meets Complex Physics? *Angew. Chem. Int. Ed.* **2009**, *48*, 60–104.

(8) Pastoriza-Santos, S.; Liz-Marzán, L. M. Colloidal Silver Nanoplates. State of the Art and Future Challenges. *J. Chem. Mater.* **2008**, *18*, 1724–1737.

(9) Millstone, J. E.; Hurst, S. J.; Metraux, G. S.; Cutler, J. I.; Mirkin, C. A. Colloidal Gold and Silver Triangular Nanoprisms. *Small* **2009**, *5*, 646–664.

(10) Linic, S.; Christopher, P.; Ingram, D. B. Plasmonic-Metal Nanostructures for Efficient Conversion of Solar to Chemical Energy. *Nat. Mater.* **2011**, *10*, 911–921.

(11) Christopher, P.; Xin, H.; Linic, S. Visible-Light-Enhanced Catalytic Oxidation Reactions on Plasmonic Silver Nanostructures. *Nat. Chem.* **2011**, *3*, 467–472.

(12) McLellan, J. M.; Siekkinen, A.; Chen, J.; Xia, Y. Comparison of the Surface-Enhanced Raman Scattering on Sharp and Truncated Silver Nanocubes. *Chem. Phys. Lett.* **2006**, *427*, 122–126.

(13) Christopher, P.; Linic, S. Engineering Selectivity in Heterogeneous Catalysis: Ag Nanowires as Selective Ethylene Epoxidation Catalysts. *J. Am. Chem. Soc.* **2008**, *130*, 11264–11265.

(14) Yang, Y.; Liu, J.; Fu, Z.; Qin, D. Galvanic Replacement-Free Deposition of Au on Ag for Core-Shell Nanocubes with Enhanced Chemical Stability and SERS Activity. *J. Am. Chem. Soc.* **2014**, *136*, 8153–8156.

(15) Zhang, J.; Winget, S. A.; Wu. Y.; Su. D.; Sun, X.; Xie, Z. X.; Qin, D. Ag@Au Concave Cuboctahedra: A Unique Probe for Monitoring Au-Catalyzed Reduction and Oxidation Reactions by Surface-Enhanced Raman Spectroscopy. *ACS Nano* **2016**, *10*, 2607–2616.

(16) Li, J.; Sun, X.; Qin, D. Ag-Enriched Ag-Pd Bimetallic Nanoframes and Their Catalytic Properties. *ChamNanoMat* **2016**, *2*, 7494−7499.

(17) Li, J.; Liu, J.; Yin, Y.; Qin, D. Bifunctional Ag@Pd-Ag Nanocubes for Highly Sensitive Monitoring of Catalytic Reactions by Surface-Enhanced Raman Spectroscopy. *J. Am. Chem. Soc.* **2015**, *137*, 7039−7042.

(18) Li, J.; Wu, Y.; Sun, X.; Liu, J.; Winget, S. A.; Qin, D. A Dual Catalyst with SERS Activity for Probing Stepwise Reduction and Oxidation Reactions. *ChamNanoMat* **2016**, *2*, 786−790.

(19) Sun, X.; Qin, D. Co-Titration of $AgNO_3$ and $HAuCl_4$: A New Route to the Synthesis of Ag@Ag–Au Core–frame Nanocubes with Enhanced Plasmonic and Catalytic Properties. *J. Mater. Chem. C* **2015**, *3*, 11833–11841.

(20) Du, J.; Cullen, J. J.; Buettner, G. R. Ascorbic Acid: Chemistry, Biology, and the Treatment of Cancer. *Biochim. Biophys. Acta* **2012**, *1826*, 443-457.

(21) Wang, S.; Qian, K.; Bi, X.; Huang, W. Influence of Speciation of Aqueous $HAuCl_4$ on the Synthesis, Structure, and Property of Au Colloids. *J. Phys. Chem. C* **2009**, *113*, 6505–6510.

(22) Goia, D. V.; Matijević, E. Tailoring the Particle Size of Monodispersed Colloidal Gold. *Colloids Surf. A Physicochem. Eng. Asp.* **1999**, *146*, 139–152.

(23) Hickling, A.; Taylor, D. The Anodic Behaviour of Metals. Part IV. Silver. *Discuss. Faraday Soc.* **1947**, *1*, 277–285.

(24) Zhang, Q.; Li, W.; Wen, L. P.; Chen, J.; Xia, Y. Facile Synthesis of Ag Nanocubes of 30 to 70 nm in Edge Length with CF_3COOAg as a Precursor. *Chem. - A Eur. J.* **2010**, *16*, 10234–10239.

(25) Yang, Y.; Zhang, Q.; Fu, Z.-W.; Qin, D. Transformation of Ag Nanocubes into Ag–Au Hollow Nanostructures with Enriched Ag Contents to Improve SERS Activity and Chemical Stability. *ACS Appl. Mater. Inter.* **2014**, *6*, 3750–3757.

(26) Sun, X.; Kim, J.; Gilroy, K. D.; Liu, J.; König, T. A. F.; Qin, D. Gold-Based Cubic Nanoboxes with Well-Defined Openings at the Corners and Ultrathin Walls Less Than Two Nanometers Thick. *ACS Nano* **2016**, *10*, 8019–8025.

(27) Chen, J.; McLellan, J. M.; Siekkinen, A.; Xiong, Y.; Li, Z.-Y.; Xia, Y. Facile Synthesis of Gold-Silver Nanocages with Controllable Pores on the Surface. *J. Am. Chem. Soc.* **2006**, *128*, 14776−14777.

(28) Venables, J. A. Introduction to Surface and Thin Film Processes; Cambridge University Press: Cambridge, United Kingdom, 2000.

(29) Zhang, Q. F.; Blom, D. A.; Wang, H. Nanoporosity-Enhanced Catalysis on Subwavelength Au Nanoparticles: a Plasmon-Enhanced Spectroscopic Study. *Chem. Mater.* **2014**, *26*, 5131−5142.

(30) Zhao, L. B.; Chen, J. L.; Zhang, M.; Wu, D. Y.; Tian, Z. Q. Theoretical Study on Electroreduction of *p*−Nitrothiophenol on Silver and Gold Electrode Surfaces. *J. Phys. Chem. C* **2015**, *119*, 4949−4958.

(31) Ansar, S.M.; Ameer, F. S.; Hu, W.; Zou, S.; Pittman, C. U.; Zhang, D. *Removal of Molecular Adsorbates on Gold Nanoparticles Using Sodium Borohydride in Water. Nano Lett.* **2013**, *13*, 1226−1229.

(32) Stuart, C. M.; Frontiera, R. R.; Mathies, R. A. Excited−State Structure and Dynamics of *cis*- and *trans*-Azobenzene from Resonance Raman Intensity Analysis. *J. Phys. Chem. A* **2007**, *111*, 12072−12080.

(33) Huang, Y. F.; Wu, D. Y.; Zhu, H. P.; Zhao, L. B.; Liu, G. K.; Ren, B.; Tian, Z. Q. Surface-Enhanced Raman Spectroscopic Study of *p*−Aminothiophenol. *Phys. Chem. Chem. Phys.* **2012**, *14*, 8485−8497.

(34) Sun, M.; Xu, H. A Novel Application of Plasmonics: Plasmon-Driven Surface-Catalyzed Reactions. *Small*, **2012**, *8*, 2777−2786.

(35) Huang, Y.; Zhu, H.; Liu, G.; Wu, D.; Ren, B.; Tian, Z. Q. When the Signal Is Not from the Original Molecule To Be Detected: Chemical Transformation of para-Aminothiophenol on Ag during the SERS Measurement. *J. Am. Chem. Soc*. **2010**, *132*, 9244–9246.

(36) Sun, X.; Yang, Y.; Zhang, Z.; Qin, D. Mechanistic Roles of Hydroxide in Controlling the Deposition of Gold on Colloidal Silver Nanocrystals. *Chem. Mater.* **2017**, *29*, 4014–4021.

CHAPTER 4. GOLD-BASED CUBIC NANOBOXES WITH WELL-DEFINED OPENINGS AT THE CORNERS AND ULTRATHIN WALLS LESS THAN TWO NANOMETERS THICK

4.1 Introduction

Gold nanostructures embrace fascinating optical properties, commonly known as localized surface plasmon resonance (LSPR), for a broad range of applications.[1–8] For Au nanoparticles with a solid structure and spherical shape, it is feasible to tune their LSPR peaks from 520 to 580 nm by increasing the diameter from 20 to 80 nm.[9] The location of LSPR peaks in the visible region is instrumental to the development of colorimetric sensing devices.[10] For most biomedical applications, however, it is essential to tailor the LSPR peaks to the near-infrared (NIR) between 700 and 1200 nm, in which soft tissues are highly transparent to enable deep penetration. By elongating spherical Au nanoparticles into nanorods, El-Sayed,[11–13] Murphy,[14–16] Liz-Marzán,[17,18] and many others[19–22] were able to shift the longitudinal LSPR peaks up to 2000 nm by increasing the aspect ratio of the nanorods. On the other hand, Halas and co-workers demonstrated the fabrication of Au nanoshells by depositing Au onto silica beads. They established the capability to manipulate the LSPR of Au nanoshells from 700 to 1050 nm by reducing the Au thickness from 20 to 5 nm.[23,24]

Parallel to those developments, Xia and co-workers introduced Au nanocages with hollow interiors and porous walls, which could be prepared with precisely tuned LSPR peaks up to 1200 nm by leveraging the galvanic replacement reaction between Ag

nanocubes and $HAuCl_4$.[25–27] In a typical process, Au atoms are derived from a Au(III) precursor at the expense of three Ag atoms, followed by their deposition onto the surface of a Ag nanocube. Ultimately, the Ag nanocube is transformed into a nanobox and then a nanocage through the interplay of alloying and dealloying between Au and Ag. Although the galvanic replacement approach is simple and versatile, it does have a number of limitations. For example, it is impossible to reduce the wall thickness down to a scale below 5 nm without breaking the hollow structure. It is difficult to separately tune the size and wall thickness of the hollow structures because the wall thickness is stoichiometrically related to the size of the Ag nanocubes.[28] It is also nontrivial to precisely control the location and size of the pores generated in the walls of nanocages. By employing Ag nanocubes with an edge length of 94 nm and truncation at the corners, Xia and co-workers demonstrated the fabrication of Au-based nanocages with pores (~10 nm) located at the corners (the sites with truncation) and 15-nm thick walls in high yields by confining the dissolution of Ag and the deposition of Au to the corners and side faces, respectively.[29] However, it is challenging to extend this synthetic approach to Ag nanocubes with sharper corners or smaller sizes because of the complications inherent to galvanic replacement, alloying, and dealloying processes.

As discussed in Chapter 3, we could reduce Au(III) ions to generate Au atoms by introducing a faster parallel reduction reaction to compete with and thus suppress the galvanic replacement reaction between Au(III) and Ag nanocubes.[30,31] More significantly, we demonstrated that the Au atoms could be deposited on the surface of a Ag nanocube in a layer-by-layer fashion to generate a $Ag@Au_{nL}$ core-shell nanocube (where *n* refers to the number of Au atomic layers), with a tightly controlled thickness for the Au shells from

three to six atomic layers.[30] Herein, we demonstrate that Ag_2O patches can be specifically generated at the corner sites of Ag nanocubes when the synthesis is conducted in the presence of sodium hydroxide (NaOH) at pH=11.9. Remarkably, we can selectively dissolve the Ag_2O patches using a weak acid, lifting off any Au overlayers deposited on the Ag_2O patches and thus exposing the Ag core at the corner sites without affecting the ultrathin Au layers on the side faces. When subjected to Ag etching with an aqueous H_2O_2 solution, the Ag core can be completely removed to transform the $Ag@Au_{nL}$ nanocube into a nanobox with well-defined openings at the corners. Due to the inter-diffusion between Au and Ag in physical contact, the final nanobox is comprised of a Au-Ag alloy, whose exact composition is controlled by the etchant used for the removal of Ag form the cores. This approach works well for Ag nanocubes of 38 nm and 18 nm in edge length and the wall thickness of the nanoboxes can be readily controlled down to 2 nm. These ultrathin nanoboxes with controllable openings at the corners exhibit strong optical absorption in the near-infrared region of 700-1200 nm, making them well-suited for biomedical applications.

4.2 Experimental Section

Chemicals and Materials. Ethylene glycol (EG) was purchased from, J. T. Baker. All other chemicals, including silver trifluoroacetate (CF_3COOAg, 98%), gold(III) chloride trihydrate ($HAuCl_4 \cdot 3H_2O$, 99.9+%), sodium hydrosulfide hydrate ($NaHS \cdot xH_2O$), poly(vinylpyrrolidone) (PVP) with an average molecular weight of 29,000 (PVP-29) or 55,000 (PVP-55), aqueous hydrochloric acid (HCl, 37%), L-ascorbic acid (H_2Asc, 99%), citric acid (CA, 99.5+%), iron(III) nitrate nonahydrate ($Fe(NO_3)_3 \cdot 9H_2O$, 99.95%) and

hydrogen peroxide (H_2O_2, 30 wt.% in H_2O) were obtained from Sigma-Aldrich. NaOH (98+%) was purchased from Alfa Aesar. All chemicals were used as received while deionized (DI) water with a resistivity of 18.2 MΩ·cm at 25 °C was used for the preparation of all aqueous solutions.

Synthesis of Ag Nanocubes. We followed the protocols reported by Xia and co-workers for the synthesis of Ag nanocubes with average edge lengths of 38 nm[32] and 18 nm,[33] respectively. For each synthesis, the final product was collected by centrifugation, washed with acetone and DI water three times, and then re-dispersed in DI water.

Synthesis of Ag@Au_{3L} and Ag@Au_{6L} Core-Shell Nanocubes. In a typical synthesis, we placed 2 mL of an aqueous solution of PVP-29k in a 23-mL glass vial and then introduced 0.5 mL of aqueous H_2Asc (0.1 M) and 0.5 mL of aqueous NaOH (0.2 M) under magnetic stirring. Immediately after the introduction of 20 μL of the suspension of 38-nm Ag nanocubes (with a final concentration of 4.2×10^{10} particles per mL), 0.4 mL or 0.8 mL of aqueous $HAuCl_4$ (0.1 mM) was injected into the reaction solution using a syringe pump at a rate of 20 μL/min. These two volumes of $HAuCl_4$ yielded Ag@Au_{3L} nanocubes and Ag@Au_{6L} nanocubes, respectively. The reaction solution was maintained under magnetic stirring at room temperature for another 20 min once the titration had been completed. The solid sample was collected by centrifugation at 6000 rpm for 15 min and washed with DI water three times. The final product was dispersed and stored in 2.5 mL of DI water for further use.

Synthesis of Au-Based Nanoboxes. We mixed 0.1 mL of the as-prepared Ag@Au_{nL} nanocubes (4.2×10^{11} particles per mL) with 0.8 mL of PVP–29k (1 mM) and 0.2 mL of H_2Asc (0.1 mM) at room temperature under magnetic stirring. After 20 min, the particles

were collected by centrifugation at 6000 rpm for 20 min, followed by re-dispersion in DI water. The collected particles were then mixed with 1 mL of 3% aqueous H_2O_2 and incubated under magnetic stirring at room temperature for 3 h. The resultant Au nanoboxes were washed twice with DI water and re-dispersed in 0.5 mL of DI water.

Synthesis of Au-Based Nanoboxes with further Dealloying. To 0.5 mL of an aqueous dispersion of the Au nanoboxes prepared by H_2O_2 etching (see above), 4 μL of aqueous $Fe(NO_3)_3$ (50 mM) was added and vortexed for a few seconds before the mixture was allowed to sit still for another one hour. The solid product was collected by centrifugation at 12000 rpm for 20 min, washed twice with DI water, and then re-dispersed in 0.5 mL of DI water.

Instrumentation and Characterization. We used a conventional centrifuge (Eppendorf 5430) for the preparation of all samples. We collected all the UV-vis-NIR spectra with a LAMDA 750 (PerkinElmer, Waltham, MA). An inductively coupled plasma mass spectrometer (ICP-MS, NexION 300Q, PerkinElmer, Waltham, MA) was used for the quantification of Ag content. We took transmission electron microscopy (TEM) images using an HT7700 microscope (Hitachi, Tokyo, Japan) operated at 120 kV. We acquired high-angle annular dark-field scanning TEM (HAADF-STEM) and high-angle annular bright-field scanning TEM (HAABF-STEM) images using a JEOL 2200FS STEM/TEM microscope equipped with a CEOS GmbH probe corrector at an accelerating voltage of 200 kV and a probe size of 1 nm. We collected energy dispersive X-ray spectroscopy (EDS) spectra under the STEM mode using an Oxford Inca x-sight spectrometer with a 1 mm^2 Si (Li) detector. EDS mapping was carried out with 25×25 or 50×50 point scans at 1500 ms dwell time.

Discrete Dipole Approximation (DDA) Calculation. A model of the structure was generated by *i*) creating a cube, *ii*) subtracting a smaller cube from the interior to create a box, and then *iii*) truncating each corner with a (111) plane, which resulted in the formation of eight triangular pores. In terms of the smaller structure (the 20-nm nanobox), truncation did not lead to pore sizes commensurate with what was observed by electron microscopy characterization. Therefore, a sphere of 1.5 nm in radius was subtracted from each one of the corners. Once the shape was generated and inspected with Visual Molecular Dynamics (VMD) 1.9.2, it was then uploaded as a shape-file into the ddscat 7.2.0 software. In all cases, the propagation (k-vector) and electric field (E-field) of the incident photon were perpendicular and parallel to the (100)-facet of the cube, respectively (as indicated in Figure 4.8B and Figure 4.10D). Furthermore, in all simulations, between 10^4 and 10^5 dipoles were used to ensure accurate results. The dielectric constant for the Au-Ag alloy was taken from the literature.[34] Since all spectra were measured when the nanoboxes were suspended in water, the dielectric constants of the medium and void spaces were taken to be $\varepsilon_m = n^2 = 1.78$.

4.3 Results and Discussion

4.3.1 Proposed Mechanism for the Transformation of Ag Nanocubes to Au-Based Nanoboxes

Figure 4.1 illustrates the four major steps involved in the fabrication of Au-based nanoboxes. The synthesis relies on the use of Ag nanocubes with slight truncation at corners as templates for the conformal deposition of ultrathin Au shells. In a typical process, the Ag nanocubes are dispersed in an aqueous solution containing NaOH, H_2Asc

(which should react with NaOH to form ascorbate monoanion ($HAsc^-$) a reducing agent), and poly(vinylpyrrolidone) (PVP, a stabilizer), immediately followed by the titration of aqueous $HAuCl_4$ using a syringe pump under ambient condition. In the first step, the initial few droplets of $HAuCl_4$ should be neutralized by OH^- for the generation of $AuCl_4^-$. We believe that a small number of Au atoms are formed and deposited on the side faces at the expense of Ag atoms dissolved from the corners through the galvanic replacement reaction between Ag nanocubes and $AuCl_4^-$. Because of the presence of NaOH in the reaction solution (pH=11.9), the resultant Ag^+ ions are supposed to react with OH^- for the generation of Ag_2O at the corners,[35] preventing the underlying Ag from further reacting with Au(III) species. In the second step, $AuCl_4^-$ evolved into $AuCl(OH)_3^-$ and $Au(OH)_4^-$ through ligand exchange with OH^- at pH=11.9.[36] These Au(III) species with lower reduction potential would be reduced by $HAsc^-$ for the generation of Au atoms, followed by their conformal deposition on the side faces of nanocubes in a layer-by-layer fashion. Some of the deposited Au atoms can migrate to corners through surface diffusion.[37] As such, the Ag nanocubes are transformed into $Ag@Au_{nL}$ core-shell nanocubes with multiple Au atomic layers on the side faces, together with some Au atoms deposited on the Ag_2O regions at the corners.

In the third step, we dissolve the Ag_2O at the corners with a weak acid, lifting-off the Au deposited on the Ag_2O regions.[38] Specifically, we collect the $Ag@Au_{nL}$ nanocubes by centrifugation and then re-disperse them in an aqueous acidic solution containing H_2Asc and PVP (pH=3.2). We confirm that H_2Asc could dissolve Ag_2O without compromising the integrity of the Au layers on the side faces. Other weak acids such as citric acid also worked. Finally, we use aqueous 3% H_2O_2 to etch away the Ag cores, leading to the

production of Au-based nanoboxes with hollow interiors, ultrathin walls, and well-defined openings at the corners. We speculate that Ag could be included in the Au walls due to the inter-diffusion between the two elements for the formation of an alloy. We could use a stronger dealloying agent based on $Fe(NO_3)_3$ to remove additional Ag in order to generate nanoboxes with a higher Au content. By varying the edge length of the Ag nanocubes and the thickness of Au layers deposited on the Ag templates, we can independently control the physical dimension and wall thickness of the Au-based nanoboxes.

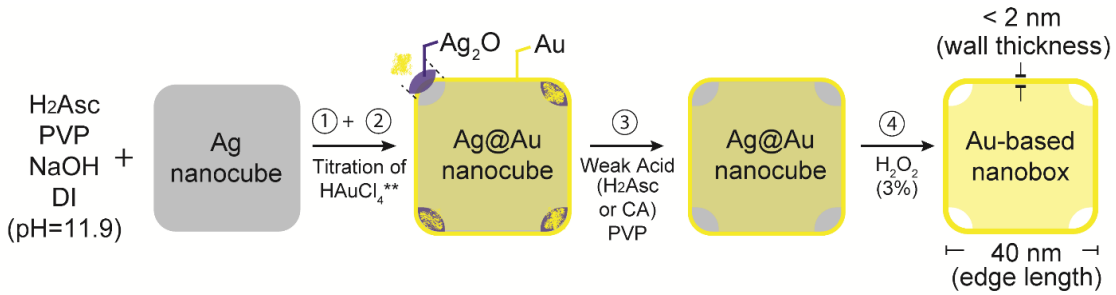

Step 1: Initial deposition of Au and formation of Ag_2O

$AuCl_4^- + Ag \longrightarrow Ag^+ + 4Cl^- + Au$ (edge)

$2Ag^+ + 2OH^- \longrightarrow Ag_2O + H_2O$ (corner)

Step 2: Conformal deposition of Au

$Au(III) \xrightarrow{HAsc^-} Au$ (side face)

Step 3: Dissolution of Ag_2O

$Ag_2O \xrightarrow[PVP]{H_2Asc/CA} 2Ag^+$ (corner)

Step 4: Removel of Ag core

$Ag \xrightarrow{H_2O_2} Ag^+$ (interior)

Ascorbic Acid (H_2Asc) Ascorbate monoanion ($HAsc^-$)
Poly(vinylpyrrolidone) (PVP) Citric Acid (CA)
Au(III): $AuCl(OH)_3^-$, $Au(OH)_4^-$
** Tititration immediately after the addition of Ag nanocubes

Figure 4.1. Schematic illustration (projected along [100] direction) of the four steps involved in the transformation of a Ag nanocube into a Au-based nanobox.

4.3.2 Fabrication of Au-Based Nanoboxes with Well-Defined Openings at the Corners

In one set of experiments, we used Ag nanocubes with an average edge length of 38.0±1.1 nm with slight truncation at the corners (see Figure 2.1 in Chapter 2) as templates to generate $Ag@Au_{6L}$ nanocubes and then Au-based nanoboxes with an outer edge length of 39.7±3.0 nm (see experimental section for details). Figure 4.2A shows a TEM image of the $Ag@Au_{6L}$ nanocubes with the introduction of 0.8 mL of aqueous $HAuCl_4$ (0.1 mM) to generate six atomic layers of Au on the side faces. To confirm the formation of a conformal shell of Au on the Ag core, we used HAADF-STEM to characterize the core-shell nanocubes (Figure 4.2B). The contrast between the shell and the core clearly verifies the conformal deposition of Au on the entire surface of the Ag nanocube, with a somewhat thinner projection along the edges. The dark contrast at the corners suggests a higher degree of truncation at the corners than the edges due to the formation of Ag_2O at the corner sites.

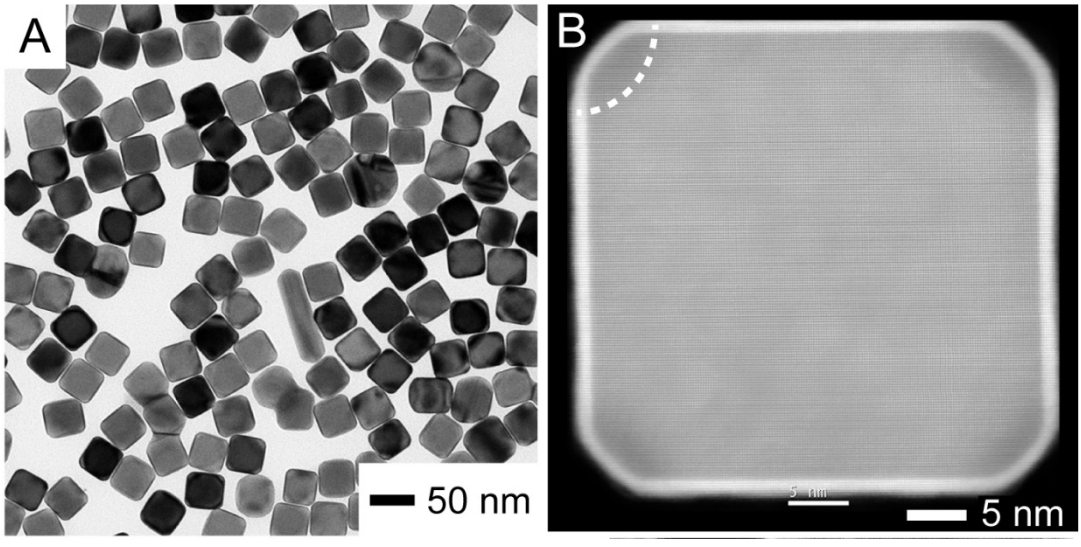

Figure 4.2. (A) TEM image of $Ag@Au_{6L}$ nanocubes. (B) HAADF-STEM image of a $Ag@Au_{6L}$ nanocube. The marked area indicates the dark contrast at a corner.

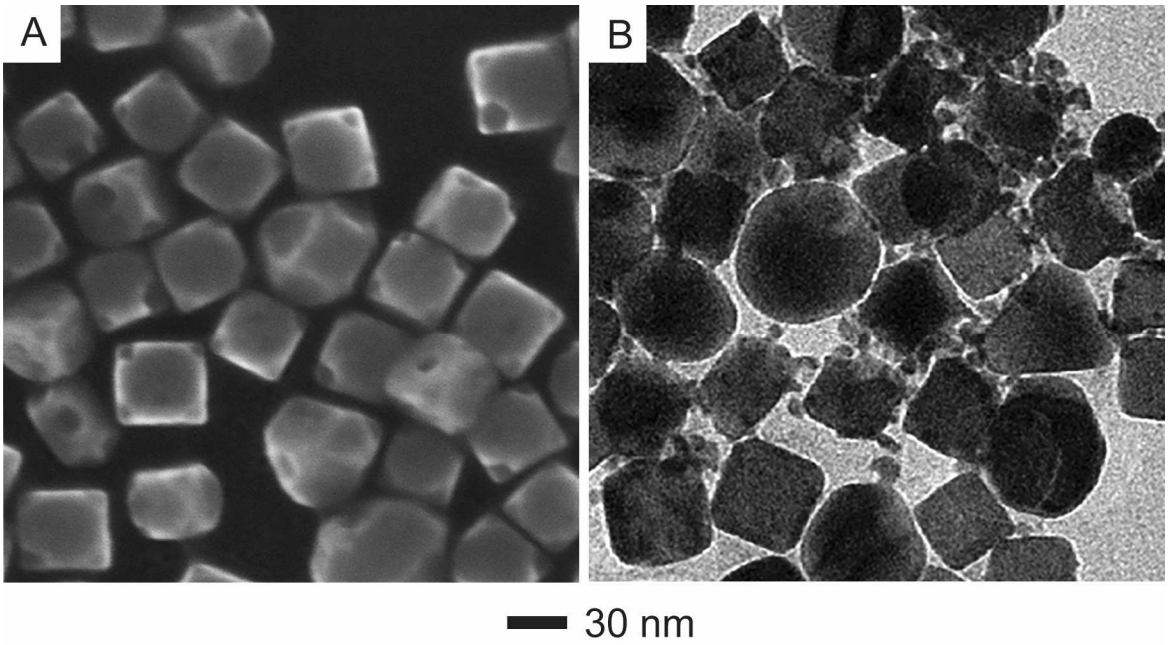

Figure 4.3. (A) SEM image of a sample obtained by reacting Ag nanocubes with 0.1 mL of 0.1 mM $HAuCl_4$ at a pH of 11.9 in the absence of H_2Asc. (B) TEM image of a sample obtained by incubating the Ag nanocubes in an aqueous solution containing NaOH, H_2Asc, and PVP for 60 min prior to the titration of 0.8 mL of $HAuCl_4$ (0.1 mM).

We also conducted a control experiment by titrating the Ag nanocubes with $HAuCl_4$ in the presence of PVP and NaOH (at pH=11.9) in the absence of H_2Asc. Figure 4.3A shows an SEM image of the sample obtained with the reaction between Ag nanocubes and 0.1 mL of $HAuCl_4$ (0.1 mM), confirming the formation of holes at the corners due to the involvement of galvanic replacement reaction. It is also worth pointing out that Ag_2O could be possibly formed over the entire surface of a Ag nanocube when it was brought into contact with a reaction solution containing NaOH, H_2Asc and PVP for a long period of time due to the involvement of oxidative etching and thus the generation of Ag^+ ions.[39,40] We performed another control experiment by leaving Ag nanocubes in the reaction solution (pH=11.9) for 60 min prior to the titration of $HAuCl_4$, and we observed the random formation of Au nanoparticles on the Ag nanocube (Figure 4.3B). This result indicates the

presence of a Ag_2O shell on the entire surface of a Ag nanocube and this oxide shell would then prevent the epitaxial deposition of Au overlayers.[41] Taken together, it is of critical importance to start the titration of $HAuCl_4$ immediately after the introduction of Ag nanocubes into the reaction solution. In this case, the involvement of galvanic replacement would immediately initiate the deposition of Au atoms on the side faces while the Ag atoms at the corners were oxidized to form Ag_2O patches.

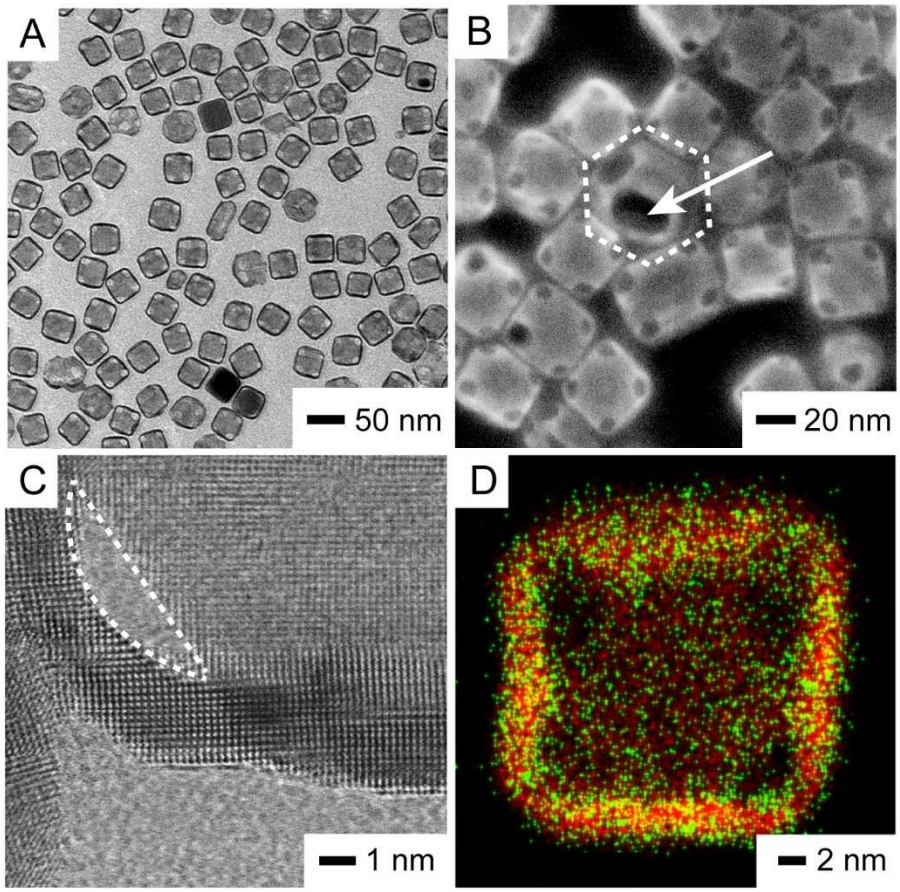

Figure 4.4. (A, B) TEM and SEM images of the nanoboxes obtained by removing the Ag cores. The particle marked by an arrow indicates the formation of hollow interior. (C) Atomic-resolution HAABF-STEM image taken from the corner region of a nanobox. (D) EDS elemental mapping of a nanobox (red, Au; green, Ag).

After treating the as-prepared $Ag@Au_{6L}$ nanocubes with an aqueous solution containing H_2Asc and PVP, we removed the Ag cores using 3% aqueous H_2O_2. Figure 4.4A shows a typical TEM image of the resultant nanoboxes with an average outer edge length of 39.9±3.2 nm, together with a well-preserved cubic shape and well-defined pores at the corners. From the TEM image, we noticed that a few of the solid core-shell nanocubes still remained in the final product. Likely, the corners of these nanocubes were covered by relatively thicker Au overlayers, preventing H_2Asc from dissolving Ag_2O and then H_2O_2 from attacking and dissolving the Ag core. Figure 4.4B shows an SEM image collected from the same sample, confirming the formation of well-defined pores at the corners. As shown by the particle marked by an arrow, the interior was indeed hollow due to the removal of the Ag core. Figure 4.4C shows an atomic-resolution aberration-corrected HAABF-STEM image recorded from the corner region of a nanobox. It reveals a highly ordered arrangement for the atoms and gives a wall thickness of about 2 nm, corresponding to ten atomic layers along the [100] direction. As indicated by the white, dashed lines, the STEM image also clearly resolved an opening at the corner. Although six atomic layers of Au were originally deposited on the side faces, the wall thickness of the nanobox was increased to ten atomic layers. This result suggests the involvement of inter-diffusion and alloying of Au and Ag and thus the retention of Ag in the walls in the form of an alloy. Elemental mapping by EDS confirms the presence of Ag in the nanoboxes, with a Au to Ag atomic ratio of 1.2:1 (Figure 4.4D). The ICP-MS analysis gives a Au to Ag atomic ratio of 1:1 for a bulk quantity of the sample. We suspect that ICP-MS result tends to underestimate the relative Au content because any solid $Ag@Au_{6L}$ nanocube remaining in the final sample would increase the Ag content.

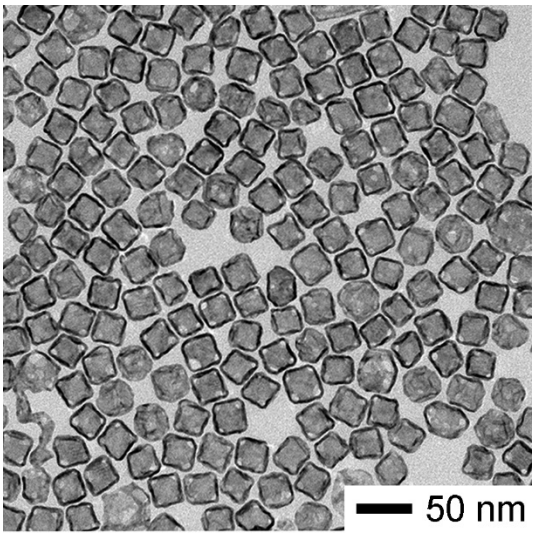

Figure 4.5. TEM image of Au-based nanoboxes obtained by titrating 0.4 mL of 0.1 mM $HAuCl_4$ into an aqueous mixture containing 38-nm Ag nanocubes, H_2Asc, PVP, and NaOH, followed by the removal of Ag cores from $Ag@Au_{3L}$ nanocubes with 3% H_2O_2.

We also fabricated $Ag@Au_{3L}$ nanocubes from Ag nanocubes with an average edge length of 38.0±1.1 nm, followed by the removal of Ag cores. Figure 4.5 shows a TEM image of the resultant nanoboxes. When the Au atomic layers on the side faces were reduced from six to three, the wall thickness of the nanoboxes would decrease, ultimately reduce their overall rigidity. On the other hand, we would anticipate that the amount of Au deposited on the corners would be reduced as the total amount of $HAuCl_4$ added into the reaction system was decreased, leading to the formation of $Ag@Au_{3L}$ nanocubes with non-uniform Au coverage at the corners and thus the formation of openings with a less uniform distribution in pore size.

To confirm the critical role of H_2Asc in transforming the $Ag@Au_{nL}$ nanocubes into nanoboxes, we recorded UV-vis spectra from the $Ag@Au_{3L}$ nanocubes that were treated with DI water, an aqueous PVP solution, or an aqueous solution containing both H_2Asc and PVP, and then etched with 3% aqueous H_2O_2. As shown in Figure 4.6, A and B, the

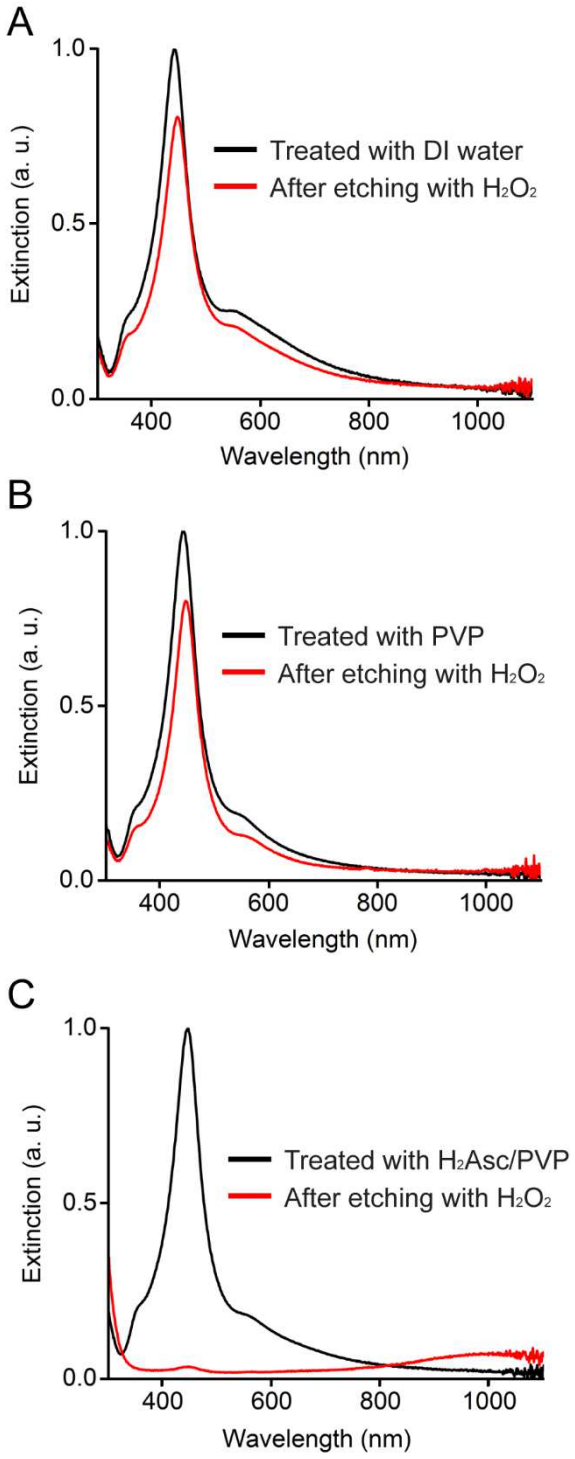

Figure 4.6. UV-vis spectra recorded from aqueous suspensions of the $Ag@Au_{3L}$ nanocubes after treatment with (A) DI water, (B) aqueous PVP, and (C) aqueous solution containing H_2Asc and PVP, respectively, followed by etching with 3% aqueous H_2O_2.

LSPR peak of Ag@Au_{3L} only dropped slightly in intensity after H_2O_2 etching when the nanocubes were treated with DI water or an aqueous PVP solution. In comparison, the original LSPR peak of the Ag@Au_{3L} treated with an aqueous solution containing both H_2Asc and PVP completely disappeared after H_2O_2 etching, with the emergence of a weak peak around 1000 nm (Figure 4.6C). These results suggest that it was H_2Asc that served as an acid to selectively dissolve the Ag_2O (a base) patches at the corner sites of nanocubes, leading to the transformation of core-shell nanocubes into nanoboxes when the Ag cores are removed by H_2O_2.

To further support our argument that the Ag_2O was removed *via* an acid-base neutralization reaction without involving the reduction function of H_2Asc, we performed a control experiment to treat the Ag@Au_{6L} nanocubes with an aqueous solution containing citric acid (CA, 0.1 mM) and PVP at pH=2.2 before the removal of Ag core by H_2O_2 etching. As shown in Figure 4.7A, we still obtained Au nanoboxes after the removal of Ag cores, confirming the formation of Ag_2O, a base that could be dissolved by an acid, at the corner sites of Ag nanocubes. Figure 4.7B shows UV-vis spectra of the Ag@Au_{6L} nanocubes after the treatment with an aqueous solution containing both CA and PVP, followed by etching with H_2O_2. We noticed that the original LSPR peak of the core-shell nanocubes completely disappeared after H_2O_2 etching, indicating the effectiveness of CA in dissolving the Ag_2O patches. Taken together, we believe that any protonic acid should be able to dissolve the Ag_2O as long as it does not compromise the integrity of the Au layers on the side faces and compromise the etching of Ag by H_2O_2 or another oxidative etchant.

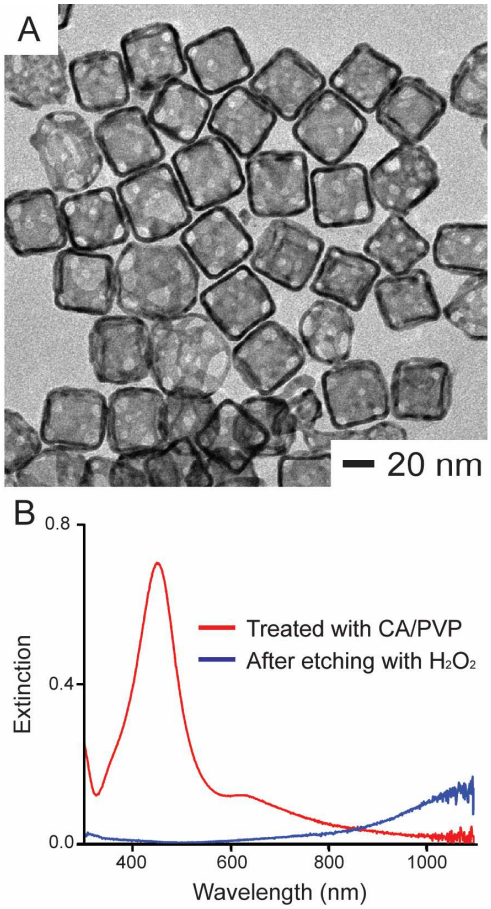

Figure 4.7. (A) TEM image of the Au-based nanoboxes prepared using the same protocol as in Figure 4.4A, except for the replacement of ascorbic acid by citric acid (CA) for the dissolution of Ag_2O patches. (B) UV-vis spectra taken from the $Ag@Au_{6L}$ core-shell nanocubes after treatment with an aqueous solution of CA and PVP, followed by etching with 3% aqueous H_2O_2.

4.3.3 Optical Properties of Au-Based Nanoboxes

We used UV-vis-NIR spectroscopy to characterize the optical properties of the as-prepared nanoboxes. As shown in Figure 4.8A, when $Ag@Au_{6L}$ nanocubes were transformed into nanoboxes by etching Ag with 3% H_2O_2, the LSPR peak was red-shifted from 447 to 1080 nm. In comparison, if $Fe(NO_3)_3$ was used to remove more Ag from the walls of the nanoboxes (Figure 4.9), the LSPR peak was further red-shifted to 1135 nm. To better understand the optical properties of the nanoboxes, we used discrete dipole

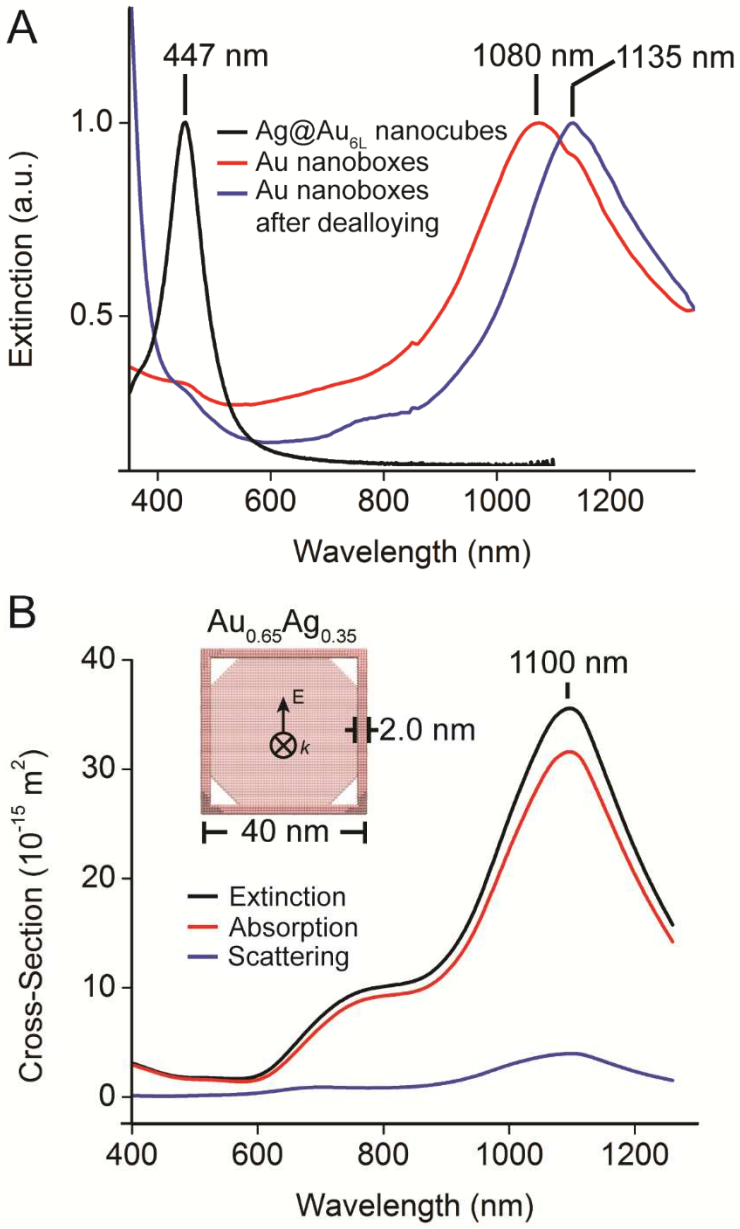

Figure 4.8. (A) UV-vis-NIR spectra taken from an aqueous suspension of the Ag@Au_{6L} nanocubes with an average edge length of 40 nm, and the corresponding nanoboxes before and after dealloying with $Fe(NO_3)_3$. (B) Extinction spectra calculated using the DDA method for a Au-based nanobox with an outer edge length of 40 nm, a wall thickness of 2 nm, a pore size of 10 nm, and an atomic composition of 65% Au and 35% Ag. The propagation direction (*k*-vector) and electric field (*E*-field) were perpendicular and parallel to the (100)-facet of the cubic box, respectively.

approximation (DDA) to calculate their absorption and scattering cross-sections.[42] In the simulation, we assumed that a nanobox is surrounded by and completely filled with water. Also, we defined the geometry of a nanobox with an outer edge length of 40 nm, a wall thickness of 2 nm, and triangular pores (10 nm in edge length) at all corners, together with a Au-Ag alloy composition of 65%Au and 35%Ag because of its available dielectric constant.[34] Figure 4.8B shows the calculated absorption, scattering, and extinction spectra. The peak was located at 1100 nm, in agreement with the experimental data (at 1080 nm). The calculated extinction, absorption, and scattering cross-sections at resonance were 35.5×10^{-15}, 31.6×10^{-15}, and 3.9×10^{-15} m^2, respectively. The absorption cross section is about five times greater than those reported for Au-Ag nanocages with an edge length of 36 nm but prepared by galvanic replacement reaction.[43]

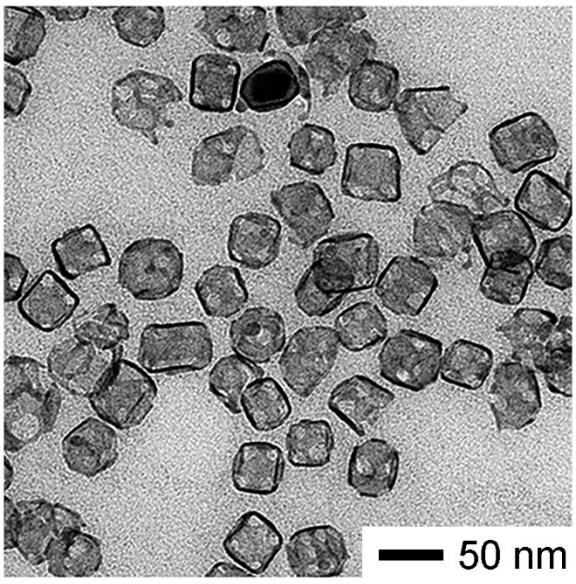

Figure 4.9. TEM image of Au-based nanoboxes obtained by titrating 0.8 mL of 0.1 mM $HAuCl_4$ into an aqueous mixture containing 38-nm Ag nanocubes, H_2Asc, PVP, and NaOH, followed by the removal of Ag cores with 3% H_2O_2 first and then dealloying with $Fe(NO_3)_3$.

We have also extended the procedure to Ag nanocubes with an average edge length of 17.7±0.9 nm (Figure 4.10A) for their transformation into nanoboxes. Specifically, we adjusted the initial concentration of these nanocubes in the reaction solution with a goal to keep the total surface area the same as that of the nanocubes with an edge length 38 nm. As a result, with the titration of 0.8 mL of aqueous $HAuCl_4$ (0.1 mM), Au atoms derived from the reduction by $HAsc^-$ could also be deposited on the nanocubes for the generation of $Ag@Au_{6L}$ nanocubes with an edge length of 19.8±1.1 nm. Figure 4.10B shows TEM image of the nanoboxes with an average outer edge length of 19.6±1.4 nm upon removal of the Ag cores, indicating a well-preserved cubic shape and holes at the corners. Because some of the small Ag nanocubes had significant truncation at the corners, the 20-nm nanoboxes were not as uniform as the 40-nm nanoboxes. When the core-shell nanocubes were transformed into nanoboxes, the LSPR peak was red-shifted from 425 nm to 835 nm (Figure 4.10C). Again, we calculated the optical cross-sections of a nanobox with an outer edge length of 20 nm and a wall thickness of 1.9 nm, together with the assumption that the pore size is 3 nm at all corners (Figure 4.10D). The resonance peak is located at 810 nm, in agreement with the experimental data. The results indicate that absorption is in dominance, with its cross-section of 1.6×10^{-15} m^2 at the resonance peak, which is five orders in magnitude greater than that of a traditional organic dye (*e.g.*, indocyanine green, 2.0×10^{-20} m^2 at 800 nm).[44] Collectively, our DDA results suggest that the extinction peak position is sensitive to the edge length and the wall thickness of the nanobox. It is also worth pointing out that the edge length could be varied to tune the ratio of absorption to scattering. For example, the absorption completely dominates for the 20-nm nanobox while

scattering would emerge with a contribution of 10% as the edge length of the nanobox was increased to 40 nm.

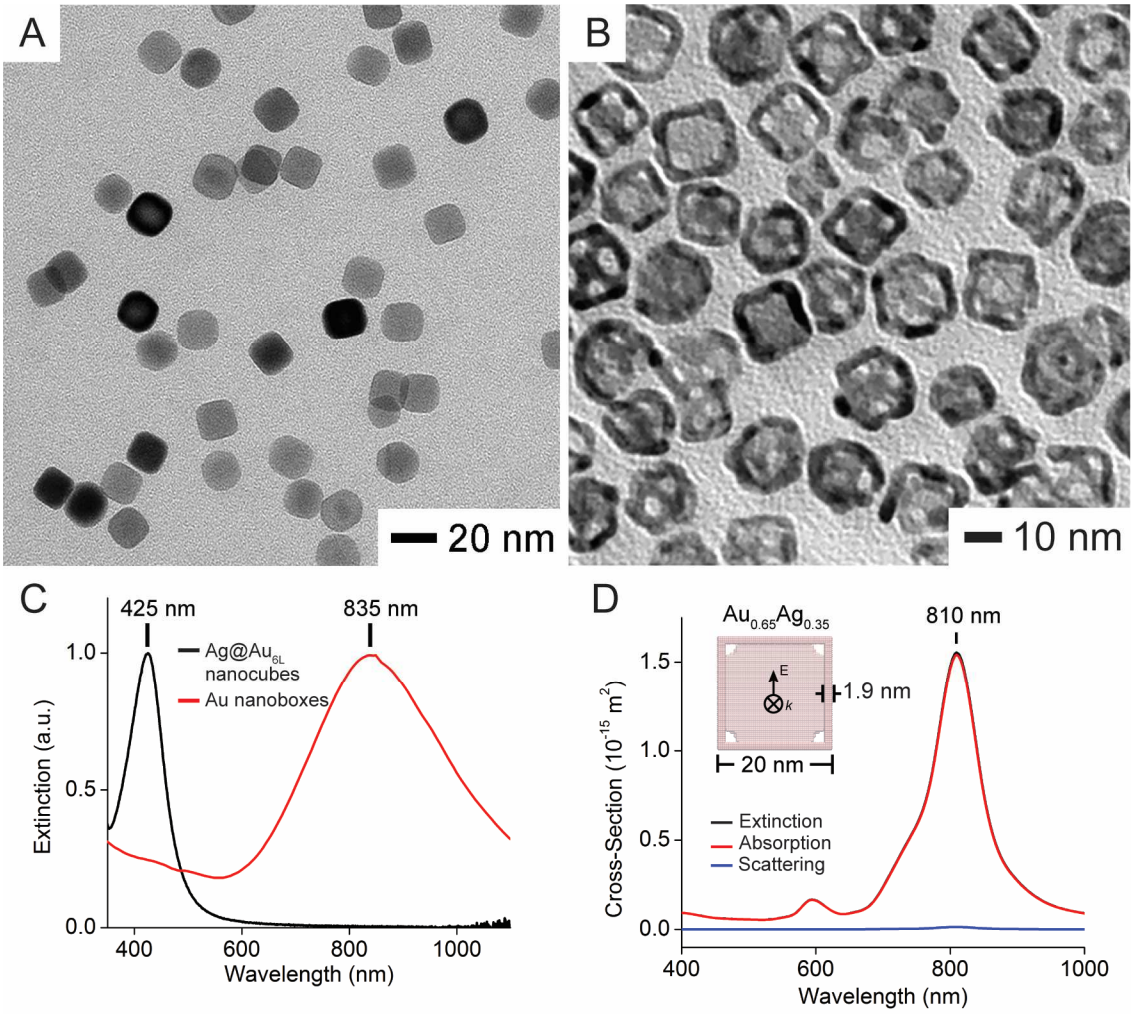

Figure 4.10. (A) TEM image of Ag nanocubes with edge lengths of 18 nm that were used as the templates for the fabrication of nanoboxes with edge length of 20 nm. (B) TEM image of Au-based nanoboxes with an outer edge length of 20 nm. (C) UV-vis-NIR spectra of an aqueous suspension of the Ag@Au$_{6L}$ nanocubes with an edge length of 20 nm, and the corresponding nanoboxes. (D) Extinction spectra calculated for a Au-based nanobox with an outer edge length of 20 nm, a wall thickness of 1.9 nm, a pore size of 3 nm, and atomic compositions of 65% Au and 35% Ag.

4.4 Conclusions

In summary, we have demonstrated a facile route to the fabrication of Au-based nanoboxes with a wall thickness less than 2 nm and well-defined openings at corners. When $HAuCl_4$ is titrated into a suspension of Ag nanocubes with slight corner truncation in the presence of NaOH and H_2Asc at the initial pH of 11.9, a small amount of Ag will be dissolved from the corners because of its galvanic replacement with Au^{3+}. Owing to the presence of OH^- ions, Ag_2O is immediately formed at the corners, impeding further dissolution of Ag from the nanocubes. Meanwhile, the resultant Au atoms are deposited onto the side faces, followed by the conformal, layer-by-layer deposition of more Au formed through the redox reaction with $HAsc^-$. Some of the deposited Au atoms can also migrate from side faces to corners for the generation of Au overlayers thinner than those on the side faces. The Ag_2O at the corners can be removed using a weak acid, such as ascorbic acid or citric acid, making it feasible to completely etch away the Ag core without breaking the Au shell as thin as 2 nm. Owing to the ultrathin wall thickness, Au nanoboxes as small as 20 nm in edge length can still be fabricated with strong absorption in the near-infrared region for immediate applications as contrast agents for optical imaging and as capsules for controlled release.

4.5 Notes to Chapter 4

Part of this chapter is adapted from the paper "Gold-Based Cubic Nanoboxes with Well Defined Openings at the Corners and Ultrathin Walls Less Than Two Nanometer Thick" published in ACS *Nano*.[45]

4.6 References

(1) Daniel, M.-C.; Astruc, D. Gold Nanoparticles: Assembly, Supramolecular Chemistry, Quantum-Size-Related Properties, and Applications toward Biology, Catalysis, and Nanotechnology. *Chem. Rev.* **2004**, *104*, 293–346.

(2) Haes, A. J.; Haynes, C. L.; McFarland, A. D.; Schatz, G. C.; Van Duyne, R. P.; Zou, S. Plasmonic Materials for Surface-Enhanced Sensing and Spectroscopy. *MRS Bull.* **2005**, *30*, 368–375.

(3) Eustis, S.; El-Sayed, M. A. Why Gold Nanoparticles Are More Precious than Pretty Gold: Noble Metal Surface Plasmon Resonance and Its Enhancement of the Radiative and Nonradiative Properties of Nanocrystals of Different Shapes. *Chem. Soc. Rev.* **2006**, *35*, 209–217.

(4) Murphy, C. J.; Gole, A. M.; Hunyadi, S. E.; Stone, J. W.; Sisco, P. N.; Alkilany, A.; Kinard, B. E.; Hankins, P. Chemical Sensing and Imaging with Metallic Nanorods. *Chem. Commun.* **2008**, *0*, 544–557.

(5) Giljohann, D. A.; Seferos, D. S.; Daniel, W. L.; Massich, M. D.; Patel, P. C.; Mirkin, C. A. Gold Nanoparticles for Biology and Medicine. *Angew. Chem. Int. Ed.* **2010**, *49*, 3280–3294.

(6) Dreaden, E. C.; Alkilany, A. M.; Huang, X.; Murphy, C. J.; El-Sayed, M. A. The Golden Age: Gold Nanoparticles for Biomedicine. *Chem. Soc. Rev.* **2012**, *41*, 2740–2779.

(7) Chen, H.; Shao, L.; Li, Q.; Wang, J. Gold Nanorods and Their Plasmonic Properties. *Chem. Soc. Rev.* **2013**, *42*, 2679–2724.

(8) Yang, X.; Yang, M.; Pang, B.; Vara, M.; Xia, Y. Gold Nanomaterials at Work in Biomedicine. *Chem. Rev.* **2015**, *115*, 10410–10488.

(9) Jain, P. K.; Lee, K. S.; El-Sayed, I. H.; El-Sayed, M. A. Calculated Absorption and Scattering Properties of Gold Nanoparticles of Different Size, Shape, and Composition: Applications in Biological Imaging and Biomedicine. *J. Phys. Chem. B* **2006**, *110*, 7238–7248.

(10) Elghanian, R.; Storhoff, J. J.; Mucic, R. C.; Letsinger, R. L.; Mirkin, C. A. Selective Colorimetric Detection of Polynucleotides Based on the Distance-Dependent Optical Properties of Gold Nanoparticles. *Science* **1997**, *277*, 1078–1081.

(11) Link, S.; Wang, Z. L.; El-Sayed, M. A. Alloy Formation of Gold-Silver Nanoparticles and the Dependence of the Plasmon Absorption on Their Composition. *J. Phys. Chem. B* **1999**, *103*, 3529–3533.

(12) Nikoobakht, B.; El-Sayed, M. A. Preparation and Growth Mechanism of Gold Nanorods (NRs) Using Seed-Mediated Growth Method. *Chem. Mater.* **2003**, *15*, 1957–1962.

(13) Huang, X.; Neretina, S.; El-Sayed, M. A. Gold Nanorods: From Synthesis and Properties to Biological and Biomedical Applications. *Adv. Mater.* **2009**, *21*, 4880–4910.

(14) Jana, N. R.; Gearheart, L.; Murphy, C. J. Wet Chemical Synthesis of High Aspect Ratio Cylindrical Gold Nanorods. *J. Phys. Chem. B* **2001**, *105*, 4065–4067.

(15) Jana, N. R.; Gearheart, L.; Murphy, C. J. Seed-Mediated Growth Approach for Shape-Controlled Synthesis of Spheroidal and Rod-like Gold Nanoparticles Using a Surfactant Template. *Adv. Mater.* **2001**, *13*, 1389–1393.

(16) Ye, X.; Jin, L.; Caglayan, H.; Chen, J.; Xing, G.; Zheng, C.; Doan-Nguyen, V.; Kang, Y.; Engheta, N.; Kagan, C. R.; Murray, C. B. Improved Size-Tunable Synthesis of Monodisperse Gold Nanorods through the Use of Aromatic Additives. *ACS Nano* **2012**, *6*, 2804–2817.

(17) Pérez-Juste, J.; Pastoriza-Santos, I.; Liz-Marzán, L. M.; Mulvaney, P. Gold Nanorods: Synthesis, Characterization and Applications. *Coord. Chem. Rev.* **2005**, *249*, 1870–1901.

(18) Pérez-Juste, J.; Liz-Marzán, L. M.; Carnie, S.; Chan, D. Y. C.; Mulvaney, P. Electric-Field-Directed Growth of Gold Nanorods in Aqueous Surfactant Solutions. *Adv. Funct. Mater.* **2004**, *14*, 571–579.

(19) Chang, S.-S.; Shih, C.-W.; Chen, C.-D.; Lai, W.-C.; Wang, C. R. C. The Shape Transition of Gold Nanorods. *Langmuir* **1998**, *15*, 701–709.

(20) Kim, F.; Song, J. H.; Yang, P. Photochemical Synthesis of Gold Nanorods. *J. Am. Chem. Soc.* **2002**, *124*, 14316–14317.

(21) Brioude, A.; Jiang, X. C.; Pileni, M. P. Optical Properties of Gold Nanorods: DDA Simulations Supported by Experiments. *J. Phys. Chem. B* **2005**, *109*, 13138–13142.

(22) Ni, W.; Kou, X.; Yang, Z.; Wang, J. Tailoring Longitudinal Surface Plasmon Wavelengths, Scattering and Absorption Cross Sections of Gold Nanorods. *ACS Nano* **2008**, *2*, 677–686.

(23) Xia, Y.; Halas, N. J. Shape-Controlled Synthesis and Surface Plasmonic Properties of Metallic Nanostructures. *MRS Bull.* **2005**, *30*, 338–348.

(24) West, J. L.; Halas, N. J. Engineered Nanomaterials for Biophotonics Applications: Improving Sensing, Imaging, and Therapeutics. *Annu. Rev. Biomed. Eng.* **2003**, *5*, 285–292.

(25) Xia, Y.; Li, W.; Cobley, C. M.; Chen, J.; Xia, X.; Zhang, Q.; Yang, M.; Cho, E. C.; Brown, P. K. Gold Nanocages: From Synthesis to Theranostic Applications. *Acc. Chem. Res.* **2011**, *44*, 914–924.

(26) Lu, X.; Au, L.; McLellan, J.; Li, Z. Y.; Marquez, M.; Xia, Y. Fabrication of Cubic Nanocages and Nanoframes by Dealloying Au/Ag Alloy Nanoboxes with an Aqueous Etchant Based on $Fe(NO_3)_3$ or NH_4OH. *Nano Lett.* **2007**, *7*, 1764–1769.

(27) Chen, J.; Yang, M.; Zhang, Q.; Cho, E. C.; Cobley, C. M.; Kim, C.; Glaus, C.; Wang, L. V.; Welch, M. J.; Xia, Y. Gold Nanocages: A Novel Class of Multifunctional Nanomaterials for Theranostic Applications. *Adv. Funct. Mater.* **2010**, *20*, 3684–3694.

(28) Xia, X.; Wang, Y.; Ruditskiy, A.; Xia, Y. Galvanic Replacement: A Simple and Versatile Route to Hollow Nanostructures with Tunable and Well-Controlled Properties. *Adv. Mater.* **2013**, *25*, 6313–6333.

(29) Chen, J.; McLellan, J. M.; Siekkinen, A.; Xiong, Y.; Li, Z.-Y.; Xia, Y. Facile Synthesis of Gold-Silver Nanocages with Controllable Pores on the Surface. *J. Am. Chem. Soc.* **2006**, *128*, 14776–14777.

(30) Yang, Y.; Liu, J.; Fu, Z. W.; Qin, D. Galvanic Replacement-Free Deposition of Au on Ag for Core-Shell Nanocubes with Enhanced Chemical Stability and SERS Activity. *J. Am. Chem. Soc.* **2014**, *136*, 8153–8156.

(31) Zhang, J.; Winget, S. A.; Wu, Y.; Su, D.; Sun, X.; Xie, Z.-X.; Qin, D. Ag@Au Concave Cuboctahedra: A Unique Probe for Monitoring Au-Catalyzed Reduction and Oxidation Reactions by Surface-Enhanced Raman Spectroscopy. *ACS Nano* **2016**, *10*, 2607–2616.

(32) Zhang, Q.; Li, W.; Wen, L. P.; Chen, J.; Xia, Y. Facile Synthesis of Ag Nanocubes of 30 to 70 nm in Edge Length with CF_3COOAg as a Precursor. *Chem. Eur. J.* **2010**, *16*, 10234–10239.

(33) Wang, Y.; Zheng, Y.; Huang, C. Z.; Xia, Y. Synthesis of Ag Nanocubes 18-32 nm in Edge Length: The Effects of Polyol on Reduction Kinetics, Size Control, and Reproducibility. *J. Am. Chem. Soc.* **2013**, *135*, 1941–8156.

(34) Peña-Rodríguez, O.; Caro, M.; Rivera, A.; Olivares, J.; Perlado, J. M.; Caro, A. Optical Properties of Au-Ag Alloys: An Ellipsometric Study. *Opt. Mater. Express* **2014**, *4*, 403-410.

(35) Hickling, A.; Taylor, D. The Anodic Behaviour of Metals. Part IV. Silver. *Discuss. Faraday Soc.* **1947**, *1*, 277-285.

(36) Wang, S.; Qian, K.; Bi, X.; Huang, W. Influence of Speciation of Aqueous $HAuCl_4$ on the Synthesis, Structure, and Property of Au Colloids. *J. Phys. Chem. C* **2009**, *113*, 6505–6510.

(37) Xia, X.; Xie, S.; Liu, M.; Peng, H.-C.; Lu, N.; Wang, J.; Kim, M. J.; Xia. Y. On the Role of Surface Diffusion in Determining the Shape or Morphology of Noble-Metal Nanocrystals. *Proc. Natl. Acad. Sci. USA* **2013**, *110*, 2607–2616.

(38) Johnston, H. L.; Cuta, F.; Garrett, A. B. The Solubility of Silver Oxide in Water, in Alkali and in Alkaline Salt Solutions. The Amphoteric Character of Silver Hydroxide. *J. Am. Chem. Soc.* **1933**, *55*, 2311–2325.

(39) Magnussen, O. M. Ordered Anion Adlayers on Metal Electrode Surfaces. *Chem. Rev.* **2002**, *102*, 679–725.

(40) Jovic, B. M.; Jovic, V. D.; Stafford, G. R. Cyclic Voltammetry on Ag(111) and Ag(100) Faces in Sodium Hydroxide Solutions. *Electrochem. Commun.* **1999**, *1*, 247–251.

(41) Hodges, J. M.; Morse, J. R.; Williams, M. E.; Schaak, R. E. Microscopic Investigation of Chemoselectivity in Ag-Pt-Fe_3O_4 Heterotrimer Formation: Mechanistic Insights and Implications for Controlling High-Order Hybrid Nanoparticle Morphology. *J. Am. Chem. Soc.* **2015**, *137*, 15493–15500.

(42) Kelly, K. L.; Coronado, E.; Zhao, L. L.; Schatz, G. C. The Optical Properties of Metal Nanoparticles: The Influence of Size, Shape, and Dielectric Environment. *J. Phys. Chem. B* **2003**, *107*, 668–677.

(43) Chen, J.; Wiley, B.; Li, Z.-Y.; Campbell, D.; Saeki, F.; Cang, H.; Au, L.; Lee, J.; Li, X.; Xia, Y. Gold Nanocages: Engineering Their Structure for Biomedical Applications. *Adv. Mater.* **2005**, *17*, 2255–2261.

(44) Gratz, H.; Penzkofer, A.; Abels, C.; Szeimies, R.-M.; Landthaler, M.; Bäumler, W. Photo-Isomerisation, Triplet Formation, and Photo-Degradation Dynamics of Indocyanine Green Solutions. *J. Photochem. Photobiol. A Chem.* **1999**, *128*, 101–109.

(45) Sun, X.; Kim, J.; Gilroy, K. D.; Liu, J.; König, T. A. F.; Qin, D. Gold-Based Cubic Nanoboxes with Well-Defined Openings at the Corners and Ultrathin Walls Less Than Two Nanometers Thick. *ACS Nano* **2016**, *10*, 8019–8025.

CHAPTER 5. PLATINUM-SILVER CUBIC NANOCAGES WITH WALL THICKNESS LESS THAN 2 NM AND THEIR ENHANCED CATALYTIC ACTIVITY TOWARD OXYGEN REDUCTION

5.1 Introduction

Platinum is a catalyst widely used for many important reactions, including CO oxidation in the catalytic converters,[1] electro-oxidation of small organic fuels such as formic acid and ethanol,[2] and oxygen reduction reaction (ORR) key to the operation of proton-exchange membrane fuel cells.[3,4] However, the expensive price and low abundance associated with Pt present a major challenge for developing cost-effective products. One approach to reducing the loading of Pt is to switch from the conventional solid nanoparticles to more open nanostructures with hollow interiors and porous walls such as Pt-based nanocages.[5] In this structure, most of the Pt atoms, including those located on the inner surface, can participate in the catalytic reaction, making it possible to achieve high specific surface areas without using extremely small particles that are highly susceptible to sintering and/or dissolution from the support.

Three different strategies have been reported in literature for the fabrication of Pt-based nanocages. The first approach relies on the overgrowth of Pt conformal shells on well-defined Pd nanocrystal seeds for the generation of Pd@Pt_{nL} (n=1–6) core-shell nanocrystals, followed by the removal of Pd cores. To this end, Xia and other groups have demonstrated the fabrication of Pt-based nanocages by templating with Pd nanocubes,[5] octahedra,[6] decahedra,[7] and icosahedra.[8,9] The second approach exploits the galvanic

replacement reaction between a Pt(II) precursor and a sacrificial template made of Ag.[10–13] In this case, Pt atoms are produced from a Pt(II) precursor at the expense of Ag atoms for their deposition onto the surface of a Ag template, leading to the formation of a nanobox and then a nanocage through the interplay of alloying and dealloying between Pt and Ag. The third approach starts with the co-reduction of Pt(II) and Pd(II) precursors to generate Pt-on-Pd bimetallic nanodendrites comprised of a Pd interior and dendritic Pt exterior.[14,15] After chemical etching of the Pd interior, Pt-Pd bimetallic hollow nanoparticles with dendritic shells are obtained.[16,17] Among these three strategies, the first one is particularly attractive as it allows for the deposition of an ultrathin, conformal shell of Pt on Pd nanocrystals with a thickness precisely controllable down to the atomic scale. It has also been demonstrated that the Pt-based nanocages with subnanometer-thick walls exhibited great catalytic performance toward ORR.[5-9] Despite the remarkable success, however, the Pt coating process involves a polyol solvent at an elevated temperature above 200 ºC. It is also rather expensive to use another scarce precious metal such as Pd as the sacrificial template.

One solution to further reduce the cost associated with Pt-based nanocages is to replace Pd with Ag as the sacrificial template. Unfortunately, it has been difficult to simply extend the standard protocol developed for the conformal deposition of Pt on Pd seeds to Ag nanocrystals due to the involvement of galvanic replacement between Ag and a Pt(II) or Pt(IV) precursor.[10-13] In this case, the Ag nanocrystal seed can be destructed to such an extent that it can no longer serve as a physical template to direct the conformal deposition of Pt. In Chapter 2–4, we have discussed the scientific basis and rules for achieving galvanic replacement-free overgrowth of Au or Pd on Ag seeds.[18–21] Our strategy is based

on the introduction of a faster parallel reaction to compete with and thereby suppress the galvanic replacement reaction. Herein, we demonstrate that the same principle can be extended to deposit conformal, ultrathin shells of Pt on the surface of Ag nanocubes for the generation of Ag@Pt core-shell nanocubes with a shell thickness as thin as three atomic layers. The facile synthesis involves the injection of H_2PtCl_6 (a precursor to elemental Pt) into an aqueous suspension of Ag nanocubes in the presence of ascorbic acid (H_2Asc), poly(vinylpyrrolidone) (PVP, a colloidal stabilizer), and NaOH at an initial pH of 11.9 under ambient conditions. Upon the removal of Ag cores with etching by a mixture of $Fe(NO_3)_3$ and HNO_3, the core-shell nanocubes can be transformed into Pt-based cubic nanocages with a wall thickness thinner than 2 nm. Upon deposition on carbon, the nanocages with a composition of $Pt_{42}Ag_{58}$ are found to exhibit enhanced catalytic activity toward ORR, with mass and specific activities of 0.30 A mg^{-1} and 0.93 mA cm^{-2}, respectively.

5.2 Experimental Section

Chemicals and Materials. Silver trifluoroacetate (CF_3COOAg, 98%), chloroplatinic acid hexahydrate ($H_2PtCl_6 \cdot 6H_2O$, 99.9+%), aqueous hydrochloric acid (HCl, 37%), sodium hydrosulfide hydrate ($NaHS \cdot xH_2O$), sodium borohydride ($NaBH_4$), H_2Asc (99%), sodium hydroxide (NaOH, 98+%), potassium tetrachloroplatinate(II) (K_2PtCl_4, 99.9+%), iron(III) nitrate nonahydrate ($Fe(NO_3)_3 \cdot 9H_2O$), nitric acid (HNO_3, 70%), and PVP with an average molecular weight of 29,000 (PVP-29) or 55,000 (PVP-55) were all acquired from Sigma-Aldrich. Ethylene glycol (EG) was purchased from J. T. Baker. All chemicals were used as received. Deionized (DI) water with a resistivity of 18.2 MΩ·cm at room temperature was

used throughout all experiments. The commercial Pt/C catalyst was obtained from Tanaka Kikinzoku Kogyo.

Synthesis of Ag Nanocubes. We synthesized the Ag nanocubes with an edge length of 38.6±1.3 nm by following the protocol developed by Xia and co-workers.[22] The nanocubes were washed with acetone and water three times, and then dispersed in water for storage and further use.

Synthesis of Ag@Pt Core-Frame and Core-Shell Nanocubes. In a standard protocol, 2 mL of aqueous PVP-29 (1 mM), 0.5 mL of aqueous H_2Asc (0.1 M), and 0.5 mL of NaOH (0.2 M) were mixed in a 23-mL glass vial under magnetic stirring, followed by the introduction of 13.4 μL of the aqueous suspension of Ag nanocubes (with a final concentration of 4.2×10^{10} particles/mL). Afterwards, a specific amount (0.01, 0.1, or 0.4 mL) of aqueous H_2PtCl_6 (0.2 mM) or K_2PtCl_4 (0.2 mM) was injected into the mixture in one shot. The mixture was kept at room temperature for another 2 h before the products were collected by centrifugation at 5500 rpm for 15 min, washed twice with water, and then dispersed in water for further use.

Selective Etching of Ag Cores from the Ag@Pt Core-Frame and Core-Shell Nanocubes. We prepare an aqueous solution by mixing $Fe(NO_3)_3$ (1 mM) with HNO_3 (3 mM) at a 1:1 volume ratio. The as-prepared Ag@Pt nanocubes were collected and dispersed in 0.1 mL of water, followed by the addition of 1 mL of the $Fe(NO_3)_3/HNO_3$ mixture and incubated at room temperature for 1 h. The final products were collected by centrifugation at 14000 rpm for 20 min, followed by washing twice with water and re-dispersed in water for further characterization.

X-ray Photoelectron Spectroscopy (XPS) Analysis of the Ag@Pt Core-Frame and Core-Shell Nanocubes. Approximately 25 μL of the as-obtained sample was drop casted on the surface of a silicon substrate and allowed to dry in air overnight. The sample was then analyzed using X-ray photoelectron spectroscopy. The Pt*4f* (65-85 eV) and Ag*3d* (360-380 eV) peaks of the sample were measured with a resolution of 0.1 eV.

Instrumentation and Characterization. We collected all the samples using a conventional centrifuge (Eppendorf 5430). The pH value was measured by FiveEasy pH Meter (Mettler Toledo, Columbus, OH). The contents of Pt and Ag were determined using an inductively coupled plasma mass spectrometer (ICP-MS, NexION 300Q, PerkinElmer, Waltham, MA). XPS was collected on a Thermo K-Alpha X-ray photoelectron spectrometer (Thermo Fisher Scientific, Waltham, MA). Transmission electron microscopy (TEM) images were taken using an HT7700 microscope (Hitachi, Tokyo, Japan) operated at 120 kV. The high angle annular dark field scanning transmission electron microscopy (HAADF-STEM) imaging and electron energy loss spectroscopy (EELS) mapping were conducted on a Hitachi HD2700 STEM operated at 200 kV and equipped with a probe aberration corrector.

Electrochemical Measurements. Firstly, 0.5 mg of the carbon-supported Pt-Ag nanocages were dispersed in a mixture of 0.8 mL of water, 0.2 mL of isopropanol, and 10 μL of 5% Nafion under ultrasonication for 1 h to produce an ink for electrochemical measurements. Next, 10 μL of the suspension was casted on a glassy carbon rotating disk electrode (RDE, Pine Research Instrumentation) with a geometric area of 0.196 cm^2, followed by drying under ambient condition at room temperature. With the same preparation procedure, the commercial Pt/C catalyst (46.6 wt%, *ca.* 2.1-nm Pt particles

supported on Ketjenblack EC-300J, Tanaka Kikinzoku Kogyo) was used as a benchmark for comparison. Electrochemical measurements were conducted using a CHI 600E potentiostat (CH Instruments). A Hydroflex hydrogen reference electrode (Gaskatel) and a Pt mesh were used as the reference and counter electrodes, respectively. All potentials were converted to values with reference to the reversible hydrogen electrode (RHE). The electrolyte (0.1 M $HClO_4$) was prepared by diluting a 70% stock solution with water. The cyclic voltammetric (CV) curves were recorded at room temperature in a N_2-saturated 0.1 M $HClO_4$ solution in the potential range of 0.08−1.1 V_{RHE} at a scanning rate of 50 mV s^{-1}. We calculated the electrochemical active surface areas (ECSA) of each catalyst based on the charges associated with the desorption of hydrogen in the region of 0.08−0.45 V_{RHE} after double-layer correction with a reference value of 210 μC cm^{-2} (for commercial Pt/C and Pt-Ag nanocages) for the desorption of a monolayer of hydrogen from Pt surface. We measured the ORR activities at room temperature in the potential range of 0.08−1.1 V_{RHE} in an O_2-saturated 0.1 M $HClO_4$ solution using the RDE method at a scanning rate of 10 mV s^{-1} (rotating speed at 1,600 rpm). The background current is measured in the potential range of 0.08−1.1 V_{RHE} by running the ORR sweep profile in an N_2-saturated 0.1 M $HClO_4$ solution at a scanning rate of 10 mV s^{-1} (rotating speed at 1,600 rpm). The ORR data were corrected by ohmic iR drop compensation and background currents. The kinetic current density (j_K) was derived from the Koutecky-Levich equation: $\frac{1}{j} = \frac{1}{j_K} + \frac{1}{j_L}$, where j is the measured current density and j_L is the diffusion-limiting current density. For the accelerated durability test, we collected CVs and ORR polarization curves after sweeping 5000 cycles in the potential range of 0.6−1.1 V_{RHE} in an O_2-saturated 0.1 M $HClO_4$ solution using the RDE method at a scanning rate of 0.1 mV s^{-1}. After the test, the particles were removed

from the electrode by sonication and then dissolved in 0.5 mL aqua regia for ICP-MS analysis.

5.3 Results and Discussion

5.3.1 Proposed Pathway for the Deposition of Pt Atoms on Ag Nanocubes

Figure 5.1 outlines a pathway proposed to account for the deposition of Pt on a Ag nanocube under ambient conditions. Because NaOH is used to adjust the initial pH of the reaction solution to the alkaline region, the hydroxide can affect the deposition of Pt atoms on Ag nanocubes in a number of different ways. First of all, the added H_2PtCl_6 is supposed to be quickly neutralized to generate $PtCl_6^{2-}$, followed by possible ligand exchange with H_2O and OH^- to generate Pt(IV) species that may include $PtCl_5(OH)^{2-}$ and $PtCl_4(OH)_2^{2-}$.[23-26] However, as confirmed by the UV-vis spectra in Figure 5.2, the Pt(IV) ions quickly formed stable complexes with the nitrogen atoms in PVP,[26] preventing them from further ligand exchange with H_2O and OH^-. On the other hand, H_2Asc was neutralized to generate ascorbate monoanion ($HAsc^-$), a strong reducing agent, for the quick production of Pt atoms through direct chemical reduction.[27] As a result, the galvanic replacement reaction would become less favorable, making the reduction of Pt(IV) by $HAsc^-$ a dominant channel for the generation of Pt atoms. Finally, any Ag^+ ions released from the Ag nanocubes due to oxidative etching can react with OH^- in the reaction solution instantaneously, resulting in the formation of Ag_2O patches on the surface of the Ag nanocubes.[27]

Because the surface free energies of the low-index facets on Ag nanocubes decrease in the order of $\gamma_{(110)} > \gamma_{(111)} > \gamma_{(100)}$ in the presence of PVP, it is anticipated that the Pt atoms derived from the chemical reduction of Pt(IV) by $HAsc^-$ should be sequentially deposited on the edges, corners, and side faces for the formation of Ag@Pt core-frame and then core-

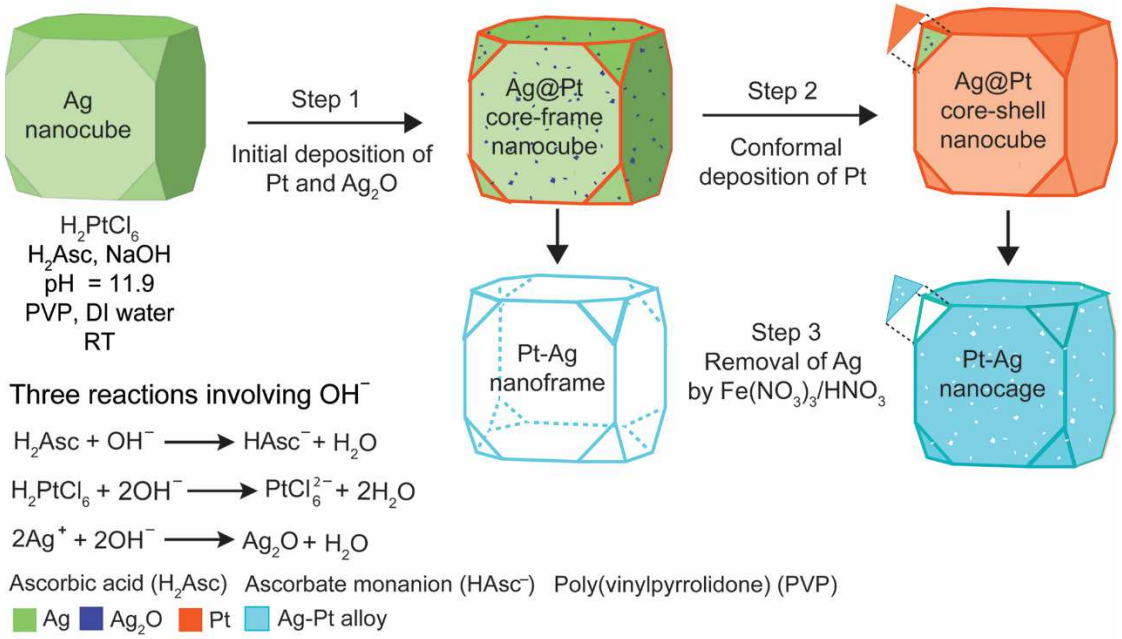

Figure 5.1. Schematic illustration of a mechanism proposed to account for the deposition of Pt on the surface of a Ag nanocube as the volume of the injected Pt(IV) precursor is increased, corresponding to Pt-Ag nanoframe and nanocage after the removal of Ag in the core.

shell nanocubes. Immediately after the injection of H_2PtCl_6 into the reaction solution, we suspect that $PtCl_6^{2-}$ derived from the neutralization by NaOH could also react with Ag nanocubes for the initial deposition of Pt atoms on the edges of Ag nanocubes at the expenses of Ag atoms located at the corners or side faces of the nanocubes. As a consequence, the Ag^+ ions released from the nanocubes can instantaneously react with the surrounding OH^- ions to generate Ag_2O patches sporadically on the corners or side faces, preventing the underlying Ag atoms from further oxidation through the galvanic replacement reaction. Afterwards, the Pt atoms should be mainly produced through the chemical reduction by $HAsc^-$, followed by their deposition onto the edges for the generation of Ag@Pt core-frame nanocubes with Ag_2O patches at the corner sites of the

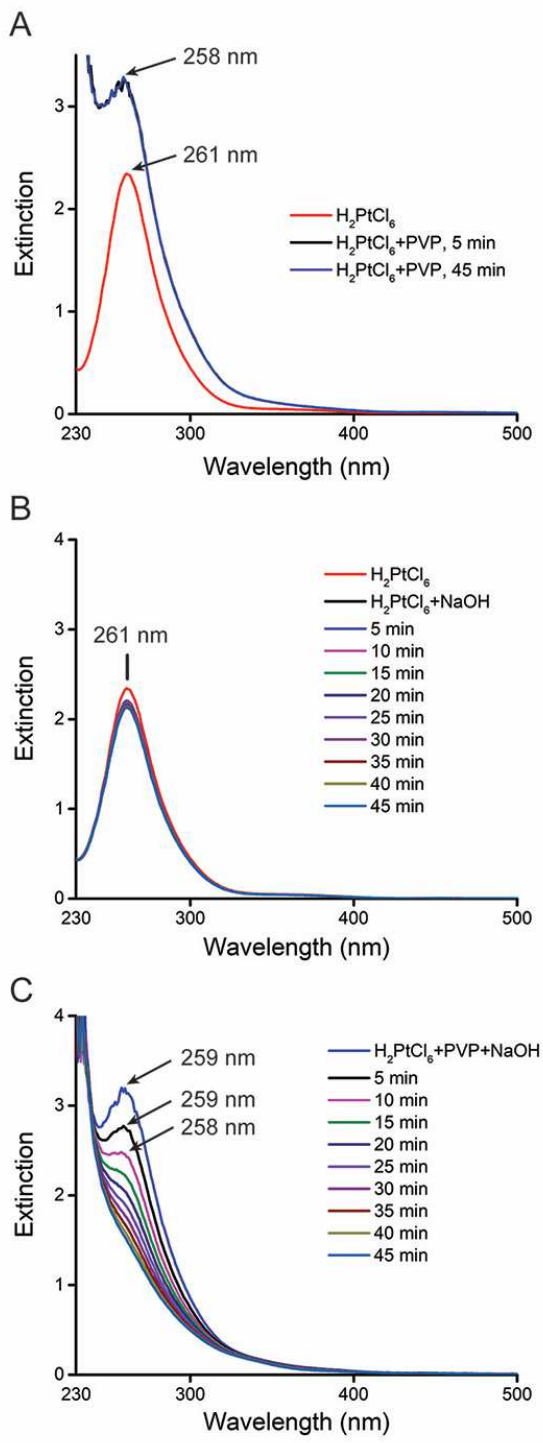

Figure 5.2. UV-vis spectra recorded from aqueous solutions of H_2PtCl_6 in the presence of (A) PVP, (B) NaOH, and (C) PVP plus NaOH. As discussed in ref. 26, the peak shift from 261 nm to 258 nm is due to the complexing between Pt(IV) and the nitrogen atoms in PVP. The addition of NaOH did not cause any change to the UV-vis peak up to 45 min, indicating a slow ligand exchange process with OH^-. In the presence of both PVP and NaOH, the Pt(IV) can be slowly reduced by the hydroxyl end groups on PVP.

nanocubes. If the synthesis is continued with a larger injection volume of aqueous H_2PtCl_6, the side faces and corners of the nanocubes can also be covered by Pt atoms through direct deposition and/or surface diffusion from the edges. Because the nucleation energy barrier on the oxide patches tends to be higher than a metal surface,[27] we argue the Pt atoms should not be directly deposited on the Ag_2O regions. Instead, they should cover the surface of oxide patches *via* surface diffusion, generating an ultrathin shell of Pt on the surface of Ag nanocubes for the generation of Ag@Pt core-shell nanocubes. When the Ag_2O patches are removed with HNO_3 to lift off the Pt deposited on these regions, followed by selective etching of the Ag cores by $Fe(NO_3)_3$, the Ag@Pt core-frame and core-shell nanocubes should evolve into Pt-Ag alloy nanoframes and nanocages, respectively.

5.3.2 Transformation of Ag Nanocubes into Ag@Pt Core-Shell Nanocubes and Pt-Ag Nanocages

In a typical synthesis, we started with the preparation of Ag nanocubes with an average edge length of 38.6±1.3 nm by following a published protocol (see Figure 2.1).[22] We then dispersed the Ag nanocubes in an aqueous solution containing H_2Asc (0.1 mM), PVP (1 mM), and NaOH (0.2 M) at an initial pH set to 11.9, followed by the one-shot injection of different volumes of aqueous H_2PtCl_6 (0.2 mM) under magnetic stirring, and finally allowed to react for 2 h at room temperature. Figure 5.3A, C, E shows the products obtained with the addition of 0.02, 0.1, and 0.4 mL of aqueous H_2PtCl_6, respectively. We found that the cubic morphology of the Ag nanocubes was preserved while their averaged edge length was slightly increased from 38.6±1.3 nm to 38.7±2.0 nm, 39.0±1.7 nm, and 39.9±1.8 nm, respectively. Our inductively coupled plasma mass spectrometry (ICP-MS) analyses indicate that the Pt contents were 2.3±0.1% and 4.7±0.2% for the two samples

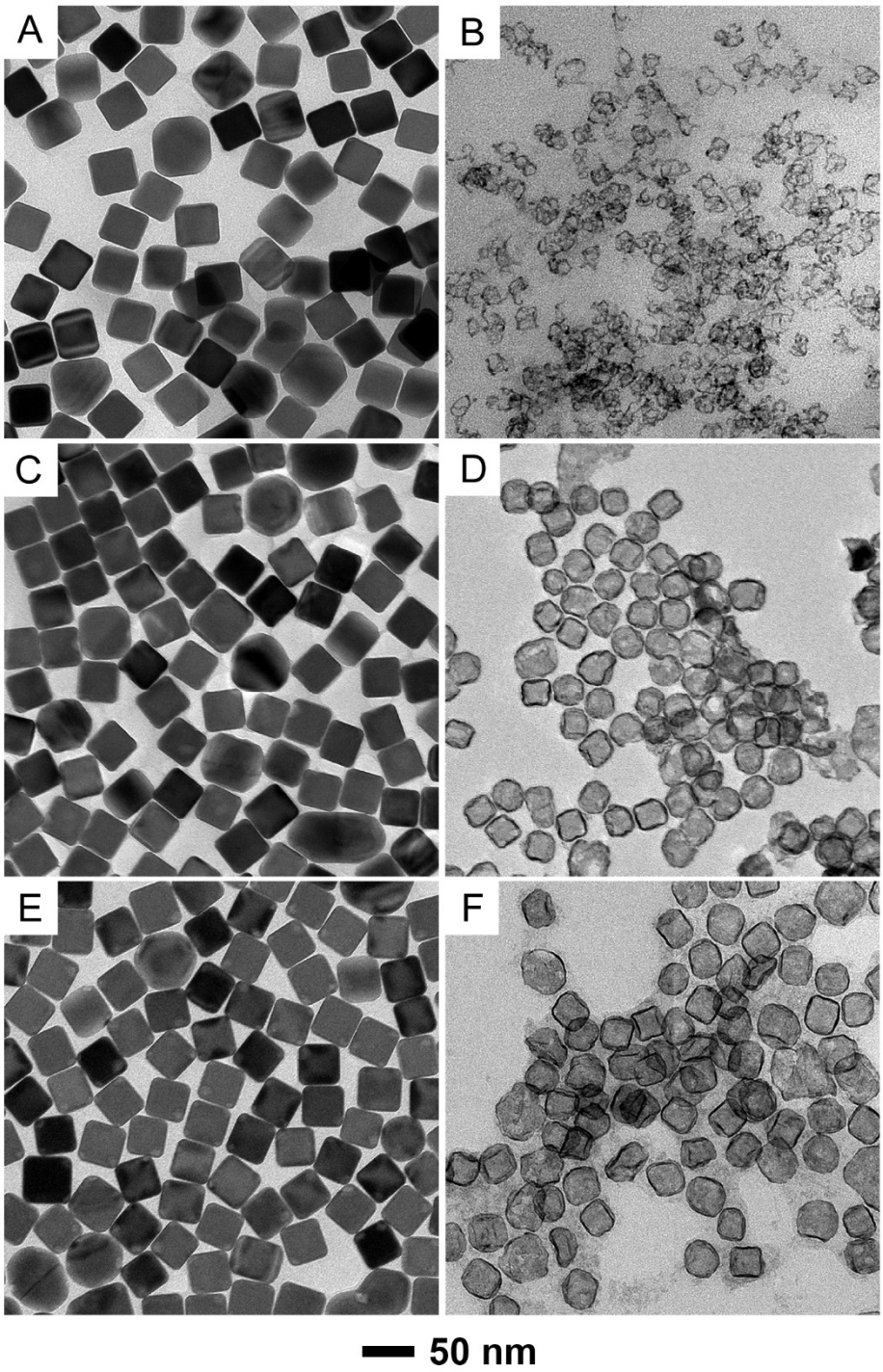

Figure 5.3. TEM images of the products before (left panel) and after (right panel) etching with an aqueous solution containing $Fe(NO_3)_3$ and HNO_3. The samples were prepared by reacting Ag nanocubes with different volumes of aqueous 0.2 mM H_2PtCl_6 in the presence of H_2Asc, PVP, and NaOH at pH=11.9: (A, B) 0.02 mL, (C, D) 0.1 mL, and (E, F) 0.4 mL, respectively.

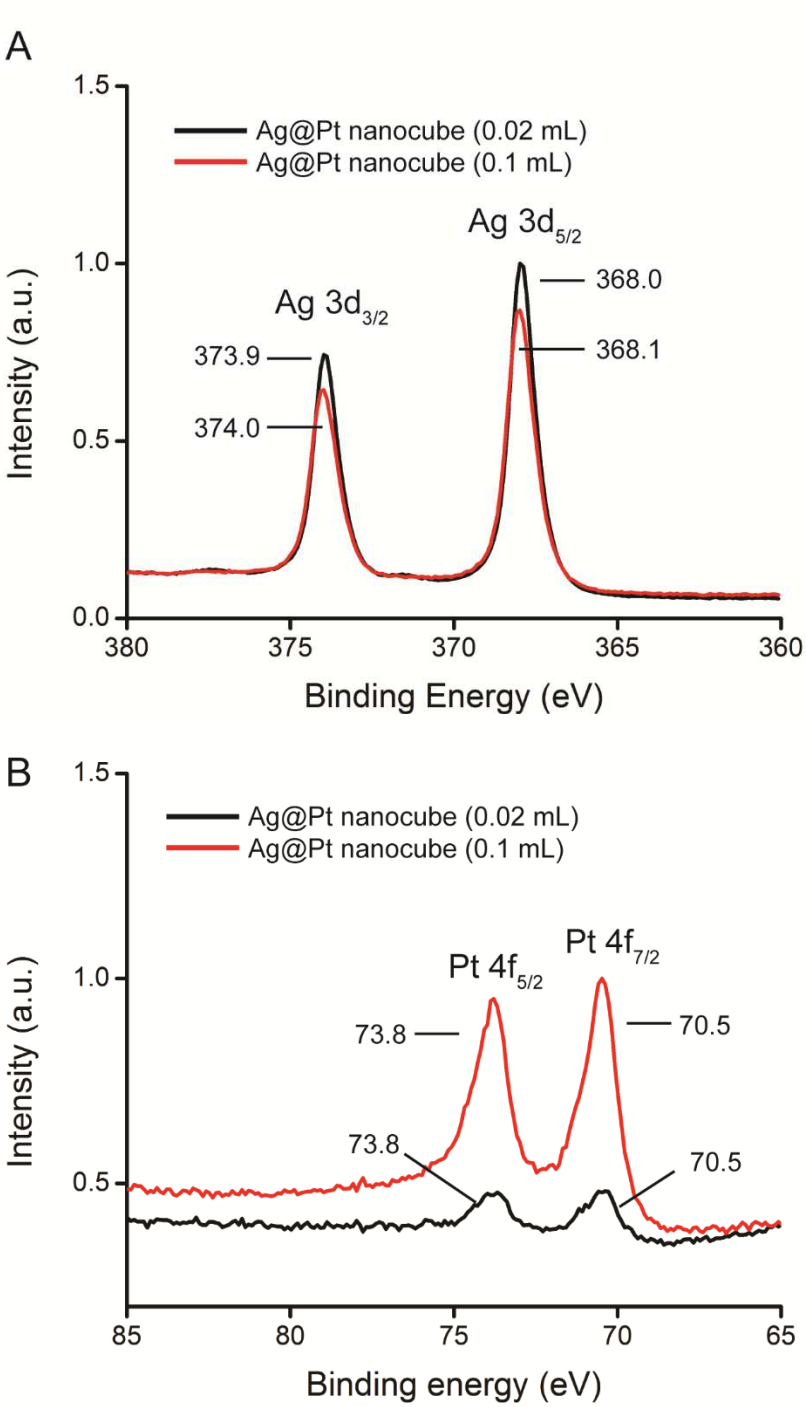

Figure 5.4. XPS of Ag@Pt nanocubes prepared with the addition of 0.02 mL and 0.1 mL, respectively, of 0.2 mM H_2PtCl_6 in the presence of H_2Asc, PVP and NaOH at pH=11.9.

corresponding to the injection volumes of 0.1 and 0.4 mL, respectively. We also used X-ray photoelectron spectroscopy (XPS) to analyze the Pt deposited on the Ag nanocubes. As shown in Figure 5.4, the amount of Pt being deposited on the Ag nanocubes was increased as the injection volume of H_2PtCl_6 solution was increased from 0.02 to 0.1 mL. To confirm the essential role of NaOH in supporting the deposition of Pt on the Ag nanocubes by suppressing the galvanic replacement reaction between Ag nanocubes and Pt(IV) precursor, we performed a control experiment by excluding NaOH while keeping all other parameters the same. As shown in Figure 5.5, we observed the formation of voids in the nanocubes, confirming the involvement of galvanic replacement reaction. Taken together, these data confirm the conformal deposition of Pt on the Ag nanocubes. By simply changing the injection volume of the Pt(IV) precursor, we can easily control the ratio of Pt to Ag in the products.

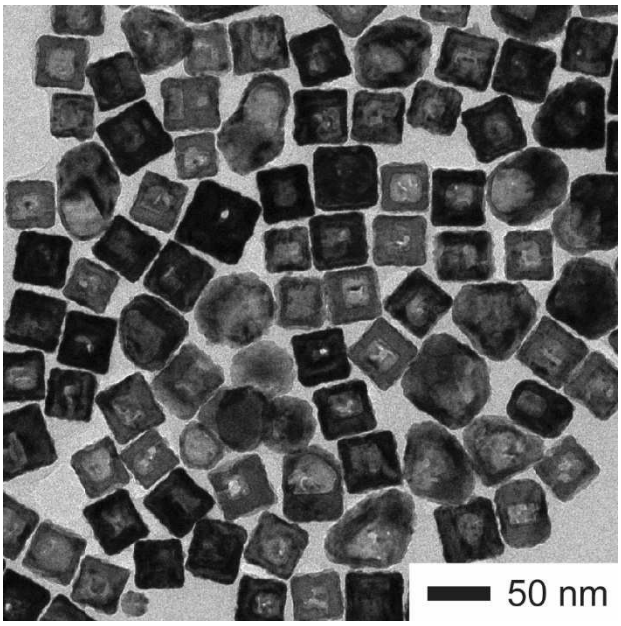

Figure 5.5. TEM image of the sample prepared by injecting 0.4 mL of aqueous H_2PtCl_6 in the presence of H_2Asc and PVP, but in the absence of NaOH.

To reveal the deposition pathway of the Pt atoms on the surface of Ag nanocubes, we used an aqueous mixture of $Fe(NO_3)_3$ (1 mM) and HNO_3 (3 mM) to selectively etch away Ag but not Pt (see experimental session for details). For the injection volume of 0.02 mL, Figure 5.3B shows the formation of broken nanoframes, indicating that the initial deposition of Pt indeed occurred on the edges of the Ag nanocubes, consistent with our findings in other systems.[27–29] We noticed that several of the core-frame nanocubes survived from the etching process and the size of a nanoframe was much smaller than that of the nanocubes shown in Figure 5.3A. It is anticipated that the Pt atoms deposited on the edges of the Ag nanocubes only generated relatively thin ridges, and as a result, the resultant nanoframes could deform and thus shrink inward due to the capillary force involved in the drying process of TEM sample prep. As the injection volume was increased from 0.02 to 0.1 mL, Figure 5.3D indicates the formation of nanocages with the presence of pores on the side surfaces. The average edge length of the nanocages was 27.2±3.8 nm, *ca.* 30% smaller than that of the original nanocubes shown in Figure 5.3C. Also, the cubic shape was not well preserved due to the involvement of ultrathin walls for the nanocages. With a further increase of injection volume to 0.4 mL, Figure 5.3F shows the formation of well-defined nanocages with small pores on the side faces. Again, the average edge length was only 31.1±3.3 nm, roughly 22% smaller than that of the original nanocubes shown in Figure 5.3E. When we increased the injection volume to 0.8 mL, we obtained nanocages with an average edge length of 33.0±3.9 nm, as shown in Figure 5.6. However, due to the involvement of ultrathin walls that are susceptible to deformation during sample prep and/or upon exposure to an electron beam, we were unable to resolve the exact wall thickness of the nanocages by TEM.

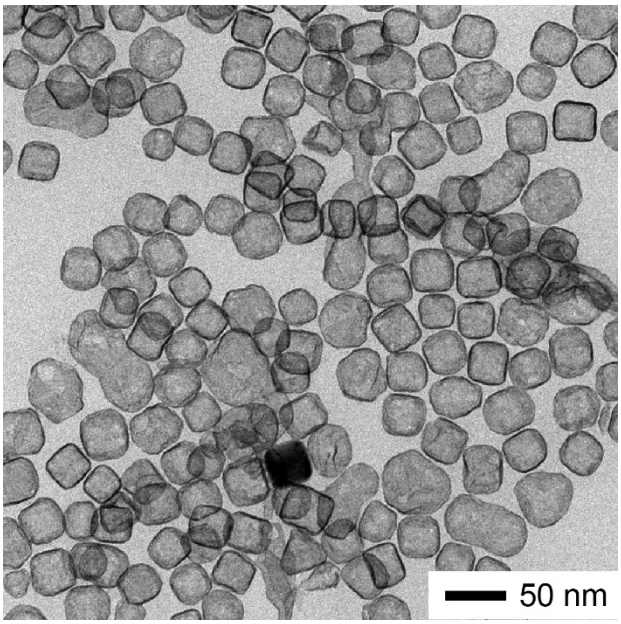

Figure 5.6. TEM image of Pt-Ag nanocages prepared by reacting Ag nanocubes with 0.8 mL of aqueous H_2PtCl_6 in the presence of H_2Asc, PVP, and NaOH at pH=11.9, followed by etching with an aqueous solution containing $Fe(NO_3)_3$ and HNO_3.

We also performed another control experiment to replace the Pt(IV) precursor based on H_2PtCl_6 with a Pt(II) precursor based on K_2PtCl_4, while keeping all other experimental parameters unaltered. At an injection volume of 0.4 mL, Figure 5.7, A and B, shows the as-obtained products before and after treatment with the $Fe(NO_3)_3/HNO_3$ etchant. The structures are similar to those shown in Figure 5.3, E and F. Collectively, our results support the aforementioned argument that the initial deposition of Pt atoms derived from the reduction of Pt(II) or Pt(IV) precursor would start from the edges of the Ag nanocubes, followed by deposition on the corners and side faces, sequentially transforming the Ag nanocubes into Ag@Pt core-frame and core-shell nanocubes.

It is worth pointing out that the HNO_3 in the etching solution could serve as an acid to selectively dissolve the Ag_2O patches located on the surface of the nanocubes, leading

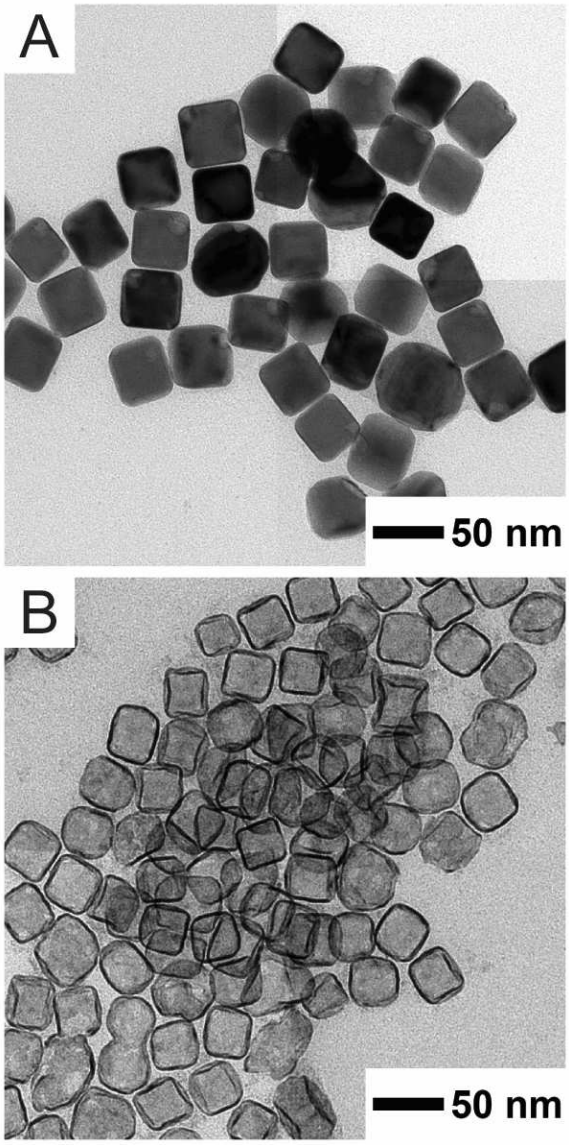

Figure 5.7. TEM images of Ag@Pt core-shell nanocubes (A) before and (B) after etching with $Fe(NO_3)_3/HNO_3$. The sample was prepared by reacting Ag nanocubes with 0.4 mL of aqueous K_2PtCl_4 (0.2 mM) in the presence of H_2Asc, PVP, and NaOH at pH=11.9.

to the transformation of Ag@Pt core-frame or core-shell nanocubes into nanoframes or nanoboxes after the further removal of Ag cores by $Fe(NO_3)_3$. To support our argument that the Ag_2O patches were removed through an acid-base neutralization reaction, we performed a control experiment to etch the as-obtained Ag@Pt nanocubes prepared with an injection volume of 0.4 mL with 3% aqueous H_2O_2 etching. As shown in Figure 5.8A,

there was no change to the morphology. In comparison, when the sample was treated with a weak acid such as H_2Asc and then aqueous H_2O_2, as shown in Figure 5.8B, we obtained

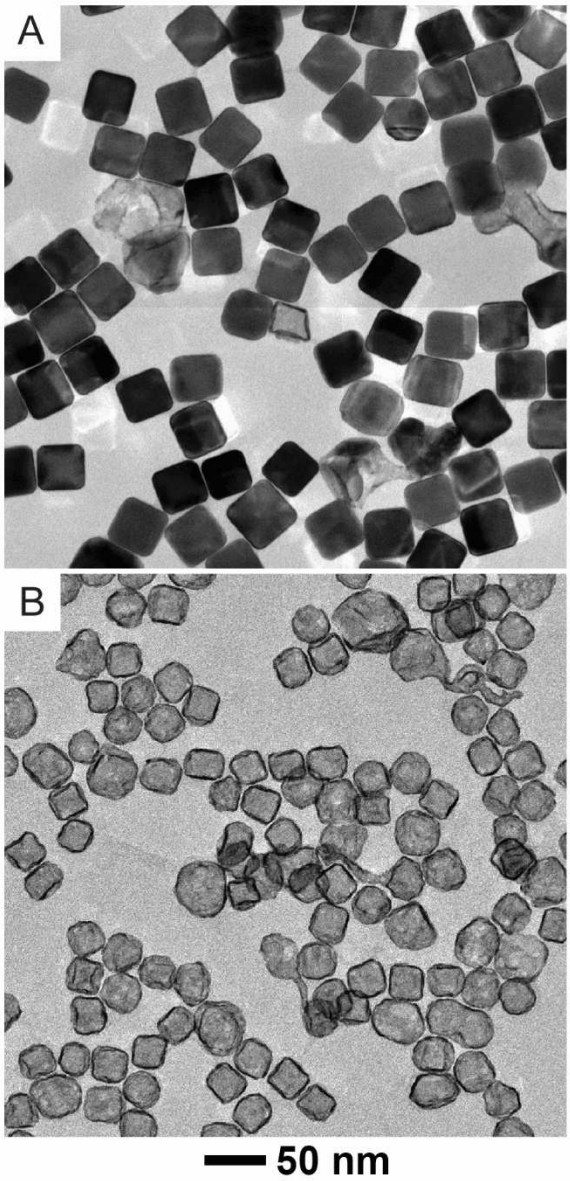

Figure 5.8. TEM images of Ag@Pt core-shell nanocubes after treatment with (A) 3% aqueous H_2O_2 and (B) H_2Asc/PVP and then 3% aqueous H_2O_2. The samples were prepared by reacting Ag nanocubes with 0.4 mL of aqueous H_2PtCl_6 (0.2 mM) in the presence of H_2Asc, PVP, and NaOH at pH=11.9.

nanocages again after the removal of Ag cores. Taken together, our results confirm the formation of Ag_2O, a base that could be readily dissolved by a protonic acid. We believe that any protonic acid can be able to dissolve the Ag_2O patches as long as it does not compromise the structural integrity of the Pt overlayers on the side faces and thus compromise the etching of Ag by $Fe(NO_3)_3$.

We also used aberration-corrected high-angle annular dark-field scanning TEM (HAADF-STEM) to characterize one of the Ag@Pt core-shell nanocubes prepared with the injection of 0.4 mL of aqueous H_2PtCl_6 (see Figure 5.3E). As shown in Figure 5.9A, Pt atoms could be readily resolved on the surface of the Ag nanocube due to their large difference in atomic number. It is interesting to acknowledge the presence of a shallow hole at the top right corner of the nanocube, suggesting the loss of Ag atoms due to galvanic replacement in the initial stage. Figure 5.9B reveals the arrangement of Ag and Pt atoms, from which we identified that 3–4 atomic layers of Pt atoms (with a thickness of about 0.6 nm) were deposited on the surface of the Ag nanocube, consistent with our aforementioned estimate based on the increase in edge length from 38.6±1.3 nm to 39.9±1.8 nm. We also analyzed the elemental distributions of Ag and Pt using STEM-electron energy loss spectroscopy (EELS). Figure 5.9C gives the STEM-EELS mapping of Ag, suggesting some loss of Ag at one of the corners of the nanocube. Figure 5.9D shows the STEM-EELS mapping of Pt, indicating the deposition of Pt on the edges, corners, and side faces of the nanocube. Taken together, this set of data confirms the formation of $Ag@Pt_{3L}$ core-shell nanocubes when the sample was prepared with 0.4 mL of 0.2 mM aqueous H_2PtCl_6.

We further used high-resolution (HR) TEM to characterize the detailed morphology and elemental composition of one of the Pt-Ag nanocages shown in Figure 5.3F.

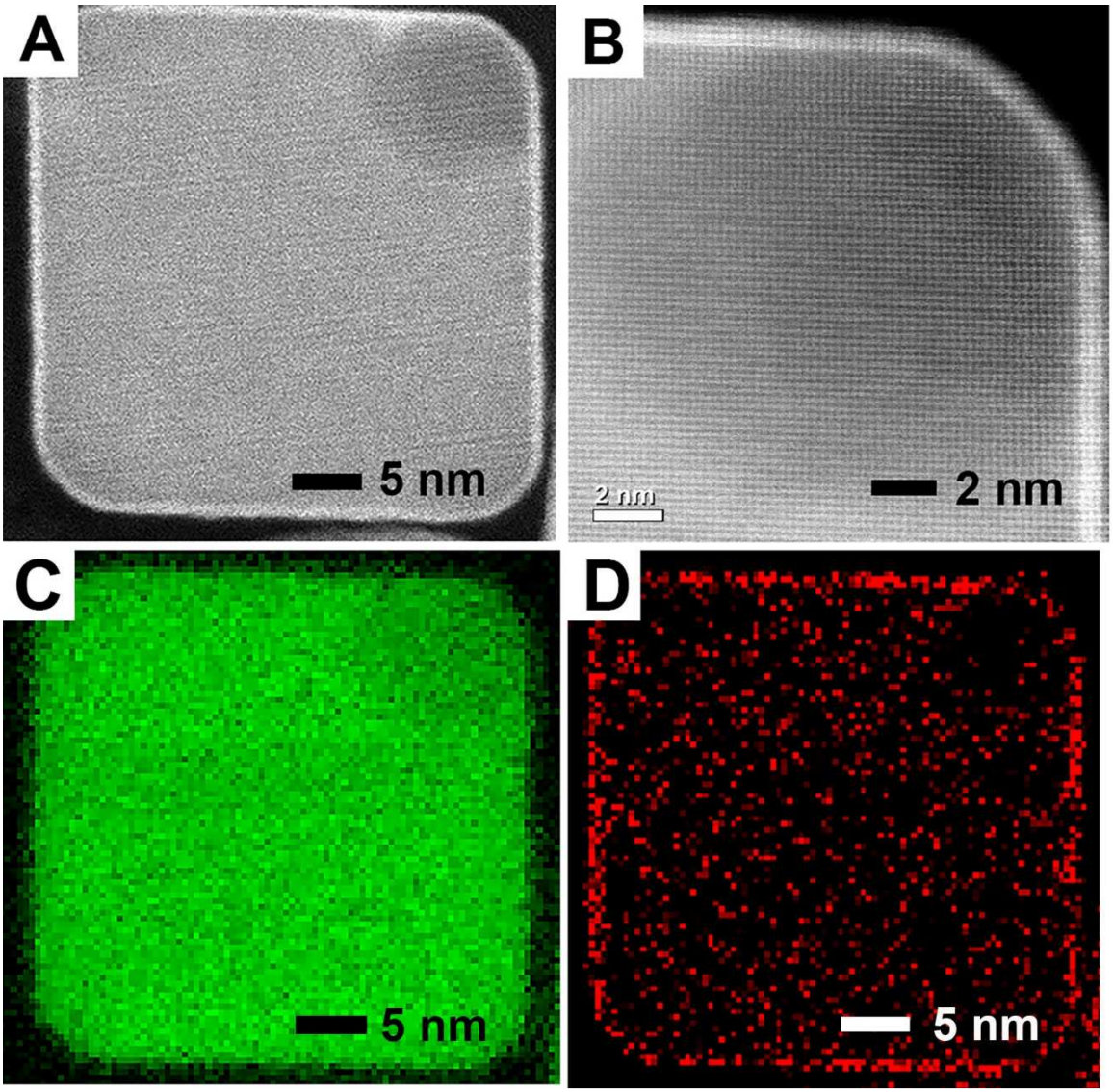

Figure 5.9. (A, B) HAADF-STEM images, at two different magnifications, of a Ag@Pt nanocube. The sample was prepared by reacting Ag nanocubes with 0.4 mL of aqueous H_2PtCl_6 (0.2 mM) in the presence of H_2Asc, PVP, and NaOH at pH=11.9 (see Figure 5.3E). (C, D) STEM-EELS mapping of Ag (green) and Pt (red) for a Ag@Pt nanocube shown in (A).

Figure 5.10A gives a HAADF-STEM image of the Pt-Ag nanocages, from which we could spot the small openings across the side faces. At atomic resolution, as shown in Figure 5.10B, we could only resolve the lattice fringes in some areas at atomic resolution because the ultrathin and fragile nanocages tended to lose their original shapes after washing and

centrifugation steps during the TEM sample preparation process. It is worth mentioning that the inter-diffusion and alloying process between Pt and Ag could result in the retention of some Ag atoms during the etching process, and as a result, Ag@Pt core-shell nanocubes with a shell thickness of 0.6 nm were transformed into Pt-Ag nanocages with a thickness less than 2 nm. We analyzed the elemental distributions of Ag and Pt for an individual nanocage using energy dispersive X-ray spectroscopy (EDS). Figure 5.10, C-F, shows the STEM image of a nanocage, and the corresponding EDS mapping results of Ag and Pt, respectively. Based on the ICP-MS measurements, the nanocages can be assigned with a composition of $Pt_{42}Ag_{58}$, corresponding to a Pt and Ag atomic ratio of roughly 1.0.

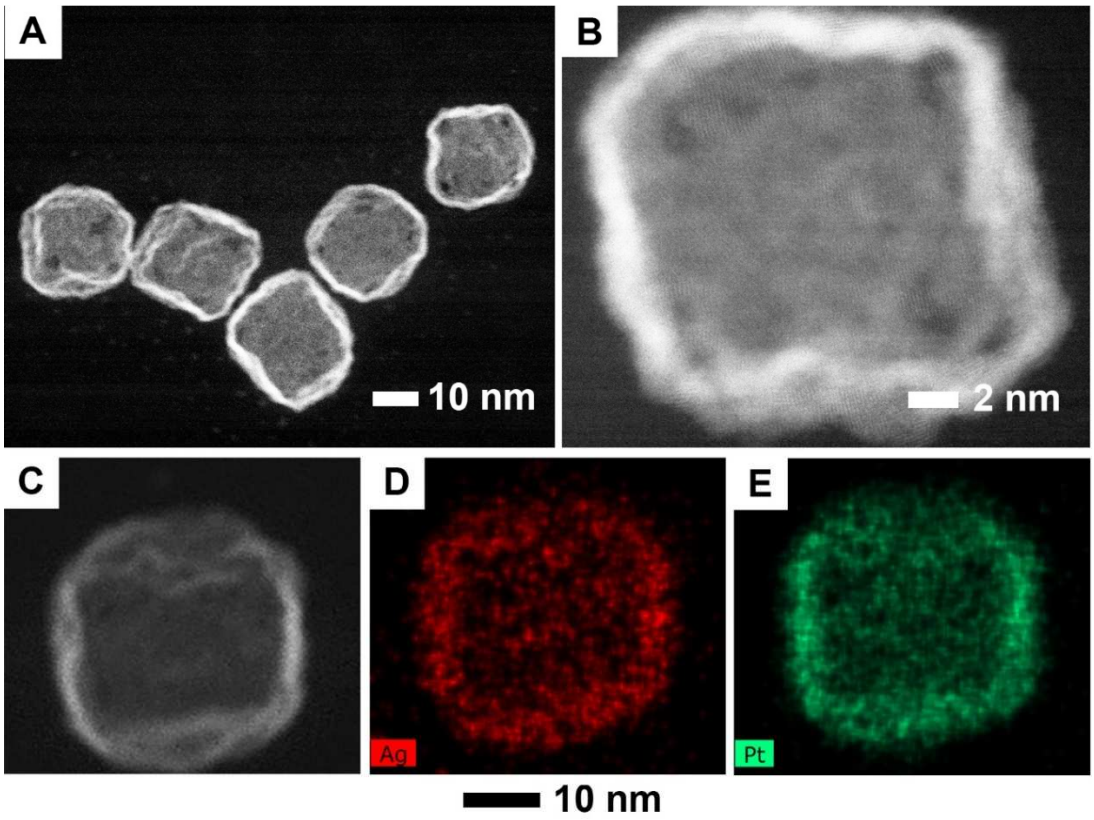

Figure 5.10. (A) HAADF-STEM image of Pt-Ag nanocages shown in Figure 5.3F. (B) Atomic resolution HAADF-STEM image of a nanocage and (C-E) STEM image and EELS mapping of Pt (green) and Ag (red) for an individual nanocage shown in (C).

5.3.3 Catalytic Activities of Pt-Ag Nanocages toward Oxygen Reduction Reaction

We evaluated the catalytic activities of $Pt_{42}Ag_{58}$ nanocages toward ORR by benchmarking against a commercial Pt/C catalyst (46.6 wt%, 2.1-nm Pt particles supported on Ketjenblack EC-300J). Figure 5.11A shows the cyclic voltammetry (CV) curves of the two catalysts in a N_2-saturated 0.1 M $HClO_4$ solution in the potential range of 0.08–1.10 V_{RHE} at a scanning rate of 50 mV s^{-1}. The specific electrochemical active surface area (ECSA) of each catalyst was calculated from the charges associated with the desorption of hydrogen in the region of 0.08–0.45 V_{RHE} by assuming the hydrogen monolayer desorption from Pt surfaces as 210 μC cm^{-2} for both catalysts. The ECSAs of the $Pt_{42}Ag_{58}$ nanocages and Pt/C are 32.16 m^2 g^{-1} and 52.30 m^2 g^{-1}, respectively. The lower specific ECSA of the $Pt_{42}Ag_{58}$ nanocages can be attributed to a number of factors, including the alloy composition, the intrinsically lower utilization efficiency of atoms for a 2D structure (*i.e.*, the side faces of the nanocages) relative to pseudo-spherical particles in Pt/C, and the aggregation of nanocages on the carbon. Figure 5.11B shows the positive-going ORR polarization curves of both catalysts when we measured the ORR current densities of the catalysts in an O_2-saturated aqueous $HClO_4$ solution (0.1 M) in the potential range of 0.08–1.10 V_{RHE} at a scanning rate of 10 mV s^{-1}. The kinetic currents of a polarization curve were then computed using the Koutecky-Levich equation and normalized to the ECSA and Pt mass of the catalyst to obtain the mass activity ($j_{k,mass}$) and specific activity ($j_{k,specific}$).[30] As shown in Figure 5.11, C and D, the $j_{k,mass}$ and $j_{k,specific}$ of the $Pt_{42}Ag_{58}$ nanocages were 0.30 A mg^{-1} and 0.93 mA cm^{-2}, respectively, at 0.9 V_{RHE}, which are 1.6 and 2.5 times greater than those of the Pt/C catalyst at 0.18 A mg^{-1} and 0.37 mA/cm^2. After 5000 cycles of

accelerated durability test, the composition of the Pt-Ag nanocages changed to $Pt_{89}Ag_{11}$ because of the

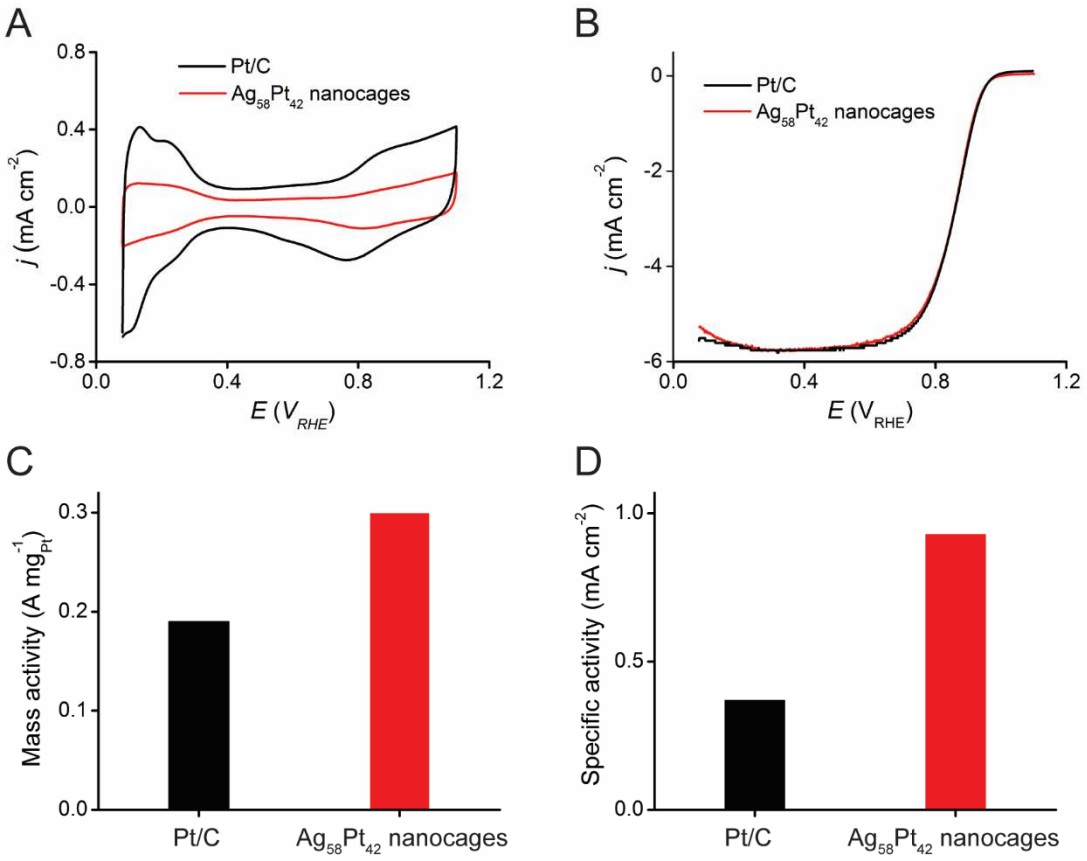

Figure 5.11. (A) CV curves recorded from $Pt_{42}Ag_{58}$ nanocages and a commercial Pt/C catalyst. (B) Positive-going ORR polarization curves of $Pt_{42}Ag_{58}$ nanocages and a commercial Pt/C catalyst. The currents were normalized to the geometric area of the rotating disk electrode. (C) Mass activity and (D) specific activities of $Pt_{42}Ag_{58}$/C nanocages and a commercial Pt/C catalyst measured at 0.9 V_{RHE}.

Selective dissolution of Ag during the potential cycling. As a result, both the mass activity and specific activity were decreased by 37% and 33%, respectively, while the specific ECSA was only reduced by 6.5%. Such composition-dependent activities of the Pt-Ag nanocages are consist with those of Pt-Ag alloy nanocages prepared through a galvanic replacement reaction.[13] Our results also support the argument that the composition of Pt-Ag bimetallic nanocages plays an essential role in affecting the O-O bond breaking

energetics, and ultimately the ORR activities. As shown in Figure 5.12, the morphology of the Pt-Ag nanocages remained the same before and after the durability test while their average edge length was reduced from 28.3±2.7 nm to 23.8±2.5 nm.

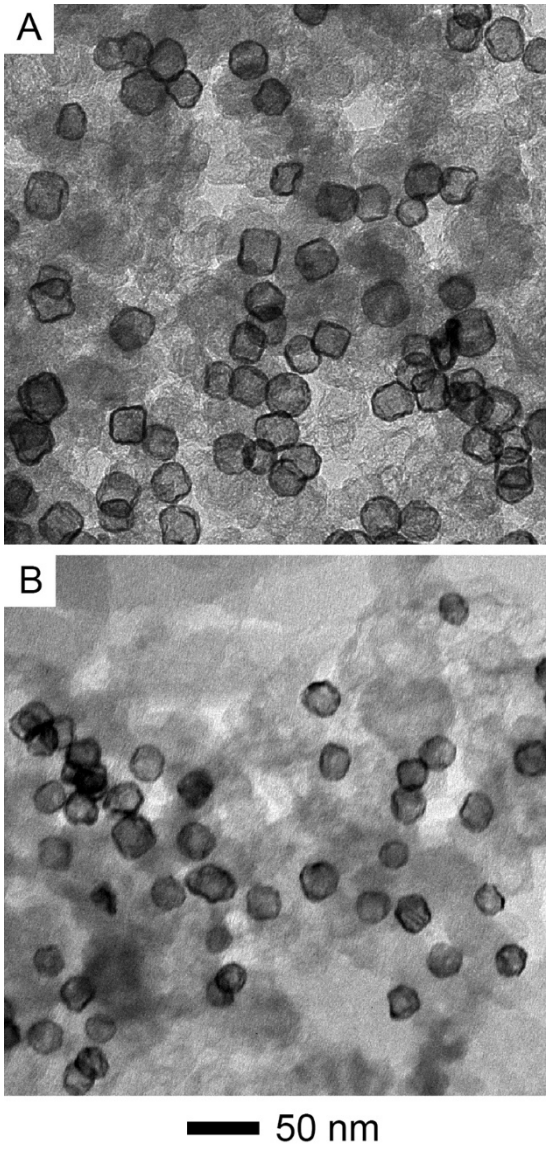

Figure 5.12. TEM images of Pt-Ag nanocages supported on carbon (A) before and (B) after the accelerated durability test.

5.4 Conclusions

In summary, we have demonstrated a facile and robust route to the fabrication of Pt-Ag nanocages with a wall thickness less than 2 nm using Ag nanocubes as the template. Our success relies on the establishment of a protocol for galvanic-free deposition of Pt on the surface of Ag nanocubes for the generation of Ag@Pt core-shell nanocubes with a shell thickness of three-atomic layers or *ca.* 0.6 nm. The synthetic protocol includes the one-shot injection of the H_2PtCl_6 precursor into an aqueous suspension of Ag nanocubes containing H_2Asc, NaOH, and PVP at an initial pH of 11.9. We discover that the galvanic replacement between Ag nanocubes and H_2PtCl_6 was effectively retarded due to the speciation of the added $PtCl_6^{2-}$ to $PtCl_5(OH)^{2-}$ and $PtCl_4(OH)_2^{2-}$ with increasingly lower reduction potentials than $PtCl_6^{2-}$. In turn, these newly formed Pt(IV) species would be reduced by $HAsc^-$ for the generation of Pt atoms, followed by their conformal deposition on the edges and then corners and side faces of Ag nanocubes in the layer-by-layer manner. After the removal of Ag cores using a wet etchant based on $Fe(NO_3)_3/HNO_3$, the core-shell nanocubes are transformed into Pt-Ag alloy nanocages with an ultrathin wall thickness as thin as 2 nm. When the resultant nanocages with a composition of $Pt_{42}Ag_{58}$ are deposited on carbon and subjected to catalytic test toward ORR, we obtain mass and specific activities of 0.30 A mg^{-1} and 0.93 mA cm^{-2}, which could be further improved by optimizing the wall thickness and elemental composition of the nanocages.

5.5 Notes to Chapter 5

Part of this chapter is adapted from the paper "Pt-Ag Cubic Nanocages with Wall Thickness Less Than 2 nm and Their Enhanced Catalytic Activity toward Oxygen Reduction" published in *Nanoscale*.[31]

5.6 References

(1) Zalc, J. M.; Sokolovskii, V.; Löffler, D. G. Are Noble Metal-Based Water–Gas Shift Catalysts Practical for Automotive Fuel Processing? *J. Catal.* **2002**, *206*, 169–171.

(2) Tian, N.; Zhou, Z.-Y.; Sun, S.-G.; Ding, Y.; Wang, Z. L. Synthesis of Tetrahexahedral Platinum Nanocrystals with High-Index Facets and High Electro-Oxidation Activity. *Science* **2007**, *316*, 732–735.

(3) Brandon, N. P.; Skinner, S.; Steele, B. C. H. Recent Advances in Materials for Fuel Cells. *Annu. Rev. Mater. Res.* **2003**, *33*, 183–213.

(4) Marković, M. N.; Ross, P. N. Surface Science Studies of Model Fuel Cell Electrocatalysts. *Surf. Sci. Rep.* **2002**, *45*, 117–229.

(5) Zhang, L.; Roling, L. T.; Wang, X.; Vara, M.; Chi, M.; Liu, J.; Choi, S.-I.; Park, J.; Herron, J. A.; Xie, Z.; Mavrikakis, M.; Xia, Y. Platinum-Based Nanocages with Subnanometer-Thick Walls and Well-Defined, Controllable Facets. *Science.* **2015**, *349*, 412–416.

(6) Jiang, M.; Lim, B.; Tao, J.; Camargo, P. H. C.; Ma, C.; Zhu, Y.; Xia, Y.; Xia, Y. Epitaxial Overgrowth of Platinum on Palladium Nanocrystals. *Nanoscale* **2010**, *2*, 2406-2411.

(7) Wang, X.; Vara, M.; Luo, M.; Huang, H.; Ruditskiy, A.; Park, J.; Bao, S.; Liu, J.; Howe, J.; Chi, M.; Xie, Z.; Xia, Y. Pd@Pt Core–Shell Concave Decahedra: A Class of Catalysts for the Oxygen Reduction Reaction with Enhanced Activity and Durability. *J. Am. Chem. Soc.* **2015**, *137*, 15036–15042.

(8) Wang, X.; Figueroa-Cosme, L.; Yang, X.; Luo, M.; Liu, J.; Xie, Z.; Xia, Y. Pt-Based Icosahedral Nanocages: Using a Combination of {111} Facets, Twin Defects, and Ultrathin Walls to Greatly Enhance Their Activity toward Oxygen Reduction. *Nano Lett.* **2016**, *16*, 1467–1471.

(9) He, D. S.; He, D.; Wang, J.; Lin, Y.; Yin, P.; Hong, X.; Wu, Y.; Li, Y. Ultrathin Icosahedral Pt-Enriched Nanocage with Excellent Oxygen Reduction Reaction Activity. *J. Am. Chem. Soc.* **2016**, *138*, 1494–1497.

(10) Chen, J.; Wiley, B.; McLellan, J.; Xiong, Y.; Li, Z. Y.; Xia, Y. Optical Properties of Pd-Ag and Pt-Ag Nanoboxes Synthesized via Galvanic Replacement Reactions. *Nano Lett.* **2005**, *5*, 2058–2062.

(11) Peng, Z.; Wu, J.; Yang, H. Synthesis and Oxygen Reduction Electrocatalytic Property of Platinum Hollow and Platinum-on-Silver Nanoparticles. *Chem. Mater.* **2010**, *22*, 1098–1106.

(12) Zhang, W.; Yang, J.; Lu, X. Tailoring Galvanic Replacement Reaction for the Preparation of Pt/Ag Bimetallic Hollow Nanostructures with Controlled Number of Voids. *ACS Nano* **2012**, *6*, 7397–7405.

(13) Yang, X.; Roling, L. T.; Vara, M.; Elnabawy, A. O.; Zhao, M.; Hood, Z. D.; Bao, S.; Mavrikakis, M.; Xia, Y. Synthesis and Characterization of Pt-Ag Alloy Nanocages with Enhanced Activity and Durability toward Oxygen Reduction. *Nano Lett.* **2016**, *16*, 6644–6649.

(14) Wang, L.; Yamauchi, Y. Block Copolymer Mediated Synthesis of Dendritic Platinum Nanoparticles. *J. Am. Chem. Soc.* **2009**, *131*, 9152–9153.

(15) Wang, L.; Yamauchi, Y. Autoprogrammed Synthesis of Triple-Layered Au@Pd@Pt Core-Shell Nanoparticles Consisting of a Au@Pd Bimetallic Core and Nanoporous Pt Shell. *J. Am. Chem. Soc.* **2010**, *132*, 13636–13638.

(16) Wang, L.; Nemoto, Y.; Yamauchi, Y. Direct Synthesis of Spatially-Controlled Pt-on-Pd Bimetallic Nanodendrites with Superior Electrocatalytic Activity. *J. Am. Chem. Soc.* **2011**, *133*, 9674–9677.

(17) Wang, L.; Yamauchi, Y. Metallic Nanocages: Synthesis of Bimetallic Pt–Pd Hollow Nanoparticles with Dendritic Shells by Selective Chemical Etching. *J. Am. Chem. Soc.* **2013**, *135*, 16762–16765.

(18) Wu, Y.; Sun, X.; Yang, Y.; Li, J.; Zhang, Y.; Qin, D. Enriching Silver Nanocrystals with a Second Noble Metal. *Acc. Chem. Res.* **2017**, *50*, 1774-1784.

(19) Yang, Y.; Liu, J.; Fu, Z. W.; Qin, D. Galvanic Replacement-Free Deposition of Au on Ag for Core-Shell Nanocubes with Enhanced Chemical Stability and SERS Activity. *J. Am. Chem. Soc.* **2014**, *136*, 8153–8156.

(20) Li, J.; Liu, J.; Yang, Y.; Qin, D. Bifunctional Ag@Pd-Ag Nanocubes for Highly Sensitive Monitoring of Catalytic Reactions by Surface-Enhanced Raman Spectroscopy. *J. Am. Chem. Soc.* **2015**, *137*, 7039–7042.

(21) Sun, X.; Qin, D. Co-Titration of $AgNO_3$ and $HAuCl_4$: A New Route to the Synthesis of Ag@Ag–Au Core–frame Nanocubes with Enhanced Plasmonic and Catalytic Properties. *J. Mater. Chem. C* **2015**, *3*, 11833–11841.

(22) Zhang, Q.; Li, W.; Wen, L. P.; Chen, J.; Xia, Y. Facile Synthesis of Ag Nanocubes of 30 to 70 nm in Edge Length with CF_3COOAg as a Precursor. *Chem. Eur. J.* **2010**, *16*, 10234–10239.

(23) Hubbard, A. T.; Anson, F. C. Linear Potential Sweep Voltammetry in Thin Layers

of Solution. *Anal. Chem.* **1966**, *38*, 58–61.

(24) Shelimov, B.; Lambert, J.; Che, M.; Didillon, B. Application of NMR to Interfacial Coordination Chemistry: A ^{195}Pt NMR Study of the Interaction of Hexachloroplatinic Acid Aqueous Solutions with Alumina. *J. Am. Chem. Soc.* **1999**, *121*, 545–556.

(25) Straney, P. J.; Marbella, L. E.; Andolina, C. M.; Nuhfer, N. T.; Millstone, J. E. Decoupling Mechanisms of Platinum Deposition on Colloidal Gold Nanoparticle Substrates. *J. Am. Chem. Soc.* **2014**, *136*, 7873–7876.

(26) Teranishi, T.; Hosoe, M.; Tanaka, T.; Miyake, M. Size Control of Monodispersed Pt Nanoparticles and Their 2D Organization by Electrophoretic Deposition. *J. Phys. Chem. B*, **1999**, *103*, 3818–3827.

(27) Sun, X.; Yang, Y.; Zhang, Z.; Qin, D. Mechanistic Roles of Hydroxide in Controlling the Deposition of Gold on Colloidal Silver Nanocrystals. *Chem. Mater.* **2017**, *29*, 4014–4021.

(28) Li, J.; Sun, X.; Qin, D. Ag-Enriched Ag-Pd Bimetallic Nanoframes and Their Catalytic Properties. *ChemNanoMat* **2016**, *2*, 494–499.

(29) Zhang, Y.; Liu, J.; Ahn, J.; Xiao, T.-H.; Li, Z.-Y.; Qin, D. Observing the Overgrowth of a Second Metal on Silver Cubic Seeds in Solution by Surface-Enhanced Raman Scattering. *ACS Nano* **2017**, *11* (5), 5080–5086.

(30) Lim, B.; Jiang, M.; Camargo, P. H.; Cho, E. C.; Tao, J.; Lu, X.; Zhu, Y.; Xia, Y. Pd-Pt bimetallic nanodendrites with high activity for oxygen reduction. *Science*, **2009**, *324*, 1302−1305.

(31) Sun, X.; Yang, X.; Zhang, Y.; Ding, Y.; Su, D.; Qin, D. Pt-Ag Cubic Nanocages with Wall Thickness Less Than 2 nm and Their Enhanced Catalytic Activity toward Oxygen Reduction. *Nanoscale* **2017**, *9*, 15107-15114.

CHAPTER 6. CONCLUSIONS AND FUTURE DIRECTIONS

6.1 Conclusions

This dissertation documents the development of two strategies to deposit a second metal M (M: Au, Pd, or Pt) on Ag nanocrystals for the fabrication of Ag@Ag-M core-frame, Ag@M core-shell bimetallic nanocrystals, and their derivatives. A typical synthesis involves the titration of M^{n+} (a precursor to M) ions into an aqueous suspension containing Ag nanocubes, ascorbic acid (H_2Asc), and poly(vinylpyrrolidone) (PVP) under ambient conditions. Specifically, when Ag nanocrystals are mixed with a salt precursor to the second metal in the presence of a reducing agent, the added precursor can be reduced by both the Ag seeds (*via* galvanic replacement at a rate of R_{gal}) and reducing agent (*via* chemical reduction at a rate of R_{red}). Under $R_{red} > R_{gal}$, the precursor will be primarily reduced by the reducing agent instead of participating in the galvanic replacement. If self-nucleation is eliminated by titrating the precursor in a dropwise fashion, the metal atoms derived from the chemical reduction can be directed to nucleate from the surface of the Ag seeds, generating bimetallic nanocrystals with a core-frame or core-shell structure.

The first approach involves the co-titration of aqueous Ag^+ and M^{n+} ions into an aqueous mixture of Ag nanocubes, H_2Asc, and PVP at a pH around 3.2. When the added Ag^+ ions are able to push the galvanic replacement backward, R_{gal} can be reduced to attain $R_{red} > R_{gal}$. Because PVP binds more strongly to the {100} facets on Ag nanocubes, the specific surface free energies of the low-index facets on Ag nanocubes decrease in the order of $\gamma_{(110)} > \gamma_{(111)} > \gamma_{(100)}$. As such, the Ag and M atoms derived from chemical co-reduction by H_2Asc are initially deposited on the edges, followed by sequential deposition on the

corners and side faces, respectively. Upon the selective removal of Ag, Ag-M alloy nanoframes with different ridge thicknesses are obtained. We performed the proof-of-concept experiments by co-titrating $AgNO_3$ and $HAuCl_4$ into the suspension of Ag nanocubes in the presence of H_2Asc and PVP for the fabrication of Ag@Ag-Au core-frame nanocubes. When the molar ratio of $AgNO_3$ to $HAuCl_4$ is equal to or larger than three, we confirmed that galvanic replacement reaction between Ag nanocubes and $HAuCl_4$ was completely inhibited. In this case, both precursors were co-reduced by H_2Asc for the generation of Au and Ag atoms, followed by their selective deposition on the edges, corners, and side faces of the nanocubes in a seeded growth manner. Additionally, by monitoring the amount of Au and Ag deposited onto the nanocubes using inductively coupled plasmon mass spectrometry (ICP-MS), we discovered that the added precursors were completely reduced to atoms for their deposition onto the nanocubes during the transformation of Ag nanocubes into Ag@Ag-Au nanocubes. Hence, the co-titration process offers an exquisite control over relative amount of Au and Ag atoms being deposited by simply varying the feeding ratio of the precursors. The resultant Ag@Ag-Au core-frame nanocubes exhibit unique localized surface plasmon resonance (LSPR) property and enhanced surface enhanced Raman scattering (SERS) activity at the excitation wavelength of 785 nm.

Most significantly, we extended the co-titration to the fabrication of Ag@Ag-Pd nanocubes by co-titrating Na_2PdCl_4 and $AgNO_3$ in the presence of H_2Asc and PVP. By varying the titration volumes to both precursors, we could manipulate the elemental composition of the Ag@Ag-Pd nanocubes and thus optimize the integrated SERS activity from Ag and the catalytic activity from Pd. We demonstrated the utility of Ag@Ag-Pd

nanocubes as a dual catalytic system for catalyzing and reporting the reduction of 4-nitrothiophenol by $NaBH_4$ to 4-aminothiophenol (4-ATP) and the subsequent oxidation of 4-ATP to *trans*-4,4'-dimercaptoazobezene by O_2 from air. After we further transformed Ag@Ag-Pd core-frame nanocubes into Ag-Pd nanoframes by the removal of Ag core using 3% aqueous H_2O_2, the resultant Ag-Pd nanoframes exhibit catalytic activities toward the reduction of 4-nitrophenol to 4-aminophenol by $NaBH_4$.

The second approach involves the titration of aqueous M^{n+} precursor into an aqueous mixture of Ag nanocubes, H_2Asc, PVP, and NaOH in the pH range of 10.3-11.9. The presence of OH^- can affect the deposition of M atoms in a number of ways. For example, the H_2Asc should be neutralized by OH^- to give ascorbate monoanion ($HAsc^-$) under alkaline condition, the actual reducing agent associated with H_2Asc, achieving the condition of $R_{red} > R_{gal}$. Again, the M atoms derived from the reduction by $HAsc^-$ are sequentially deposited on the edges, corners, and side faces for the formation of Ag@M core-frame and then core-shell nanocubes.

In the case of Au deposition, with the involvement of OH^-, the titrated $AuCl_4^-$ precursor can undergo ligand exchange to generate $AuCl(OH)_3^-$ and $Au(OH)_4^-$ with lower reduction potentials and thus slower rates for both the reduction and galvanic reactions than the original precursor. In this case, galvanic replacement can still occur between the first few drops of $AuCl_4^-$ precursor and the Ag atoms situated at the corners. We argue that the released Ag^+ ions can react with OH^- instantaneously to generate Ag_2O patches at the corner sites, protecting the underlying Ag from further galvanic oxidation. After a few drops, the precursor is mostly reduced by $HAsc^-$ for the generation of Au atoms, followed by their deposition on the edges, side faces, and then corners for the generation of Ag@Au

core-frame and then core-shell nanocubes. The core-frame nanocubes can be converted to Au-based nanoframes by directly etching away the Ag. For the core-shell nanocubes, they can be transformed into Au-based nanoboxes with well-defined openings at corners by dissolving the Ag_2O patches with a weak acid, followed by the removal of Ag.

When the 40-nm Ag@Au core-shell nanocubes with Au shells of six atomic layers were transformed into Au nanoboxes with Au to Ag atomic ratios of 1:1, the resonance peak of the Ag@Au core-shell nanocubes was shifted from 447 to 1080 nm after the selective removal of Ag cores. We also used the discrete dipole approximation (DDA) method to calculate the optical spectra for a nanobox model with an outer edge length of 40 nm, a wall thickness of 2 nm, and triangular pores (10 nm in edge length) at all corners. In this calculation, we selected an atomic composition of 65%Au and 35%Ag because it was the closest composition with dielectric constants available in literature. The calculation showed that the resonance peaked at 1100 nm, in agreement with the experimental value at 1080 nm. Owing to the ultrathin wall thickness, the optical resonance of the nanobox is dominated by absorption, with a peak cross-section of 31.6×10^{-15} m^2, five times greater than those reported for Au nanocages with a similar edge length that were prepared using the galvanic replacement route.

We also demonstrated the fabrication Ag@Pt core-shell nanocubes by injecting H_2PtCl_6 into an aqueous mixture of Ag nanocubes, H_2Asc, PVP, and NaOH at an initial pH of 11.9 under ambient conditions. In this case, Pt(IV) ions quickly formed stable complexes with the nitrogen atoms in PVP, preventing them from evolving into $PtCl_5(OH)^{2-}$ and $PtCl_4(OH)_2^{2-}$ through ligand exchange with H_2O and OH^-. The Pt(IV) precursor is mostly reduced by $HAsc^-$ derived from the neutralization of H_2Asc with NaOH

under an alkaline condition. The newly formed Pt atoms are deposited onto the edges and then corners and side faces of Ag nanocubes, leading to the generation of Ag@Pt_{3L} core-shell nanocubes with a conformal Pt shell thickness of only about three atomic layers (or *ca.* 0.6 nm). After the selective removal of Ag cores using an etchant based on $Fe(NO_3)_3$, we transform the core-shell nanocubes into Pt-Ag alloy nanocages with an ultrathin wall thickness of less than 2 nm. We further demonstrated that the as-obtained nanocages with a composition of $Pt_{42}Ag_{58}$ exhibit enhanced catalytic activity toward the oxygen reduction reaction, with mass activity of 0.30 A mg^{-1} and specific activity of 0.93 mA cm^{-2}, which are 1.6 and 2.5 times greater than those of the Pt/C catalyst, respectively.

6.2 Future Directions

This work has established the scientific foundation for achieving seeded growth with two metals that are plagued by galvanic replacement reaction. By using Ag nanocubes as the model system, we demonstrated the galvanic replacement-free seeded growth of Au, Pd, and Pt on the surface of Ag nanocubes for the fabrication of Ag-based bimetallic core-frame and core-shell nanocubes and their derivatives. Moving forward, we can fabricate diversified bimetallic nanostructures by changing the experimental parameters such as the shape of the seeds, the precursor to the other metal, and the choice of capping agent. For example, we can replace the nanocubes with nanorods as the seeds to fabricate Ag@Au core-shell nanorods with tunable LSPR properties in the near infrared region for bio-sensing and imaging. On the other hand, we can deposit Pt on the Ag tetrahedral seeds for the generation of Pt-nanocages enclosed by {111} facets with desired catalytic properties. We can also extend our well-established protocols to investigate the deposition of other

transition metals such Rh, Ir, and Ru onto the surface of Ag nanocrystal seeds. Because the precursors of these elements are insoluble to water, we need to change the solvent to ethylene glycol and then revise our protocols accordingly to fabricate Ag-based core-frame and core-shell nanocubes and their derivatives.[1–3] These resultant nanoframes may find applications in catalysis. Finally, our group is investigating the role of cetyltrimethylammonium chloride (CTAC) in directing the growth of Au on Ag nanocubes for the generation of Ag-Au concave nanocubes with enhanced SERS activity. By replacing the PVP with CTAC in the standard protocol, we anticipate additional growth pathways of second metal on the Ag nanocrystals due to the selective binding of CTAC on the facets of {100} of Ag nanocrystals and possible involvement of AgCl in the syntheses of bimetallic nanocrystals.[4,5]

Another direction to pursue is to develop the scale-up production of Ag nanoparticles as the template and then achieve the large-scale synthesis of bimetallic nanocrystals for the applications in catalysis. In this work, the synthesis was mainly conducted in 23-mL vials or 60 mL-jars, with slow titration or injection of the metal precursors. Although the set-up is optimized for the syntheses of bimetallic nanocrystals at the scale of microgram, it is time consuming to achieve milligram scale required by industrial applications. In practice, it is impossible to multiply the volume of the reaction solution and size of the container because the reaction kinetics strongly depends on the mixing of reagents, temperature gradient, and the local concentration of precursors. To address the challenges, continuous flow and droplet reactors are potential solutions toward automation.[6] Advancements in this direction may ultimately bridge the gap between academic study and industrial applications.

6.3 Notes to Chapter 6

Part of the chapter is adapted from the article "Enriching Silver Nanocrystals with a Second Noble Metal" published in *Accounts of Chemical Research*.[7]

6.4 References

(1) Bonet, F.; Delmas, V.; Grugeon, S.; Herrera Urbina, R.; Silvert, P.-Y.; Tekaia-Elhsissen, K. Synthesis of Monodisperse Au, Pt, Pd, Ru and Ir Nanoparticles in Ethylene Glycol. *Nanostructured Mater.* **1999**, *11*, 1277–1284.

(2) Zhang, Y.; Grass, M. E.; Habas, S. E.; Tao, F.; Zhang, T.; Yang, P., Somorjai, G. A. One-Step Polyol Synthesis and Langmuir−Blodgett Monolayer Formation of Size-Tunable Monodisperse Rhodium Nanocrystals with Catalytically Active (111) Surface Structures. *J. Phys. Chem. C*, **2007**, *111*, 12243–12253.

(3) Viau, G.; Brayner, R.; Poul, L.; Chakroune, N.; Lacaze, E.; Fiévet-Vincent, F.; Fiévet, F. Ruthenium Nanoparticles: Size, Shape, and Self-Assemblies. *Chem. Mater.*, **2003**, *15*, 486–494.

(4) Zeng, J.; Zheng, Y.; Rycenga, M.; Tao, J.; Li, Z. Y.; Zhang, Q.; Zhu, Y.; Xia, Y. Controlling the Shapes of Silver Nanocrystals with Different Capping Agents. *J. Am. Chem. Soc.* **2010**, *132*, 8552–8553.

(5) Xia, X.; Zeng, J.; Oetjen, L. K.; Li, Q.; Xia, Y. Quantitative Analysis of the Role Played by Poly(vinylpyrrolidone) in Seed-Mediated Growth of Ag Nanocrystals. *J. Am. Chem. Soc*. **2012**, *134*, 1793-1801.

(6) Niu, G.; Ruditskiy, A.; Vara, M.; Xia, Y.; Haque, S. A.; Sloan, J.; Drury, C.; McIntyre, R.; deMello, J. C. Toward Continuous and Scalable Production of Colloidal Nanocrystals by Switching from Batch to Droplet Reactors. *Chem. Soc. Rev.* **2015**, *44*, 5806–5820.

(7) Wu, Y.; Sun, X.; Yang, Y.; Li, J.; Zhang, Y.; Qin, D. Enriching Silver Nanocrystals with a Second Noble Metal. *Acc. Chem. Res.* **2017**, *50*, 1774–1784..